

ABSTRACT

Title of Document:

**SEISMIC BEHAVIOR OF SELF-CENTERING
POST-TENSIONED ECCENTRICALLY
BRACED STEEL FRAME STRUCTURES
WITH STAINLESS STEEL FUSE MEMBERS**

Ruipeng Li,
Doctor of Philosophy, 2015

Directed By:

Yunfeng Zhang, Professor
Department of Civil & Environmental Engineering

Eccentrically braced frame (EBF) is a highly effective seismic-resistant structural system when properly designed. However, permanent drift after design basis earthquakes may affect the structure's continuous occupancy and induce very costly retrofit. To address the resilience issues, self-centering behavior is incorporated into EBF through post-tensioning to develop the self-centering eccentrically braced frame (SC-EBF) system. Post-tensioned connections are formed at the interfaces between rocking link beam and EBF beams using post-tensioned (PT) tendons. Gaps are allowed to open at these post-tensioned connections in strong earthquakes; and can be firmly closed under the re-centering force of the PT tendons. The columns, beams, braces, and the rocking link beam are designed to behave elastic under the design basis earthquake. Therefore, no

residual drift is expected to occur in the SC-EBF system and damage is concentrated to replaceable fuse members.

The proposed SC-EBF system provides a competitive design option in high seismic hazard regions with its self-centering behavior, stiffness and strength comparable to conventional EBF structural systems, and tunable energy dissipation capacity provided by conveniently replaceable fuse devices made of highly ductile AISI 316L stainless steel which are designed to utilize the large deformation in the SC-EBF systems for energy dissipation during strong earthquakes. It is observed that the ductility of the SC-EBF with short rocking link beam is generally lower than that of the SC-EBF with longer rocking link beam if the same PT tendon length is used for both cases.

To take advantage of the SC-EBF systems with short rocking link beam and with long rocking link beam, a modified design of the SC-EBF with two parallel short rocking link beams is proposed. Nonlinear finite element analysis was conducted, showing that this type of SC-EBF system exhibits improved self-centering performance, strength, ductility, and energy dissipation behaviors. The fuse members are redesigned with simple configuration, ease of fabrication and installation.

SEISMIC BEHAVIOR OF SELF-CENTERING POST-TENSIONED
ECCENTRICALLY BRACED FRAME STRUCTURES WITH
STAINLESS STEEL FUSE MEMBERS

By

Ruipeng Li

Dissertation submitted to the Faculty of the Graduate School of the
University of Maryland, College Park, in partial fulfillment
of the requirements for the degree of
Doctor of Philosophy
2015

Advisory Committee:

Professor Yunfeng Zhang, Chair/Advisor
Professor Sherif M. Aggour
Professor Amde M. Amde
Professor Chung C. Fu
Professor Sung Lee

ACKNOWLEDGEMENTS

I would like to take this opportunity to express my sincerest appreciation to my advisor, Dr. Yunfeng Zhang, who has always guided, challenged and encouraged me. I also thank Dr. Aggour, Dr. Amde, Dr. Fu and Dr. Lee for their valuable time serving on my dissertation committee and providing their insight and comments.

I cherish the University of Maryland in which I had some of the best experiences of my lifetime. I would like to express my gratitude to Department of Civil and Environmental Engineering for granting me with A. James Clark School Fellowship, providing me with the great experience, and for the Structural Engineering Laboratory facilities in which the experimental tests of this study were conducted. I also appreciate the state key laboratory for Disaster Reduction in Civil Engineering, Tongji University for providing the experiments on stainless steel specimens and cast steel link beams.

Table of Contents

ACKNOWLEDGEMENTS	II
CHAPTER 1 INTRODUCTION	1
1.1. Introduction.....	1
1.2. Research Motivation.....	3
1.3. Research Objectives.....	5
1.4. Organization of the Dissertation.....	7
CHAPTER 2 : LITERATURE REVIEW	11
2.1. Constitutive Modeling of Stainless Steel.....	11
2.2. Shear Link & Steel Plate Shear Wall Research.....	13
2.2.1. Conventional Shear Link.....	13
2.2.2. Shear Links with Reduced Web sections.....	15
2.2.3. Steel Plate Shear Walls with Reduced Web Sections.....	16
2.3. Research on Self-Centering Structures.....	19
CHAPTER 3 : MECHANICAL CHARACTERIZATION OF AISI 316L STAINLESS STEEL UNDER LARGE INELASTIC STRAINS	38
3.1. SS316L Experiment.....	38
3.2. Test Results.....	42
3.3. Engineering Material Properties Determination.....	42
3.4. Plasticity Hardening Model.....	45
3.5 Void Growth Model (VGM) and Parameter Calibration.....	52

3.6. Cyclic Void Growth Model (CVGM) and Parameter Calibration.....	54
3.7. Characteristics Length l^*	56
3.8. Model Validation of VGM and CVGM for Q345 Steel.....	57
CHAPTER 4 : NUMERICAL SIMULATION OF CYCLIC LOADING BEHAVIOR OF LINK BEAM WITHOUT WEB PERFORATION.....	80
4.1. ASTM A992 Steel Shear links.....	80
4.2. AISI 316L Stainless Steel Shear Links.....	89
4.3. Cast Steel Shear Links.....	92
4.4. Relation to Next Chapter.....	96
CHAPTER 5 : LINK BEAMS WITH WEB PERFORATIONS.....	125
5.1. Stainless Steel Link Beams with Perforated Circular Holes.....	126
5.2. Perforated Stainless Steel Link Beams with Web Slits.....	135
5.3. Cast Steel Shear Links with Perforated Circular Holes.....	148
5.4. Cast Steel Link Beams with Perforated Slits.....	154
5.5. Relation to the Next Chapter.....	158
CHAPTER 6 : NONLINEAR FE ANALYSIS OF SELF-CENTERING ECCENTRICALLY BRACED FRAMES UNDER CYCLIC LOADING.....	231
6.1. Introduction.....	231
6.2. Case Study on K-type SC-EBF Structures.....	234
6.3. Case Study on D-type SC-EBF Structures.....	256
6.4. Limit States of the SC-EBF Structure.....	264
6.5. Relation to the Next Chapter.....	265
CHAPTER 7 : NONLINEAR FE ANALYSIS OF THE SELF-CENTERING	

ECCENTRICALLY BRACED FRAMES WITH TWO ROCKING LINK BEAMS UNDER CYCLIC LOADING	298
7.1. Introduction.....	298
7.2. Case Study on the K-type SC-EBF Structure with Two Short Rocking Link Beams.....	299
CHAPTER 8 : SUMMARY, CONCLUSIONS, AND FUTURE WORKS	332
8.1. Research Summary.....	332
8.2. Outcomes and Conclusions.....	336
8.3. Recommendations for Future Research.....	339
REFERENCE	340

Chapter 1 Introduction

1.1. Introduction

Growing needs and interests in structural damage control have facilitated the development and use of highly ductile replaceable fuse devices into fruition for seismic resilient structures, in which the main gravity carrying structural components would remain elastic during design basis earthquakes. Examples of such structural systems include concentrically braced frames (CBF) with buckling restrained braces and eccentrically braced frames (EBF) with replaceable link beams. EBFs combine the advantages of moment resisting frame (MRF) and CBF which provide high ductility and stiffness of the structures, and make them a very competitive seismic force resistant system to use in seismic active region. The other benefit of EBF versus CBF is the more flexible architectural design that allows for windows and openings. High ductility and stiffness of the EBFs are provided by the link beams between two braces or between brace and column. Link beams develop large plastic deformation and thus play sacrificial role to provide the required ductility and energy dissipation for the entire structure.

Ductile seismic design traditionally relies on the plastic deformation of structural members at selected locations for seismic energy dissipation, which would inevitably cause permanent deformation in the structural system after a strong earthquake like design basis earthquake. For instance, residual drift is induced to the EBF system due to the severe plastic deformation of the link beam. Large residual drift not only compromise the aesthetic appearance of the affected structure and disrupt continuous occupancy, but

also requires financially costly retrofit work. Hence, development of high performance low-damage seismic resistant structure system that can concentrate the damage in replaceable fuse devices and remain damage free in primary gravity load carrying system is very appealing to addressing the need for resilient civil infrastructure.

In line with the current research trend for seismic resilient structure, the concept of self-centering eccentrically braced frames (SC-EBF) is examined in this study. Very few research has been done in the past on SC-EBF partly due to the high demand on link beam rotation, especially for short links. The SC-EBF systems under current investigation possess the same structural properties (i.e., stiffness and strength) compared to conventional EBF systems under low to moderate seismically induced lateral load, and have negligible residual drifts after the design basis earthquake. To cope with the large link rotation demand, replaceable fuse devices in the SC-EBF systems are made of highly ductile AISI 316L stainless steel and are carefully designed to accommodate the large deformations of the SC-EBF systems. Stainless steel is chosen here for the fuse devices because of its high corrosion resistance and high strength and ductility, which permits the use of lighter sections to dissipate comparable amounts of seismic energy and thus easy to be replaced. Special configurations are conceived to tune the performance of fuse devices made of AISI 316L stainless steel, including circular hole perforations and slit perforations in the fuse web.

Compared to conventional EBF systems, the SC-EBF systems are believed to outperform with the following advantages: 1) self-centering mechanism is introduced so that no or

little residual drift exists after the design basis earthquake; 2) damage in the structural system is concentrated to the fuse devices that can be inspected and replaced very easily. Other structural components are designed to remain elastic during a design basis earthquake; 3) the strength, stiffness, ductility and energy dissipation properties of the SC-EBF can be tuned with more flexibility than the conventional EBF.

1.2. Research Motivation

A comprehensive study has been performed on the behaviors of self-centering moment resisting frames (SC-MRF). The self-centering behavior of the one bay one story self-centering moment resisting frame (SC-MRF) taken from the multi-story prototype structure was experimentally and analytically studied by many researchers (e.g., Christopoulos et al. 2002, Ricles et al. 2002, Garlock et al. 2007, and Kim and Christopoulos 2008), and design methods were also proposed for the design of the SC-MRF systems (Garlock et al. 2007; Kim and Christopoulos 2009). However, MacRae and Clifton (2013) pointed out that the composite effect of the beam slab intersection would result in unacceptable column damage or slab damage. Moreover, in the multiple-story SC-MRF system, as the depth of girder sections were generally larger in the lower floors and smaller in the upper floors, the girders in the upper floors tend to be pulled away from the column when columns were designed to be very rigid, which could result in serious problems such as the falling of the partial story. According to MacRae and Clifton (2013), the variation in gap opening values among different floor levels is related to the girder depth difference and varying inter-story drift ratio along building height. To

mitigate this problem, complex design has been proposed for floor and columns by MacRae and Clifton (2013).

SC-EBF is proposed with the expectation of overcoming the above identified problems in the SC-MRF systems. Compared to the main girders in the SC-MRF systems, the rocking link beams in the SC-EBF systems are much shorter and can be designed to have the same depth along building height without significantly increasing the design budget, in order to eliminate the gap opening discrepancy at different floor levels. Furthermore, instead of providing special design for the entire floor slab and collector beams proposed for the SC-MRF systems, only the floor slab in the vicinity of the link beam needs special design in the SC-EBF, which substantially reduces the work for floor design and construction. However, currently only one research work (Cheng et al. 2012) is reported on investigating the behaviors of SC-EBF systems under seismic load, more research needs to be done to make this promising SC-EBF systems a reality by providing knowledge base that could support design and construction for real-world adoption.

On the other hand, the energy dissipation capacity of the self-centering structures is generally lower than the conventional seismic resistant structures (Seo and Sause 2005) due to their typical flag-shaped hysteresis and usually fuse devices are provided externally to ensure a minimum of 12.5% hysteretic energy dissipation ratio to prevent excessive ductility demands (Seo and Sause 2005). For the SC-EBF systems, as substantial rotation demand would occur at the link beam location, large deformation capacity is required for the installed fuse devices. The use of highly ductile materials

such as stainless steel is ideal for such fuse devices, because of its highly ductile deformation capacity up to 50% strain. Furthermore, to reduce the risk of fracture at the heat treatment zone due to welding, hot-rolled sections of stainless steel is preferred for fuse devices. To obtain particular stiffness and strength values of the fuse devices specified by the SC-EBF design, circular perforations or slit perforations can potentially be utilized to tune the properties of fuse devices. Similar approaches have been used by other researchers in modifying the link beam for conventional EBF design by Vian et al. (2009), Jacobsen et al. (2010), and Bhowmick et al. (2014). Along this line, the behaviors of stainless steel link beams with a variety of perforation patterns are examined in this study; nonlinear static analysis of a one-story SC-EBF frame equipped with fuse devices with circular perforations or slit perforations are conducted to demonstrate the seismic performance and the occurrence of different limit states.

1.3. Research Objectives

This dissertation pursues the following two objectives with an emphasis on establishing the design and knowledge base of a low-damage SC-EBF system with replaceable fuse devices specially designed for sustaining large deformation demand:

1. The first objective is to develop stainless steel fuse links that can sustain large deformation demand as usually encountered in EBF. For this purpose, a highly ductile material – AISI 316L stainless steel is first identified and experimental test data verifies its suitability for use in the fuse link beam. Analytical expressions are formulated to quantify the link beam’s load-deformation behavior and validate the finite element model.

Four key parameters that characterize the load-deformation behaviors of AISI 316L stainless steel link beams are stiffness, strength, ductility, and energy dissipation capacity. To enable nonlinear finite element analysis, constitutive model is calibrated against experimental data from both monotonic and cyclic loading of stainless steel coupon. To adjust the mechanical property of stainless steel fuse device, circular perforation or slit perforation is employed. Because low-cycle induced fatigue crack (i.e., ductile fracture) is viewed as an important failure model for the perforated or slit link beams, a micro-mechanical fracture model termed void growth model is adopted here to determine the ductile fracture initiation point of the stainless steel link beams under monotonic or cyclic loading conditions. . To optimize the stainless steel fuse device configuration, stainless steel link beams with varying parameters values including length ratio, web perforation pattern, and lateral restraint type are investigated via the finite element analysis.

2. The second objective is to investigate the nonlinear static behaviors of one-bay one-story prototype SC-EBF frame equipped with replaceable stainless steel fuse devices through finite element analysis and to establish the performance goals of SC-EBF system under different load levels. A parametric study is conducted on the prototype SC-EBF frame with two types of link beams and varying post-tensioned (PT) strand area.

Different designs of fuse devices are examined for use in the prototype SC-EBF frames. The effects of the control parameters in the SC-EBF design, including the PT strand area and initial PT stress, as well as link beam length, are quantified. Performance limit states are defined accordingly and analytical formulas to calculate the lateral force vs.

displacement relationship of the SC-EBF systems are derived and presented with the goal of facilitating future design of such SC-EBF systems.

1.4. Organization of the Dissertation

In this study, finite element simulations are conducted on various link beams made of different steel materials for their performance assessment. Experiments data from cyclic testing of full-scale cast steel link beams were used for validating the analytical formulas and finite element analysis results on the link beams' behaviors. The behaviors of different designs of SC-EBF systems are studied through nonlinear static analysis of finite element models.

Chapter 2 reviews previous research work on the material plasticity theory for characterizing the material strain hardening effect, micro-mechanical fracture models in predicting the low-cycle fatigue fracture, experiments conducted on A992 steel, cast steel, and A36 steel for monotonic and cyclic stress-strain relationship characterization, performance of various conventional and perforated steel plate shear walls and shear links, current research and achievements in SC-MRF systems, and pilot study on SC-EBF systems.

Chapter 3 describes the material coupon tests conducted on AISI 316L stainless steel specimens to determine its mechanical properties. The AISI 316L stainless steel coupon specimens include standard tensile coupon bar for uniaxial tension test, specially designed short-gauge-length round bars for cyclic loading test, and circumferentially

notched round bars for both monotonic tension and cyclic loading tests. Plastic strain hardening models for AISI 316L stainless steel were calibrated against the experimental stress-strain data obtained from cyclic loading tests on short-gauge-length round bars. Micromechanics-based models were calibrated with the test results of the notched round bars. With reference to the results of the material coupon test conducted on A992 steel, cast steel, and A36 steel (Kaufmann 2001, Sun and Wang 2015), plastic strain hardening models are calibrated for these materials and presented in this chapter.

Chapter 4 presents the finite element simulation results of conventional link beams made of A992 steel and AISI 316L stainless steel respectively. Four different designs of link beams with the varying link length e ($e=1.3M_p/V_p$) and section sizes are considered. Performances of conventional link beams are evaluated and analytical formulas are derived to predict the link beams' behaviors.

Chapter 5 presents the numerical study results on link beams with perforated web sections. Two types of web perforation methods are considered: perforated web sections with circular holes and perforated web sections with longitudinal slits. Ductile fracture initiation predicted by the micromechanics-based fracture model is viewed as one of the important failure modes of the perforated link beams. Factors affecting the perforated link beams' behaviors are assessed, including perforated circular hole diameter, hole spacing, and stiffener spacing for the perforated link beams with circular holes, and slit length, slit width, and slit spacing for the perforated link beams with longitudinal slits. Theoretical expressions are derived to predict the behaviors of the link beams with

different perforation patterns. Experimental data from cyclic load test of perforated cast steel link beams are used to verify the accuracy of the proposed theoretical formulas as well as finite element analysis results.

Chapter 6 involves finite element simulation study of one-bay one-story prototype SC-EBF frames and target performance goals for SC-EBF design under different earthquake intensity levels. Two SC-EBF frame designs are considered. The first type of the SC-EBF system is modified from the SC-EBF frame studied by other researcher, which contains one rocking link beam in a K-type EBF configuration. The second type of the SC-EBF system is for comparison with the first one, which contains one rocking link beam in a D-type EBF configuration. Specific designs of fuse devices are proposed for each type of the concerned SC-EBF systems. The main structural members of the SC-EBF frame are made of ASTM A992 steel while the fuse devices are made of AISI 316L stainless steel. Target performance goals are proposed for both types of SC-EBF systems on the basis of the analytical relations derived for predicting their behaviors under pushover load.

Chapter 7 presents a different K-type SC-EBF system in that it has two parallel rocking link beams and the two link beams rotate in parallel with each other under the lateral load. Fuse devices are installed between its two rocking link beams. This type SC-EBF system is more ductile than the K-type SC-EBF system with short rocking link beam, and has higher initial stiffness and strength than the K-type SC-EBF system with long rocking link beam.

Chapter 8 presents the summaries and conclusions of this dissertation research, and suggestions for possible future research work.

Chapter 2 : Literature Review

This chapter begins with introducing previous research in characterizing the constitutive relationship of stainless steel, followed by current research on structural steel shear links and steel plate shear walls. In the last section of this chapter, current research on self-centering structures, including the advantages for seismic resistant structural systems and potential problems with the self-centering moment resisting frames (SC-MRF), self-centering eccentrically braced frames (SC-EBF), self-centering reinforced concrete rocking walls, and self-centering concentrically braced frames (SC-CBF), is presented.

2.1. Constitutive Modeling of Stainless Steel

Ramberg and Osgood (1943) proposed the expression given in Equation 2-1 for characterizing the nonlinear stress-strain relationships of materials, where E_0 is the material's elastic modulus and K and N are constants. The most commonly used version of Ramberg-Osgood Equation for characterizing the stress-strain relationship of stainless steel is expressed in Equation 2-2, where $\sigma_{0.2}$ is the stress value corresponding to 0.2% plastic strain and n is the calibrated material constant. The Ramberg-Osgood equation provides accurate prediction on the stress strain relationship of stainless steel up to $\sigma_{0.2}$, while it significantly over-estimates the stress values beyond that level, which is revealed by the experiments conducted by Rasmussen (2003). The discrepancies between the stress-strain curve predicted by the Ramberg-Osgood equation and the stress-strain curve obtained from the experiment on AISI 304L stainless steel are plotted in Figure 2-1 (Rasmussen 2003).

$$\varepsilon = \frac{\sigma}{E_0} + K \left(\frac{\sigma}{E_0} \right)^N \quad \text{Equation 2-1}$$

$$\varepsilon = \frac{\sigma}{E_0} + 0.002 \left(\frac{\sigma}{\sigma_{0.2}} \right)^n \quad \text{Equation 2-2}$$

Mirambell and Real (2000) modified the Ramberg-Osgood equation and proposed the expression for predicting the stress-strain relationship of stainless steel after the $\sigma_{0.2}$ point. The stress-strain relation after the $\sigma_{0.2}$ point suggested by Mirambell and Real (2000) is expressed in Equation 2-3.

$$\varepsilon = \frac{\sigma - \sigma_{0.2}}{E_{0.2}} + \varepsilon_u \left(\frac{\sigma - \sigma_{0.2}}{\sigma_u - \sigma_{0.2}} \right)^m + \varepsilon_{0.2} \quad \text{Equation 2-3}$$

Where ε_u is the plastic strain at ultimate strength; m is the strain hardening parameter; and $E_{0.2}$ is the tangent stiffness at $\sigma_{0.2}$.

Rasmussen (2003) modified the Ramberg-Osgood model extended by Mirambell and Real (2000) and did tensile tests on a variety of stainless steel coupons to calibrate the material constants of the constitutive model for stainless steels. Based on the experimental results, different formulas were proposed by Rasmussen to determine the material coefficients in Equation 2-2 and Equation 2-3, which are expressed in Equation 2-4. The mechanical properties determined by Rasmussen (2003) for several types of stainless steels are listed in Table 2-1.

$$n = \frac{\ln(20)}{\ln(\sigma_{0.2}/\sigma_{0.01})}$$

$$e = \frac{\sigma_{0.2}}{E_0}$$

$$E_{0.2} = \frac{E_0}{1 + 0.002n/e}$$

$$m = 1 + 3.5 \frac{\sigma_{0.2}}{\sigma_u}$$

Equation 2-4

Ellis et al. (1977) performed monotonic and cyclic biaxial loading test on AISI 316 stainless steel at room temperature. Ellis et al. (1977) concluded that the Von Mises yield criterion provides an accurate characterization of the AISI 316 stainless steel's yield behavior while careful attention should be paid to the loading rate as significant time-dependent deformations occurred during the hold periods at the constant stress level. Chaboche and Rousselier (1983) conducted cyclic strain-controlled test on AISI 316 stainless steel coupon bars and verified that the yield surface was characterized by the Von Mises yield criterion; significant isotropic hardening effect was induced during cyclic loading; and the cyclic stress-strain curves varied with the strain rate and the mean strain level. The cyclic stress strain relationship obtained from the experiment conducted by Chaboche and Rousselier (1983) is plotted in Figure 2-2.

2.2. Shear Link & Steel Plate Shear Wall Research

2.2.1. Conventional Shear Link

Hjelmstad and Popov (1983) performed experimental investigations on the inelastic behaviors of short wide-flange steel beams which were commonly used in EBFs. The

sections of the investigated shear links varied from W12x22 to W18x40. The investigated link beams were under increasing cyclic loading until failure occurred, such as severe web buckling or web fracture. Hjelmstad and Popov (1983) concluded that the unfavorable inelastic web buckling could be controlled by providing web stiffeners which substantially enhanced the shear links' capability in energy dissipation.

Malley and Popov (1984) conducted intensive experiments on W18x40 shear links with varying stiffener details, connection details, and loading histories and then developed the design procedure for shear links in the applications of EBFs. Recommendations were made on determining the appropriate EBF structural configurations, member sizes, link connection details, and web stiffener details. Kasai and Popov (1986) further investigated the cyclic web buckling control for shear link beams with varying section sizes and proposed a simplified equation that can be used to determine the proper spacing of web stiffeners for shear links.

Richards and Uang (2006) performed a series of cyclic loading tests on W14 shear links under different loading protocols. The loading protocol in AISC Seismic Provisions (2002) was found to result in underestimation of the shear links' inelastic rotation capacity. A modified cyclic testing protocol was proposed by Richards and Uang (2006) and is currently adopted by AISC Seismic Provisions (2010).

Mansour et al. (2011) conducted a series of tests on replaceable links used in EBF systems and MRF systems. The replaceable links were bolted between the beams in the

EBF systems. It was found that the replaceable links exhibited behaviors similar to conventional welded links in the EBF systems (Mansour et al. 2011).

2.2.2. Shear Links with Reduced Web sections

Prinz and Richards (2009) performed nonlinear finite element analysis on a series of web-perforated 635 mm long W18x40 links with column connections and with varying hole alignment pattern and hole diameter under the cyclic loading protocol prescribed by AISC Seismic Provisions (2005). The stress modified critical strain (SMCS) criterion was adopted to determine the ultimate state which is the fracture initiation of the perforated links with column connections (Prinz and Richards 2009). The predicted ultimate link rotation was generally low (Prinz and Richards 2009), which was around 0.04 radians, as the SMCS model tends to over-estimate the cyclic stress triaxiality level of the materials (Kanvinde and Deierlein 2007) and the loading protocol in AISC Seismic Provision (2005) imposed higher ductility demands on shear links (Richards and Uang 2006). Prinz and Richards (2009) evaluated the plastic yield strength values of different perforated shear links and concluded that the strength deduction caused by web perforation was related to the web area perforation ratio. Furthermore, Prinz and Richards (2009) concluded that the perforated links exhibited a different failure mode from the imperforated ones.

Henry et al. (2010) performed nonlinear finite element analysis and experimental validations on the slotted flexural plates, the flexural plates with holes, the J-shaped flexural plate, and the oval-shaped flexural plate which were made of structural steel and

used as the energy dissipation devices in the self-centering precast concrete walls. Fuse devices were installed between two adjacent precast concrete walls and dissipated energy once the concrete walls rocked relative to each other. The large relative deformations between the precast concrete walls imposed very high ductility demands for the fuse devices, and Henry et al. (2010) found that only the J-shaped flexural plate and the oval-shaped flexural plate were capable of undergoing the required large deformations before failure. Hence the approach of tuning the strength and stiffness properties of link beams via web perforation appears to be less appealing in link beams made of ordinary structural steel.

Tsavdaridis and D'Mello (2012) performed finite element analysis in search of the optimized design of perforated links with reduced web sections. Numerical simulations were performed to the link beams with standard and non-standard web opening shapes. Tsavdaridis and D'Mello (2012) found that the perforated links with vertical and inclined elliptical web openings (3:4 width to depth ratio) behaved more efficiently in energy dissipation than the perforated link beams with circular and hexagonal web openings.

2.2.3. Steel Plate Shear Walls with Reduced Web Sections

Perforated slits and perforated circular holes are two typical perforation patterns used in the perforated steel plate shear walls. The energy dissipation mechanisms were different for these two types of perforated shear walls. Vian et al. (2009) and Bhowmick et al. (2014) hypothesized that for the perforated shear walls with circular holes, the applied lateral load was resisted by the tension and compression forces developed along the paths

between the diagonally aligned holes. The imposed seismic energy was dissipated by the tension-compression behaviors of the web paths. Jacobsen et al. (2010) and Ke and Chen (2014) stated that the imposed seismic energy to the perforated structural steel shear walls with vertical slits was dissipated by the strips which were in between of the perforated slits and behaved as a series of flexural links. Jacobsen et al. (2010) performed experiments on the perforated structural steel shear walls with vertical slits under increasing cyclic displacement. The gradual peeling off of the paint near the ends of the perforated slits indicated that plastic hinges were formed at the strip ends and were expanding with the increasing of the applied load.

Alavi and Nateghi (2013) conducted experiments and numerical simulations on three types of shear walls, including an un-stiffened imperforated shear wall, a stiffened imperforated shear wall, and a stiffened perforated shear wall with a circular opening in the center. The perforated shear wall was verified to possess adequate ductility and the analytical equation in predicting the strength of the perforated shear wall was proposed thereby (Alavi and Nateghi 2013).

Further investigation on analytically predicting the shear strength of the perforated shear walls with circular holes were conducted by Vian et al. (2009) and Bhowmick et al. (2014). Based on the experiment results of the shear walls with various perforated hole diameter and spacing, Vian et al. (2009) performed linear regression on the experiment results of the strength ratios of the perforated shear walls to the imperforated shear walls versus the perforation characteristics and concluded that the shear strength values of the

perforated shear walls were proportionally reduced by the ratio of the perforated hole diameter to the hole spacing. The relationship between the strength ratio of the perforated shear wall to the conventional shear wall (V_{yp_perf}/V_{yp}) and the perforated hole diameter to spacing ratio (D/S_{diag}) is plotted in Figure 2-3 (Vian et al. 2009). It is seen that within the D/S_{diag} range between 0.2 and 0.7, a strong linear correlation is suggested between V_{yp_perf}/V_{yp} and D/S_{diag} .

Bhowmick et al. (2014) performed numerical investigations on the perforated shear walls with similar dimensions to the perforated shear walls investigated by Vian et al. (2009). Under the assumption that the tension ties which were developed in between of the diagonally aligned perforated circular holes provided the lateral load resistance of the perforated shear wall, Bhowmick et al. (2014) concluded that the strength of the perforated shear wall is linearly related to the ratio of the net length to the full length at the perforated section, which is essentially the same as the conclusion drawn by Vian et al. (2009).

Koppal and Eatherton (2013) proposed a different perforation design for the perforated shear wall. Circular or hexagonal perforations were only made along the edges of the infill steel plate. High plastic strains were concentrated within the “butterfly” sections in between the perforated holes or hexagons while buckling is triggered within the center infill plate. The “butterfly” sections served as energy dissipation devices and the shear strength and lateral stiffness of the perforated shear wall were contributed from both the infill plate and the “butterfly” section. It was verified that this type of perforation design

also provided tunable properties of the perforated shear walls (Koppal and Eatherton 2013).

2.3. Research on Self-Centering Structures

2.3.1. Self-Centering Moment Resisting Frame (SC-MRF)

Seismic energy is expected to be dissipated by the plastic hinges formed at the beam ends in a conventional MRF, which causes permanent deformations at the beam ends and may lead to residual drift in the MRF under large loading. In the SC-MRF systems, beams are not welded or bolted to the columns; instead, the posttensioned (PT) strands compress the beams and columns to be in contact and form rigid connections between them. The SC-MRF behaves exactly the same as the conventional MRF under low to moderate lateral load before gap opening. Under large lateral load, instead of allowing plastic deformations to form near the beam ends, all primary structural members in the SC-MRF systems remain elastic after gaps are formed between the beams and the columns. The post-gap-opening tangential lateral stiffness of the SC-MRF is provided by the force couple between the tension force within the PT strands and the compression force over the contact surface, which is tunable and is generally much lower than the SC-MRF's elastic stiffness. Unlike the conventional MRF systems, gaps formed in the SC-MRFs are closed after the lateral load is reduced below a critical level and ideally since all structural components remain elastic during the loading process, no damage is induced to the SC-MRF system except for fuse members and no or very little residual drift would happen.

Comprehensive studies were conducted on investigating the behaviors of the SC-MRF systems. Ricles et al. (2002) developed a post-tensioned (PT) steel moment connection. In the PT steel moment connection, high strength steel strands were post-tensioned and aligned along the two web sides of the beams. Seat angles were bolted between the floor beams and columns to facilitate shear force transfer and serve as energy dissipaters. The test set up in the research conducted by Ricles et al. (2002) is plotted in Figure 2-4; and the experimental hysteresis loop at the maximum drift of 3% is plotted in Figure 2-5. As observed in Figure 2-5, the PT moment connection exhibited good stiffness, strength, and self-centering behavior.

Rojas et al. (2004) performed numerical analysis on the behaviors of a six-story MRF with post-tensioned friction damped connections (PFDC-MRF) under different recorded earthquake ground motions. The seismic behaviors of the PFDC-MRF were compared with the seismic behaviors of the six-story special moment resisting frame with welded connections (FR-MRF). Rojas et al. (2004) observed that the maximum inter-story drifts of both types of MRFs were identical under each given earthquake ground motion record, yet the stabilized drift of the PFDC-MRF after the peak ground motion was much smaller, manifesting that the inelastic response and the permanent deformation were not involved. The comparison on the responses of the two types of MRFs under a given earthquake record is plotted in Figure 2-6. The research conducted by Rojas et al. (2004) further verified the advantages of self-centering MRFs.

Garlock et al. (2007) proposed design principle and design methodology for the designing of self-centering moment resisting frame (SC-MRF). The performance limit states of the SC-MRF were categorized into three classifications: performance that conforms to immediate occupancy (IO) level, performance that conform to the collapse prevention (CP) level but not IO level, and performance that does not conform to the CP level. Connection decompression and angle yielding were permitted at the IO level. Yielding of the collector beams, columns, and panel zones, fracture of the angles, and excessive drift beyond the IO limits were regarded as the performances conforming to the CP level but not IO level. While beam local buckling, PT strand yielding, and the excessive drift beyond the CP limits were regarded not conforming to the CP level. Garlock et al. (2007) conducted a nonlinear time history analysis on the prototype SC-MRF designed with the proposed design procedure and verified that the design method provided conservative estimations on the internal forces within the SC-MRF and the maximum drift ratio.

Kim and Christopoulos (2008) experimentally evaluated the behaviors of the post-tensioned moment resisting connections. No residual drift was observed within the self-centering limit. At the maximum considered earthquake level, which is beyond the self-centering limit, plastic hinges were formed within the beam ends and the yielding of the prestress strands and buckling of the beams were prevented. The post-tensioned moment resisting connection under investigation exhibited stable and good energy dissipation capacity.

Although the beam/column assemblies without slabs exhibited very good self-centering behaviors during the experiments, deformation discontinuities and incompatibilities occurred when slabs were connected to the beams or multiple bays and stories were considered in a structure (MacRae and Clifton 2013). Generally the girders at the higher levels of the SC-MRF have smaller depth values than the girders in the lower levels. In the case when the columns are very rigid, the discontinuity in the gap opening distance occurs in the higher levels, which is shown in Figure 2-7. Furthermore, when the composite sections between the floor slabs and the beams are considered, as the floor slabs are far stiffer than the beams but the elastic deformations of the slabs are much smaller than the target gap opening distance, the deformation incompatibility occurs between the beams and slabs, leading to the excessive cracking of floor slabs, which is unacceptable in the damage resistant design; or the failure of the gap openings between the beams and columns, which further results in the damage of columns or beams, is also unacceptable in the damage resistant design. The slab cracking of the SC-MRF system composited with concrete slabs was observed from the test conducted by Clifton (2005), which is plotted in Figure 2-8.

The deformation discontinuity shown in Figure 2-7 is equal to the girder depth difference times the drift ratio if the columns are assumed to be perfectly rigid. Hence changing all the girders to have the same depth would be the most effective approach in solving the deformation discontinuity problem. However, in the MRF design, as lower load is transferred from the girders at higher levels, these girders are sized with smaller sections for economic concerns. Typically the girders are long, so changing all the girders to have

the same depth would be uneconomical. MacRae and Clifton (2013) suggested columns at the higher levels being designed less laterally rigid so that the deformation discontinuity can be accommodated. However, this will complicate the design procedure for columns in the MRF.

Regarding the floor slab cracking issue, MacRae and Clifton (2013) suggested two approaches in solving the deformation incompatibility problem between the floor slabs and beams in the seismic-resistant frames. The first option involves the disconnecting between the floor slabs and the collector beams in the gravity load-carrying frames, which is illustrated in Figure 2-9. The floor slabs are only connected to the seismic-resistant frames and after the gap opening, the floor slabs move along with the seismic resistant frame. Since collector beams and the gravity frames are disconnected from the floor slabs, the movement of the floor slabs will not be restrained; hence floor slab cracking will not occur. Although this option seems attractive, the lateral force transferred within certain segments of the seismic resistant frames is substantially increased, which increases the strength demands of the seismic resistant frames. Furthermore, this option significantly complicates the construction process to make the floor slabs theoretically isolated from the gravity load-carrying frames and the collector beams, which is very difficult in the real implementation. For a real structure in the three-dimensional space, the implementing of this method in two transverse directions becomes even more difficult.

The second option suggested by MacRae and Clifton (2013) involves of the floor slabs being connected only to the gravity load-carrying frames. Shown in Figure 2-10, under the lateral load, the floor slabs act as diaphragms and first transfer the lateral load to the gravity load-carrying frames and then the gravity load-carrying frames transfer the lateral load to the seismic-resistant frames via the collector beams. Since the floor slabs are only connected to the gravity frames and the associated collector beams, the beam elongation due to gap opening at the seismic-resistant frames has little effect on the deformation of the floor slabs. However, the drawback of this option is also obvious. The lateral load transfer system from the floor slabs to the seismic-resistant frames is very complicated, and the successful operation of this lateral force transfer system and the gap opening at the seismic-resistant frames are highly dependent upon the stiffness of the collector beams. If the collector beams are too stiff, the deformation of the beams at the seismic-resistant frames are significantly restrained, so gaps will not open between the beams and columns which results in column damage. On the contrary, if the collector beams are too flexible, then barely little lateral load can be transferred into the seismic-resistant frame and excessive lateral deformations will be induced to the floor slabs, i.e., the floor slabs have the tendency of flying out. Similarly, this design option imposes a significant challenge in the construction process to ensure the desired slip planes are achieved and becomes even more complicated in the two directions of the real structure.

2.3.2. Self-Centering Eccentrically Braced Frame (SC-EBF)

As indicated in the first chapter, self-centering EBF (SC-EBF) systems are proposed to solve the problems identified in the SC-MRF systems. Similar to the SC-MRF systems, the SC-EBF systems possess the same stiffness and strength properties as conventional EBF systems before gap opening between the link beam and the beams. After gap opening is triggered, the stiffness of the SC-EBF is controlled by the link beam's depth and the PT strand area, which is tunable and is generally much smaller than the elastic stiffness of the SC-EBF; hence the base shear in the SC-EBF is significantly reduced. The tension force in the PT strands provides the restoring force to re-center the structure. Similar to the SC-MRF systems, all major structural components (fuse members excluded) in the SC-EBF systems remain elastic during the cyclic loading process and no residual drift is induced under design load.

The deformation discontinuity at higher levels and the deformation incompatibility between the floor slab and the seismic-resistant frames may also occur in SC-EBF systems; however, these problems can be solved at much lower cost in SC-EBF systems. In the SC-EBF systems, since the link beams are designed with large sections and are generally short, designing all the link beams to have the same height is economically acceptable, which completely diminishes the deformation discontinuity between different floor levels. Hence columns do not have to be specially designed to accommodate the deformation discontinuity. As the lateral force is primarily resisted by the braces in the SC-EBF systems, which is no different from the conventional EBF systems, conventional

construction procedure is still applicable to the SC-EBF systems to create composite sections between the floor slabs and the floor beams in the gravity load-carrying frames and seismic-resistant frames. The only change is to cut the floor slabs apart at the link beam sections of the seismic-resistant frames. In doing so, the lateral load transferring system is not interrupted and each separated floor slabs can move along with the floor beams in the seismic-resistant frames.

Cheng et al. (2012) conducted an experimental investigation on a prototype self-centering eccentrically braced frames (SC-EBF) installed with friction energy dissipation devices. The post-tensioned joint connections are formed at the interfaces between the central link beam and the adjacent beams. The test setup for the prototype SC-EBF frame is plotted in Figure 2-11. The prototype SC-EBF frame has a span of 5.15 m and the height of 3.2 m. The length of the link beam is 2 m. The cross sections for the columns, link beam, floor beams, and braces are 400x400x13x21 mm, 400x200x8x13 mm, 600x200x11x17 mm, and 150x150x7x10 mm respectively. Two DSI 6808 Gr 270 prestress strands are post-tensioned to 260 kN and aligned at the two sides of the floor beams. Cyclic loading applied to the prototype SC-EBF frame was measured by story drift ratio, which involved 6 cycles of 0.25%, 0.5%, 0.75%, 4 cycles of 1%, and 2 cycles of 1.5% and 2.0%.

The hysteresis pushover force displacement obtained from one test on the prototype SC-EBF frame is plotted in Figure 2-12 (Cheng et al. 2012). Although the authors claimed that all structural members remained elastic during the experiment, it is clearly observed from the experimental hysteresis loop that very little energy was dissipated during the

cyclic loading process and the self-centering behavior was generally not achieved. Furthermore, the effective yield strength of the SC-EBF frame which is equal to the pushover force leading to imminent gap opening was not distinguishingly visible; and the elastic stiffness and the post-gap-opening stiffness of the prototype SC-EBF frame were very close, which were reflected by the experimental hysteresis loop. Based on the observation on Figure 2-12, it can be concluded that the section sizes of the SC-EBF frame were not properly selected, as the key performance parameters of the prototype SC-EBF, which are the elastic stiffness, the effective yield strength, and the post-gap-opening stiffness, were not in agreement with common practice.

This dissertation research is inspired by the numerical simulation process on the prototype SC-EBF investigated by Cheng et al. (2012). Finite element analysis was first conducted on the duplicate finite element model of the prototype SC-EBF investigated by Cheng et al. (2012) to identify the reasons for failing to achieve the self-centering behaviors of the SC-EBF prototype. The duplicate finite element model created by the author had identical beam, column, brace, and link beam section sizes as the prototype SC-EBF investigated by Cheng et al. (2012), yet the rocking link beam's length was changed from 2 m to 1 m and the column height was slightly increased from 3.2 m to 3.37 m. Based on the finite element analysis results from the duplicate model, the original rocking link beam was found to yield due to end bending moment during the cyclic loading process. As the rocking link beam's end bending moment was even larger in the case of the Cheng's prototype SC-EBF frame, it is concluded that the lack of self-centering behavior in the experiment conducted by Cheng et al. (2012) was likely to be

caused by the yielding of the link beam, which was under-sized for such application. Moreover, compared to the initial tensile stress in the PT strands of the duplicate model was approximately 60% of the strand's minimum yield stress, the initial tension stress in the PT strands adopted by Cheng et al. (2012) was very small. It was also observed in the duplicate model that the maximum Von Mises stress in the SC-EBF's braces was close to the structural steel's yield stress; hence the bracing section size should be enlarged. Therefore, further study is warranted on the SC-EBF system to facilitate the proper selection of the section sizes of the SC-EBF's structural components, the size of the PT strands, the initial tension stress of the PT strands, and the suitable fuse devices. Numerical evaluation on the SC-EBF's properties and the effects of its rocking link beam length and the PT strands' area on the SC-EBF's behaviors is presented in Chapter 6 of this dissertation.

2.3.3. Other Types of Self-Centering Structures

Self-centering behavior can also be achieved in a structure when the PT strands are post-tensioned along the vertical members of the structure. The PT connections are formed between the column or wall bases and the structure's foundation. Under the lateral load, gaps are formed between the column/wall bases and the foundation, which is achieved by the rocking of the entire structure. The structure's self-weight or the post-tension force within the PT strands or tendons provides the re-centering mechanism. Fuse devices are typically installed between the segregated walls or between the column/wall bases and the foundation. This type of self-centering mechanism is frequently applied to precast

wall systems and concentrically braced frames (CBF), which is appealing in that both the structure's self-weight and the provided compression force of the PT strands can support the self-centering behavior; hence the cost for anchoring PT strands can be saved for some low budget projects.

Hu et al. (2012) performed numerical analysis on the seismic behavior of the reinforced concrete frame combined with self-centering hybrid wall. The schematics of the self-centering wall are plotted in Figure 2-13. Hu et al. (2012) numerically verified the self-centering behavior of the self-centering hybrid wall and concluded that the total area of the PT tendons and the yield strength of the base hysteretic dampers were the primary factors affecting the hysteresis behaviors of the self-centering hybrid wall. The applicability of utilizing the self-weight of the wall alone to achieve self-centering behavior was also verified by Hu et al. (2012).

Seo and Sause (2005) researched the ductility properties of the self-centering precast concrete walls under seismic force. The self-centering precast wall systems investigated by Seo and Sause is plotted in Figure 2-14. Seo and Sause (2005) verified that self-centering systems had larger ductility demands than conventional systems, and could be designed to have large ductility capacities with little post-earthquake damage.

Sause et al. (2010) performed experimental studies on the self-centering concentrically braced frames (SC-CBF). The schematics of the investigated SC-CBF are plotted in Figure 2-15. The SC-CBF is designed to decompress at the base after the critical lateral pushover load is exceeded, which initiates the rigid body rotation (rocking) of the frame.

Vertically aligned post-tensioned steel tendons resist the uplift movement of the SC-CBF and provide the restoring force to re-center the system. The PT tendons elongate due to the uplifting of the structure, which results in the increasing of the post-tension force and provides the positive stiffness to the lateral force displacement behavior of the SC-CBF. The gradually occurring limit performance states for the SC-CBF are: (1) the decompression of the column at one side of the SC-CBF, (2) the yielding of PT tendons, (3) the significant yielding of beams, columns, or braces of the SC-CBF, (4) failure of the beams, columns, or braces (Sause et al. 2010). Under the design objective that the structure conforms to the immediate occupancy (IO) performance level under the design base earthquake (DBE) and to the collapse prevention (CP) performance level under the maximum considered earthquake (MCE), the first limit performance state conforms to the IO performance level while the second and the third performance limit states conform to the CP performance level (Sause et al. 2010). Reflected by the experiment results, the self-centering behavior of the SC-CBF was experimentally achieved under the DBE level ground motions and MCE level ground motions (Sause et al. 2010).

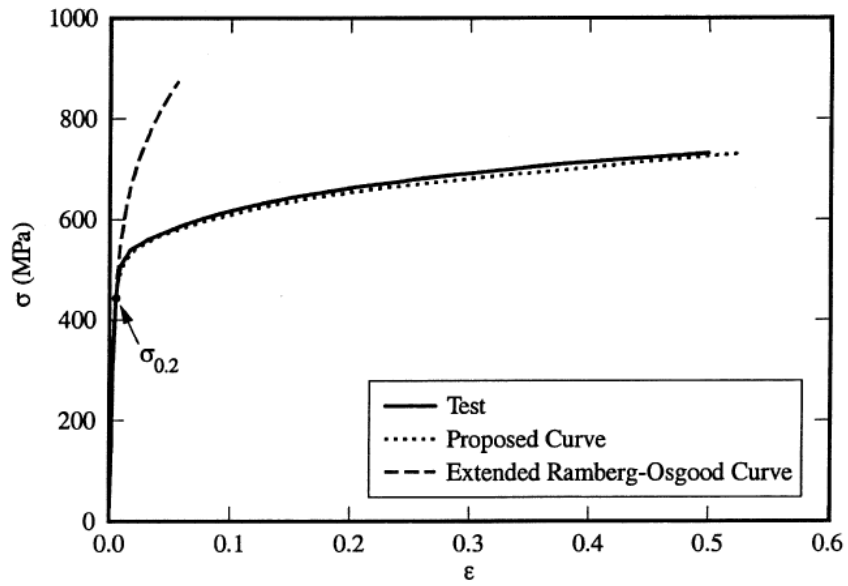


Figure 2-1 Stress strain curves for AISI 304L stainless steel (Rasmussen 2003)

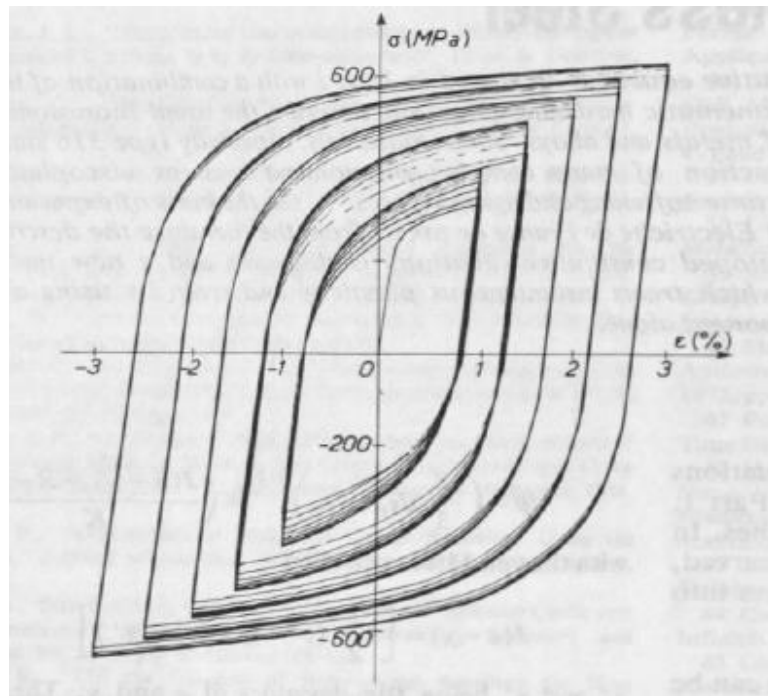


Figure 2-2 Cyclic stress strain relationship for 316 stainless steel (Chaboche and Rousselier 1983)

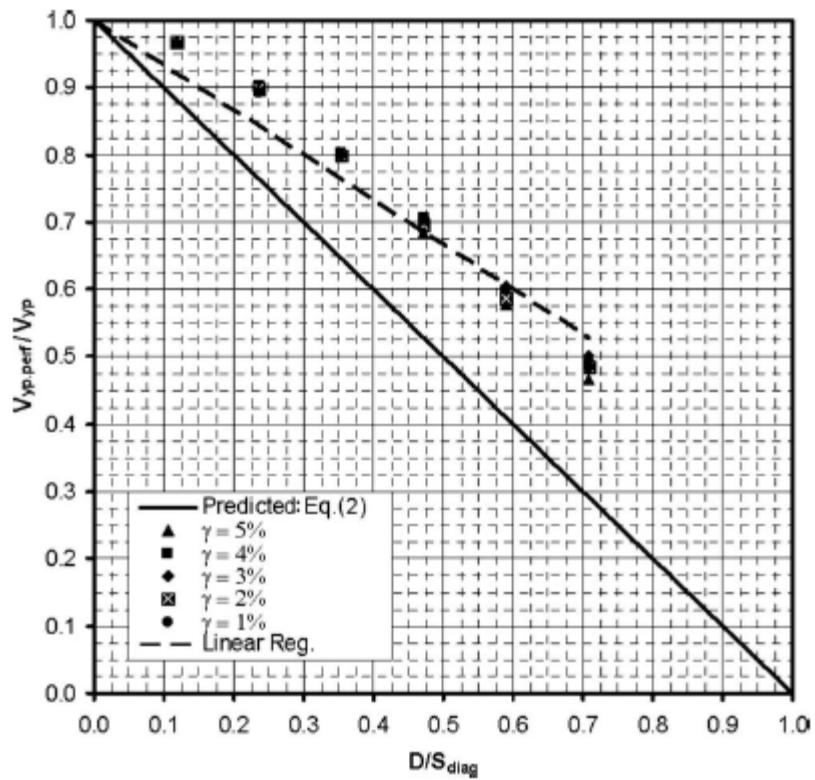


Figure 2-3 Infill plate strength ratios (V_{yp_perf}/V_{yp}) versus perforation ratio (D/S_{diag}) (Vian et al. 2009)

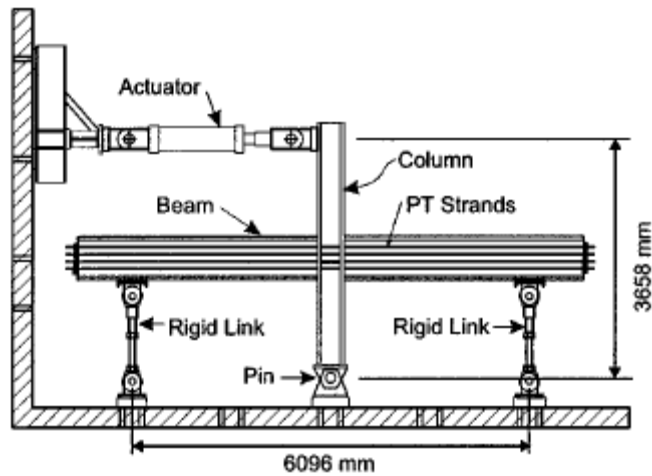


Figure 2-4 Post-tensioned connection test setup (Ricles et al. 2002)

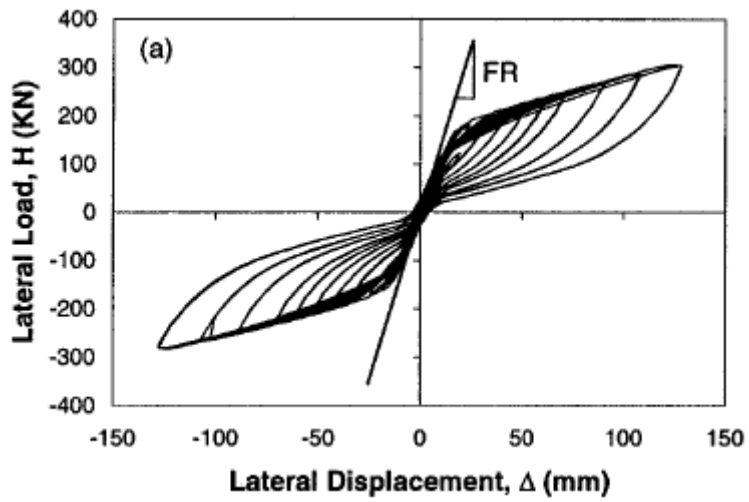


Figure 2-5 Hysteresis force displacement relationship (Ricles et al. 2002)

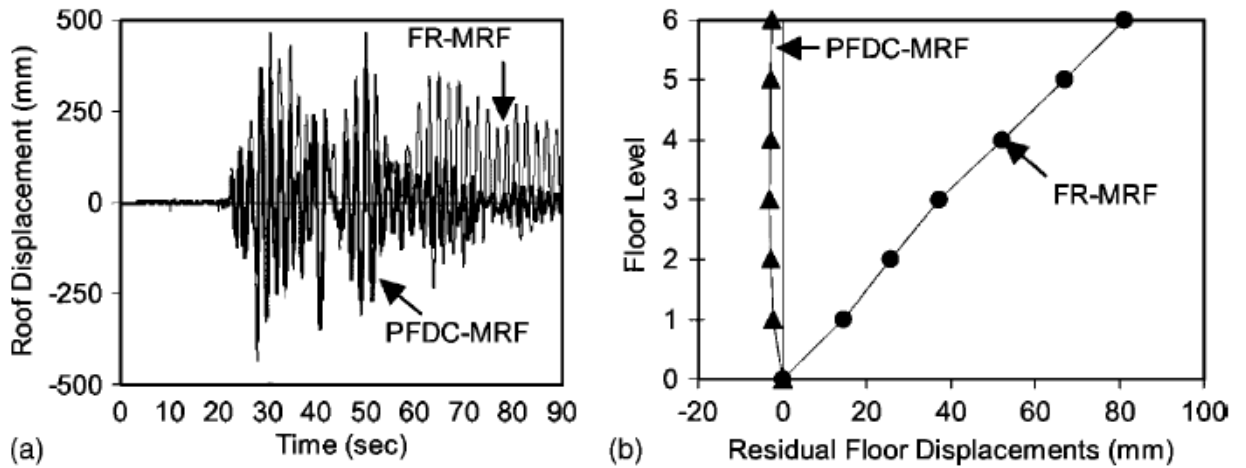


Figure 2-6 Frame response to the Chi-Chi maximum considered earthquake (Rojas et al. 2004)

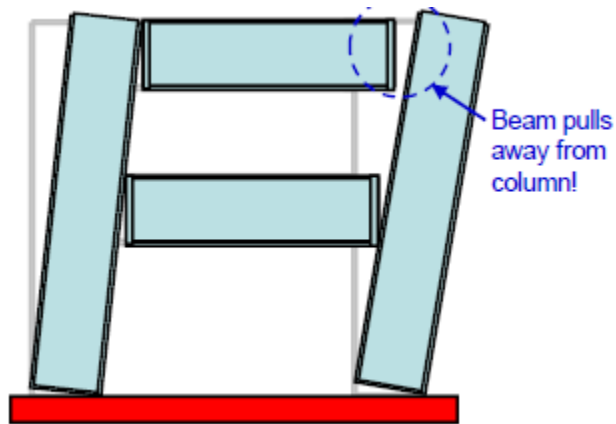


Figure 2-7 Gap opening effect on the two-story frame with stiff columns (MacRae 2010)



Figure 2-8 Slab damage in a post-tensioned beam subassembly (Clifton 2005)

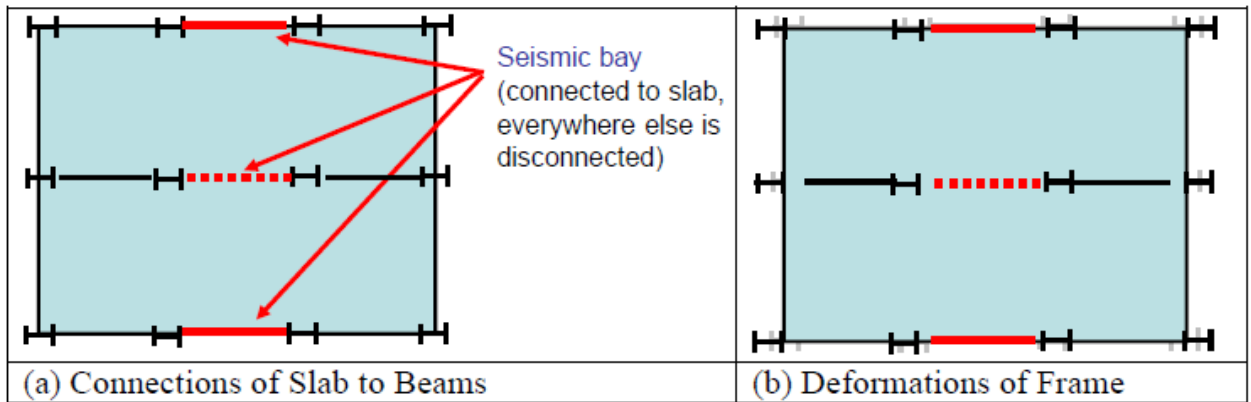


Figure 2-9 Floor slabs only connect to seismic frames (Lin et al. 2009)

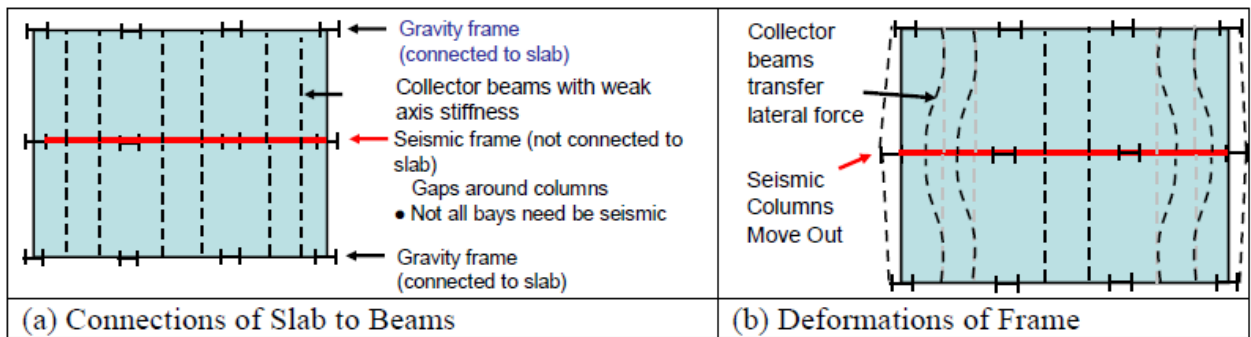


Figure 2-10 floor slabs only connect to gravity frame (Garlock 2009)

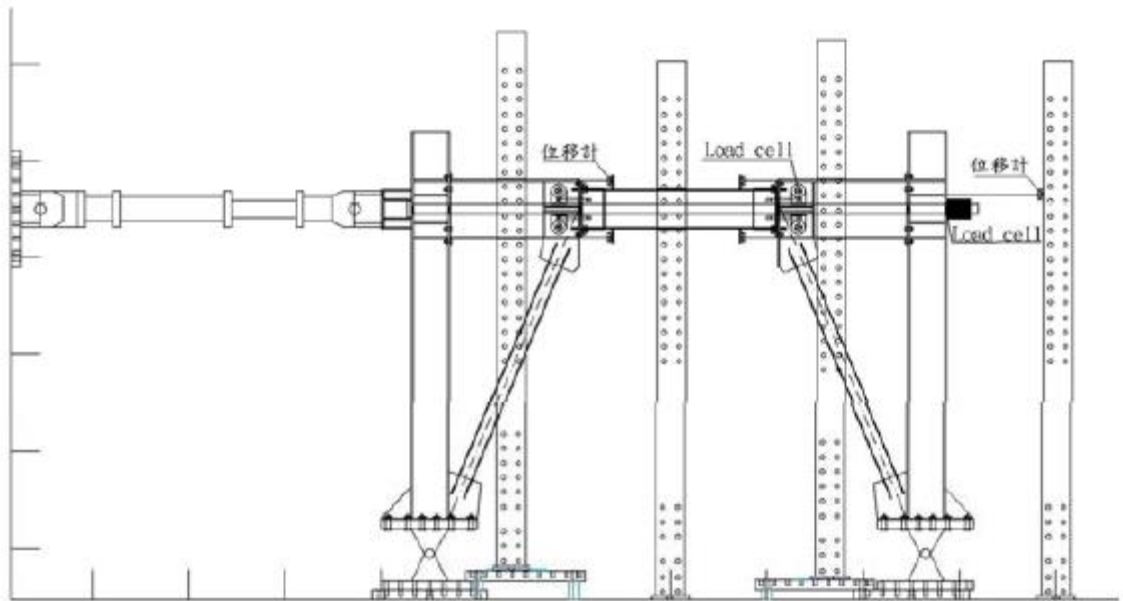


Figure 2-11 SC-EBF test setup (Cheng et al. 2012)

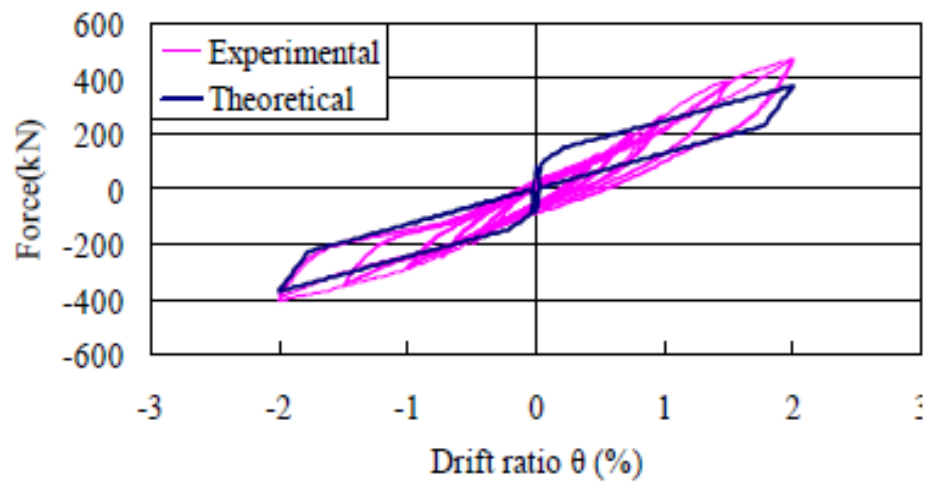


Figure 2-12 Experiment hysteresis force displacement (Cheng et al. 2012)

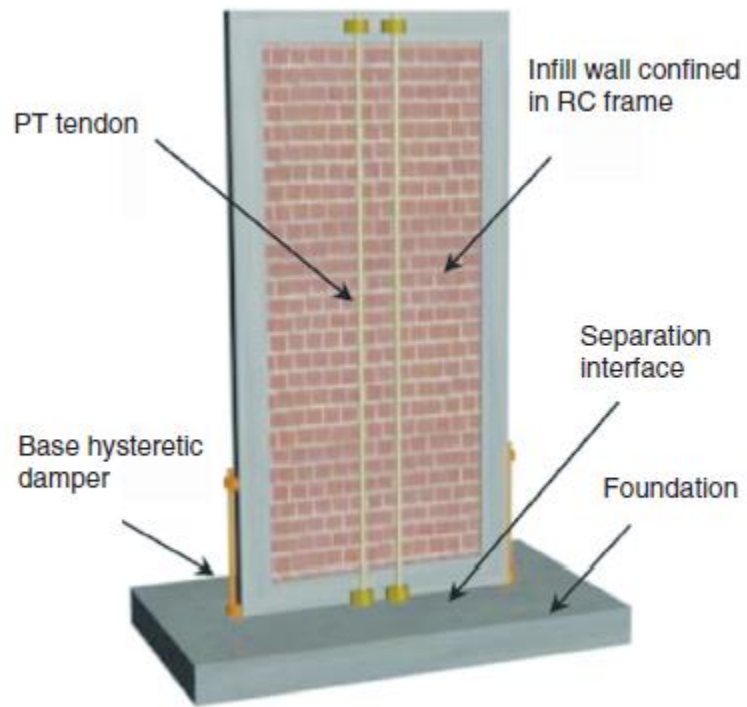


Figure 2-13 Schematics of self-centering wall (Hu et al. 2012)

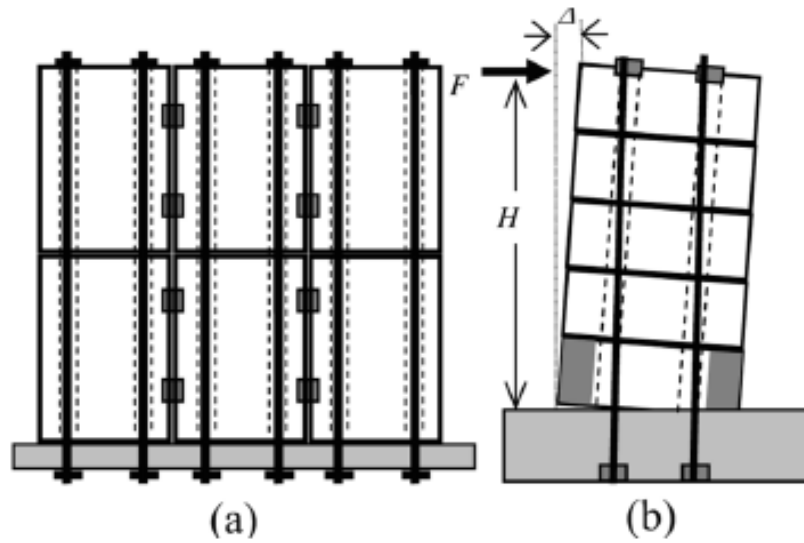


Figure 2-14 Self-Centering precast concrete wall systems (Seo and Sause 2005)

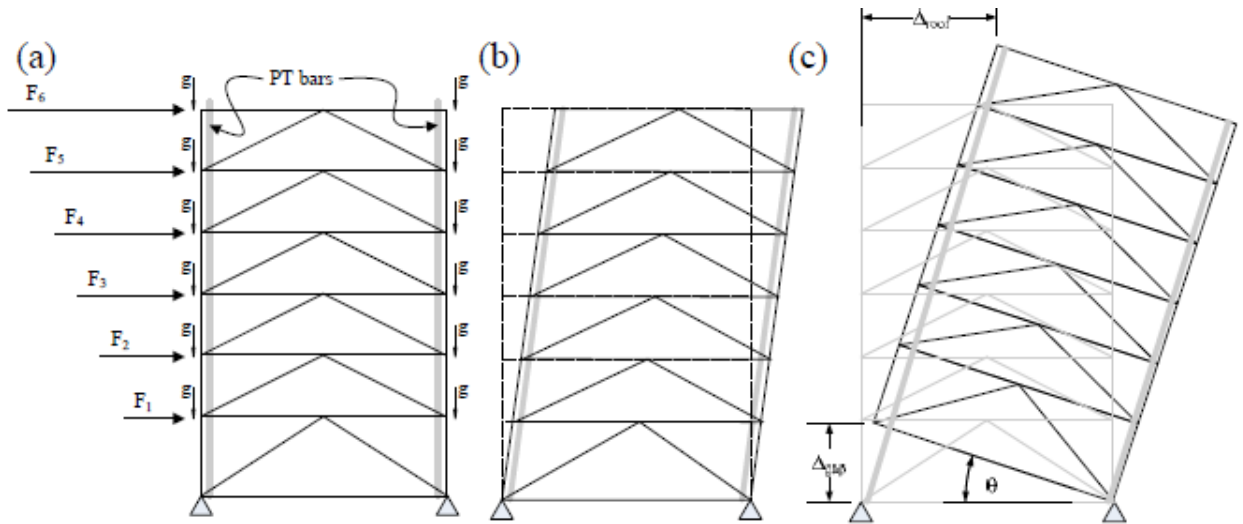


Figure 2-15 Schematics of the SC-CBF system (Sause et al. 2010)

Table 2-1 Material properties for different types of stainless steels (Rasmussen 2003)

Alloy	E_0 (GPa)	$\sigma_{0.01}$ (MPa)	$\sigma_{0.2}$ (MPa)	σ_u (MPa)	ϵ_u	e	n	m
AISI 304	189	234	403.5	672.3	0.528	0.0021	5.88	3.1
AISI 304L	195	245	428.8	702.5	0.51	0.0022	5.51	3.2
AISI 316L	190	190	316.0	616.0	0.51	0.0017	5.88	2.8
Duplex 2205	205	424	636.0	830.8	0.245	0.0031	7.70	3.7
AISI 430	200	200	320.0	622.0	0.48	0.0016	6.37	2.8
3Cr12	195	215	275.0	444.0	0.38	0.0014	12.2	3.2

Chapter 3 : Mechanical Characterization of AISI 316L Stainless Steel under Large Inelastic Strains

This chapter presents the details of the experiments conducted on AISI 316L stainless steel (SS316L) test bars for characterizing its material characteristics and calibrating parameters for the plastic strain hardening model and the micromechanics-based fracture model. SS316L is selected for this study, which is an extra low carbon grade of 316 stainless steel, and is widely used in the marine applications due to its even higher corrosion resistance. The chemical compositions of SS316L are listed in Table 3-1. The SS316L test specimens in this research include one standard tensile coupon, two specially designed short-gauge-length round bars, and three notched round bars. Cyclic finite element analysis (FEA) of the notched bar tests was conducted to provide inputs to calibrate the material parameters used in the micromechanics-based fracture models. The calibrated material parameters of SS316L include the Young's modulus (E), yield stress (σ_y), ultimate stress (σ_u), plastic strain hardening parameters, void growth index (VGI), and decay parameter λ . The calibration results for the VGI and λ parameters are validated by repeating the calibration on A992 steel and comparing with the calibration results on Q345 steel (similar to ASTM A992 steel) by Liao et al. (2012).

3.1. SS316L Experiment

3.1.1. Specimen Description

A total of 6 SS316L specimens were fabricated and tested in the Mechanics Test Center at Shanghai Jiaotong University in Shanghai, China in July 2014. MTS servo-hydraulic

controlled testing machine (see Figure 3-6-a) was used for cyclic testing and specimen 7-1 while Zwick electrodynamic universal testing machine (see Figure 3-6-b) was used for monotonic loading test of specimen 3-1. Specimens were labeled with the notation “SS”, which denoted stainless steel; followed by a number ranging from 3 to 7, which represents the different types of tests; and ends with number 1 or 2, which identifies the specimen number in duplicate testing. All test specimens were machined from square-section bars. The transition radius between the end and the middle test portion was set to be 30-mm for all test specimens.

Specimen SS3-1 is a standard tensile coupon machined from a square-section bar measuring 305-mm long and 19-mm in section width in accordance with ASTM E8/E8M, which was used for the monotonic tension test. The geometric shape and dimensions of Specimen SS3-1 are plotted in Figure 3-1. Within the test portion, the specimen has a diameter of 9 mm and a length of 81 mm. Axial strain was measured during test by an extensometer with the gauge length of 45 mm. Extensometers were used for measuring the specimen deformation over the gauge length of the extensometer. For cyclic loading test of notched bars, MTS extensometer with a gauge length of 20 mm (Model #: 632.27F-20, S/N: 10292042) was used. For all other cyclic loading tests, MTS extensometer with a gauge length of 10 mm (Model #: 632.13F-23, S/N: 10287834) was used. For specimen SS7-1, MTS extensometer with a gauge length of 50 mm (Model #: 634.25F-24, S/N: 102921698) was used.

Specimen SS4-1 and SS4-2 were loaded cyclically under large inelastic strain. Previous research on cyclic large inelastic strain test for ASTM A992 or Q345B steel manifested the lateral instability problem when large compression force was applied to the specimen (Wu et al. 2012, Dusicka et al. 2007, Shi et al. 2012). To allow for the accurate stress strain acquisition of the specimens during large inelastic strain amplitudes, the stainless steel specimens were designed with short gauge length on the basis of the research by Wu et al. (2012). The length for specimen SS4-1 and SS4-2 was 12 mm within the test section of a 12-mm diameter. Loading rate was intentionally made different for these two identical specimens, in order to check the loading rate effect on SS316L. Axial nominal strain was measured within the gauge length of 10 mm using an MTS extensometer (Model #: 632.13F-23). Section details of the specimens SS4-1 and SS4-2 are plotted in Figure 3-2.

Specimen SS5-1 was a notched specimen used for cyclic loading test. As shown in Figure 3-3, the length of SS5-1 was 70 mm within the test section of the diameter of 12.5 mm. The specimen was circumferentially notched with a notch radius of 1.5 mm and the diameter of the notched section was reduced to 6.25 mm. The notch radius was machined to a ± 0.1 -mm tolerance.

Specimen SS6-1 and SS7-1 were two identical notched specimens with a nominal notch radius of 6.25 mm. Specimen SS6-1 was used for cyclic loading test, while specimen SS7-1 was tested with monotonic tension loading protocol. Both specimens had the parallel length of 70 mm and the diameter of 12.5 mm at their test part. As shown in

Figure 3-4, the specimens were circumferentially notched at the center with a notch radius of 6.25 mm and the diameter of the notched section was reduced to 6.25 mm. The notch radius was machined to a ± 0.1 -mm tolerance.

A general view of the stainless steel specimens is shown in Figure 3-5.

3.1.2. Loading Protocol

Loading protocol applied to each specimen was defined with the nominal strain measured within the extensometer gauge length, which was calculated by dividing the measured deformation within the gauge part by its initial length.

For specimens SS3-1 and SS7-1, monotonic tension loading was applied until the specimen fracture. The specimen SS3-1 was first loaded to 11 kN under force control at a loading rate of 50 N/s and then loaded till fracture under displacement control at a loading rate of 3 mm/min. The test setup for specimen SS7-1 is shown in Figure 3-11-b.

Loading protocol applied to specimens SS4-1 and SS4-2 were measured by the nominal strain amplitude within the gauge part, which included 5 cycles of ± 0.03 strain, 5 cycles of ± 0.06 strain, 5 cycles of ± 0.09 strain, and 5 cycles of ± 0.12 strain. The loading protocol for SS4-1 and SS4-2 is shown in Figure 3-7. The loading rate varied for the two specimens, which was 0.001 mm/mm/s for SS4-1 and 0.005 mm/mm/s for SS4-2 respectively. Similarly, the cyclic loading applied to SS5-1 and SS6-1 were represented by the nominal strain within the gauge part, which was calculated as the ratio of the measured deformation to the initial gauge. The designated loading protocols for SS5-1

and SS6-1 are plotted in Figure 3-8 and Figure 3-9 respectively. The tests setup for SS5-1 and SS6-1 are plotted in Figure 3-10 and Figure 3-11-a respectively.

3.2. Test Results

All stainless steel specimens were loaded till fracture. Instability was not observed in the specimens during cyclic loading. For specimen SS3-1, specimen was fractured under monotonic loading when the axial elongation reached 19.85 mm, and the corresponding load was 26.7 kN. For specimen SS4-1, failure occurred during the 16th loading cycle when the measured deformation within the gauge part was -1.45 mm at the applied loading of 99.81 kN. For specimen SS4-2, failure occurred during the 16th loading cycle when the axial deformation within the measured part was -1.03 mm at the applied load of 110.6 kN. Specimen SS5-1 was fractured during the 3rd loading cycle. When fracture occurred, the axial deformation and the applied load were 0.64 mm and 33.3 kN respectively. For specimen SS6-1, fracture was observed in the 9th loading cycle, where the corresponding axial deformation and the applied force were 0.81 mm and 22.5 kN respectively. Specimen SS7-1 was fractured when the applied monotonic force reached 20.0 kN. The failure deformation of SS7-1 when fracture occurred was 3.09 mm. A summary of the test results are listed in Table 3-2.

3.3. Engineering Material Properties Determination

The uniaxial tension test was performed on specimen SS3-1 in accordance with the requirements of ASTM E8/E8M. The modulus of elasticity E , the yield stress σ_y , and the

ultimate stress σ_u were determined from the uniaxial tension test on SS3-1. The data acquired from the uniaxial tension test included the test time, actuator displacement, force, axial nominal stress, and axial nominal strain. After fracture occurred, the diameter of the necked section was measured for true stress strain calculation.

The axial engineering (nominal) stress and strain of SS3-1 were calculated according to Equation 3-1.

$$\sigma_{eng} = \frac{F}{A_0}$$
$$\varepsilon_{eng} = \frac{\Delta}{L_0}$$

Equation 3-1

Where F is the applied tension force; A_0 is the initial section area within the test part; Δ is the measured axial elongation within the gauge part; L_0 is the gauge length.

The axial engineering (nominal) stress strain relationship for specimen SS3-1 under monotonic tension force is plotted in Figure 3-12. The nominal yield stress σ_y was defined as the nominal axial stress corresponding to 0.2% inelastic strain, and the nominal ultimate stress σ_u was defined as the ratio of the maximum applied uniaxial tension force to the gauge part's initial section area, which are also indicated in Figure 3-12. Terms ε_y and ε_u are the axial strains corresponding to σ_y and σ_u . The Young's modulus E of SS316L was calculated as the slope of the engineering stress strain curve's linear portion. Detailed values of σ_y , ε_y , σ_u , ε_u , and E are listed in Table 3-3.

The engineering (nominal) stress strain relationship was then converted into true stress-strain relationship for use in finite element analysis (FEA). On the basis of the nominal yield stress point and the nominal ultimate stress point, the engineering stress-strain curve was divided into three segments for the true stress strain calculation. Segment 1 was from the initial unloaded point to the nominal yield stress point. The nominal stress strain relationship for this segment should be linear elastic characterized by Hooke's law. The second segment was from the nominal yield stress point to the nominal ultimate stress point. Plastic deformation was initiated after the nominal yield stress point. Within the stress range between the nominal yield stress and the nominal ultimate stress, it was hypothesized that the volume within the gauge part is unchanged with the initiated plastic deformation. The nominal stress strain values in segment 1 and segment 2 of the engineering stress strain curve were converted into true stress strain values based on Equation 3-2.

$$\sigma_{true} = \sigma_{eng}(1 + \varepsilon_{eng})$$

Equation 3-2

$$\varepsilon_{true} = \ln(1 + \varepsilon_{eng})$$

The third segment in the nominal stress strain curve was from the nominal ultimate stress point to the failure point. Necking occurred after the nominal ultimate stress was reached and the cross section area at the necked section was considerably reduced during this loading process; i.e., the material volume no longer remains constant within the necked section. As the stress distribution within the necked section was no longer uniform, a linear relationship was assumed between the true stress strain corresponding to the

nominal ultimate stress strain and the true stress strain when the specimen fractured. The true stress-strain at the fracture point of the specimen was calculated based on Equation 3-3. The converted true stress versus true strain relationship for specimen SS3-1 is plotted in Figure 3-13.

$$\sigma_{true}^{fracture} = \frac{F_{fracture}}{\pi d_f^2 / 4}$$

$$\varepsilon_{true}^{fracture} = \ln \left[\left(\frac{d_0}{d_f} \right)^2 \right]$$

Equation 3-3

Where $F_{fracture}$ is the applied axial force when the specimen fracture is imminent to happen; d_0 is the initial diameter of the specimen at the gauge part; d_f is the diameter of the fractured section.

3.4. Plasticity Hardening Model

To facilitate the numerical analysis of SS316L under large cyclic inelastic strain, plasticity hardening parameters were calibrated using the measured true stress-strain data for SS4-1 and SS4-2. As both specimens failed in the 16th loading cycle, only the converted true stress-strain data from the first 15 loading cycles will be used for calibrating the strain hardening parameters of SS316L. The true plastic strain values were calculated from the converted true strain values via Equation 3-4. The true stress versus true plastic strain relationships for specimen SS4-1 and SS4-2 are plotted in Figure 3-14.

$$\varepsilon_{p_true} = \varepsilon_{true} - \frac{\sigma_{true}}{E}$$

Equation 3-4

Metallic materials exhibit strain hardening behaviors once the initial yield strength values are exceeded. For materials loaded at room temperature, rate-independent plasticity can be assumed (Chaboche and Rousselier 1983), i.e., plastic strains are assumed to be developed instantly. The following five types of strain hardening models for characterizing material's stress strain relationship after yielding are frequently used and are also available in most commercial FEA software packages including ANSYS: Bilinear Isotropic Hardening (BISO) Model; Bilinear Kinematic Hardening (BKIN) Model; Nonlinear Isotropic Hardening (NLISO) Model; Nonlinear Kinematic Hardening (Chaboche) Model; Combination of NLISO and Chaboche Model (Chaboche 2008).

Isotropic hardening example: BISO Model

BISO model involves the use of the Von Mises yield criterion and isotropic work hardening assumption for characterizing the yield surface changes (Lee et al. 2009). The evolution of the yield surface change is illustrated in Figure 3-15. Reflected in the uniaxial tension test, the axial stress increment is linearly proportional to the axial plastic strain increment. The size of the yield surface is represented by the instantaneous yield stress σ'_y . The yield surface characterized by BISO is expressed in Equation 3-5.

$$f(\sigma) = \sqrt{\frac{3}{2} \mathbf{s} : \mathbf{s}} = \sigma'_y \quad \text{Equation 3-5}$$

Where s is the deviatoric stress tensor; σ'_y is the instantaneous yield stress; and $f(\sigma)$ represents the yield surface.

Although the BISO model can be used to characterize the monotonic behaviors of materials with adequate accuracy, it significantly over-estimates the stress increment of materials under cyclic loadings (Muransky et al. 2012).

Kinematic hardening example: BKIN Model

The linear kinematic hardening rule was first introduced by Prager (1956). Bauschinger effect is included in the BKIN model, in which the total stress range is presumed to be equal to twice of the material's initial yield stress. BKIN model characterizes the subsequent translational movement of the yield surface, and the size of the yield surface is assumed unchanged (Lee et al. 2009). Reflected in the uniaxial tension test, the back stress is linearly increasing with the plastic strain. The yield surface change characterized by the BKIN model is plotted in Figure 3-16. The definition of the yield surface characterized by the BKIN model is expressed in Equation 3-6.

$$f(\sigma - \alpha) = \sqrt{\frac{3}{2}(\mathbf{s} - \mathbf{a}) : (\mathbf{s} - \mathbf{a})} = \sigma_y \quad \text{Equation 3-6}$$

Where $f(\sigma - \alpha)$ is the equivalent Von Mises stress potential with respect to the back stress α ; \mathbf{a} is the deviatoric back stress tensor; σ_y is the size of the yield surface, which is equal to the material's initial yield stress.

The relationship between the back stress tensor \mathbf{a} and the plastic strain tensor $\boldsymbol{\varepsilon}_p$ characterized by BKIN model is expressed in Equation 3-7.

$$d\mathbf{a} = C \cdot d\boldsymbol{\varepsilon}_p$$

Equation 3-7

Where C is the kinematic hardening modulus specified in the BKIN model. Although the BKIN model can simulate the cyclic stress strain behaviors of materials at large plastic strain levels with adequate accuracy, its prediction of the nonlinear stress strain transition curve at low plastic strain levels is less accurate.

NLISO Model

The NLISO model is proposed to overcome the limitations of the BISO model. The NLISO model is based on the Voce hardening law (Chaboche 1989). Reflected in the uniaxial tension test, the isotropic stress increment with respect to accumulated plastic strain characterized by the NLISO model is expressed in Equation 3-8:

$$\sigma_0 = k + R_0 \hat{\varepsilon}_p + R_\infty (1 - e^{-b \hat{\varepsilon}_p})$$

Equation 3-8

Where: σ_0 represents the size of the yield surface; k is the elastic limit; R_0 , R_∞ , and b are material-related constants; $\hat{\varepsilon}_p$ represents the accumulated plastic strain. The nonlinear term associated with $\hat{\varepsilon}_p$ is introduced to redress the over-estimation of stress increment predicted by the BISO model.

Chaboche Model

The Chaboche model also incorporates the Bauschinger effect in characterizing the yield surface evolution of a material which is similar to the BKIN model, and it also provides

the refined characterization of the nonlinear stress strain transition curve at low plastic strain levels. The back stress tensor characterized by the Chaboche model is expressed in Equation 3-9 (Chaboche 1989):

$$\dot{\alpha} = \sum_{i=1}^n \dot{\alpha}_i = \frac{2}{3} \sum_{i=1}^n C_i \dot{\epsilon}_p - \gamma_i \alpha_i \dot{\lambda} \quad \text{Equation 3-9}$$

Where n is the number of nonlinear kinematic models; γ_i and C_i are material parameters in each nonlinear kinematic model; $\dot{\lambda}$ is the accumulated plastic strain rate.

Combined Model of NLISO and Chaboche

Generally for most metallic materials, the change of the yield surface involves of both translational position change and surface size expansion. The combined model is described by the theory of Von Mises yield condition, the associated flow rule, and isotropic-kinematic hardening. The stress strain relationship after initial yielding of the material is characterized in Equation 3-10 (Khan and Huang 1995):

$$\dot{\alpha} = C \dot{\bar{\epsilon}}_p \frac{1}{\sigma_0} (\sigma - \alpha) - \gamma \alpha \dot{\bar{\epsilon}}_p \quad \text{Equation 3-10}$$

Where: $\dot{\alpha}$ is the rate on the back stress tensor; σ_0 is the yield surface size characterized in Equation 3-8; C and γ are material constants stated in Equation 3-9; $\dot{\bar{\epsilon}}_p$ is the equivalent plastic strain rate.

Based on the research conducted by Chaboche and Rousselier (1983), the combined strain hardening model which accounts for both the isotropic hardening effect and the kinematic hardening effect should be utilized for characterizing the stress-strain relationship of stainless steel after initial yielding. The material's yield condition is hypothesized to follow the Von-Mises yield condition, i.e., the yielding occurs when the distortional strain energy of a unit volume equals to its distortional strain energy when it is uniaxially loaded to yield. The Von-Mises yield condition can be represented by the plastic potential f , which is a parameter defined by Equation 3-11. Term f is equal to zero when the material yields, or less than zero if the material remains elastic.

$$f = \frac{1}{2}(\vec{\sigma}^D)^T \cdot \vec{\sigma}^D - \sigma_Y^2 \quad \text{Equation 3-11}$$

Where σ_Y is the instantaneous yield stress value; $\vec{\sigma}^D$ is the 9x1 deviatoric stress tensor. Each of its elements σ_{ij}^D is calculated as shown in Equation 3-12.

$$\sigma_{ij}^D = \sigma_{ij} - \frac{1}{3}\sigma_{ij}\delta_{ij} \quad \text{Equation 3-12}$$

Where σ_{ij} represents each of the 9 components from the Cauchy stress tensor; δ_{ij} is the Kronecher Delta taking the value of 1 when i equals to j or otherwise the value of 0.

The combined hardening model which consists of the NLISO model and Chaboche model is adopted in this study for characterizing the plastic strain hardening properties of SS316L. For improved accuracy, a total of three Chaboche models were superimposed in

the combined hardening model. The stress-strain relationship of SS4-1 and SS4-2 which is characterized by the combined strain hardening model is expressed in Equation 3-13.

$$\sigma = \begin{cases} \chi + (R + k)sgn(\sigma - \chi) & \text{for } f = 0 \\ E(\varepsilon - \varepsilon_p) & \text{for } f < 0 \end{cases} \quad \text{Equation 3-13}$$

where χ is the back stress characterized by the Chaboche model, which is expressed in Equation 3-14; R is the yield stress increment characterized by the NLISO model, as expressed in Equation 3-15. Term k is the calibrated yield stress.

$$\chi = \sum_{i=1}^3 \frac{C_i}{\gamma_i} (1 - e^{-\gamma_i \varepsilon_p}) \quad \text{Equation 3-14}$$

$$R = R_0 \hat{\varepsilon}_p + R_\infty (1 - e^{-b \hat{\varepsilon}_p}) \quad \text{Equation 3-15}$$

Terms C_i , γ_i , k , R_0 , R_∞ , and b are the calibrated material-related constants. Terms ε_p and $\hat{\varepsilon}_p$ denote plastic strain and accumulated plastic strain values respectively. Values for the calibrated constants based on the cyclic test results are shown in Table 3-4 for ASTM 316L stainless steel.

FEA was conducted in ANSYS Academic 15.0 for validating the accuracy of the calibrated plasticity hardening model. The stress-strain relationships obtained from the FEA were compared with the experimental true stress-strain curves of SS4-1 and SS4-2, which is shown in Figure 3-17.

3.5 Void Growth Model (VGM) and Parameter Calibration

Based on the research work by Anderson (1995), the mechanism of the mechanical fracture initiation of structural steels involves the process of void nucleation, void growth, and void coalescence. Research conducted by McClintock (1968), Rice and Tracey (1969), and Kanvinde and Deierlein (2004) suggested that void growth was related to the equivalent plastic strain and the stress triaxiality, which is the ratio of the hydrostatic stress to the Von Mises stress.

Research conducted by Rice and Tarcey (1969) suggested that ductile fracture initiated when the void growth index (VGI) exceeded the critical value $VGI_{critical}$ within the critical volume. This relationship was captured in the void growth model (VGM) proposed by Kanvinde and Deierlein (2006), which is expressed in Equation 3-16. The ductile fracture initiation is corresponding to the macroscopic phenomenon, reflected by a significant drop of the material's load carrying capacity during the uniaxial tension test.

$$VGI = \int_0^{\varepsilon_p^{critical}} \exp(1.5 \frac{\sigma_m}{\sigma_e}) d\varepsilon_p > VGI_{critical} \quad \text{over } r > l^* \quad \text{Equation 3-16}$$

where σ_m and σ_e are the hydrostatic stress and Von Mises stress respectively; $\varepsilon_p^{critical}$ is the critical equivalent plastic strain corresponding to the failure deformation.

Finite element analysis of specimen SS7-1 was performed to determine the $VGI_{critical}$ of SS316L, as σ_m , σ_e , and ε_p cannot be directly measured from the experiment on SS7-1. An axisymmetric model representing the test segment of specimen SS7-1 was built in the

ANSYS Academic 15.0, as shown in Figure 3-18. Plane 182 element which was assigned with axisymmetric behavior was used for the finite element model of the notched test bar specimen. The calibrated strain hardening parameter values of SS316L in Table 3-4 were applied to the finite element model. Only the test part was simulated in FEA, as negligible elastic deformations occurred within the rest parts of the specimen during the test. Meshing was refined at the notched section, as shown in Figure 3-18. The size of the elements within the notched section was approximately 0.2 mm. The finite element model was loaded axially until the failure deformation was reached at 3.09 mm.

Validation of the calibrated VGM parameters for SS316L was done by comparing the FEA-derived force-displacement curve with the experimental force-displacement data from SS7-1, as shown in Figure 3-19. A good agreement was generally observed. At the failure deformation, the equivalent plastic strain, Von Mises stress, hydrostatic stress, 1st principal stress, 2nd principal stress, and 3rd principal stress contours were plotted in Figure 3-20 through Figure 3-25, which is used to determine the critical fracture initiation location. Reflected by the stress and strain intensities in Figure 3-20 and Figure 3-21, it can be concluded that fracture initiates at the center of the notched section.

The stress strain results from FEA in the entire loading history till the failure deformation of 3.09 mm was reached were substituted into Equation 3-16 to calculate the critical void growth index ($VGI_{critical}$) for SS316L, which was determined as 2.50.

3.6. Cyclic Void Growth Model (CVGM) and Parameter Calibration

Kanvinde and Deierlein (2007) extended the void growth model (VGM) to the cyclic void growth model (CVGM) in order to model the ductile fracture of materials under cyclic loading. In CVGM, a macroscopic crack initiates via microscopic void coalescence when the cyclic void growth index exceeds the critical cyclic void growth index value. The tension loading cycles and compression loading cycles have opposite effects on the cyclic void growth index (CVGI). Under tension loading cycles, the voids nucleate and grow, which is reflected as the increasing of the CVGI value. On the other hand, during the compression loading cycles, the voids are squeezed and the nucleated voids could even close. This is analogous to a “healing” process for the void growth and is reflected as the decreasing of CVGI (CVGI can be decreased up to zero which means all voids are closed). However, the void tips become sharper during the applied compression loading cycles, rendering the material more susceptible to cracking. This effect is reflected by the degradation of the critical cyclic void growth index ($CVGI_{critical}$). The degradation process of the cyclic void growth index is assumed to follow the exponential decay function which is only related to the accumulated plastic strains during the compression loading cycles.

The CVGM criterion in predicting the fracture initiation of materials under cyclic loading is expressed in Equation 3-17.

$$\begin{aligned}
CVGI = & \sum_{tensile\ cycles} \int_{\varepsilon_1}^{\varepsilon_2} \exp(|1.5T|) d\varepsilon_p - \sum_{compressive\ cycles} \int_{\varepsilon_1}^{\varepsilon_2} \exp(|1.5T|) d\varepsilon_p & \text{Equation} \\
> CVGI_{critical} = & VGI_{critical} \cdot \exp(-\lambda \varepsilon_p^{accumulated}) & 3-17
\end{aligned}$$

Where λ is the decay parameter to be calibrated; $\varepsilon_p^{accumulated}$ is the equivalent plastic strain that has accumulated up to the beginning of each tension loading cycle.

The decay parameter λ is the additional parameter to be calibrated for the CVGM. The calibration of λ involves a two-step process. The first step is to determine the CVGI when fracture initiates, which is calculated from the left side of Equation 3-17. The integral is computed up to the failure deformation in the cyclic loading history, which corresponds to the sudden load capacity drop in the force displacement hysteresis curve. The second step is to determine the decay parameter λ using Equation 3-17.

Analogous to the determination of $VGI_{critical}$, the calculation of CVGI has to involve finite element analysis of the notched specimens. Axisymmetric models were built in ANSYS Academic 15.0 for specimens SS5-1 and SS6-1, as shown in Figure 3-26 and Figure 3-18 respectively. Meshing was refined within the notched section. The element size within the notched section was approximately 0.2 mm.

The accuracies of the finite element models (FEM) for SS5-1 and SS6-1 are verified by comparing the experimental force-displacement curves with the FEA-derived ones. As shown in Figure 3-27 and Figure 3-28, a good agreement is generally observed for

specimens SS5-1 and SS6-1. Therefore, the decay parameter λ for SS316L stainless steel was determined to be 0.50.

3.7. Characteristics Length l^*

Both the VGM and CVGM criteria must be satisfied within the critical volume, which is represented by the characteristics length l^* . Various methods were proposed to determine l^* . Panontin and Sheppard (1995) suggested to correlate the steel grain size with l^* ; Ritchie et al. (1979), Panontin (1995), and Chi (2000) suggested correlating l^* with the inclusion spacing (the distance between two coalescing voids) and dimple diameter (the diameter of the coalesced void); Beremin (1981), McMeeking (1977), and Norris et al. (1978) suggested to back-calculate l^* from the FEA on the experiments for the specimens with sharp crack tips; Hancock and Mackenzie (1977) suggested to directly measure the distance between two coalesced voids and to take the average as l^* . Compared to other methods, the method proposed by Hancock and Mackenzie (1977) was straight forward and involved no assumptions in determining l^* . The characteristic length l^* was directly related to physical events (material fracture). Therefore, the method proposed by Hancock and Mackenzie (1977) was adopted in this study for determining the characteristic length of SS316L.

Fractographs of the fracture surface of specimen SS7-1 was taken using scanning electron microscope (SEM) in order to measure the characteristics length l^* . The SEM fractograph was taken using the equipment at the Shanghai Institute of Ceramics, Chinese Academy of Sciences. The fracture surface of SS7-1 is shown in Figure 3-29. Characteristic length

measurement is indicated in Figure 3-30 from the magnified fracture surface of SS7-1. The average value of the characteristic length l^* for SS316L was calculated as 85.5 μm .

3.8. Model Validation of VGM and CVGM for Q345 Steel

The VGM and CVGM were also calibrated for Q345 steel based on the notched bar test results by Liao et al. (2012), which followed the same procedure as that adopted for calibrating the VGM and CVGM of SS316L. The calibrated VGM and CVGM results of Q345 steel were then compared with the calibration results by Liao et al. (2012). The calibrated results for Q345 steel were expected to be close, which serves to validate the computation process for the VGM and CVGM parameter calibration.

Validation tests on VGM calibration were repeated on specimen 4-1 (notch radius=1.5 mm) and specimen 16-1 (notch radius=6.25 mm) which were selected from the experimental tests by Liao et al. (2012). The plasticity hardening parameter values for Q345 steel were calibrated using the cyclic tension test results by Liao et al. (2012). The NOTCHED bars used by Liao et al. (2012) were designed with the same dimensions as the stainless steel NOTCHED bars used in this research; hence the finite element models for specimens 4-1 and 16-1 were established in the same way as the ones shown in Figure 3-26 and Figure 3-18. Comparison was made between the force-displacement curve from the FEA conducted by the author and the experimental force-displacement curve from Liao et al. (2012), as shown in Figure 3-31 and Figure 3-32 for specimen 4-1 and 16-1 respectively. It can be observed that generally the force displacement curves obtained

from FEA agree well with the experimental force-displacement curves from Liao et al. (2012).

The critical void growth index ($VGI_{critical}$) for Q345 steel was determined using Equation 3-16, where σ_m , σ_e , and ε_p were obtained from FEA and the critical equivalent plastic strain at fracture initiation corresponds to the failure deformation, which was determined from the experiment data of specimens 4-1 and 16-1 (Liao et al. 2012). The critical void growth index was determined as 3.11 for specimen 4-1; and 3.54 for specimen 16-1.

Validation tests on CVGM calibration were repeated on specimen 9-1 (notch radius=1.5 mm), 18-1 (notch radius=6.25 mm), and specimen 20-1 (notch radius=6.25 mm) from the research conducted by Liao et al. (2012). Similar to the determination of $VGI_{critical}$, finite element models were built in ANSYS Academic 15.0 for the selected specimens. The meshed model of specimen 9-1 had the same dimensions as the specimen SS5-1 in this research, which is plotted in Figure 3-26. Simultaneously, the meshed model of specimens 18-1 and 20-1 had the same dimensions as the specimen SS6-1 in this research, which is plotted in Figure 3-18. Comparisons between the force displacement relationships for specimens 9-1, 18-1, and 20-1 obtained from the FEA conducted in this study and the experiments performed by Liao et al. (2012) are plotted in Figure 3-33 through Figure 3-35. It can be observed that generally the force displacement relationships obtained from FEM agree well with the experimental force displacement relationship from Liao et al. (2012).

The decay parameter (λ) for Q345 steel was determined using Equation 3-17, where σ_m , σ_e , and ε_p were obtained from FEA and the critical equivalent plastic strain at fracture initiation corresponds to the displacement at which the load carrying capacity dropped abruptly, which was determined from the experiments on specimens 9-1, 18-1, and 20-1 conducted by Liao et al. (2012) respectively, shown in Figure 3-33 through Figure 3-35. The decay parameter was determined as 0.38 using the regression method.

Kanvinde and Deierlein (2006, 2007) calibrated the VGM and λ for A992 steel, which has its mechanical properties similar to Q345 steel. For comparison purpose, the results of $VGI_{critical}$ and λ on A992 steel calibrated by Kanvinde and Deierlein, on Q345 steel calibrated by Liao et al. (2012), and on Q345 steel calibrated in this study are listed in Table 3-5. It is seen that the calibrated parameter values from this study are closer to the results obtained from Kanvinde and Deierlein, yet higher than the numbers given by Liao et al.

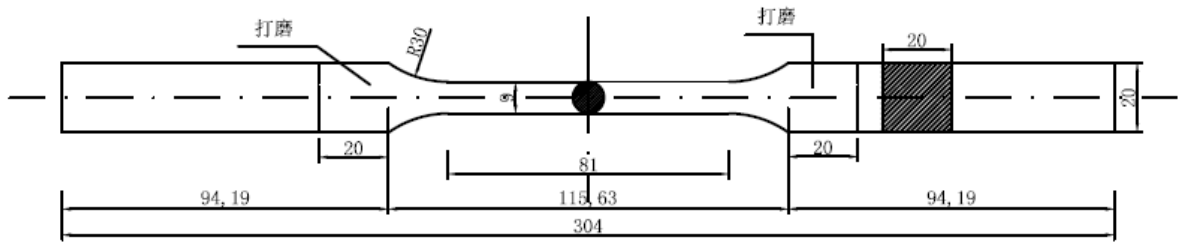


Figure 3-1 Geometric dimensions of SS3-1 (unit: mm)

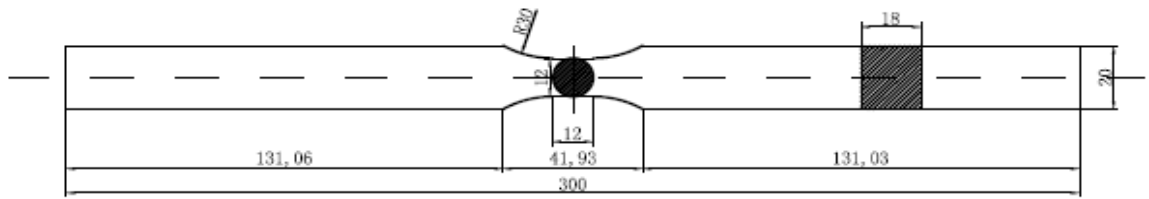


Figure 3-2 Geometric dimensions of SS4-1 and SS4-2 (unit: mm)

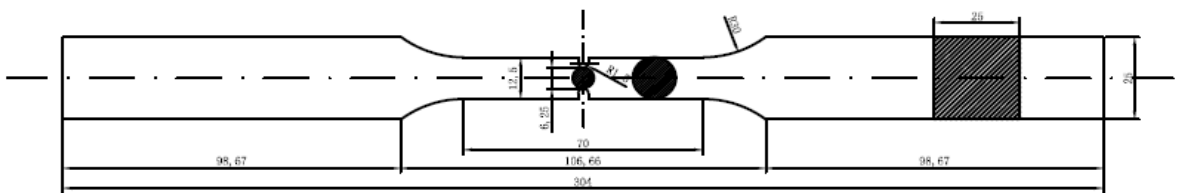


Figure 3-3 Geometric dimensions of SS5-1 (unit: mm)

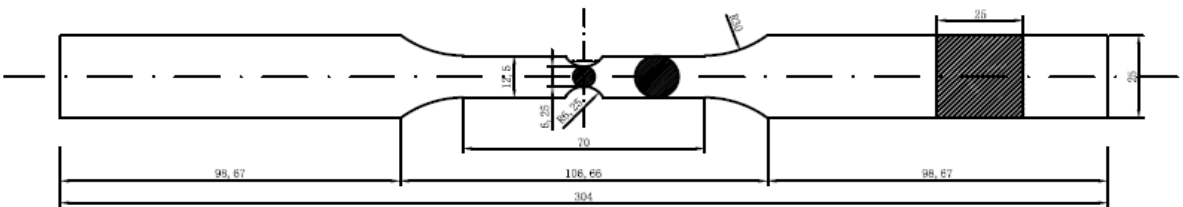


Figure 3-4 Geometric dimensions of SS6-1 (unit: mm)



Figure 3-5 General view of the SS316L specimens



Figure 3-6 (a) MTS servo-hydraulic test machine for cyclic loading test; (b) Test setup for specimen SS3-1 under monotonic loading with Zwick Z100 universal testing machine

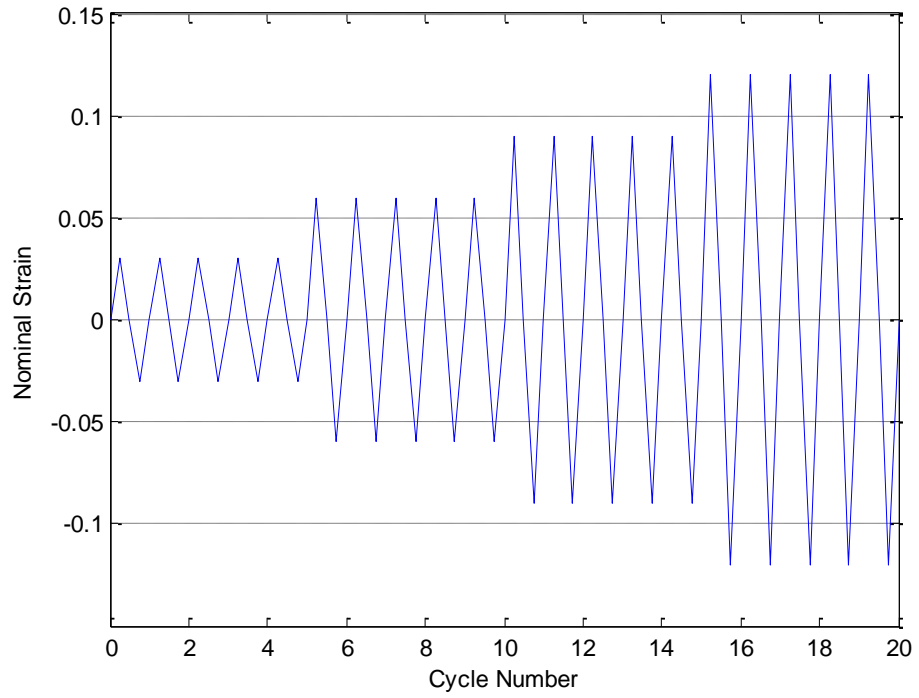


Figure 3-7 Loading protocol for specimen SS4-1 and SS4-2

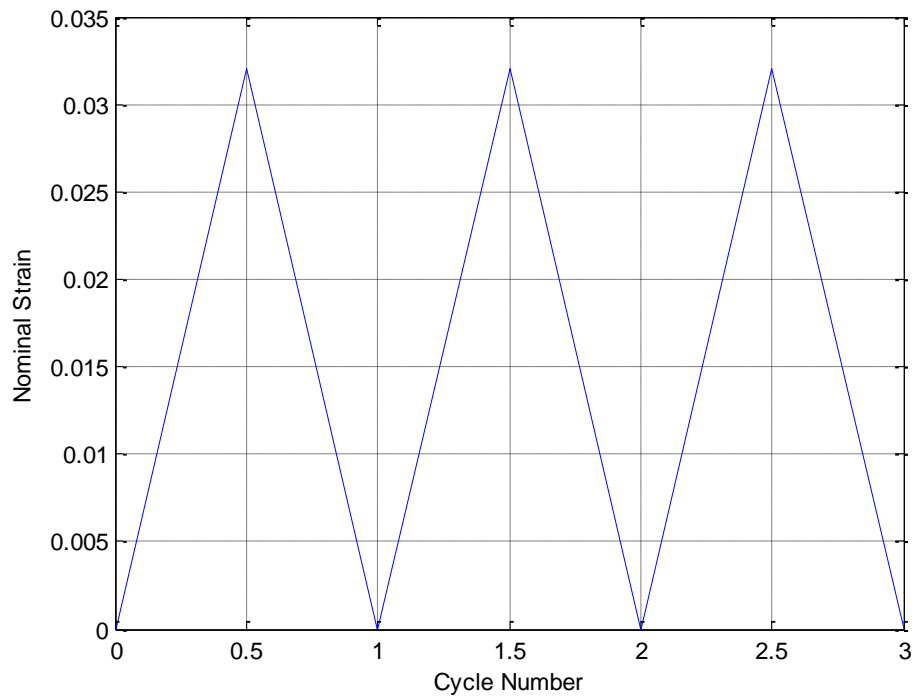


Figure 3-8 Loading protocol for specimen SS5-1

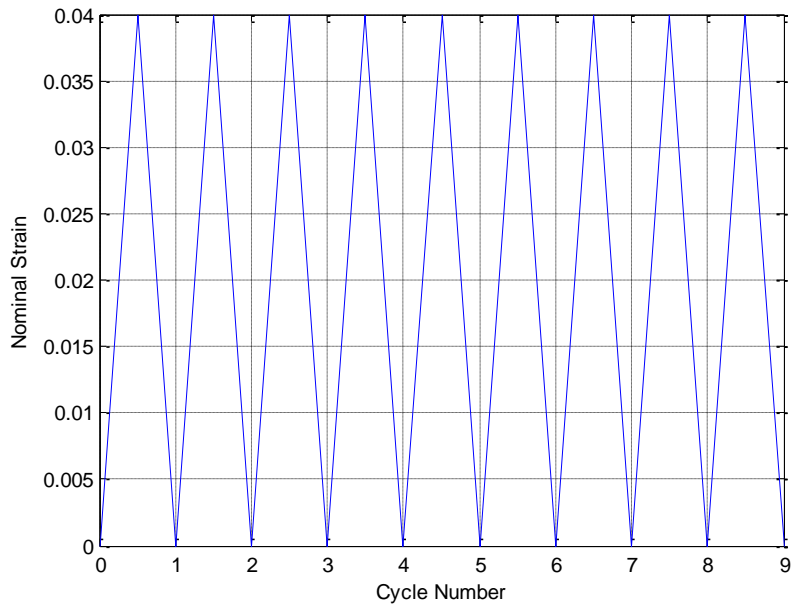


Figure 3-9 Loading protocol for specimen SS6-1



Figure 3-10 Test set up for specimen SS5-1 under cyclic loading

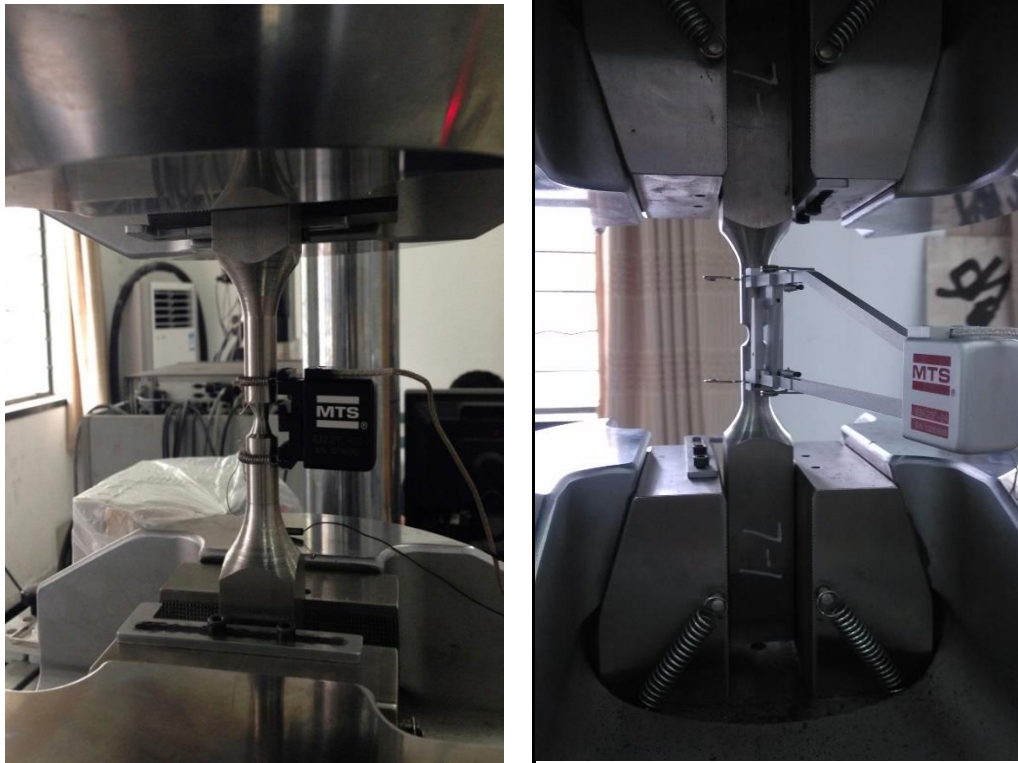


Figure 3-11 Test setup for specimens: (a) SS6-1 under cyclic loading; (b) SS7-1 under monotonic loading

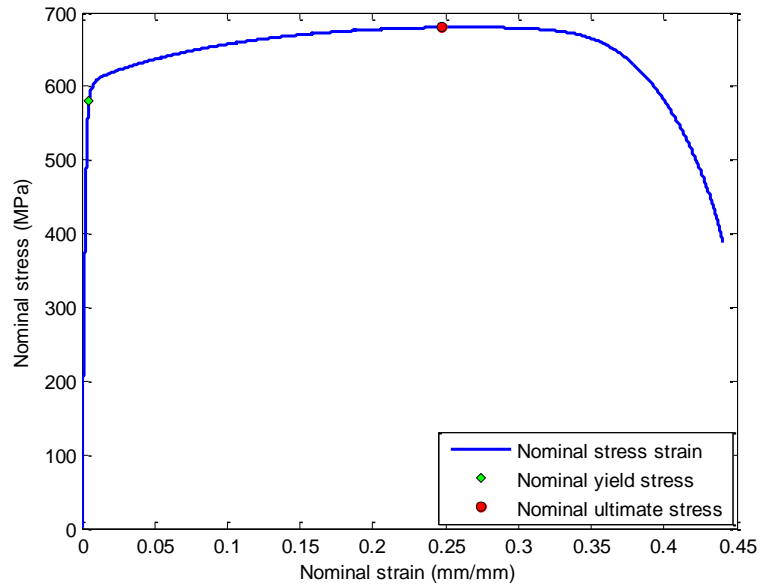


Figure 3-12 Engineering (nominal) stress strain relationship for AISI 316L stainless steel (SS7-1)

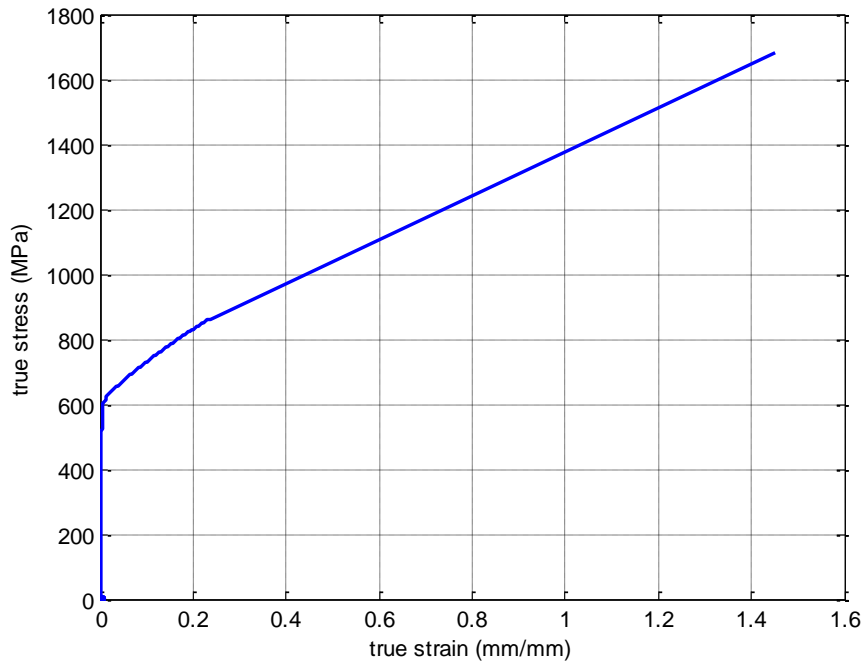


Figure 3-13 True stress strain relationship for AISI 316L stainless steel

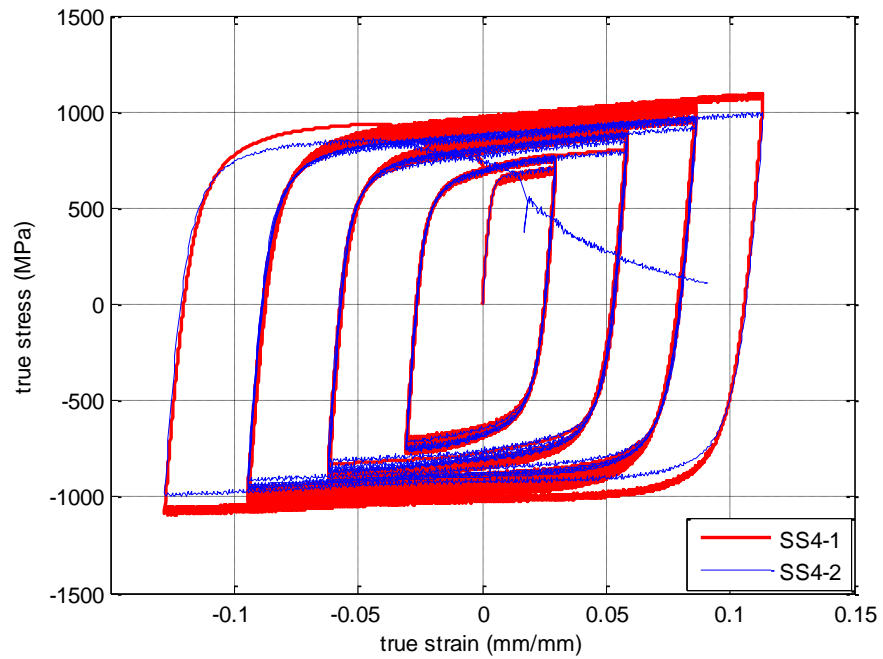


Figure 3-14 True stress versus true plastic strain for AISI 316L stainless steel

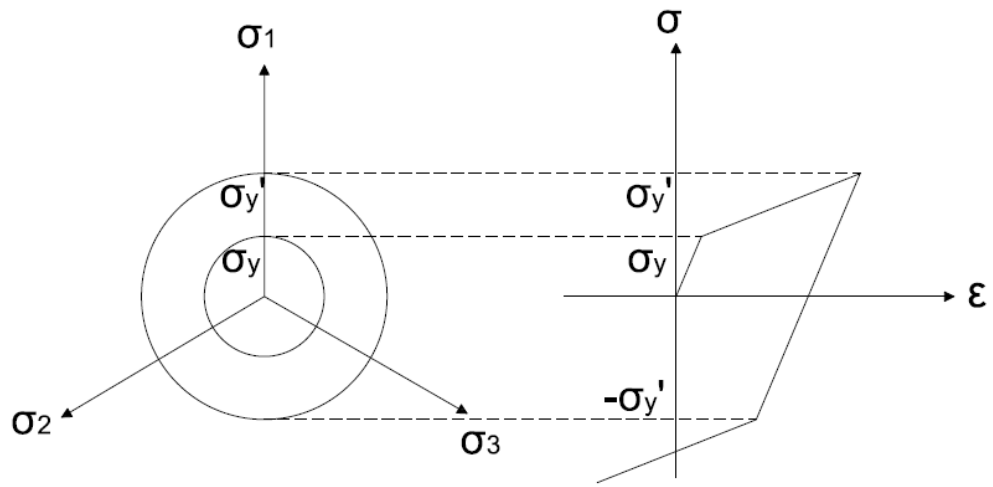


Figure 3-15 Isotropic yield surface evolution

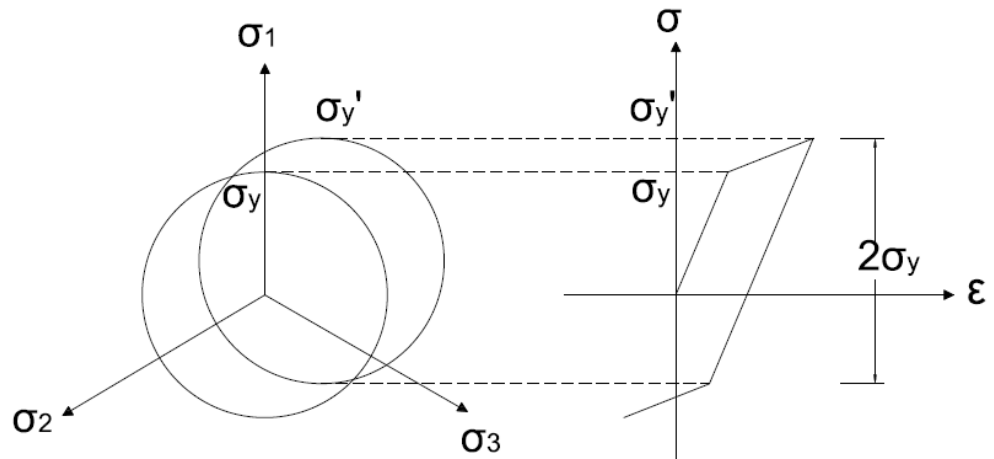


Figure 3-16 Kinematic yield surface evolution

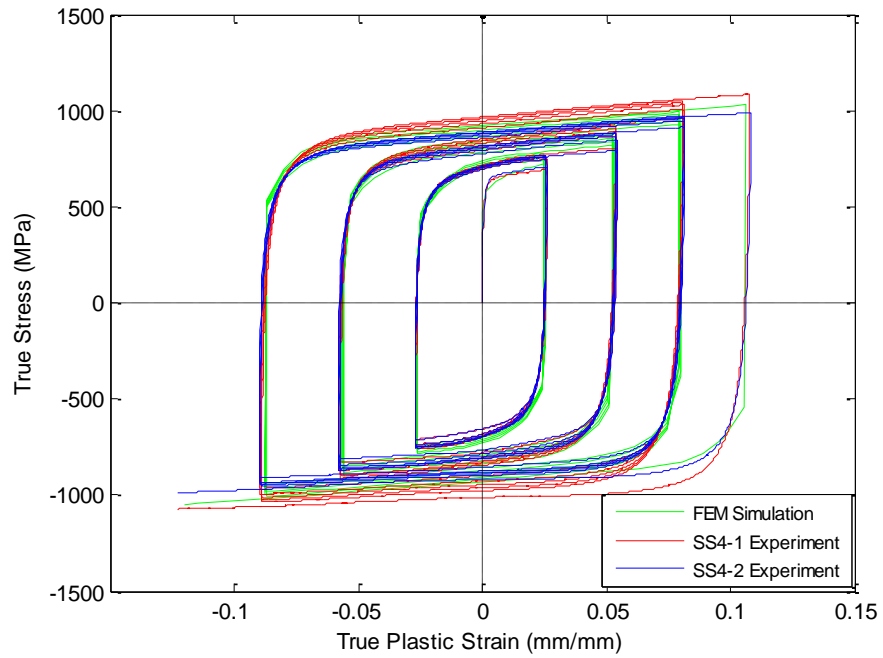


Figure 3-17 AISI 316L plastic strain hardening properties validation

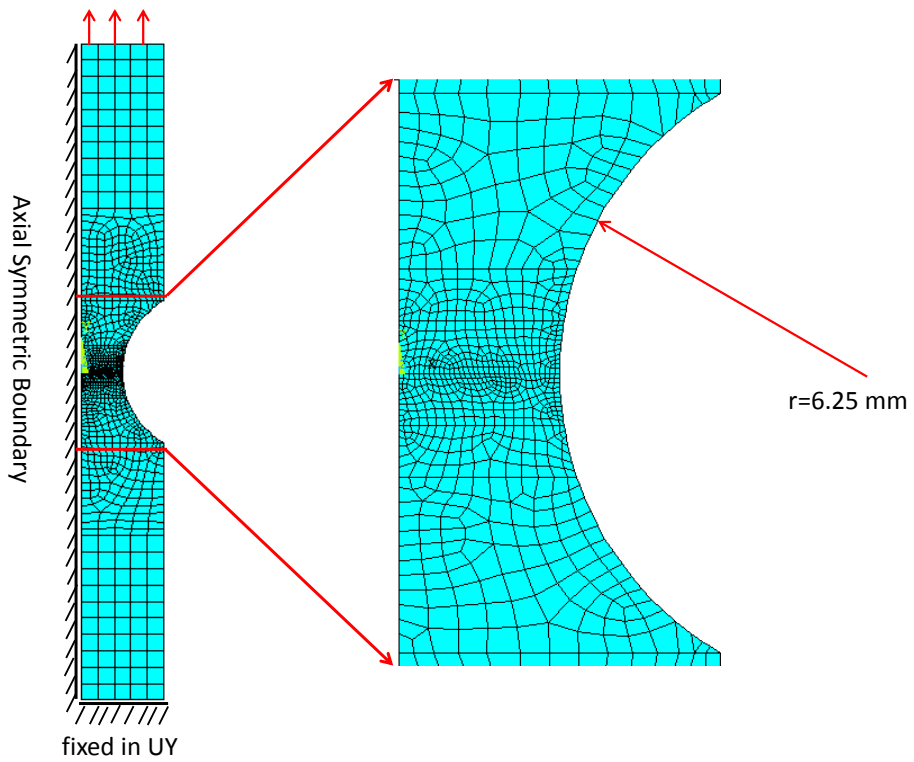


Figure 3-18 Finite element model establishment for SS6-1 and SS7-1

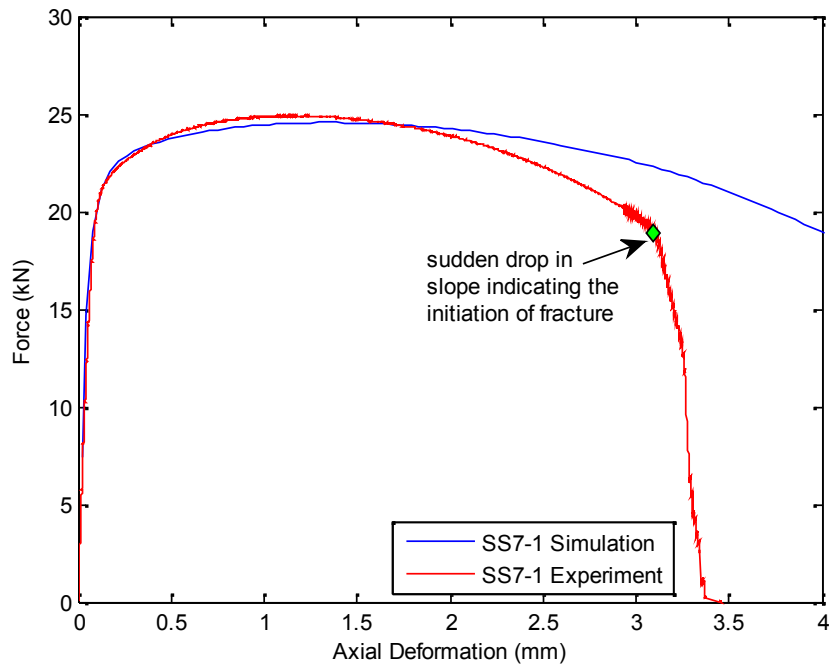


Figure 3-19 Force deformation relationship of NOTCHED specimen SS7-1

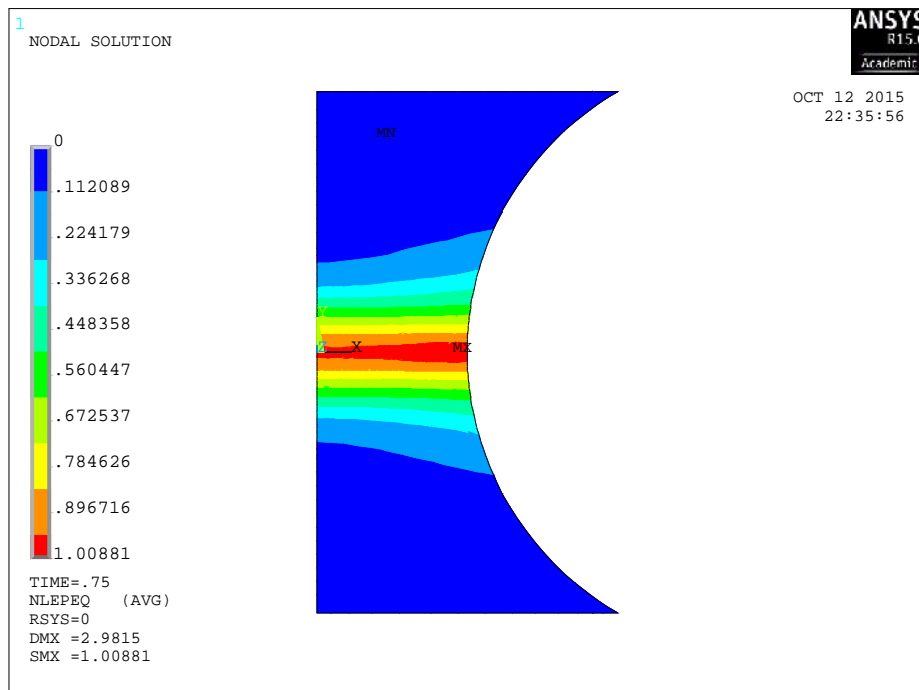


Figure 3-20 Equivalent plastic strain of SS7-1 at fracture initiation

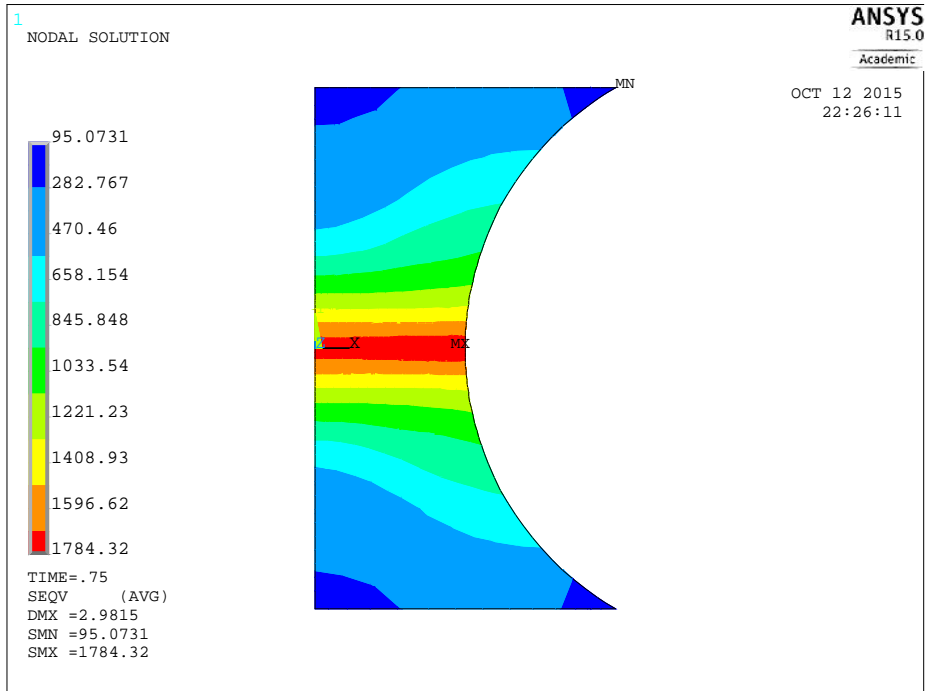


Figure 3-21 Von Mises stress of SS7-1 at fracture initiation

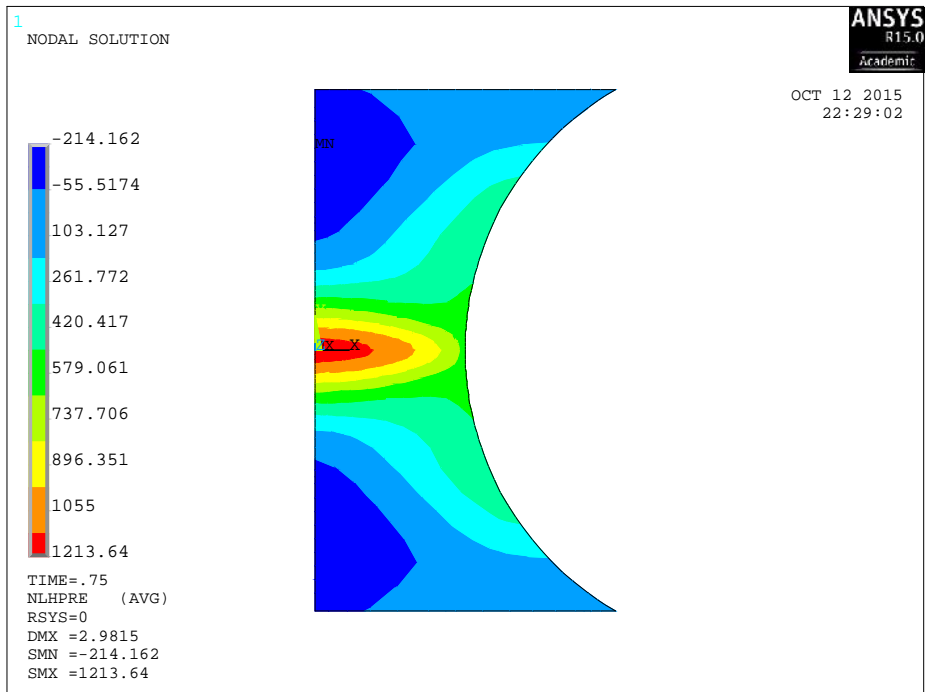


Figure 3-22 Hydrostatic stress of SS7-1 at fracture initiation

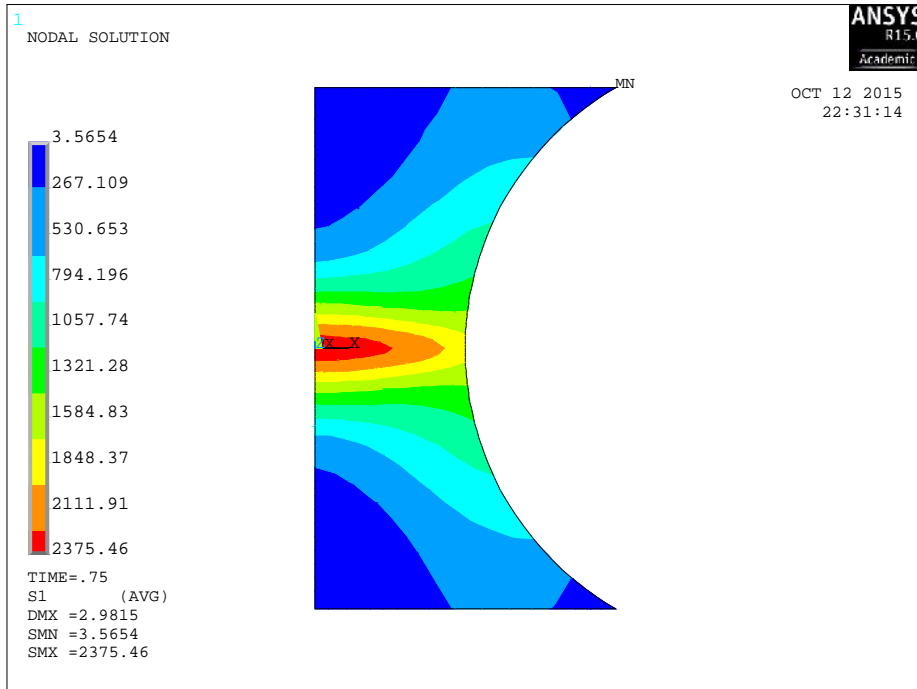


Figure 3-23 1st principal stress of SS7-1 at fracture initiation

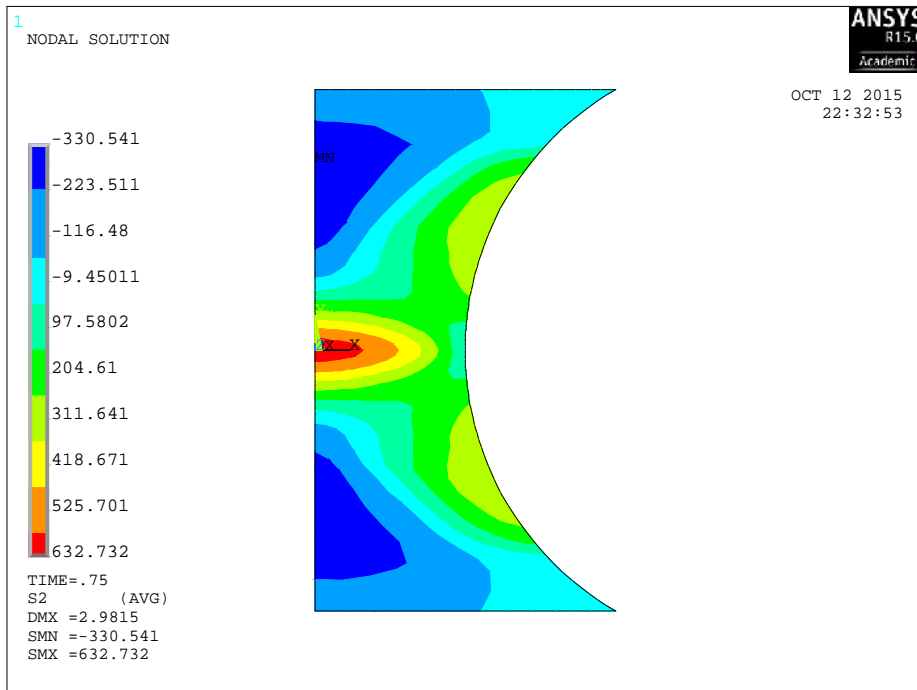


Figure 3-24 2nd principal stress of SS7-1 at fracture initiation

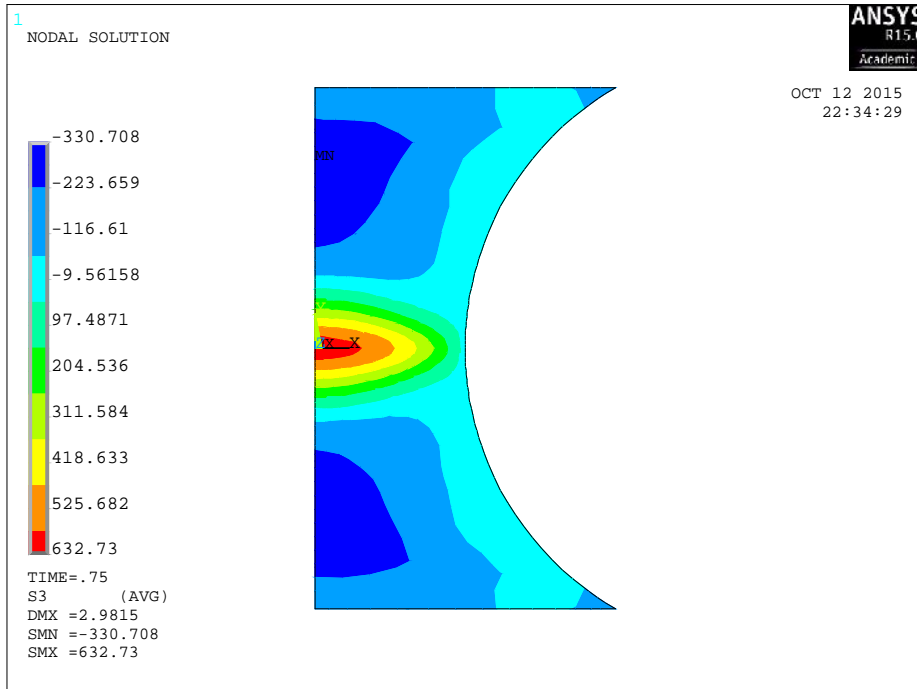


Figure 3-25 3rd principal stress of SS7-1 at fracture initiation

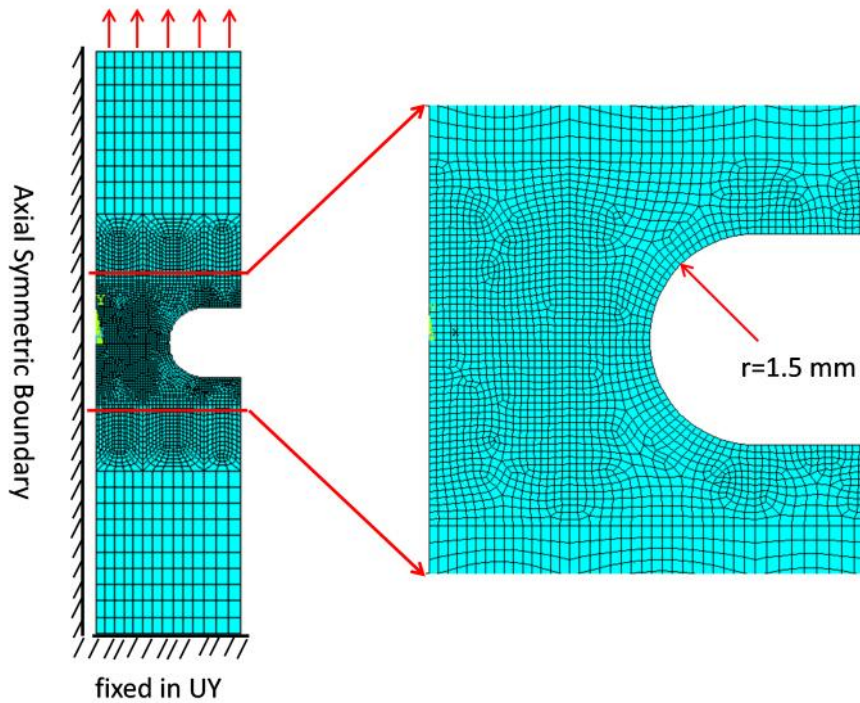


Figure 3-26 Meshed finite element model establishment of SS5-1

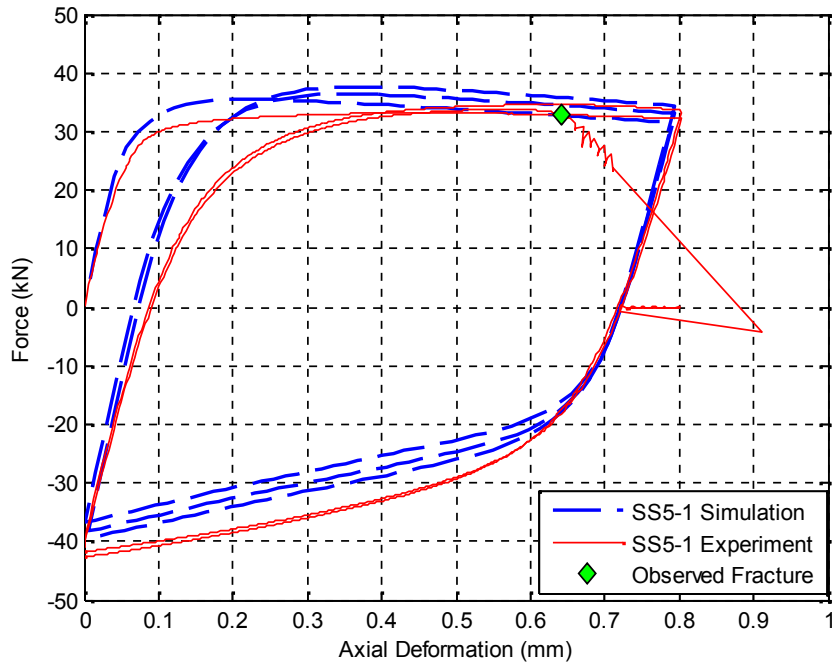


Figure 3-27 Comparisons on the experiment and FEM simulation for SS5-1

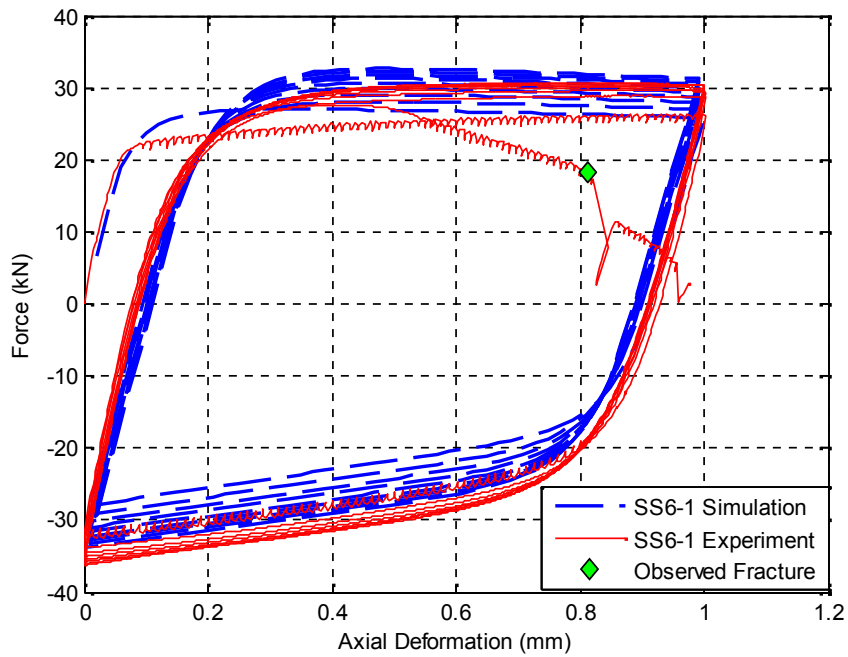
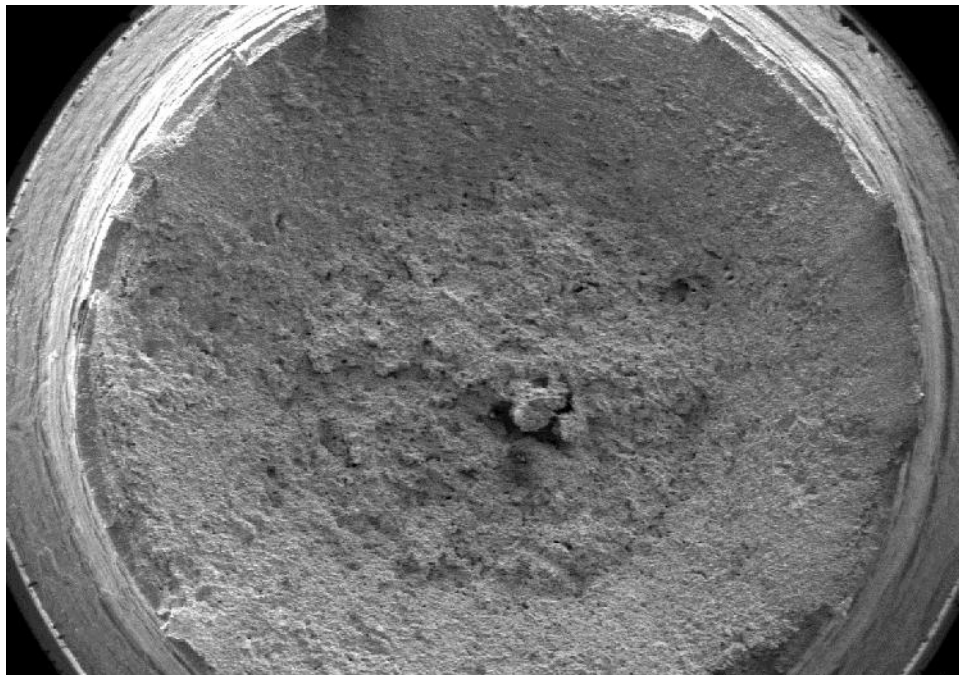


Figure 3-28 Comparisons on the experiment and FEM simulation for SS6-1



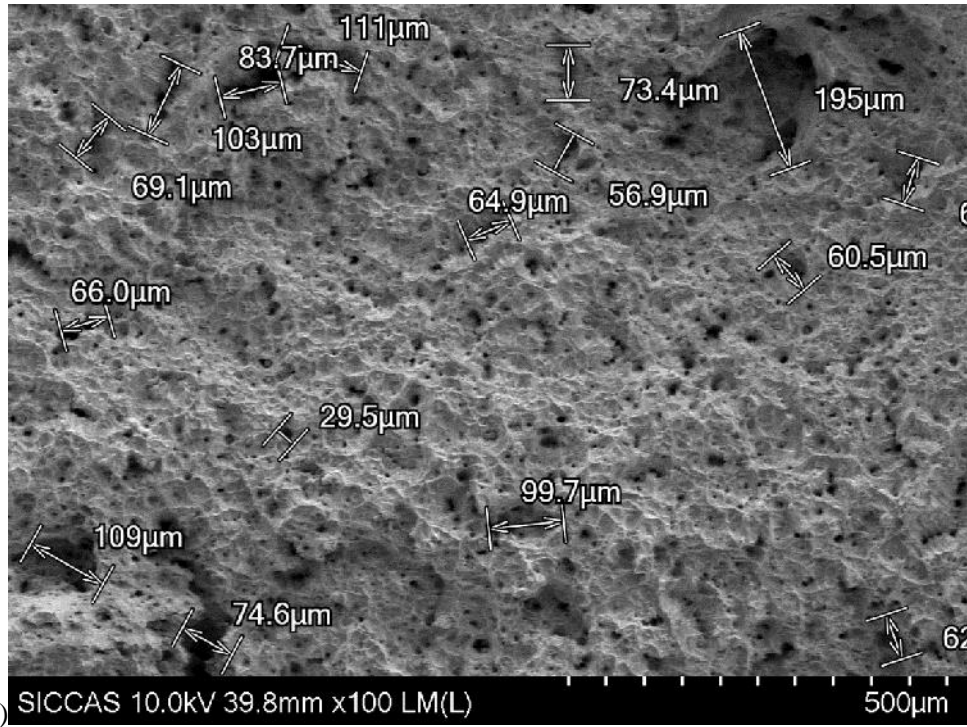
(a)



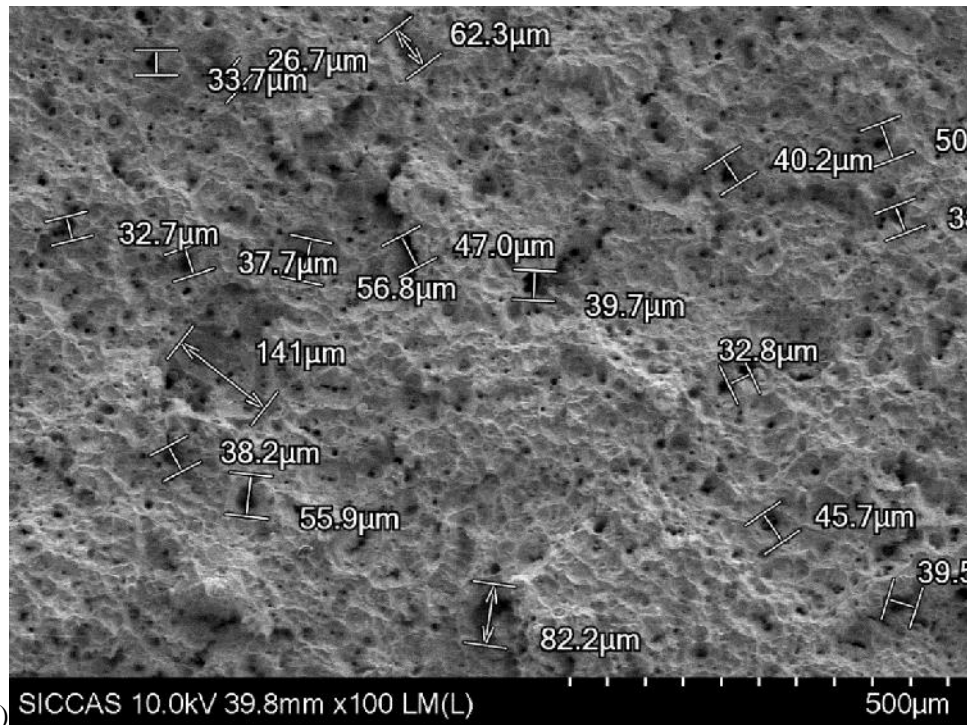
(b) SICCAS 10.0kV 39.8mm x20 LM(L)

2.00mm

Figure 3-29 Fractured surface of SS7-1



(a)



(b)

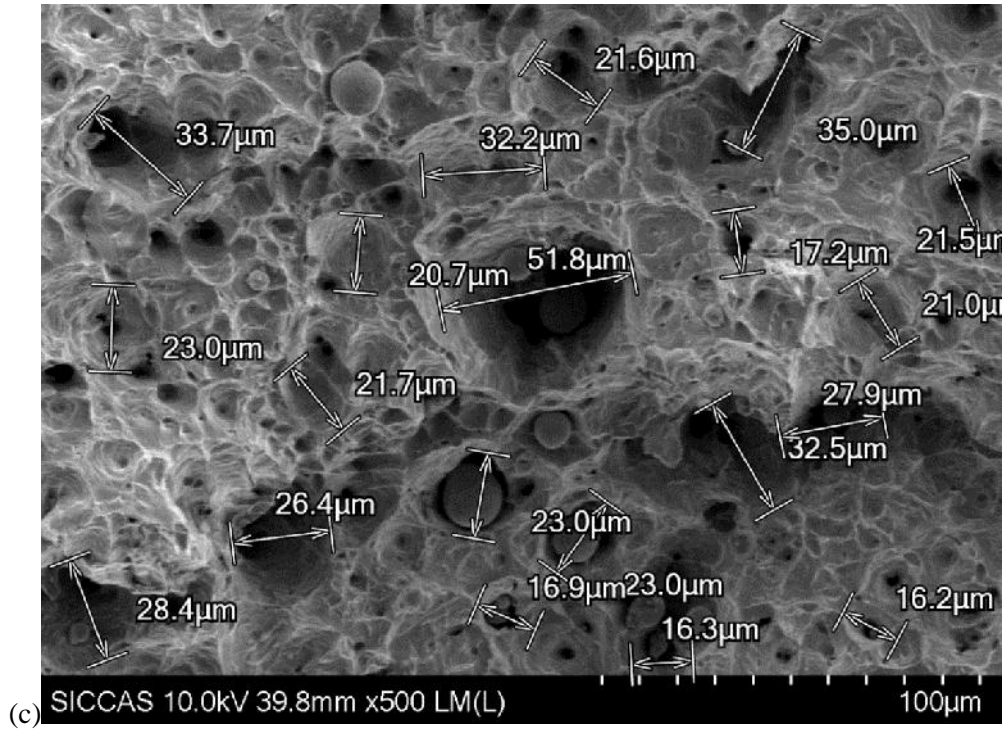


Figure 3-30 Characteristic Length l^* determination

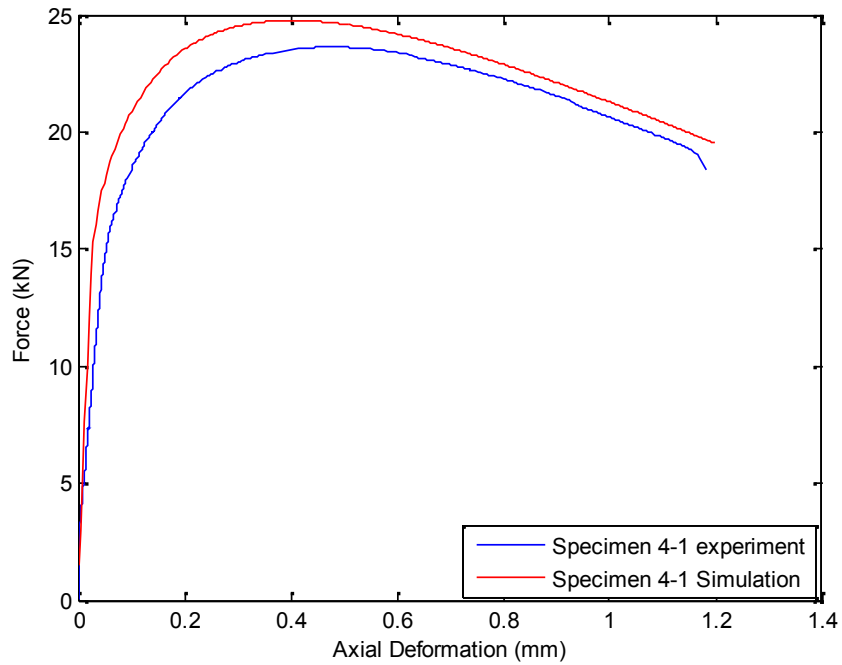


Figure 3-31 Comparisons on experiment (Liao et al.) and FEM simulation for specimen 4-1

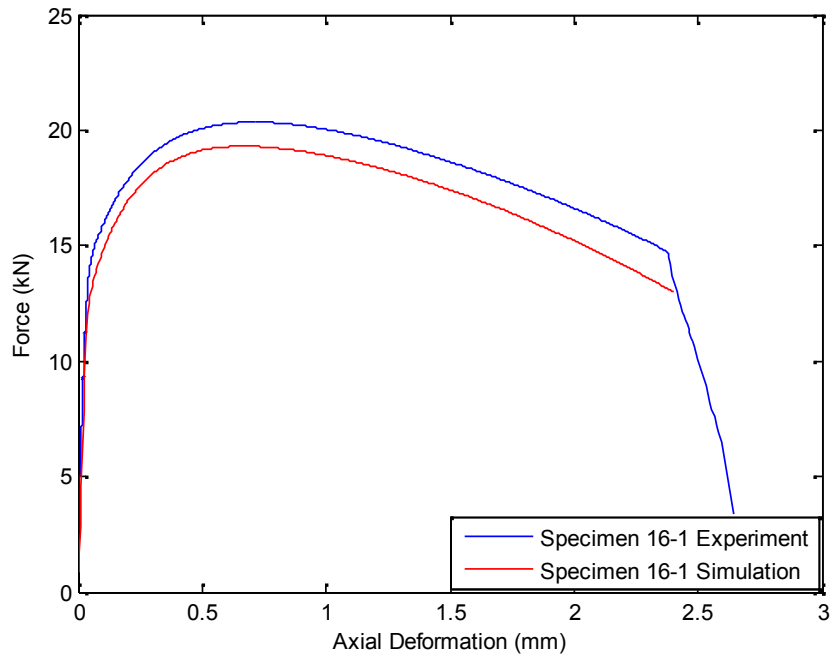


Figure 3-32 Comparisons on experiment (Liao et al.) and FEM simulation for specimen 16-1

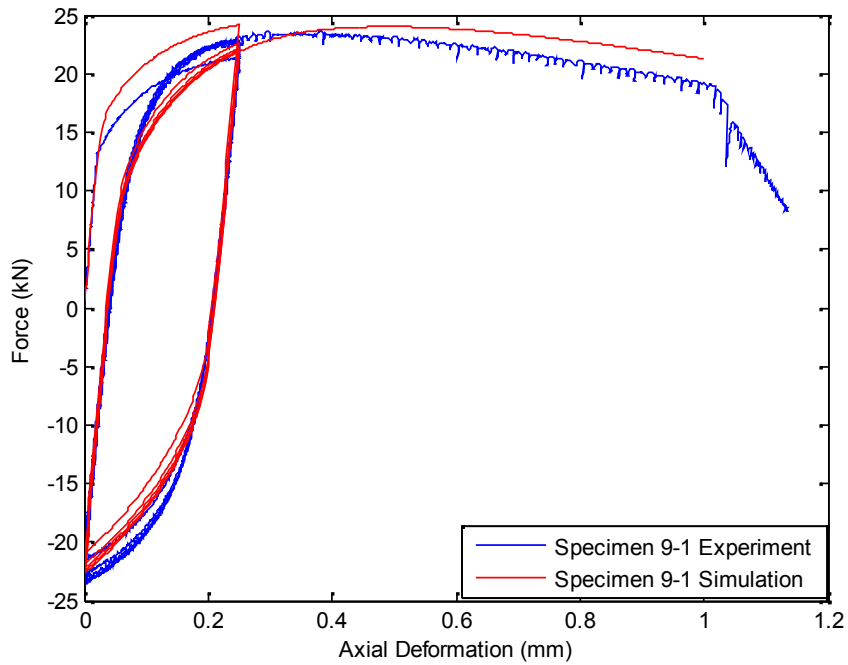


Figure 3-33 Comparisons on experiment (Liao et al.) and FEM simulation for specimen 9-1

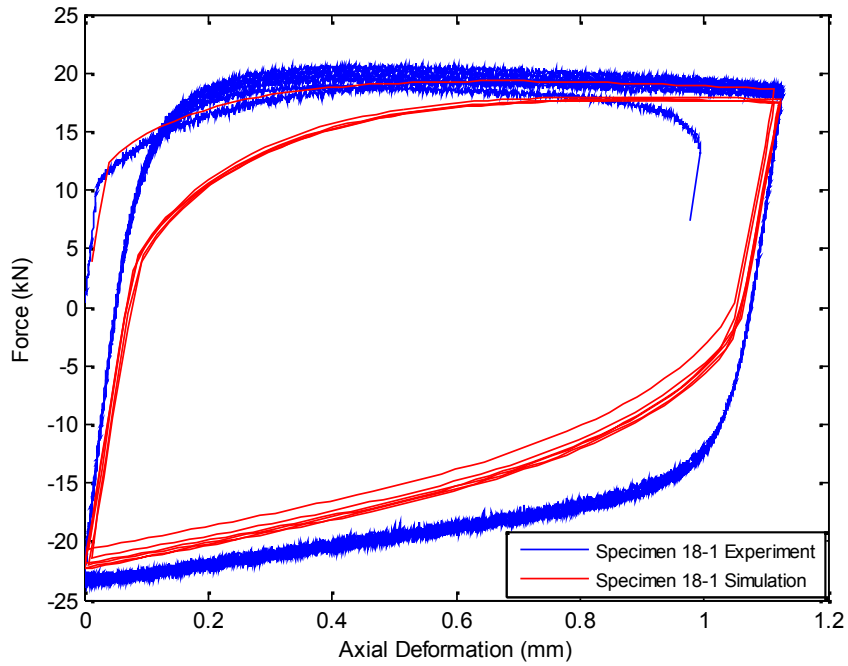


Figure 3-34 Comparisons on experiment (Liao et al.) and FEM simulation for specimen 18-1

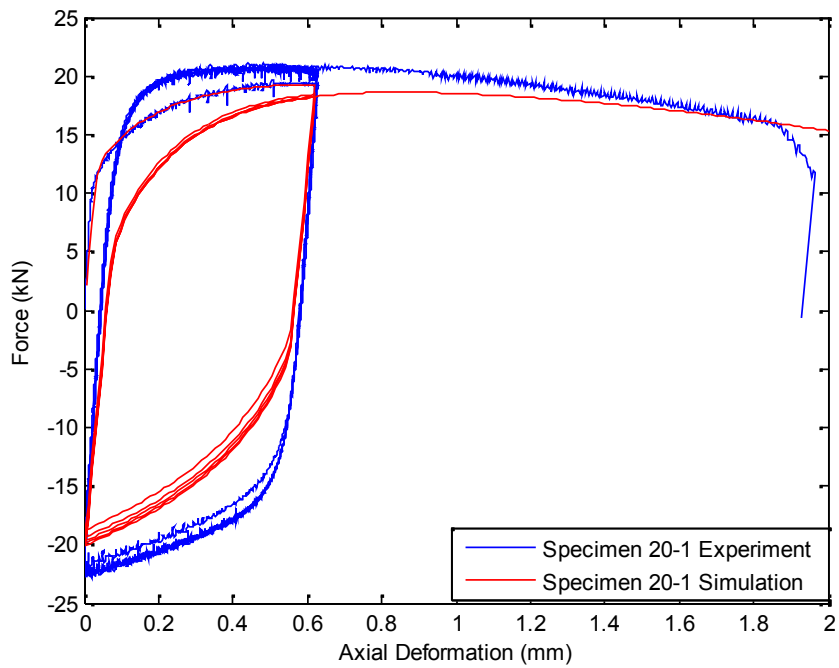


Figure 3-35 Comparisons experiment (Liao et al.) and FEM simulation for specimen 20-1

Table 3-1 Chemical compositions of AISI 316L stainless steel

Cr%	Ni%	C%	Mn%	Si%	P%	S%	N%	Other
16-18	10-14	0.03	2	0.75	0.045	0.03	0.10	2.0-3.0 Mo

Table 3-2 Specimen dimensions and test results

Specimen No.	Loading	Failure
SS3-1	monotonic	LTF (19.85,26.7)
SS4-1	cyclic	CTF [16,-1.45,99.81]
SS4-2	cyclic	CTF [16,-1.03,110.6]
SS5-1	cyclic	CTF [3,0.64,33.3]
SS6-1	cyclic	CTF [9,0.81,22.5]
SS7-1	monotonic	LTF (3.09,20.0)

Note: LTF=load to failure. The specimen is monotonically loaded until failure. The deformation within the gauge part with respect to the initial state and the applied force when failure occurs are recorded in the parentheses. For example, (19.85,26.7) refers to a monotonically loaded specimen and failure was observed at the specimen deformation of 19.85 mm and the corresponding applied force was 26.7 KN. CTF=cycle to failure. The specimen is cyclically loaded until failure. The cycle number, failure deformation, and the corresponding force are recorded in the square brackets. For example, [16,-1.45,99.81] refers to a cyclically loaded specimen and failure was observed at the 16th loading cycle when the specimen deformation within the gauge part was -1.45 mm with respect to initial state and the corresponding applied force was 99.81 KN.

Table 3-3 Engineering properties of AISI 316L stainless steel

Specimen	σ_v (MPa)	ϵ_v	σ_u (MPa)	ϵ_u	E (MPa)
SS3-1	531.6	0.0047	680.2	0.2667	197100

Table 3-4 Calibrated material parameters of 316L stainless steel for the combined hardening model

C_1	γ_1	C_2	γ_2	C_3	γ_3	k	R_0	R_∞	b
15064	100.74	576.68	0.0158	400	0	556.94	0	300.01	0.40

Table 3-5 CVGM calibration results comparison for A992 steel

A992/Q345	$VGI_{critical}$	λ
Kanvinde (2007)	2.80	0.38
Liao et al. (2012)	2.29~2.69	0.15
Current Study	3.11~3.56	0.38

Chapter 4 : Numerical Simulation of Cyclic Loading Behavior of Link Beam without Web Perforation

The finite element analysis results of ASTM A992 steel, AISI 316L stainless steel, and G20Mn5QT cast steel shear links without web perforations are discussed in this chapter. To verify the accuracy of finite element model, experimental test data of the cast steel shear links from Zhang (2015) are compared with the numerical simulation results from this study. Cyclic quasi-static loading protocol following the recommended protocol of the AISC seismic provisions (AISC 2010) for link beams is applied to the shear links in finite element analysis. The behaviors of the shear links are evaluated in terms of five key parameters: elastic stiffness, yield strength, ultimate strength, ductility, and energy dissipation.

4.1. ASTM A992 Steel Shear links

Based on the AISC Seismic Provisions, the link length ratio ρ is defined as the ratio between link length e and the ratio of the plastic moment capacity M_p to the plastic shear capacity V_p of the link section, i.e., $\rho = e/(M_p/V_p)$. AISC Seismic Provisions defines the link types based on the value of the link length ratio ρ , that is, shear link for $\rho < 1.6$, flexural link for $\rho > 2.6$, and intermediate link for $1.6 < \rho < 2.6$.

A total of four shear link specimens with a constant link length ratio ρ of 1.3 were selected for the numerical investigation on the behaviors of the shear links under cyclic loading. The selected shear link specimens are from the hot-rolled sections of W10x33,

W12x50, W14x74, and W16x77. The thickness and the spacing of the web stiffeners of the A992 shear link specimens are designed according to the AISC Seismic Provisions.

4.1.1. Finite Element Modeling (FEM) of A992 Steel Shear links

4.1.1.1. Plasticity Hardening Model Parameters

The material properties for ASTM A992 structural steel used in this study is with reference to the experimental data from cyclic coupon tests performed by Kaufmann et al. (2001) on ASTM A572 Grade 50 structural steel. Von Mises yield criterion is assumed for the yielding of the material, which is associated with the flow rule characterized by the combined kinematic and isotropic hardening. The combined plastic strain hardening rule which is superimposed by the bilinear isotropic hardening model and the Chaboche model was applied to characterize the stress strain relationship of A992 steel after material yielding, which is expressed in Equation 4-1. The material parameters calibrated from the cyclic coupon tests conducted by Kaufmann et.al. (2001) for the combined hardening model are listed in Table 4-2.

$$\sigma = \sum_{i=1}^4 \frac{C_i}{\gamma_i} (1 - e^{-\gamma_i \epsilon_p}) + k + E_t \cdot \hat{\epsilon}_p \quad \text{Equation 4-1}$$

Where: C_i and γ_i are the calibrated material parameters characterizing the kinematic hardening effect; E_t is the calibrated material parameter characterizing the isotropic

hardening effect; k is the yield stress of A992 steel, taken as 380 MPa; ϵ_p and $\hat{\epsilon}_p$ are the instantaneous plastic strain and the accumulated plastic strain respectively.

4.1.2.2. Failure Point Estimation: Fracture Initiation Criterion

The finite element program ANSYS Academic 15.0 was employed to perform finite element simulations on the shear links. The finite element models are intended to predict the cyclic loading behaviors of the investigated shear links, including strength, ductility, and strength degradation due to local buckling in flange and web or fracture. Though the fracture initiation and propagation mechanism was not explicitly modeled in the finite element modeling, ductile fracture initiation due to low cycle fatigue was set as the limiting state of the shear links subjected to large inelastic strain cycles. The ductile fracture initiation point was estimated using the cyclic void growth model (CVGM) proposed by Kanvinde and Deierlein (2007), as expressed in Equation 4-2.

Damage

$$= \frac{\sum_{tensile\ cycles} \int_{\epsilon_1}^{\epsilon_2} \exp(|1.5T|) d\epsilon_p - \sum_{compressive\ cycles} \int_{\epsilon_1}^{\epsilon_2} \exp(|1.5T|) d\epsilon_p}{VGI_{critical} \cdot \exp(-\lambda \epsilon_p^{accumulated})} \quad \text{Equation 4-2}$$

where T is the stress triaxiality, which is defined as the ratio of the hydrostatic stress to the Von Mises stress; ϵ_p is the equivalent plastic strain; and $\epsilon_p^{accumulated}$ is the accumulated plastic strain to the beginning of each tensile cycles. Ductile fracture initiation is expected in the shear link when the damage index exceeds 1 within its critical volume. The required material properties listed in Equation 4-2 were referenced from the CVGM calibration experiments conducted by Kanvinde and Deierlein (2007), which are

for low carbon steel cut from rolled plate shape A572-Grade 50. The $VGI_{critical}$ and λ used for the A992 steel in this study are 1.1 and 0.49 respectively.

4.1.2.3. Finite Element Model Establishment

Shell element 181 in ANSYS was utilized for the finite element establishment. This type of element has four nodes with six degrees of freedom (DOF) at each node, including three translational DOF and three rotational DOF. The geometry dimensions of the finite element model corresponded to the centerlines of the shear link cross section. Web stiffener welding was not explicitly modeled in the finite element model.

Mesh refinement studies were conducted to determine the level of refinement necessary to achieve reasonable accuracy for cyclic behavior study of the shear links. The meshed model of the investigated A992 shear links of different sections are plotted in Figure 4-1. The mesh size can be estimated from Figure 4-1 since the section size is known. Large displacement option has been taken into account in FE analysis to capture local buckling.

4.1.2.4. Boundary Conditions

The boundary constraints applied to the finite element model are analogous to the boundary constraints of a double curvature beam. A short length of rigid segment (100 mm long) was added to the model on the left side to supply the restraining effects on model provided by loading fixture. The rigid segment restrained the left end of the finite element model against rotations, while allowed the translational (lateral and longitudinal)

movement of the model. In order to make the rigid segment stiff enough to minimize its own deformation, the thickness of the flange and web plates of the rigid segment were 20 and 40 times larger than the flange and web thickness of the shear link. All nodes at the left side of the rigid segment were restrained against rotations and out-of-plane movement. Simultaneously, all nodes at the right side of the shear link model were restrained from all rotations and translational movements. The applied boundary restraints to a meshed model (e.g., W10x33) are plotted in Figure 4-2.

4.1.2.5. Cyclic Loading Protocol

According to Richards and Uang (2003), monotonic loading underestimate buckling load amplitude and strength degradation. To determine the ductility ratio, performing cyclic load analysis is essential. In other words, cyclic loading was necessary to consider local buckling and the associated strength degradation accurately. A cyclic load testing provides a more realistic loading to structures under an earthquake loading. Iwasaki et al. (1987) concluded that loading rate has insignificant effect on hysteresis loops and for large displacement the energy dissipation capability is smaller when loading rate is lower.

Load on the shear link specimen was applied by controlling transverse displacements of the nodes at the left end section of the shear link model. The investigated shear link specimens were under quasi-static loading. The cyclic loading protocol prescribed by AISC Seismic Provisions (AISC 2010) was adopted in this study, which is measured by link rotation angle γ . The loading protocol applied for the finite element analysis includes 6 cycles of γ at the amplitude of 0.00375 radians, 6 cycles of γ at the amplitude of 0.005

radians, 6 cycles of γ at the amplitude of 0.0075 radians, 6 cycles of γ at the amplitude of 0.01 radians, 4 cycles of γ at the amplitude of 0.015 radians, 4 cycles of γ at the amplitude of 0.02 radians, 2 cycles of γ at the amplitude of 0.03 radians, 1 cycle of γ at the amplitude of 0.04 radians, 1 cycle of γ at the amplitude of 0.05 radians, and the following each cycle of γ increased in the amplitude by 0.02 radians. The loading history is plotted in Figure 4-3.

4.1.3. Results and Discussion

4.1.3.1. Ductility

Ductility is the ability of the structure to sustain large permanent deformation without significant reduction in strength. Earthquake energy absorbed through inelastic deformation is one of the important seismic resistant structures characteristics. Ductility of properly designed EBF is directly related to the ductility of the shear links (Kasai and Popov 1986). Shear links (short links) dissipate energy primarily through shear distortion which provides more ductility than longer links (flexural links). Well detailed shear links exhibited stable and ductile cyclic behavior without brittle failure before reaching a plastic rotation of 0.1 rad. The ductility of a shear link is quantitatively measured by the ductility ratio, which is calculated from the shear link's backbone curve.

Based on the finite element analysis results, the hysteresis loops of the four A992 shear link specimens are plotted in Figure 4-4. For the A992 shear links in this study, fracture initiation was predicted on the basis of the CVGM for the specimens W10x33, W12x50,

and W14x74 during the loading cycle with the link rotation amplitude of 0.15 radians. The hysteresis loops of these shear links after the predicted fracture initiation were plotted in the dashed line, which is shown in Figure 4-4. The backbone curves from the corresponding hysteresis loops of the shear link specimens are plotted in Figure 4-5. The ductility ratio μ of each shear link specimen was determined from the backbone curve, which was calculated as the ratio of the link rotation γ_u to the link rotation γ_y . The positions of γ_u and γ_y are denoted in the backbone curves shown in Figure 4-5. Term γ_u is determined as the link rotation corresponding to the occurrence when ductile fracture was initiated in the finite element model of a shear link, or when significant buckling was observed, whichever came first. The term γ_y is taken as the product of the ultimate shear link strength divided by the shear link's elastic stiffness ($\gamma_y = V_u / K_0$). Detailed ductility properties for the investigated A992 shear links are listed in Table 4-3.

4.1.3.2. Elastic Stiffness K_0

The elastic stiffness K_0 is a key parameter in influencing a link's elastic deformation. For the investigated A992 shear links, the elastic stiffness K_0 (unit: kN/mm) values were calculated from the linear portions of the backbone curves shown in Figure 4-5. To facilitate engineering design of the shear links, the analytical calculation of the elastic stiffness for the investigated shear links are also presented. The elastic stiffness of a shear link is calculated by considering both the effect of bending moment and shear force on the deformation of the shear link, which is expressed in Equation 4-3.

$$K_0 = \frac{K_b K_s}{K_b + K_s} \quad \text{Equation 4-3}$$

Where $K_b = 12EI/L^3$ is the bending stiffness; E is the elastic modulus; I is the second moment of area. $K_s = GA_w/L$ is the shear stiffness; G is the shear modulus; A_w is the web area. The elastic stiffness K_0 values determined from the analytical method and the FEM simulation results were verified to be very close, which are listed in Table 4-4.

4.1.3.3. Yield Strength V_p and Ultimate Shear Strength V_u

Yield Strength V_p and Ultimate Shear Strength V_u were also determined from the backbone curves of the A992 shear links. With reference to the research conducted by Uang (Uang 1989) and Alavi and Nateghi (Alavi and Nateghi 2013), the shear strength V_p of a shear link was equal to the shear force at the transition point starting from the nonlinear segment of the backbone curve; and the ultimate strength V_u was defined as the maximum shear force in the backbone curve. Over-strength factor Ω was thereby defined as the division of V_u to V_p . The positions of V_p and V_u were also denoted in the backbone curves of the investigated A992 shear links. Detailed values of V_p , V_u , and Ω are listed in Table 4-5.

To facilitate the engineering design of the shear links, the yield strength of the selected A992 shear links were also calculated via the theoretical approach. The yield strength of the A992 shear link is equal to the shear force leading to the yielding initiation of the shear link web, which is expressed in Equation 4-4. The analytically computed yield strength values of the A992 shear links are listed in Table 4-6 for comparison. Generally

the V_p values determined from the FEM simulation results and the analytical method are very close.

$$V_p = 0.6\sigma_y A_w \quad \text{Equation 4-4}$$

4.1.3.5. Plastic Strain Contour

Von Mises plastic strain contours for the A992 shear links at the link rotation angle γ of 0.02 radians and at the link rotation angle γ of 0.11 radians are also recorded. The Von Mises plastic strain is determined based on Equation 4-5.

$$\varepsilon_{ep} = \frac{\sqrt{2}}{3} \sqrt{(\varepsilon_1^p - \varepsilon_2^p)^2 + (\varepsilon_2^p - \varepsilon_3^p)^2 + (\varepsilon_3^p - \varepsilon_1^p)^2} \quad \text{Equation 4-5}$$

Where: ε_{ep} is the Von Mises plastic strain; ε_1^p , ε_2^p , and ε_3^p are the first principal, second principal, and third principal stresses respectively.

It is expected that at the link rotation γ of 0.02 radians, plastic strain has just initiated within the web area of the investigated shear links; and at the link rotation γ of 0.11 radians, plastic strain has substantially accumulated with the web areas of the shear links. The Von Mises plastic strain contours for the investigated A992 shear links at $\gamma=0.02$ radians and $\gamma=0.11$ radians are plotted in Figure 4-6 and Figure 4-7 respectively. Shown in Figure 4-7, web buckling was observed for A992 shear links W12x50 and W14x74 at the link rotation angle of 0.11 radians.

4.2. AISI 316L Stainless Steel Shear Links

Four AISI 316L stainless steel shear links with the same section sizes and the link lengths as the A992 shear link specimens were investigated in this study. Web stiffeners of the AISI 316L stainless steel shear links were designed the same as the A992 shear links. It should be noted that the hot-rolled sections with the section depth greater than 6 inches are not available for stainless steel, yet the stainless steel shear links can still be fabricated by welding the plates.

4.2.1. FEM of the AISI 316L Stainless Steel Shear Links

The material properties for AISI 316L stainless steel were experimentally determined from the coupon bars, which can be referenced from Chapter 3. Von Mises yield criterion is assumed for the yielding of the material, which is associated with the flow rule characterized by the combined kinematic and isotropic hardening. The combined plastic strain hardening rule which is superimposed by the nonlinear isotropic hardening model and the Chaboche model was applied to characterize the stress strain relationship of AISI 316L stainless steel after material yielding, which is expressed in Equation 4-6. The material plastic strain hardening parameters are listed in Table 3-4.

$$\sigma = \sum_{i=1}^3 \frac{C_i}{\gamma_i} (1 - e^{-\gamma_i \varepsilon_p}) + k + R_{\infty} (1 - e^{-b \cdot \hat{\varepsilon}_p}) \quad \text{Equation 4-6}$$

Where: C_i and γ_i are the calibrated material parameters characterizing the kinematic hardening effect; E_t is the calibrated material parameter characterizing the isotropic hardening effect; k is the yield stress of A992 steel, taken as 380 MPa; ϵ_p and $\hat{\epsilon}_p$ are the instantaneous plastic strain and the accumulated plastic strain respectively.

Shell element 181 in ANSYS was utilized for the finite element establishment. The finite element model building was the same as the one used for A992 shear link specimens. The boundary constraints applied to the AISI 316L stainless steel shear link specimens were the same as the boundary constraints applied to the A992 shear link specimens, which is plotted in Figure 4-2. Loading history plotted in Figure 4-3 was applied to the AISI 316L stainless steel shear links.

4.2.2. Results and Discussion

4.2.2.1. Ductility

Based on the finite element analysis results, the hysteresis loops of the four AISI 316L stainless steel shear link specimens are plotted in Figure 4-8. The backbone curves from the corresponding hysteresis loops of the shear link specimens are plotted in Figure 4-9. For the selected AISI 316L stainless steel shear links, fracture initiation was not triggered during the entire loading history; yet during the loading cycle with the amplitude of 0.15 radians, buckling was observed for the shear link specimens W10x33 and W14x74. Hence the ultimate link rotation γ_u for each stainless steel shear link was taken as the lesser of the link rotation angle corresponding to 15% load carrying capacity drop or 0.15

radians. The buckled shapes of the investigated AISI 316L stainless steel shear links are plotted in Figure 4-10. It can be observed that at the maximum applied link rotation of 0.15 radians, web local buckling occurred in specimens W12x50, W14x74, and W16x77, and both flange and web local buckling occurred in specimen W10x33.

Analogously, the ductility ratio μ of each stainless steel shear link specimen was determined from the backbone curve, which was calculated as the ratio of the link rotation γ_u to the link rotation γ_y . Detailed ductility properties for the investigated AISI 316L stainless steel shear links are listed in Table 4-8.

4.2.2.2. Elastic Stiffness K_θ

The elastic stiffness K_θ is a key parameter in influencing a link's elastic deformation. For the investigated AISI 316L stainless steel shear links, the elastic stiffness K_θ (unit: kN/mm) values were calculated from the linear portions of the back bone curves shown in Figure 4-9. Similarly, the elastic stiffness values of the AISI 316L stainless steel shear links were determined from Equation 4-4. The comparisons between the K_θ values determined from FEM simulation results and the analytical method are listed in Table 4-9.

4.2.2.3. Yield Strength V_p and Ultimate Shear Strength V_u

Yield Strength V_p and Ultimate Shear Strength V_u were also determined from the backbone curves of the AISI 316L stainless steel shear links via the same approach utilized to determine the V_p and V_u values for A992 shear links. Over-strength factor Ω was thereby computed from the division of V_u to V_p . Detailed values of V_p , V_u , and Ω are

listed in Table 4-10. Analogously, the theoretical values of V_p were determined for the AISI 316L stainless steel shear links via Equation 4-6, which are listed in Table 4-10.

4.2.2.4. Plastic Strain Contour

Von Mises plastic strain contours for the AISI 316L stainless steel shear links at the link rotation angle γ of 0.02 radians and at the link rotation angle γ of 0.11 radians are recorded. It is expected that at the link rotation γ of 0.02 radians, plastic strain has just initiated within the web area of the investigated shear links; and at the link rotation γ of 0.11 radians, plastic strain has substantially accumulated with the web areas of the shear links. The Von Mises plastic strain contours for the investigated AISI 316L stainless steel shear links at $\gamma=0.02$ radians and $\gamma=0.11$ radians are plotted in Figure 4-11 and Figure 4-12 respectively.

As expected, at the link rotation of 0.02 radians, local web area of the AISI 316L stainless steel shear links yielded under shear. At the link rotation of 0.11 radians, much larger web portions of the shear links yielded under shear, and web local buckling was triggered.

4.3. Cast Steel Shear Links

Two duplicate G20Mn5QT cast steel shear link specimens with identical design were investigated for cyclic loading behaviors. Section details of these two cast steel shear link specimens are listed in Table 4-11.

4.3.1. FEM of Cast Steel Shear Links

The material properties for G20Mn5QT cast steel used in this study were calibrated from the experimental data from experimental data. Von Mises yield criterion is assumed for the material, which is associated with the flow rule characterized by the combined kinematic and isotropic hardening. The combined plastic strain hardening rule which is superimposed by the nonlinear isotropic hardening model and the Chaboche model was applied to characterize the stress strain relationship of G20Mn5QT cast steel after material yielding, which is expressed in Equation 4-7. The calibrated material parameters for the combined hardening model are listed in Table 4-12.

$$\sigma = \frac{C_1}{\gamma_1} (1 - e^{-\gamma_1 \varepsilon_p}) + k + R_\infty (1 - e^{-b \cdot \varepsilon_p}) \quad \text{Equation 4-7}$$

Ductile fracture initiation due to low cycle fatigue was assumed to be the controlling limiting state for the cast steel shear links, as observed in experimental tests. The ductile fracture initiation was predicted by the CVGM which is used for predicting the ductile fracture initiation of A992 steel. For cast steel, the critical void growth index (VGI_{critical}) is assumed to be the same as A572 steel cut from rolled plate, which is 1.1, and the decay parameter λ is assumed to be higher than A572 steel, taken as 0.6 (Kanvinde and Deierlein 2007).

Shell element 181 in ANSYS was utilized for the finite element establishment. The meshed model for the cast steel shear link is plotted in Figure 4-13. Large displacement

option has been taken into account in FE analysis to capture local buckling. The boundary constraints applied to the finite element model of the cast steel shear link are the same as the ones used for the A992 steel shear links shown in Figure 4-2. The same loading protocol as defined by AISC Seismic Provisions (AISC 2010) (see Figure 4-3) was applied to the cast steel shear links in both FEA and experiments.

4.3.2. Cast Steel Shear link Results and Discussion

The experiment tests by Zhang (2015) was conducted to study the cyclic loading behavior of the shear links in an eccentrically braced frame (EBF) when both ends of the shear link are connected to the EBF frame beams. The experiment setup for the cast steel shear link specimens is shown in Figure 4-14.

The hysteresis loops of the cast steel shear link specimens determined from FEM simulations and the experiments on specimens L1 are plotted in Figure 4-15. The corresponding backbone curves of the hysteresis loops are plotted in Figure 4-16. The ductility ratio μ of the cast steel shear link specimens was determined from the backbone curves, which was calculated as the ratio of the link rotation γ_u to the link rotation γ_y . The positions of γ_u and γ_y are indicated in the backbone curves shown in Figure 4-16. In the FEM backbone curve, γ_u is determined as the link rotation angle corresponding to the observed significant buckling, which corresponds to the point when substantial strength degradation occurred in the backbone curve. The term γ_y is the yield link rotation angle, which is equal to the link rotation angle of the equivalent elasto-plastic backbone curve

with the same elastic stiffness and ultimate load as the real backbone curve, i.e., $\gamma_y = V_u / K_0$ (Park 1989). Detailed values of the ductility ratio μ for the cast steel shear links are listed in Table 4-13.

The mechanical properties of the cast steel specimen including the elastic stiffness K_0 (unit: kN/mm), yield Strength V_p , and ultimate shear strength V_u were also determined from the backbone curves of the cast steel shear links shown in Figure 4-16. Over-strength factor Ω was thereby defined as the ratio of V_u to V_p . Detailed values of V_p , V_u , and Ω determined from the FEM simulation results and the experiment results are listed in Table 4-13.

4.3.3. Fracture Observation

For the cast steel shear link specimen L1 during the cyclic loading experiment, crack was first observed in the flange during the loading cycle at the amplitude of the link rotation angle γ equal to 0.09 radians. During the loading cycle at the amplitude of the link rotation angle γ equal to 0.13 radians, another crack was observed at the intersection between the web portion near flange and stiffener. The cracks propagated into the web area with the increasing of the link rotation amplitude. During the loading cycle with the link rotation angle γ equal to 0.15 radians, multiple cracks are connected and load capacity started to drop (Zhang 2015). The observed crack propagation process at the link rotation angle γ of 0.09 radians, 0.13 radians, and 0.15 radians are plotted in Figure 4-17. The ultimate load capacity for specimen L1 was 1,010 kN from the experimental data.

For the cast steel shear link specimen L2 under cyclic loading, crack was first observed in the flange during the loading cycle of the link rotation angle γ equal to 0.07 radians. During the load cycle at the amplitude of the link rotation angle γ equal to 0.13 radians, another crack was observed at the intersection between the central web portion and the web stiffener. In the loading cycle up to the link rotation angle γ equal to 0.17 radians, the central web portion was completely fractured (Zhang 2015). The observed fracture propagation at the link rotation angle γ of 0.17 radians is plotted in Figure 4-18. The ultimate load carrying capacity for specimen L2 was 1,013.4 kN from the experimental data.

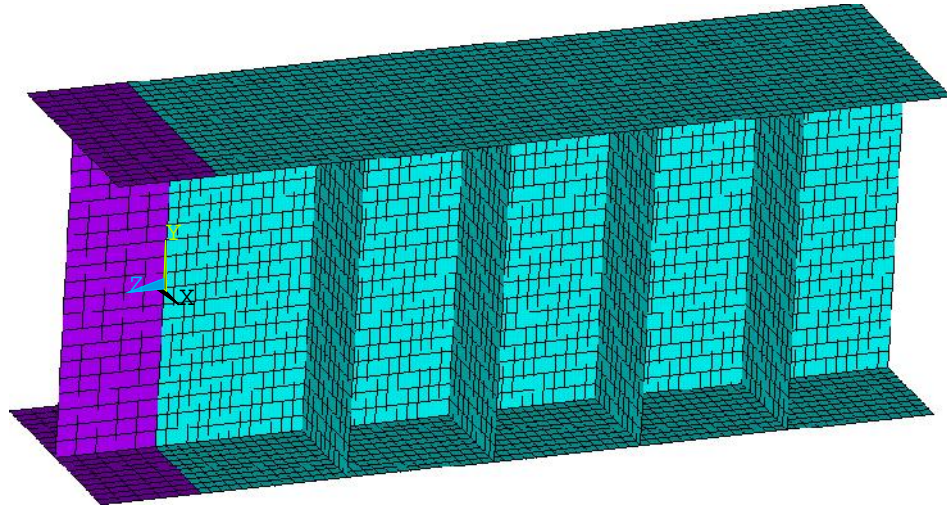
4.4. Relation to Next Chapter

The cyclic loading behavior of the ASTM A992 steel shear links, AISI 316L stainless steel shear links, and G20Mn5QT cast steel shear links are studied. The AISI 316L stainless steel shear links generally have much higher yield strength values due to its high strength. From numerical simulation results, the ultimate load state of the A992 shear links and the cast steel shear links is controlled by web fracture under cyclic loading, while the AISI 316L stainless steel shear links is found to be dominated by flange or web local buckling in its ultimate state. For AISI 316L stainless steel shear links, severe flange or web local buckling occurred without any sign of ductile fracture initiation. To have more flexibility in adjusting the strength and stiffness of shear link, web perforation will be considered for the shear link. Usually stress concentrations would be introduced near web perforations of shear links, which would reduce the ductility of the shear links

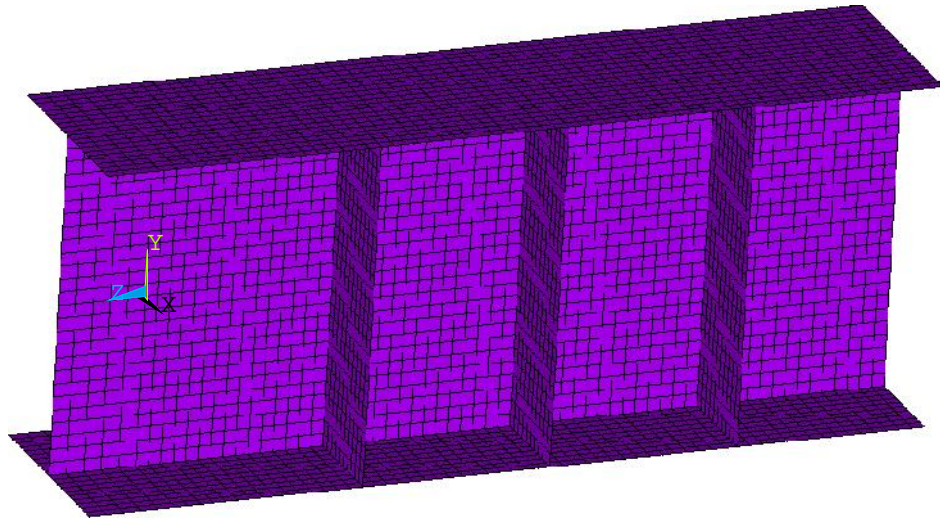
and result in the shear links more susceptible to ductile fracture under cyclic loading.

Considering that AISI 316L stainless steel shear links are much less susceptible to ductile fracture under cyclic load, web perforation can provide a cost-effective method in tuning their mechanical properties without compromising the ductility to unacceptable level.

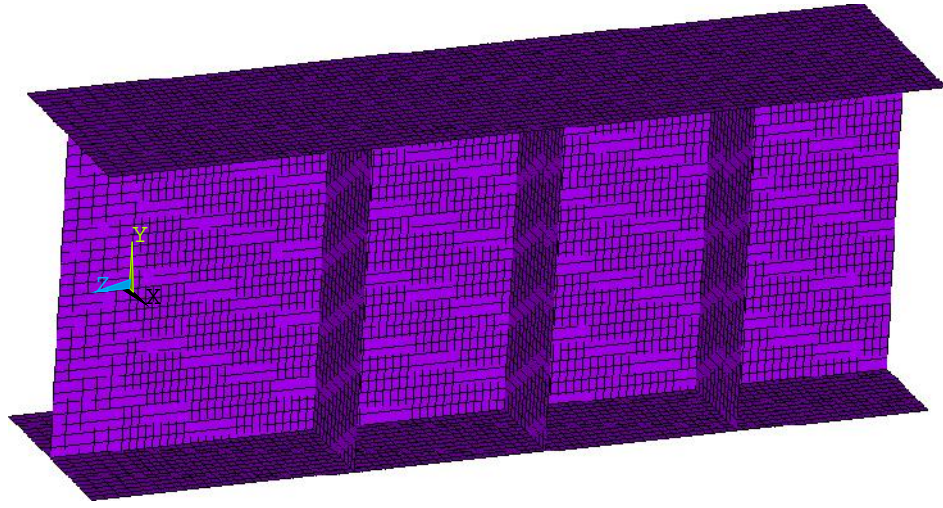
The results and discussion of the AISI 316L stainless steel with different web perforation patterns are presented in Chapter 5.



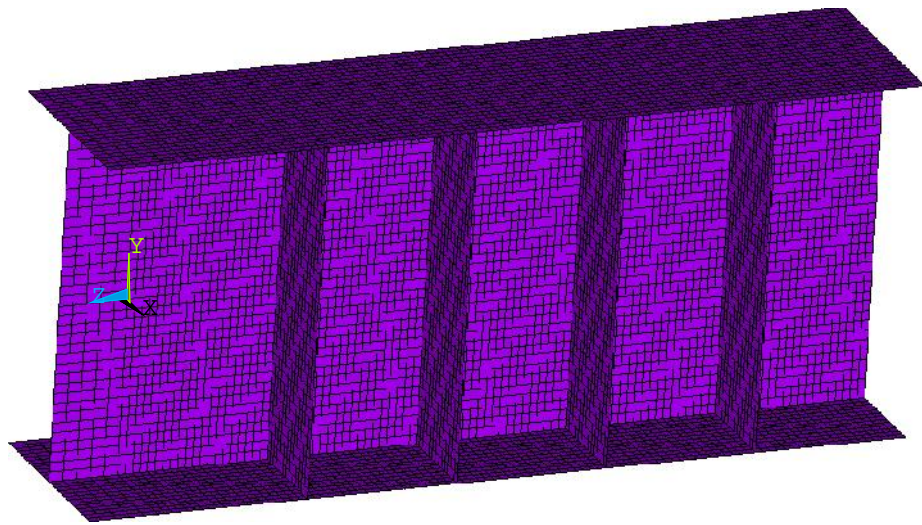
(a) Meshed finite element model for W10x33



(b) Meshed finite element model for W12x50



(c) Meshed finite element model for W14x74



(d) Meshed finite element model for W16x77

Figure 4-1 Meshed finite element models for conventional shear links

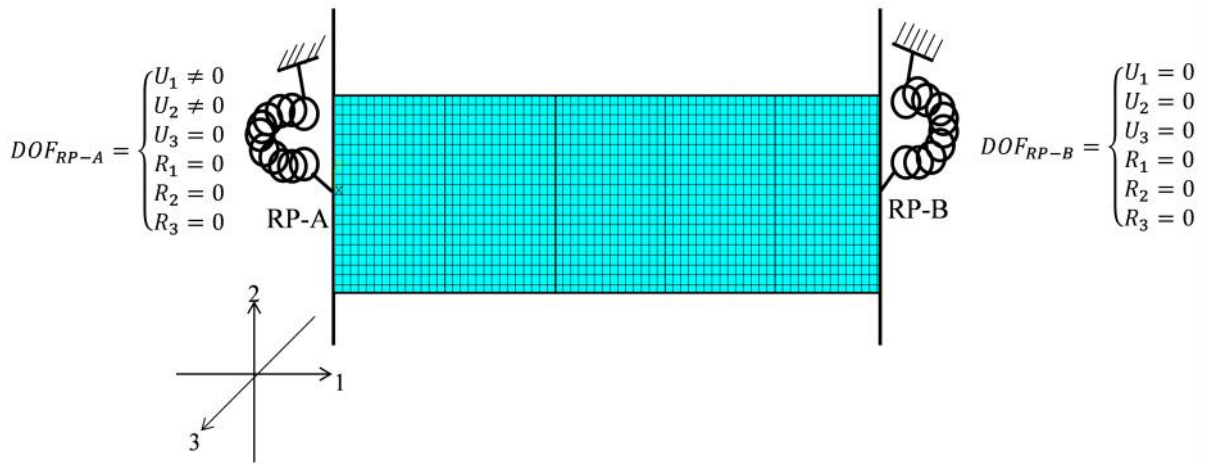


Figure 4-2 Boundary constraints for the finite element model

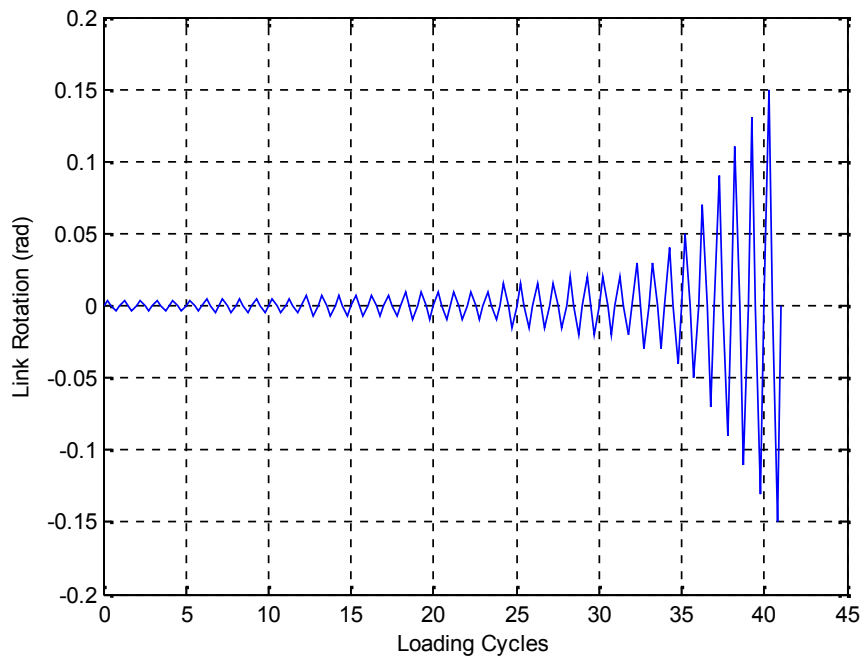
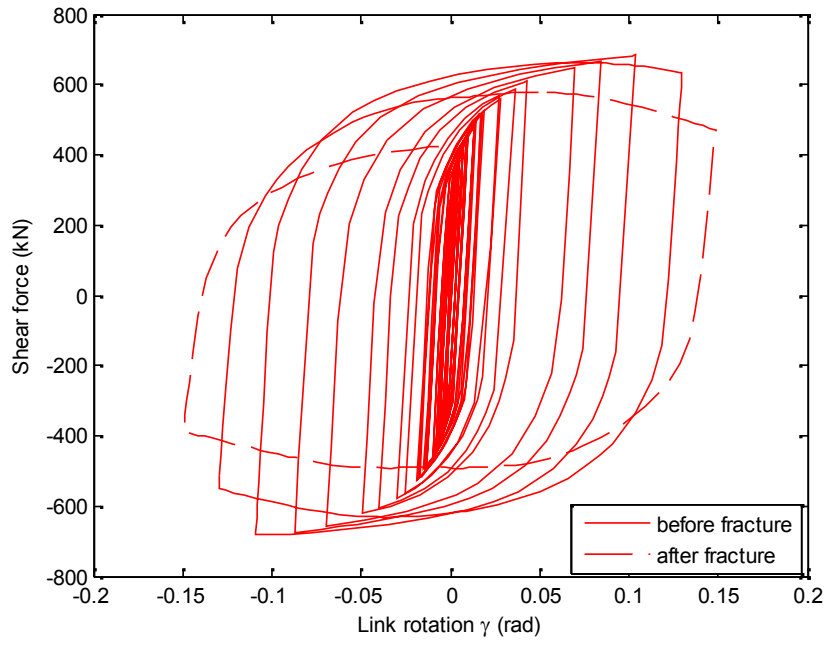
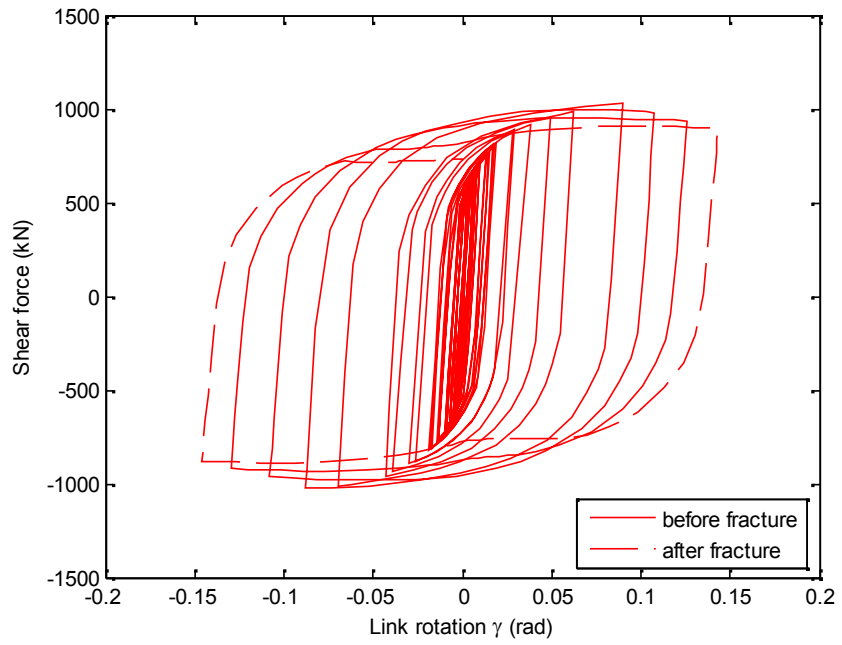


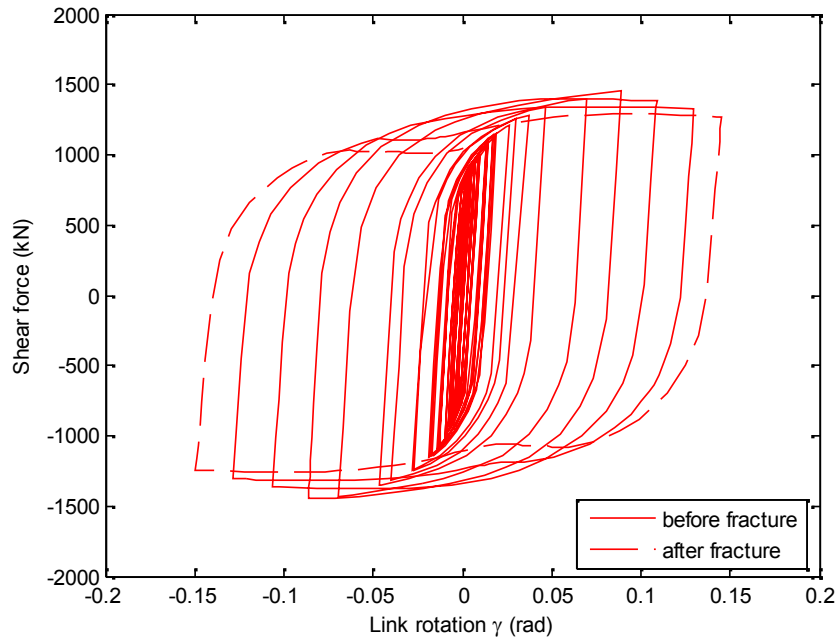
Figure 4-3 AISC loading protocol for the shear links



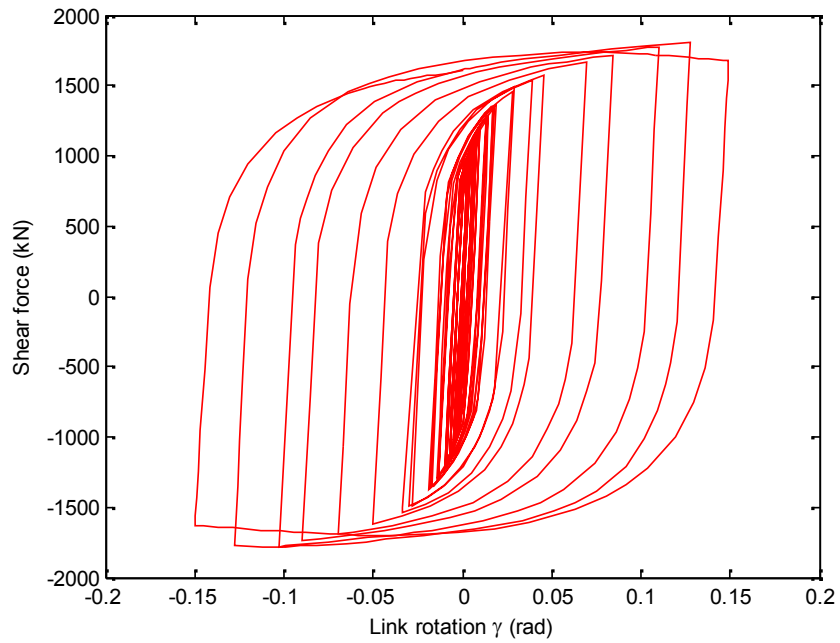
(a) Hysteresis loop for A992 W10x33



(b) Hysteresis loop for A992 W12x50

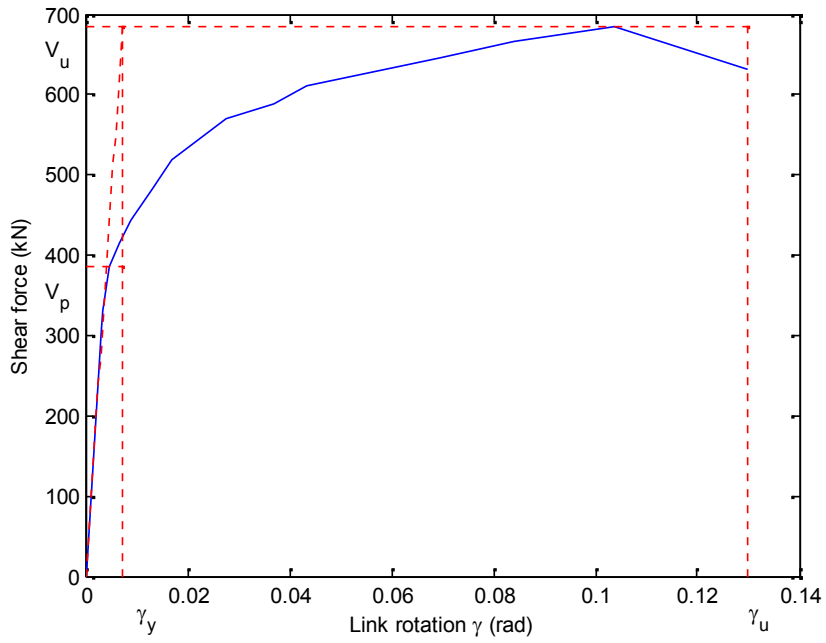


(c) Hysteresis loop for A992 W14x74

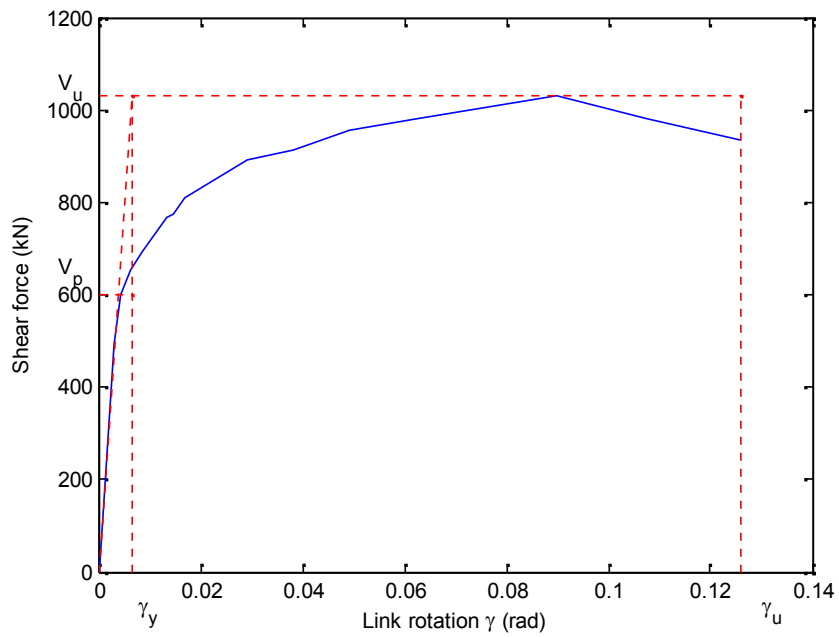


(d) Hysteresis loop for A992 W16x77

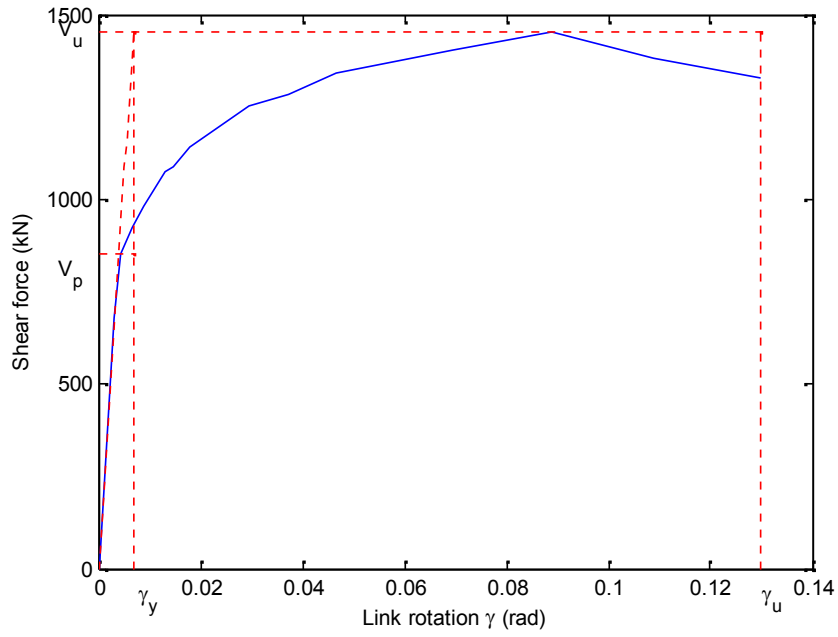
Figure 4-4 Hysteresis loops for the A992 conventional shear links



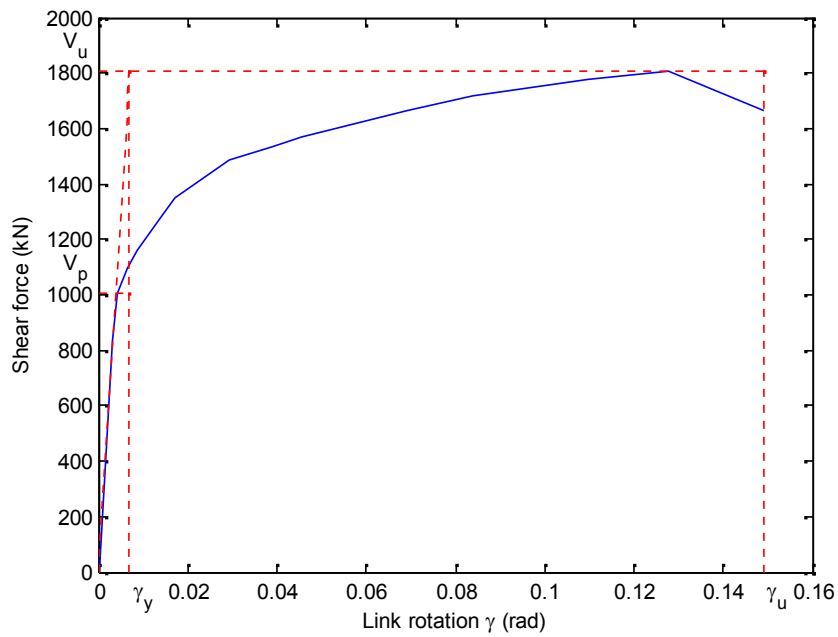
(a) Backbone curve for A992 W10x33



(b) Backbone curve for A992 W12x50

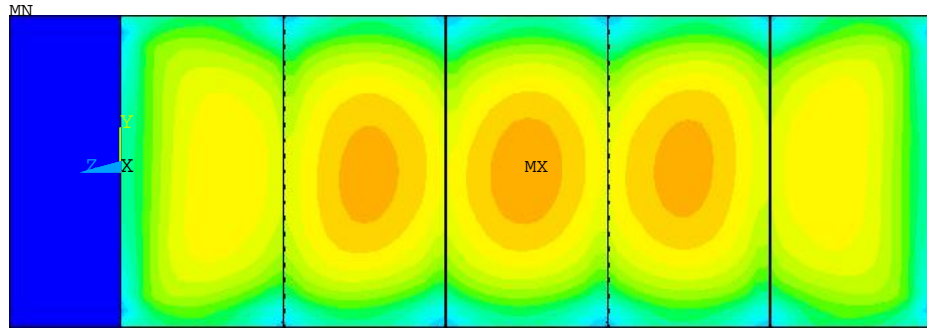


(c) Backbone curve for A992 W14x74

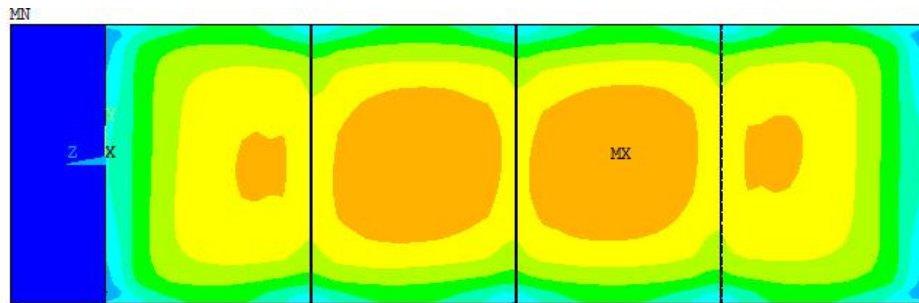


(d) Backbone curve for A992 W16x77

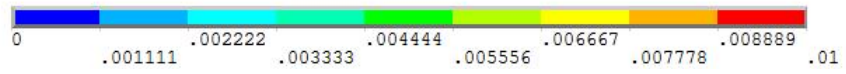
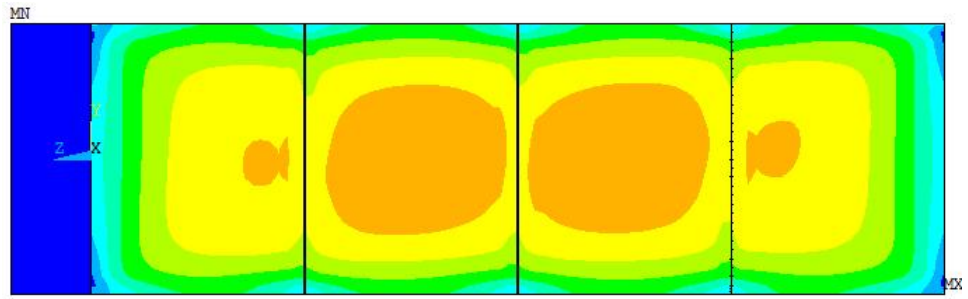
Figure 4-5 Backbone curves for A992 conventional shear links



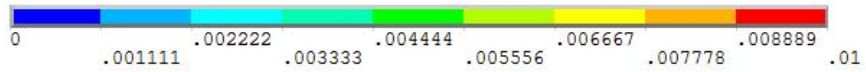
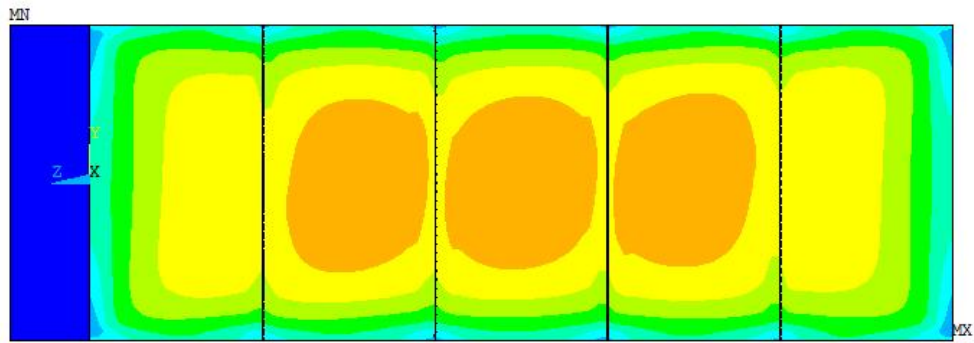
(a) Von Mises plastic strain contour for A992 W10x33



(b) Von Mises plastic strain contour for A992 W12x50

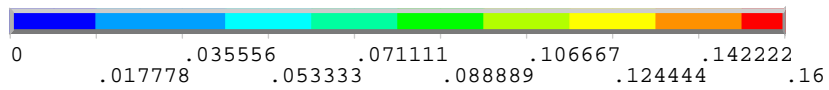
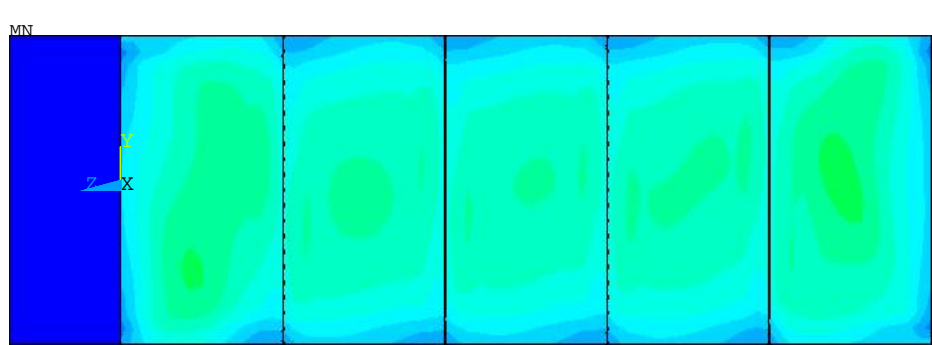


(c) Von Mises plastic strain contour for A992 W14x74

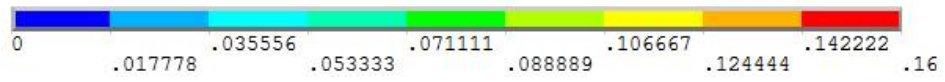
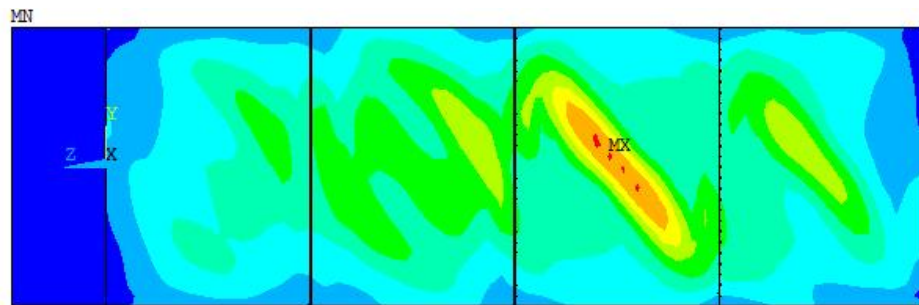


(d) Von Mises plastic strain contour for A992 W16x77

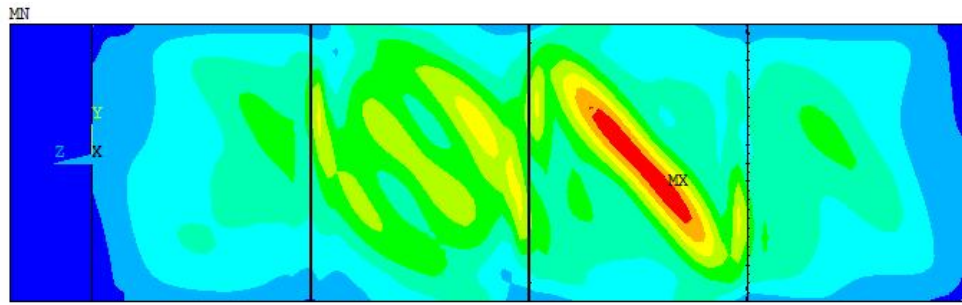
Figure 4-6 Von Mises plastic strain contours for A992 conventional shear links at $\theta = 0.02$ radians



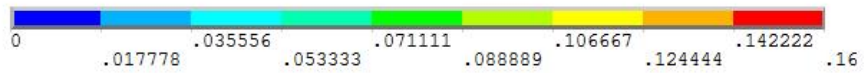
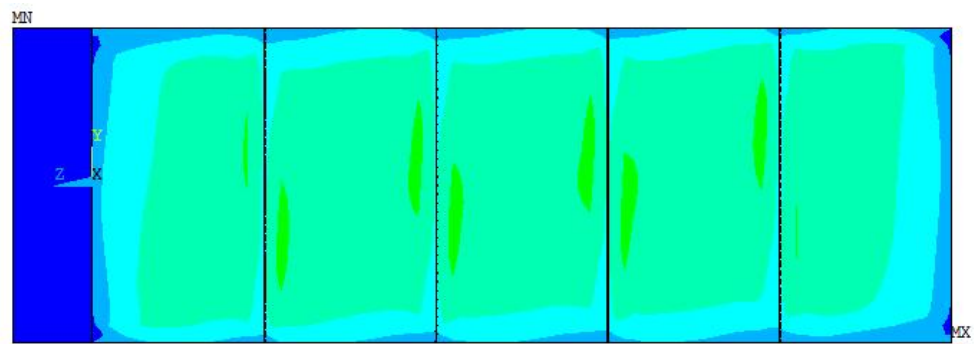
(a) Von Mises plastic strain contour for A992 W10x33



(b) Von Mises plastic strain contour for A992 W12x50

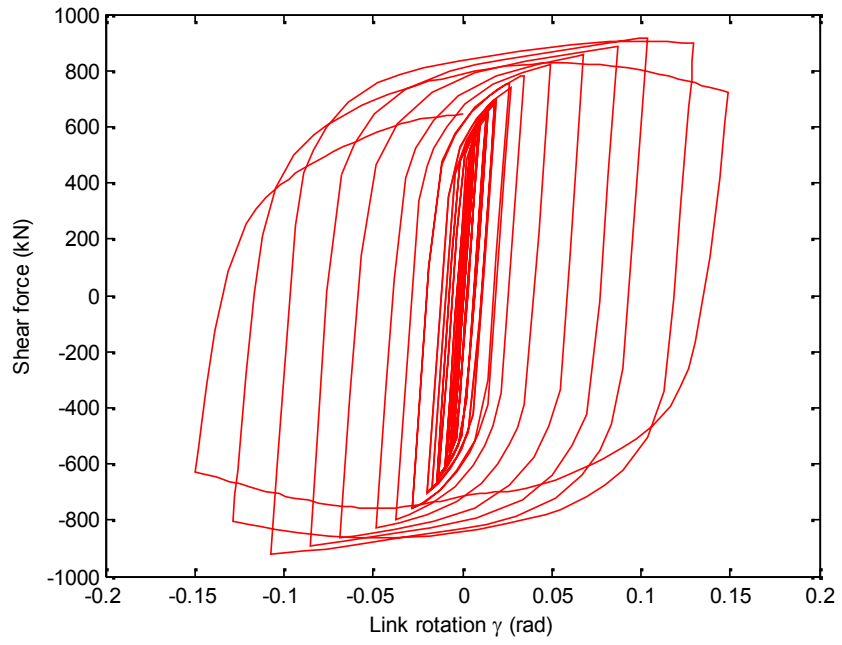


(c) Von Mises plastic strain contour for A992 W14x74

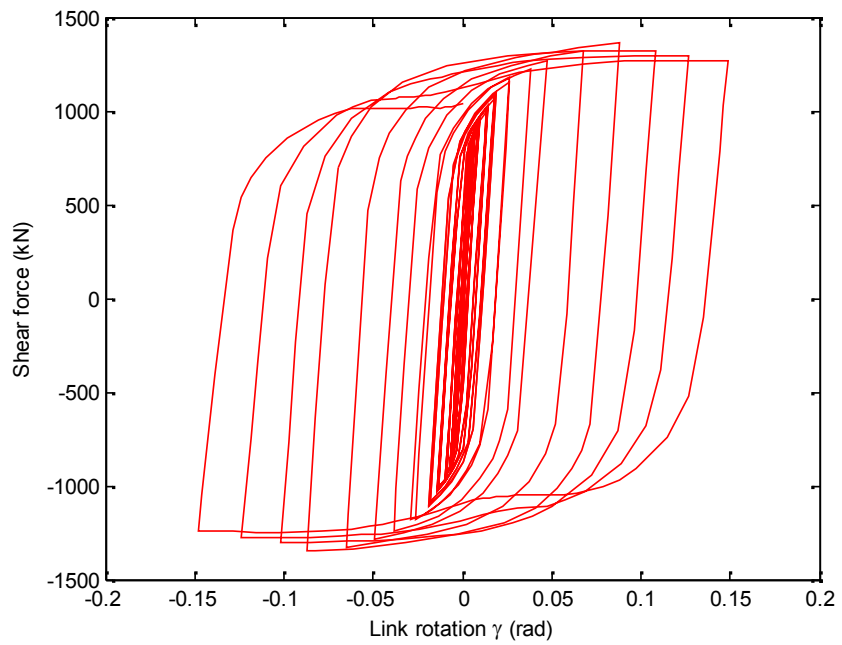


(d) Von Mises plastic strain contour for A992 W16x77

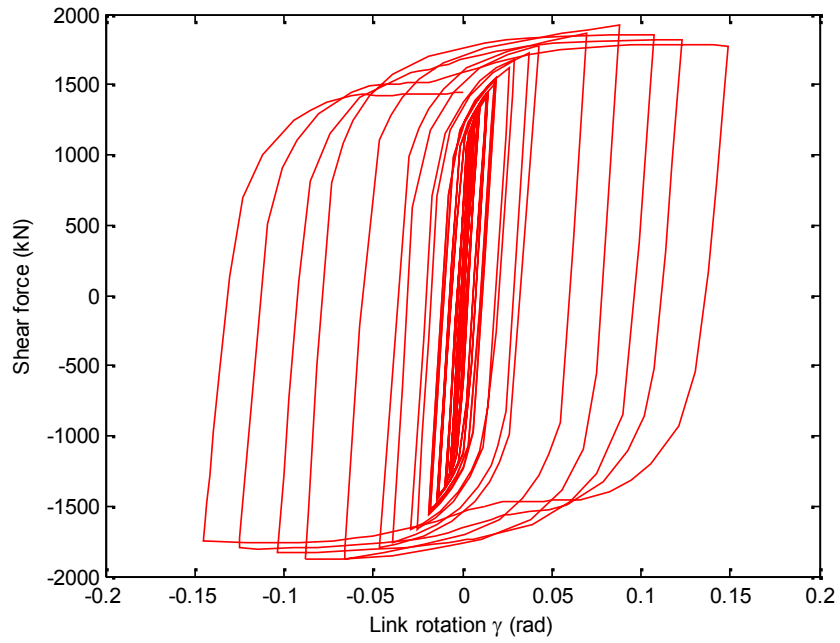
Figure 4-7 Von Mises plastic strain contours for A992 conventional shear links at $\theta = 0.11$ radians



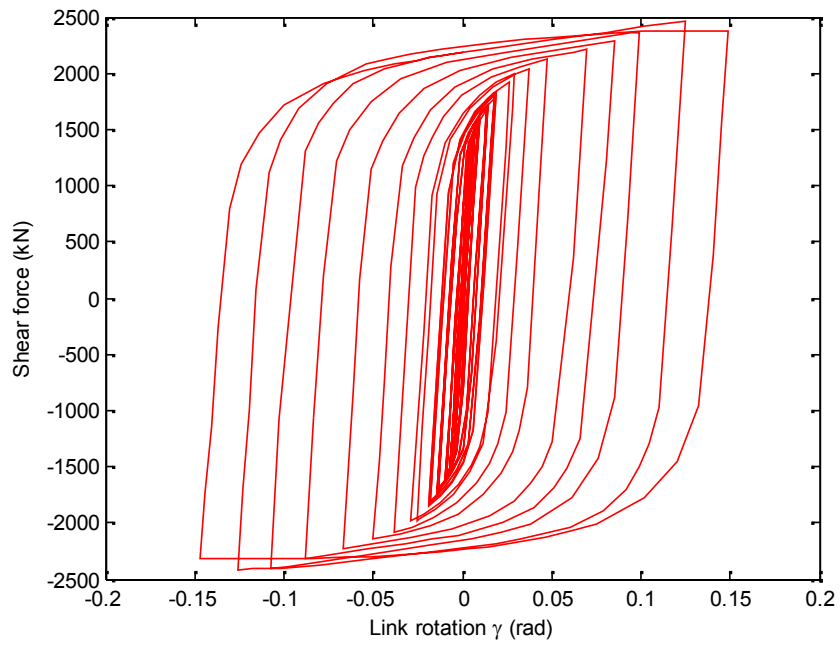
(a) Hysteresis loop for AISI316L W10x33



(b) Hysteresis loop for AISI316L W12x50

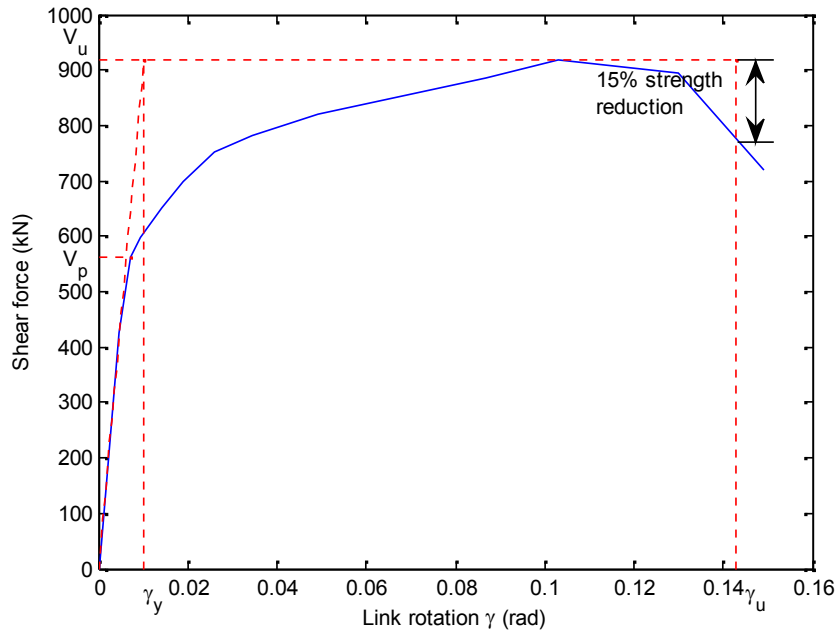


(c) Hysteresis loop for AISI316L W14x74

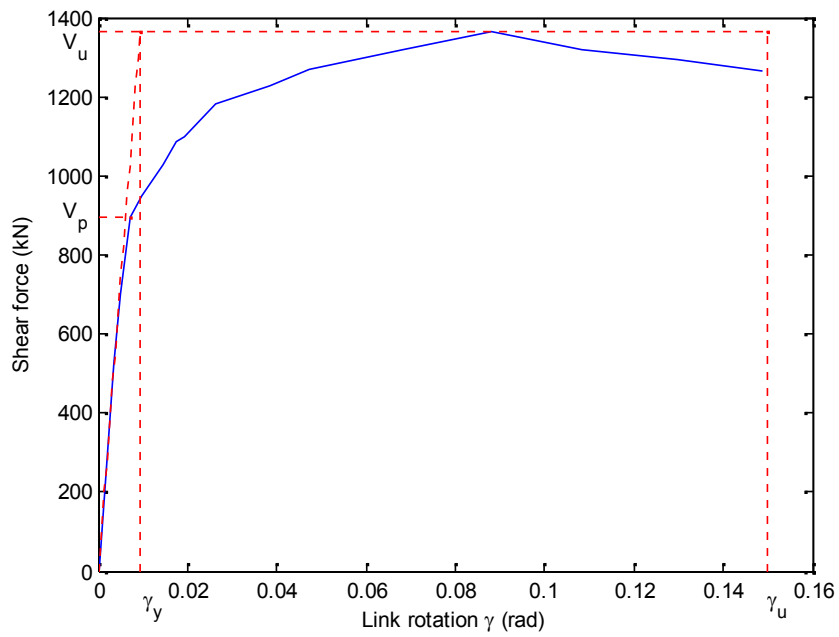


(d) Hysteresis loop for AISI316L W16x77

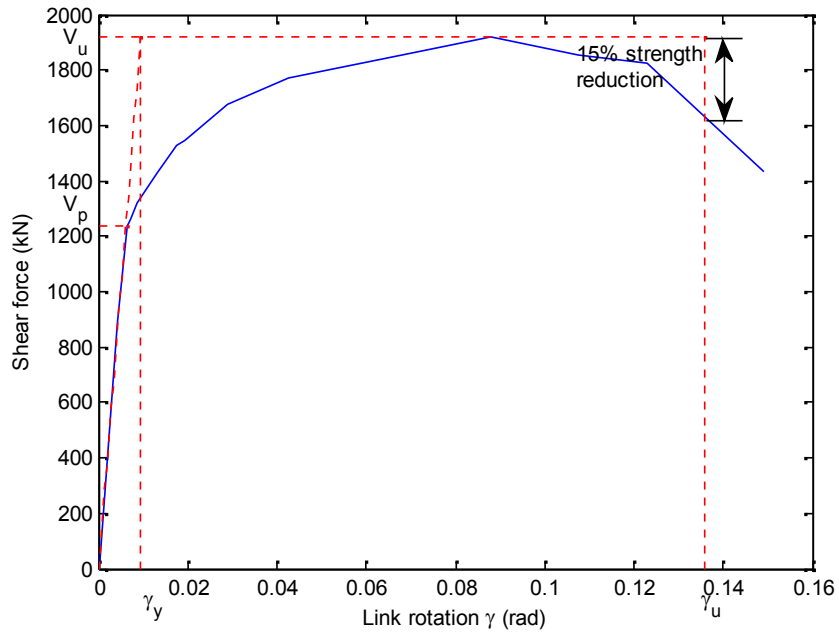
Figure 4-8 Hysteresis loops for AISI 316L stainless steel conventional shear links



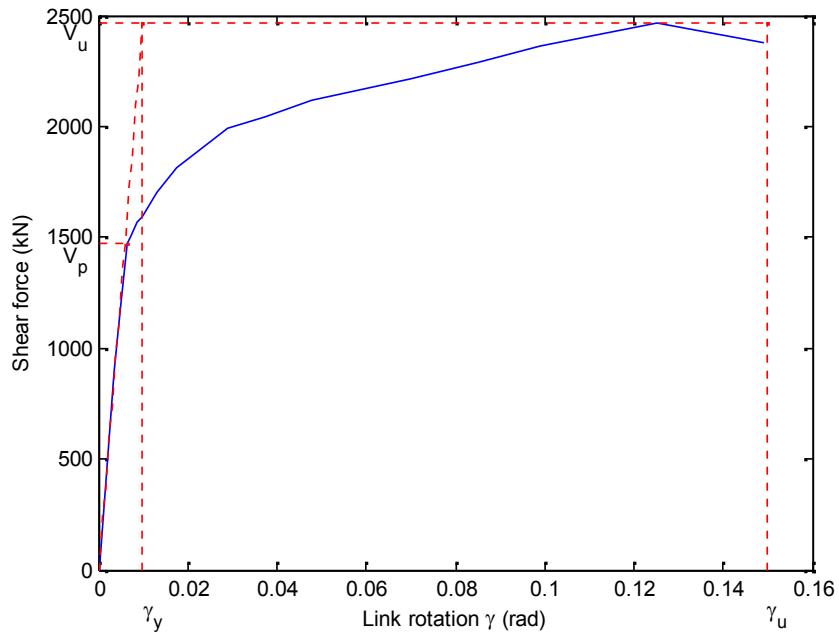
(a) Backbone curve for AISI 316L W10x33



(b) Backbone curve for AISI 316L W12x50

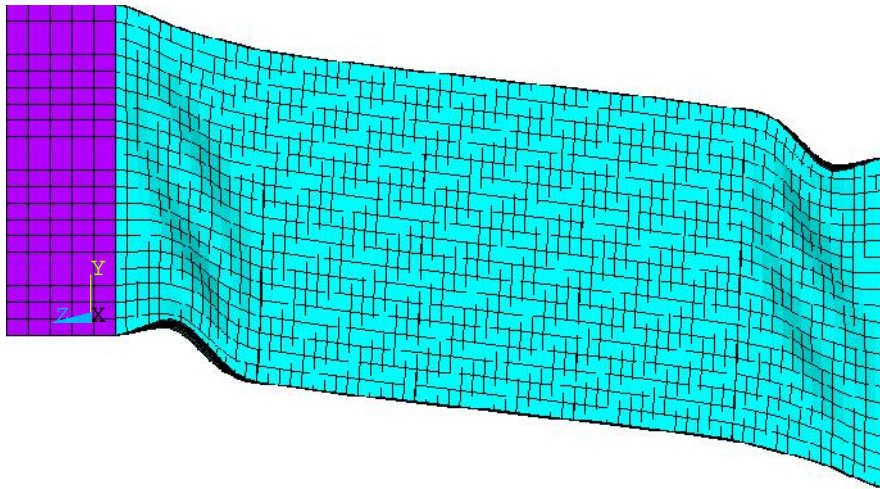


(c) Backbone curve for AISI 316L W14x74

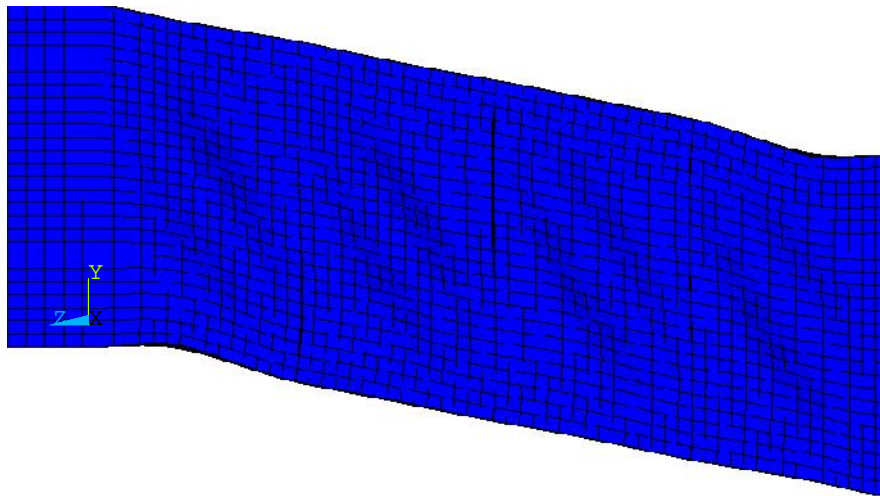


(d) Backbone curve for AISI 316L W16x77

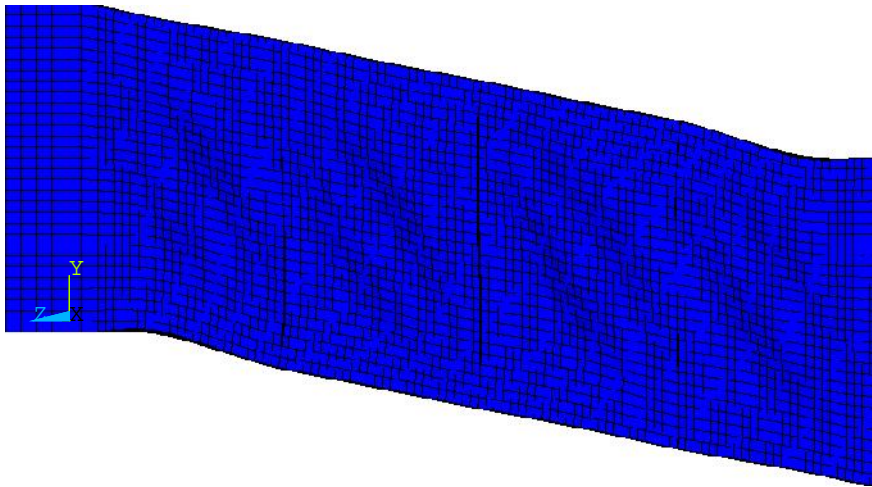
Figure 4-9 Backbone curves for AISI 316L stainless steel shear links



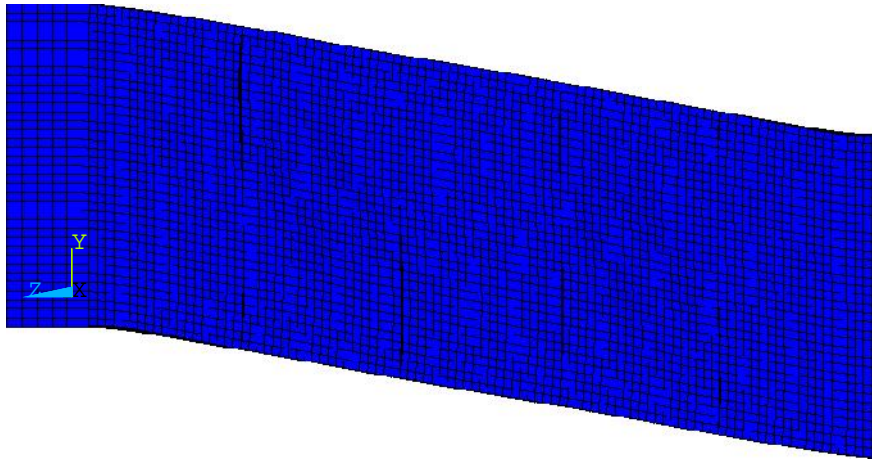
(a) Displacement in y direction for AISI 316L W10x33 at $\theta = -0.15$ radians



(b) Displacement in x direction for AISI 316L W12x50 at $\theta = -0.15$ radians

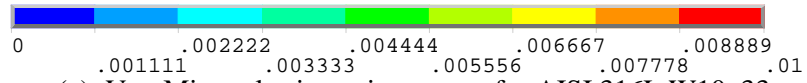
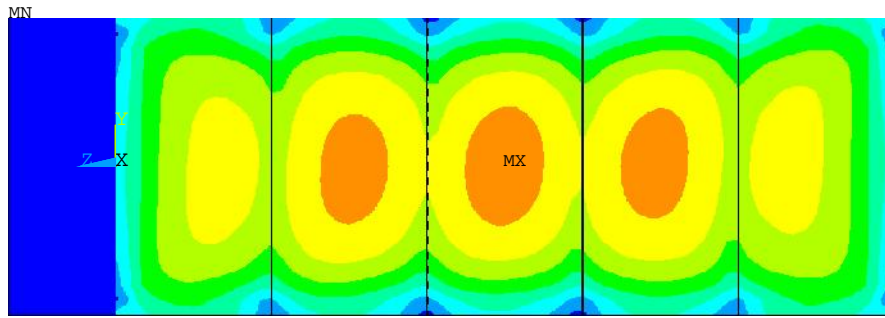


(c) Displacement in x direction for AISI 316L W14x74 at $\theta = 0.15$ radians

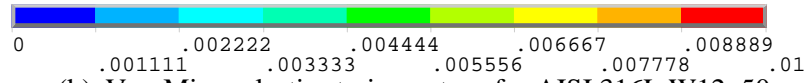
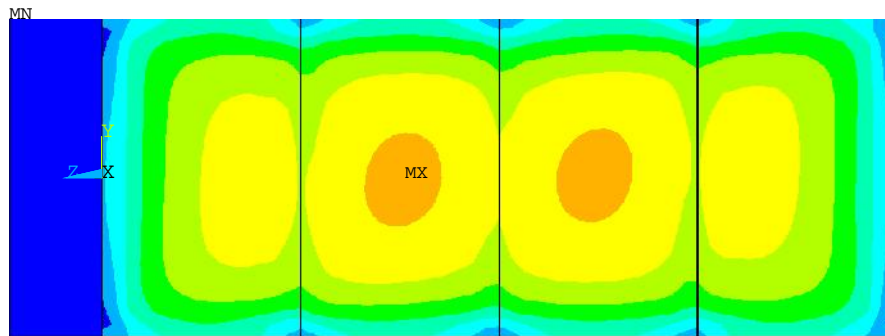


(d) Displacement in x direction for AISI 316L W16x77 at $\theta = 0.15$ radians

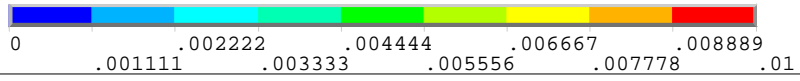
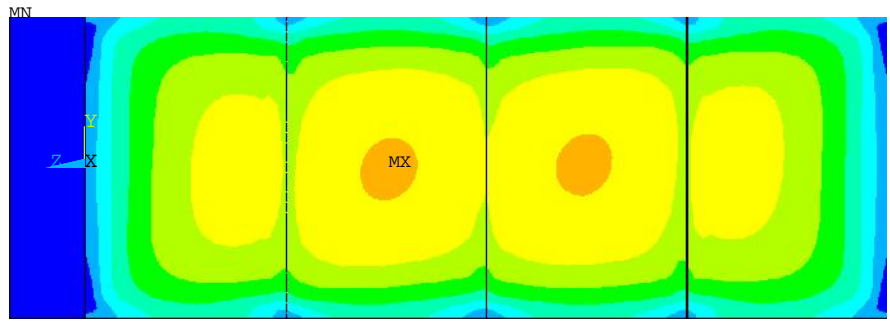
Figure 4-10 Buckled shapes for AISI 316L stainless steel shear links at $\theta = 0.15$ radians



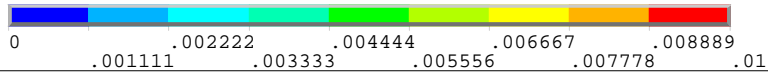
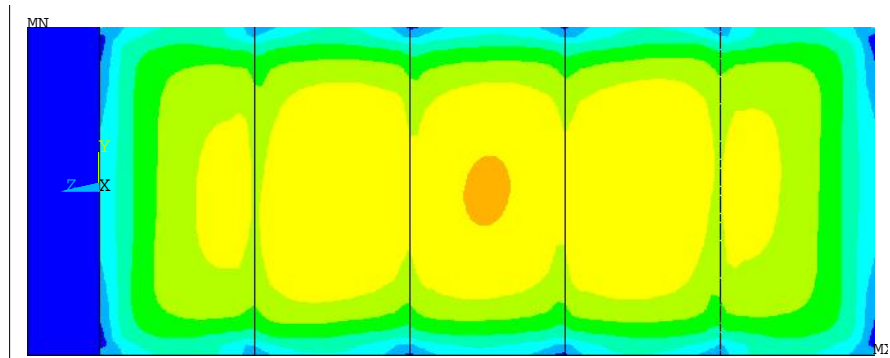
(a) Von Mises plastic strain contour for AISI 316L W10x33



(b) Von Mises plastic strain contour for AISI 316L W12x50

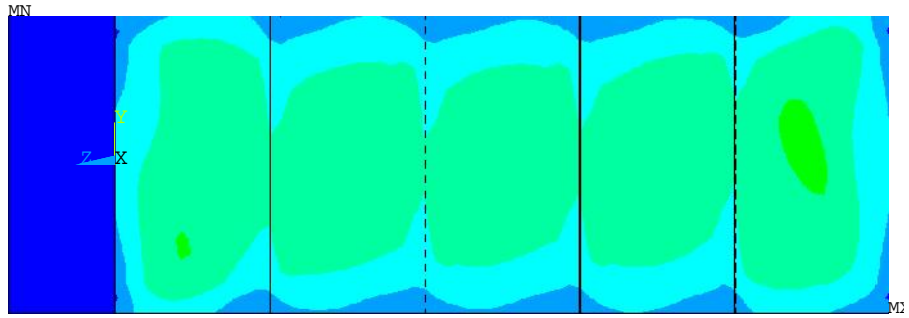


(c) Von Mises plastic strain contour for AISI 316L W14x74

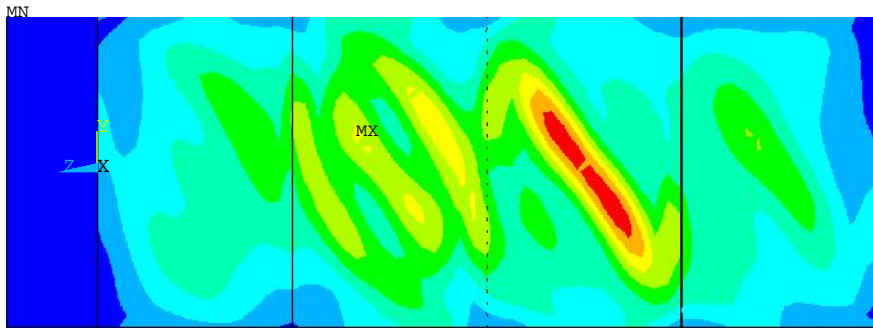


(d) Von Mises plastic strain contour for AISI 316L W16x77

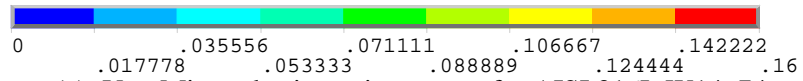
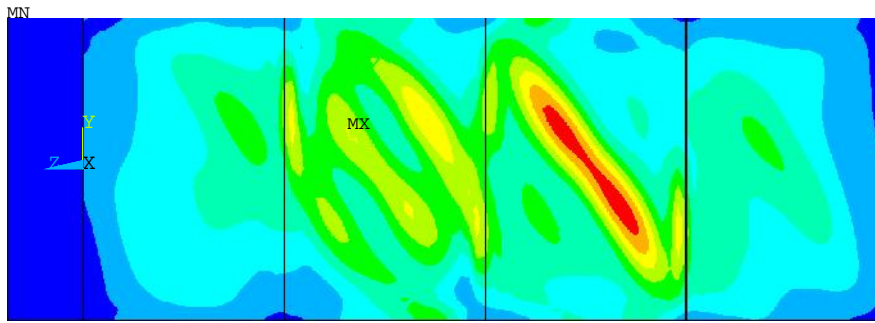
Figure 4-11 Von Mises plastic strain contours for stainless steel shear links at $\theta = 0.02$ radians



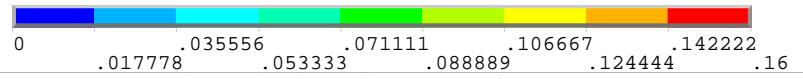
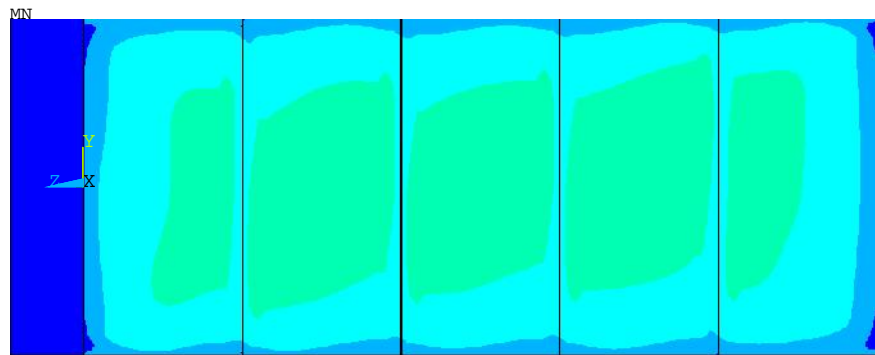
(a) Von Mises plastic strain contour for AISI 316L W10x33



(b) Von Mises plastic strain contour for AISI 316L W12x50



(c) Von Mises plastic strain contour for AISI 316L W14x74



(d) Von Mises plastic strain contour for AISI 316L W16x77

Figure 4-12 Von Mises plastic strain contours for stainless steel shear links at $\theta = 0.11$ radians

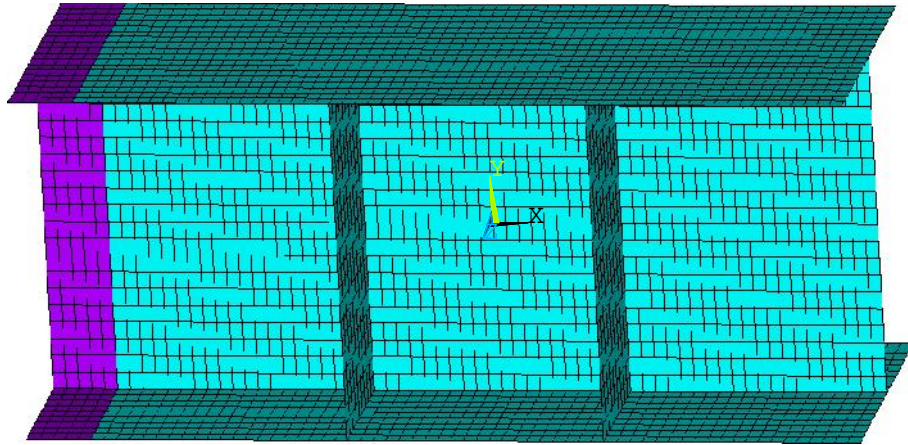


Figure 4-13 Meshed finite element model for the cast steel specimen



Figure 4-14 Experiment setup for the cast steel shear link specimens (Zhang, 2015)

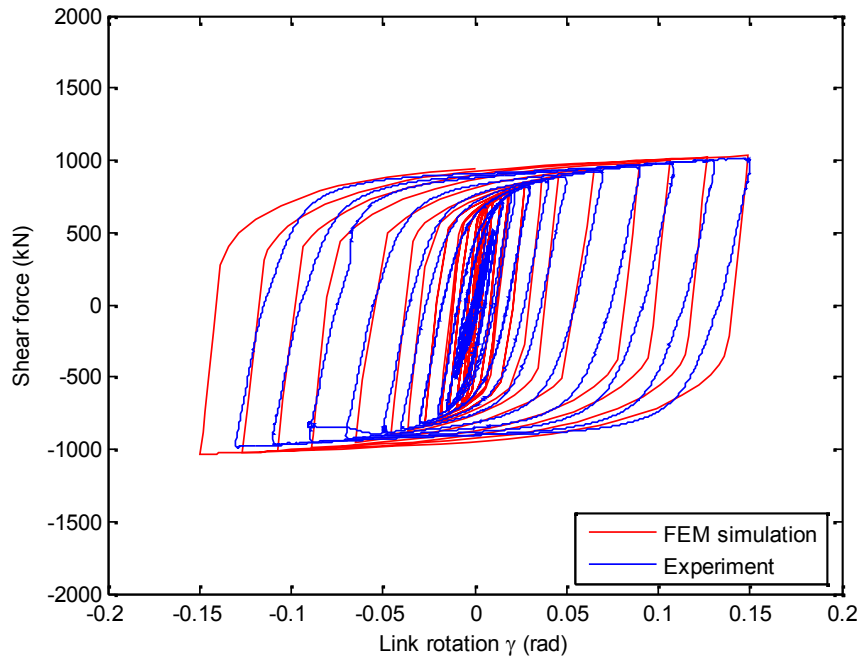


Figure 4-15 Hysteresis loops of cast steel specimen

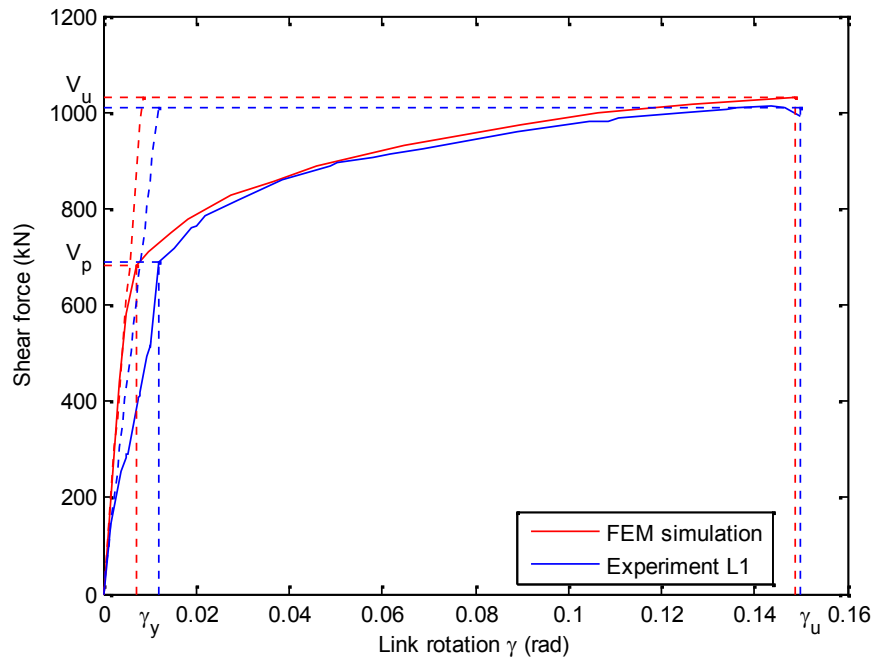


Figure 4-16 Backbone curves of cast steel specimen



(a) Crack initiated within flange at $\theta = 0.09$ radians



(b) Crack initiated within web at $\theta = 0.13$ radians



(c) Web fracture at $\theta = 0.15$ radians

Figure 4-17 Fracture propagation of the cast steel specimen L1 (Zhang, 2015)



Figure 4-18 Observed crack for specimen L2 at $\theta = 0.17$ radians (Zhang, 2015)

Table 4-1 Section details of the four shear links

Section	b_f , mm	t_f , mm	t_w , mm	d, mm	L , mm	t_s , mm	Web Stiffeners
W10x33	202.2	11.0	7.4	247.0	733.2	10.0	4@147 mm
W12x50	205.2	16.3	9.4	309.9	863.3	10.0	3@216 mm
W14x74	256.5	19.9	11.4	360.7	1070.6	11.4	3@268 mm
W16x77	261.6	19.3	11.6	419.1	1090.3	11.6	4@218 mm

Table 4-2 Calibrated plastic strain hardening constants for A992 steel

C_1 (MPa)	γ_1	C_2 (MPa)	γ_2	C_3 (MPa)	γ_3	C_4 (MPa)	γ_4	k (MPa)	E_t (MPa)
7993	175	6773	116	2854	34	1450	29	380	20

Table 4-3 Ductility properties of the A992 shear links

Section	γ_v (rad)	γ_u (rad)	μ
W10x33	0.00729	0.130	17.8
W12x50	0.00676	0.126	18.6
W14x74	0.00688	0.130	18.9
W16x77	0.00698	0.149	21.4

Table 4-4 Elastic stiffness K_0 (kN/mm) comparisons for A992 shear links

	W10x33	W12x50	W14x74	W16x77
FEM Simulation	128.0	176.8	197.2	237.3
Analytical	127.7	173.4	193.1	232.5

Table 4-5 Strength properties of A992 shear links from FEM simulations

	V_p (kN)	V_u (kN)	Ω
W10x33	385.8	683.8	1.77
W12x50	599.2	1032.0	1.72
W14x74	851.0	1452.0	1.71
W16x77	1004.0	1807.0	1.80

Table 4-6 Shear yield strength V_p (kN) Comparisons for A992 shear links

	W10x33	W12x50	W14x74	W16x77
FEM Simulation	385.8	599.2	851.0	1004.0
Analytical	379.6	594.3	834.1	1006.3

Table 4-7 Calibrated plastic strain hardening constants for AISI 316L stainless steel

C_1	γ_1	C_2	γ_2	C_3	γ_3	k	R_0	R_∞	b
15064	100.74	576.68	0.0158	400	0	556.94	0	300.01	0.40

Table 4-8 Ductility properties of the stainless steel shear links from FEM simulations

Section	γ_v (rad)	γ_u (rad)	μ
W10x33	0.01021	0.143	14.0
W12x50	0.00935	0.150	16.0
W14x74	0.00950	0.136	14.3
W16x77	0.00992	0.150	15.1

Table 4-9 Elastic stiffness K_0 (kN/mm) comparisons for stainless steel shear links

	W10x33	W12x50	W14x74	W16x77
FEM Simulation	122.5	169.2	188.7	227.8
Analytical	122.2	165.9	184.8	222.5

Table 4-10 Strength properties of stainless steel shear links

Section	FEM Simulation			Analytical
	V_p (kN)	V_u (kN)	Ω	V_p (kN)
W10x33	562.1	917	1.63	556.4
W12x50	894.9	1366	1.53	871.0
W14x74	1237.0	1920	1.55	1222.5
W16x77	1474.0	2464	1.67	1474.9

Table 4-11 Section details of the cast steel shear links (Zhang, 2015)

Specimen	b_f , mm	t_f , mm	t_w , mm	h , mm	L , mm	t_s , mm	Web Stiffeners
L1	180	15	12	215	600	14	2@200 mm
L2	180	15	12	215	600	14	2@200 mm

Table 4-12 Calibrated plastic strain hardening constants for cast steel

C_1 (MPa)	γ_1	k (MPa)	R_0	R_∞	b
5872.7	31.51	483	0	21	1.2

Table 4-13 Mechanical properties of cast steel specimen (Experiment by Zhang 2015)

	K_0 (kN/mm)	V_p (kN)	V_u (kN)	Ω	γ_y (rad)	γ_u (rad)	μ
Experiment	141.6	687.6	1009	1.47	0.0119	0.150	12.6
FEM simulation	201.7	681.3	1032	1.51	0.0085	0.149	17.5

Chapter 5 : Link Beams with Web Perforations

The link beams are usually designed to serve as fuse devices in eccentrically braced frames (EBF). In EBF structure systems, short links ($e < 1.6M_p/V_p$, referred to as “shear link” or short link) are generally preferred, since they are more ductile than the long links ($e > 2.4M_p/V_p$, referred to as “flexural link” or long link) with the same section sizes.

Shown in Chapter 4, AISI 316L stainless steel shear links are very ductile in deformation and have stable hysteretic energy dissipation capacity compared to A992 steel shear links, yet high their strength may cause unintended problems and thus requires tuning by perforation in web sections. Particularly for fuse devices, link beams made of hot-rolled sections are commonly used for lower cost and avoiding potential welding defects. Yet only limited types of hot-rolled section sizes are available, especially for AISI 316L stainless steel sections. One alternative solution to tune the properties of the link beams is to make perforations over the link beams’ web area in order to achieve the desired mechanical properties.

In this chapter, two types of perforated link beams with reduced web sections are investigated: shear links with perforated circular holes on the web sections and the link beams with perforated slits. Web perforations are created for the link beams made of AISI 316L stainless steel and cast steel. FEM simulations are conducted on the perforated AISI 316L stainless steel shear yielding links; and both FEM simulations and experiments are conducted on the perforated cast steel link beams. The cyclic void growth model (CVGM) is applied to determine the ductile fracture initiations in the finite element models of the investigated link beams with web perforations, which are viewed

as the ultimate states of the finite element models. The mechanical behaviors of the perforated link beams are evaluated in terms of the following parameters, including the elastic stiffness, nominal shear strength, ultimate shear strength, ductility, and energy dissipation capacity. Analytical formulas (some are empirical formulas based on FEM results) are also derived to predict the strength and stiffness properties of the perforated link beams, which can be used for engineering design of the perforated link beams.

5.1. Stainless Steel Link Beams with Perforated Circular Holes

5.1.1. Finite Element Modeling

The perforated AISI 316L stainless steel link beams are classified into the following five groups: (1) Group I contains four link beams (W10x33 section, W12x50 section, W14x74 section, and W16x77 section) with a constant perforated circular hole diameter of 25.4 mm. All web nodes are fully restrained against lateral movements in the model. (2) Group II contains the same four sections of the links in Group I, but web stiffeners are added. (3) Group III contains six links with W10x33 section. The perforation pattern was varied in each link case. (4) Group IV is included as a comparison case for Group II to study the web stiffener spacing effect. Group IV contains four links with the same section sizes and hole diameter as those of the links in Group II, but web stiffeners with wider spacing were provided and the link length was adjusted accordingly. (5) Group V serves as a comparison case for Group III to study web stiffener spacing effect. Group V contains six links with the W10x33 section, but the web stiffener spacing was increased

and the link length was adjusted accordingly. Section details of the perforated link beams in each group are listed in Table 5-1, and their geometry can also be found in Figure 5-1.

Shell element 181 was used for finite element modeling of the perforated link beams in ANSYS Academic version 15.0. Large displacement analysis option was selected in the nonlinear finite element analysis. Mesh refinement studies were conducted to determine the desired level of fine meshing to achieve reasonably accurate results. To illustrate the meshing actually used in current analysis, the meshed models of link beams from Group I-1, Group II-1, and Group III-1 are shown in Figure 5-2.

Boundary restraints equivalent to the constraints in the experiment were applied to the finite element models of the perforated link cases. One end of the model was completely restrained against all rotations and translation movements while the other end was restrained against all rotations. Cyclic loading protocol in terms of the link rotation angles suggested by AISC Seismic Provision (AISC 2010) was applied to the finite element model, which is shown in Figure 5-3. CVGM was adopted to determine the fracture initiation point which is used to decide when to terminate the finite element analysis as fracture is considered one of the ultimate limit states of the perforated links.

5.1.2. FEM Analysis: Results and Discussions

The following parameters were determined from the cyclic loading response of the perforated AISI 316L stainless steel links with web circular holes: elastic stiffness K_0 , nominal shear strength V_n , ductility ratio μ , over-strength factor Ω , and energy

dissipation capacity. The shear force vs. link chord rotation angle hysteresis loops of the perforated link beams in Group I and Group II under cyclic loading are plotted in Figure 5-4. The hysteresis loops of three link beams - Group III-1, III-2, and III-3 are plotted in Figure 5-5. The hysteresis loops of link beams from Group IV and Group V are plotted in Figure 5-6 and Figure 5-7 respectively. The plotted hysteresis loops were truncated after the marked fracture initiation point predicted by using the CVGM criteria. The backbone curves were determined from the hysteresis loops thereby, which are plotted in Figure 5-8 and Figure 5-9.

For the investigated perforated links with web circular holes, the elastic stiffness K_0 (unit: kN/rad) values were calculated from the linear portion of the back bone curves or monotonic loading response. Normalized elastic stiffness \bar{K}_0 is defined as the elastic stiffness ratio between a perforated link and corresponding link without perforation and is also presented in Table 5-2. It is observed that links in Group I and one link (Group V-3) from Group V have much lower \bar{K}_0 values than that of the other perforated link beams. It is speculated that the lateral restraint type and web area perforation ratio might be the reasons for causing this phenomenon. Full lateral restraints are provided for all nodes of the link models in Group I, while the perforated link beam Group V-3 has the largest web area perforation ratio value of 16.9% among all perforated link beams.

Nominal shear strength V_n and over-strength factors were determined from the FE analysis results for the perforated links. Citing the research work by Uang (1989) and Alavi and Nateghi (2013), the nominal shear strength V_n of a link represented the first

significant yield, and the ultimate strength V_u was defined as the maximum shear force in the backbone curve. Over-strength factor Ω was thereby defined as the ratio of V_u to V_n . Similarly, normalized nominal shear strength \bar{V}_n was also calculated, which is defined as the ratio between the nominal shear strength of a perforated link and the plastic shear strength of the corresponding link without perforation. Detailed values of V_n , \bar{V}_n , and Ω for the selected link beam cases are listed in Table 5-2. Similar to the observations on the normalized stiffness values of the links, the links in Group I and the link beam Group V-3 have much lower normalized nominal shear strength values than that of the rest link beams. The over-strength factor values are around 2.0 for the links in Group II and III whose web stiffeners are densely spaced; and they are around 1.7 for the links in Group IV and V with sparsely spaced web stiffeners. Hence the stiffener spacing is a factor that plays a role in the ultimate strength of the perforated links.

Ductility represents a link's ability to sustain large deformation without apparent strength deterioration. A link's ductility is quantitatively measured by its ductility ratio μ , which was computed as the ratio of the maximum link rotation angle γ_u to the elastic link rotation γ_y ($\gamma_y = V_u / K_\theta$) (Park 1989, Uang 1989, Alavi and Nateghi 2013). The positions of γ_u and γ_y are marked in Figure 5-8 and Figure 5-9 for the selected link beams from Groups I, II, and III. Detailed values of γ_y , γ_u , and μ for the selected link beams are listed in Table 5-3. It is seen that all the links can reach the link rotation of 0.08 radians without strength degradation, and some of them can even reach a link rotation angle as high as 0.15 radians.

The energy dissipation capacity is a crucial factor in evaluating the seismic performance of link beams. Hysteretic energy dissipated by a link beam during one load cycle is equal to the area enclosed by the hysteresis loop. Energy dissipated by a perforated link in each cycle is normalized by dividing it with the energy which would be dissipated by an ideal elasto-plastic model. The strength and stiffness of the ideal elasto-plastic hysteresis model are set to be equal to the plastic shear yield strength V_p and the elastic stiffness K_0 of the corresponding imperforated link of the same section and length (Rai and Wallace 1998). The normalized energy dissipation capacity (left y axis) in each loading cycle versus the load cycle (x axis) and the link rotation angle γ (right y axis) are plotted in Figure 5-10 for the perforated links. Data points of the energy dissipation versus load cycle are seen to be more scattered for Group I link beams. Generally perforated links from Group II and III have greater normalized energy dissipation capacities.

The Von Mises plastic strain contour plots are shown in Figure 5-11 for the selected link beams at the link rotation angle of 0.09. Generally peak plastic strains occur around the edge of the holes due to stress concentrations, and relatively moderate plastic strains are observed in between the holes. The Von Mises plastic strains are seen to occur over almost the entire web area of the perforated links. Hence such spread-out yielding in the web of the perforated AISI 316L stainless steel links is helpful to energy dissipation at large link rotation angles.

5.1.3. Factors Influencing Seismic Behaviors of Perforated Links with Circular Holes

Different relations are proposed by researchers to characterize the cyclic loading behaviors of perforated steel plate shear walls with circular holes on the webs. Vian et al. (2008) suggested that the elastic stiffness and the yield strength of a perforated steel plate shear wall were related to the ratio of hole diameter to hole center-to-center spacing (D/S_{diag}). Prinz and Richards (2009) suggested that the performance of a perforated link was related to the percentage of removed web area (ρ). Bhowmick et al. (2014) suggested that the yield strength of a perforated steel shear wall was related to the ratio of net length at the perforated section to the full length (L_n/L) in the loading direction. For the perforated link beams with web stiffeners in this study, as web stiffeners divide the link webs into several panels with each subpanel behaving like a small-size perforated plate shear wall panel, the behaviors of the perforated links in this study are believed to be analogous to the perforated plate shear walls. Therefore, the stiffness and strength of the perforated links are directly related to the perforation characteristics suggested by the above-cited researchers. The following factors are assessed for their effects on the elastic stiffness and yield strength of the perforated AISI 316L stainless steel links in this study, including the type of lateral supports, the ratio of hole diameter to hole center-to-center spacing (D/S_{diag}), the ratio of the net link length to full link length (L_n/L), the ratio of net link depth to full link depth (h_n/h), and web area perforation ratio (ρ).

5.1.3.1. Effect of D/S_{diag}

Data points of \bar{K}_0 versus D/S_{diag} and \bar{V}_n versus D/S_{diag} are plotted in Figure 5-12 for the selected links. Generally linear relationships are observed for \bar{K}_0 versus D/S_{diag} and \bar{V}_n versus D/S_{diag} for the links in Group III and the links in Group V (except for one link V-3). However, at a particular D/S_{diag} value, \bar{K}_0 and \bar{V}_n of the link beams from Group V are lower than those of Group III link beams. On the other hand, \bar{K}_0 and \bar{V}_n values are varying for the links with varying section sizes in Group I, II, and IV, even though D/S_{diag} ratio is the same. An outlier – link V-3 is observed away from the trend line. Link V-3 has the largest D/S_{diag} ratio among all the investigated link beams. This observation suggests that the relationship proposed by Vian et.al. (2008) is only applicable to the perforated links with the same section size and is accurate only if the perforated links' D/S_{diag} ratio falls within a certain range.

5.1.3.2. Effects of L_n/L

Data points of \bar{K}_0 versus L_n/L and \bar{V}_n versus L_n/L for the considered perforated link beams are plotted in Figure 5-13. Generally the data points are randomly scattered and no clear pattern can be identified from the plots on stiffness and strength values with respect to the L_n/L ratios.

5.1.3.3. Effects of h_n/h

Data points of \bar{K}_0 versus h_n/h and \bar{V}_n versus h_n/h are plotted in Figure 5-14. The \bar{K}_0 and \bar{V}_n data points are generally proportional to the h_n/h ratio for all the links with web stiffeners. However, the relationships of \bar{K}_0 versus h_n/h and \bar{V}_n versus h_n/h are more scattered around compared to the \bar{K}_0 versus D/S_{diag} and \bar{V}_n versus D/S_{diag} plots for the perforated links with web stiffeners. Hence the relationship proposed by Bhowmick et.al. (2014) is decided not accurate enough to describe the behaviors of perforated links.

5.1.3.4. Effects of ρ

Data points of \bar{K}_0 versus ρ and \bar{V}_n versus ρ are plotted in Figure 5-15 for the link beams. It is clear in Figure 5-15 that \bar{K}_0 and \bar{V}_n are basically linearly related to web area perforation ratio ρ for all the link beams with web stiffeners except for link V-3, yet the relationships of \bar{K}_0 versus ρ and \bar{V}_n versus ρ are more difficult to identify for the link beams in Group I. From Figure 5-15, it is concluded that the normalized elastic stiffness and normalized shear strength are linearly related to the web area perforation ratio ρ for all the perforated links with web stiffeners and with web area perforation ratio less than 16%.

5.1.4. Analytical Formulation of Mechanical Properties of Perforated Links with Circular Holes

Initial Stiffness

Shown in Figure 5-15, it is observed that the normalized elastic stiffness values of the perforated link beams with web circular holes are approximately linearly related to the web area perforation ratio. An empirical relation is calibrated from the data set for the perforated links with circular holes, as expressed in Equation 5-1.

$$K_0' = (1 - 1.79\rho) \cdot K_0 \quad \text{Equation 5-1}$$

Where: K_0' and K_0 are the elastic stiffness of the perforated link beam and corresponding imperforated link beams of the same length and section size; the value of K_0 can be calculated using the equation given in Chapter 4.

Nominal shear strength

From Figure 5-15, it is observed that the normalized nominal shear strength values of the perforated link beams with web circular holes are approximately linearly correlated with the web area perforation ratio. An empirical relation is presented below to characterize the relationship between \bar{V}_n and ρ , as expressed in Equation 5-2.

$$V_n' = (1.12 - 1.81\rho) \cdot V_p \quad \text{Equation 5-2}$$

where: V_n' is the nominal shear strength of the perforated link beam; V_p is the shear yield strength of the corresponding imperforated link beam of the same length and section size, which can be calculated using the equation given in Chapter 4.

5.2. Perforated Stainless Steel Link Beams with Web Slits

5.2.1. Finite Element Modeling

All perforated link beams with longitudinal web slits in this study are designed based on the W10x33 section with a link length of 733.2 mm. The link beams are grouped into three categories based on the modified flange width. Group 1 contains four perforated links (case 1 through case 4 shown in Figure 5-16), with a reduced flange of 80 mm.

Group 2 has four perforated links with the same web perforation patterns as Group 1, but their flanges are 150 mm wide. Group 3 contains four perforated links with the same web perforation patterns as Group I, but with the same flange width as W10x33. Geometry and dimensions of the web perforation pattern (case 1 through case 4) are listed in Table 5-4 for these perforated link beams with web slits.

Boundary constraints shown in Figure 5-17 are applied to the ends of the finite element models of these link beams. The right-side end section of the link beam is fully restrained against all translational and rotational movements, while the other end of the link model is restrained against all rotational movements and only translational rigid body motion is allowed.

Shell element 181 was used for the finite element modeling of the links in ANSYS Academic version 15. The material properties considered for FE modeling of the perforated AISI 316L stainless steel links can be found from Chapter 3. Cyclic reversal displacement prescribed by AISC Seismic Provisions (2010) is applied to the FEM to simulate the quasi-static loading test to the link beams, which is shown in Figure 5-3.

5.2.2. Finite Element Analysis: Results and Discussions

The cyclic loading behavior of the perforated link beams with web slits are evaluated in terms of the following key parameters: elastic stiffness K_0 , nominal shear strength V_n , ultimate strength V_u , ductility ratio μ , and the energy dissipation capacity.

Initial Stiffness K_0

The elastic stiffness K_0 are calculated from the backbone curves of the perforated links. The elastic stiffness K_0 (unit: kN/rad) of a link is taken as the slope of the initial linear segment of the backbone curve of shear vs. link rotation angle hysteresis loop. These values are also compared with that of the corresponding unperforated link beams with the same section size. Detailed values of K_0 for the perforated links and the corresponding imperforated links are listed in Table 5-5 and Table 5-6 respectively. Compared to the unperforated links, the elastic stiffness K_0 values are significantly reduced due to web perforations. For the perforated links in the same group, case 1 links (with smaller strip length) or case 4 links (with larger strip width) are seen to have the highest stiffness

values among the links in all four cases. The backbone curves for the perforated links in each group are plotted in Figure 5-18.

Nominal shear strength V_n and Ultimate strength V_u

The nominal shear strength V_n and the ultimate strength V_u are determined from the backbone curves for both the perforated links and the corresponding unperforated one. The nominal shear strength V_n is defined as the linear limit shear force from the backbone curve of the link shear vs. link rotation angle hysteresis curves. The ultimate strength V_u is defined as the maximum shear force value in the entire backbone curve. Locations of V_n and V_u for the perforated links with web slits are indicated in the backbone curves shown in Figure 5-18. Over-strength factor Ω is defined as the ratio of V_u to V_n . Detailed values of V_n , V_u , and Ω for the perforated links and the corresponding imperforated one are listed in Table 5-7 and Table 5-6 respectively.

Comparison of the nominal shear strength V_n values and the ultimate strength V_u values were conducted among the perforated links with web slits and the corresponding imperforated links with the same flange widths. Similar to the prior observation made for the perforated links' stiffness properties, the link's flange width has a minor effect on the V_n and V_u values of the perforated links. For the perforated links within the same group, V_n and V_u values vary significantly with the web perforation patterns, corroborating the statement that the strength of the perforated links can be tuned via adjusting the size of the perforated web slits. Furthermore, case 1 and case 4 links with the highest stiffness values generally also have the highest V_n and V_u values among the four cases.

The relationship between K_0 and V_n is also investigated for both the perforated and the corresponding unperforated links of different sections. The V_n vs. K_0 relation is shown in Figure 5-19. It is seen in Figure 5-19 that data points of V_n vs. K_0 for the perforated links are in general located along the same line, and is slightly deviating from the regression line of V_n vs. K_0 for the unperforated links. Thereby, it can be concluded that the nominal shear strength are adjusted proportionally with the elastic stiffness values by the web slits; and the nominal shear strength versus the elastic stiffness relationship is almost constant.

Ductility

The ductility of the perforated links with web slits is described by the ductility ratio μ . The ductility ratio μ is determined from γ_y and γ_u with the same approach illustrated before in Figure 5-18. Detailed values of γ_y , γ_u , and μ of the perforated links in this study are listed in Table 5-8. Both γ_y and γ_u values vary with the web perforation patterns and the flange widths. The variance of γ_y is much smaller compared to the variance of γ_u . Basically all the perforated links can sustain the link rotation angles of at least 0.08 radians, satisfying the minimum ductility requirements for short links by AISC Seismic Provisions (2010). The ultimate link rotation γ_u values for certain perforated links such as case 1 in Group II and Group III are relatively low, indicating that particular attention should be paid to the perforated slit sizes to prevent premature fracture in early stage.

Hysteretic Energy Dissipation

Hysteretic energy dissipated by a link in each loading cycle is equal to the area enclosed by the shear force vs. link rotation angle hysteresis loop of that load cycle. The hysteresis loops for the perforated links are shown in Figure 5-20. Similarly, the hysteretic energy of a perforated link dissipated in each cycle is normalized by the dissipated hysteretic energy of the ideal elastic-plastic model. The yield strength and elastic stiffness of the ideal elastic-plastic model are taken as the yield strength and elastic stiffness of the corresponding imperforated link with the same section. The normalized hysteretic energy dissipation versus the loading cycle and link rotation angles for the perforated links are shown in Figure 5-21.

Shown in Figure 5-20, strength degradation is only observed in the case 4 link beams from Group I and Group III. Generally the links with higher elastic stiffness values possess greater energy dissipation capacity. Therefore, for the perforated links, their elastic stiffness values K_0 , nominal shear strength values V_n , and the energy dissipation capacity are correlated with each other. It is also observed that for all perforated links, the dissipated energy remains fairly low at small link rotation angles, and increases rapidly with increasing link rotation at large link rotation angles, likely due to the plasticity hardening effect of the stainless steel material.

Von Mises Plastic Strain Contour Plot

Von Mises plastic strain contours for the perforated links at link rotation angles of 0.02 radians and 0.11 radians are also recorded. The Von Mises plastic strain contours of the perforated links in Group III at the link rotations of 0.02 radians and 0.11 radians are shown in Figure 5-22 and Figure 5-23 respectively. Observed from Figure 5-22, the Von Mises plastic strain first occurs in the regions close to the slit corners. With increasing link rotation angle, area with plastic strain expands around the strip edges, especially in the case 2 links, as shown in Figure 5-23. This observation support the web perforation design objective that plastic deformation (and ductile fracture) is localized around the slit edges and the rest parts of the links remain elastic.

5.2.3. Parametric Study on Perforation Module

5.2.3.1. Finite Element Modeling

Finite element models of typical perforation modules that represent the web unit cells separated by slits in the perforated links are built in ANSYS version 15.0 for shape optimization study. The layout of a typical perforation module is shown in Figure 5-24. In this parametric study, two parameters are varied to generate different module shapes: module's parallel length (L) and width (d). The corner radius (R) of the module is set as half of the module width (d). Round corner is used for the perforation to reduce the stress concentrations near corner cut.

A total of six cases of the perforation modules were investigated in the parametric study. The thickness (t) of each module case was fixed at 6 mm. Three values were selected for L : 50 mm, 100 mm, and 150 mm; and two values were selected for d : 25 mm and 50 mm respectively. For each module case, the corner radius was set as half of the width (d). Detailed geometry and dimensions for each module case are shown in Table 5-9.

The material of the perforation module is AISI 316L stainless steel. Boundary constraints were modeled for the module perforations. For a typical layout of the perforation module shown in Figure 5-24, the end edges of the module are 30 mm away from the rounded corners, which are highlighted by the extension regions boxed in the red dashed lines shown in Figure 5-25. The extension region was enclosed by a loading fixture block with much larger thickness (20 times thicker than the strip module) and more rigid (10 times higher than the Young's modulus of AISI 316L) outside the red dashed line to simulate the externally provided constraint. Out-of-plane restraints in z direction shown in Figure 5-25 were provided along the red dashed line. Rotational degrees of freedom (DOF) in all three directions were restrained at the end edge of the left fixture block. All six DOFs (3 translational DOFs and 3 rotational DOFs) were restrained at the end edge nodes of the right fixture block. The finite element models were built using shell elements 181 in ANSYS ver. 15. Cyclic load was applied with displacement control to the left-side restrained side. The cyclic loading protocol specified by AISC Seismic Provision (2010) for link beams is adopted here for the perforation module.

5.2.3.2. Finite Element Analysis: Results and Discussion

Figure 5-26 shows the hysteresis loops of the force vs. displacement relationships of the module cases 1, 2 and 3; the hysteresis loops of the module cases 4, 5, and 6 are plotted in Figure 5-27. Strength degradation is observed for all the module cases. As fracture was not explicitly modeled, the strength degradation is due to local buckling, which occurred in the loading cycles at module chord rotation angle amplitude of ± 0.11 radians to ± 0.13 radians.

Backbone curves of hysteresis loops were recorded for the investigated module cases to determine the elastic stiffness K_0 , nominal shear strength V_n , and ultimate strength V_u , as shown in Figure 5-28 to Figure 5-33. The elastic stiffness K_0 of the perforation module is the slope of the initial straight line of the backbone curve. The nominal strength V_n represents the first significant yield of the module. The ultimate strength V_u is taken from the peak load point in the backbone curve before strength degradation occurs. Detailed values for the initial stiffness (K_0), nominal shear strength (V_n), and ultimate strength (V_u) for each module case are listed in Table 5-10.

Reflected by the backbone curves shown in Figure 5-28 through Figure 5-33, yielding of the module generally occurred shortly after the chord rotation angle reached 0.02 radians; and buckling occurred approximately at link rotation angles between 0.11 radians and 0.13 radians. The Von Mises plastic strain contour plots for each module case recorded at the chord rotation angle of 0.02 radians and 0.11 radians are plotted in Figure 5-34 and Figure 5-35 respectively.

The occurrence of yielding is indicated by the initiation of plastic strains. In Figure 5-34, a snapshot of Von Mises plastic strain contour at the chord rotation angle of 0.02 radians, plastic strains are observed near the round corners of all module cases, where maximum moments occur. Shown in Figure 5-35, at the chord rotation angle of 0.11 radians, plastic deformed areas expand towards interior from the corners at both ends. Except for case 4, relatively high plastic strains are concentrated to a localized area at the strip's end sections. In case 4, high plastic strains also expand into the strip's mid-span area. It is concluded that for all the module cases excluding case 4, bending moment is the lead factor causing the yielding of the module strip. For case 4, as the strip span length is relatively short, shear force also played an important role in yielding besides end moments.

5.2.3.3. Analytical Formulation of Mechanical Properties of Perforation Module

Based on the above plastic strain contour plots, it can be concluded that plastic strains initiated primarily by the bending moment in the investigated module cases other than case 4. For case 4, the plastic strains were caused by the combined effect of bending moment and shear. Generally the strip module can be modeled as a fix-fixed beam, as illustrated in Figure 5-36. The elastic stiffness K_0 and the nominal shear strength V_n of the module can be calculated using this simplified beam model.

The elastic stiffness of each module is calculated by adding its flexural stiffness and shear stiffness together. The total length of the simplified beam representing the module is $L+2R$. The elastic stiffness of each module case - K_0 is calculated from Equation 5-3.

$$K_{bending} = \frac{12EI}{(L + 2R)^3}$$

$$K_{shear} = \frac{GA_s}{L + 2R} \quad \text{Equation 5-3}$$

$$K_0 = \frac{K_{bending} \cdot K_{shear}}{K_{bending} + K_{shear}}$$

where: E is the Young's modulus of AISI 316L stainless steel, which is taken as 197.1 GPa; I is the module's moment of inertia about the strong axis, which is equal to $1/12 \cdot t \cdot d^3$ for rectangular section; A_s is the module's effective shear area, which is equal to $5/6 \cdot t \cdot d$.

For a fix-fixed beam, maximum normal stress occurs at the end sections of the beam. As the module section is rectangular shape, the tensile and compressive stresses are uniformly distributed about the neutral axis for fully yielded section (hardening effect neglected), as shown in Figure 5-37. The normal stress at the end sections of the module is equal to yield stress, from Equation 5-4.

$$\sigma_n = \frac{M}{Z} = \frac{V \cdot \frac{1}{2}L}{\frac{1}{4}td^2} = \frac{2VL}{td^2} \quad \text{Equation 5-4}$$

The plastic shear force associated with the plastic moment is constant along the length of the module. Based on the Von Mises yield criterion, yielding of a material occurs when the Von Mises stress (effective stress) exceeds the material's yield stress, i.e., the normal stress calculated from Equation 5-4 exceeds the material's yield stress. Therefore, the nominal shear strength V_n of a module perforation is calculated from Equation 5-5.

$$V_n = \frac{\sigma_y \cdot t d^2}{2L} \quad \text{Equation 5-5}$$

where σ_y is the material's yield stress of AISI 316L stainless steel, and can be referenced from Chapter 3.

The analytically calculated module properties including the elastic stiffness K_0 and nominal shear strength V_n are validated with the FE analysis results, as listed in Table 5-11. It can be seen that except for case 4, where the analytical method significantly overestimates the elastic stiffness K_0 , the K_0 and V_n results determined from analytical method and the FEM simulations are very close to each other. For case 4, its span length is too short and shear deformation and yielding also significantly contribute to its overall behavior, which is not modeled by the above formulas. Generally it can be concluded that the analytical formula is applicable only for modules with span-depth ratio L/d greater than 2.

5.2.4. Analytical Formulation of Mechanical Properties of Link Beams with Perforated Slits

As shown in Figure 5-23, high plastic strains only concentrate around the corners of the perforated slits when the perforated links are subjected to large link rotations, while the rest regions including the web area far away from the slits remain elastic. The high plastic strain regions can be considered as plastic hinges. This is analogous to a moment resisting frame (MRF) with plastic hinges formed at the column ends. Therefore, for a typical perforated link with web slits shown in Figure 5-38, its strength and stiffness can

be calculated analogously to a MRF with rigid beams and flexible columns. The panels divided by the web stiffeners can be imagined as different stories in an equivalent MRF, and in each panel the top T-section module formed by the top flange and the upper web portion, as well as the bottom T section module and the strip modules in between them, can be imagined as the columns in an MRF story. The schematics of breaking up the T section modules and strip modules are shown in Figure 5-38. Therefore, the analytical computation of the perforated links' strength and stiffness properties involves the computation of the individual strength and stiffness of the T-section modules and the strip modules first and then combine them together.

The connections of the T-section modules and the strip modules to the rest parts of the perforated link are assumed to be the same as the beam-to-column connections in an MRF with rigid beams. Therefore, the end restraints of the T-section modules and the strips are assumed to be rigid prior to the formation of plastic hinges at the slit corners. The strength of the perforated link is the same as that of the panel, and the stiffness of the perforated link is equal to $1/n$ that of any panel (n is the number of panels in the link).

5.2.4.1. Elastic Stiffness

The elastic stiffness K_0 calculation of the T-section module and the strip module involves of the calculation of the bending stiffness K_b and shear stiffness K_s , which are expressed in Equation 5-6.

$$K_b = \frac{12EI}{L_b^3}$$

$$K_s = \frac{GA_s}{L_s}$$

Equation 5-6

$$K_0 = \frac{K_{bending} \cdot K_{shear}}{K_{bending} + K_{shear}}$$

Where: E is the material's modulus of elasticity. Terms I , A_s , L_b , and L_s are the moment of inertia, shear area, length for bending stiffness calculation, and length for shear stiffness calculation respectively for the T section module or the strip module. The length for bending stiffness calculation is differentiated from the length for shear stiffness calculation because the ends of a panel (i.e., floors of the imaginary MRF model) are expected to have substantially larger bending stiffness. The determination of L_b and L_s for the T section module and the strip module is expressed in Equation 5-7.

$$L_b = \begin{cases} L + 2R & \text{for a middle strip} \\ L + 2R & \text{for a T section} \end{cases}$$

Equation 5-7

$$L_s = \begin{cases} L + 2R & \text{for a middle strip} \\ L_{seg} & \text{for a T section} \end{cases}$$

where L is the length of a strip within the round corners; R is the corner radius; L_{seg} is the center-line distance between two adjacent web stiffeners.

5.2.4.2. Nominal shear strength

For the perforated links with web slits, it is assumed that the nominal shear strength of the perforated link is equal to the sum of the nominal shear strength values of the two T-section modules and the nominal shear strength of the strip modules. The nominal shear

strength of each T section module and the inner strip module is expressed in Equation 5-8. Therefore, the nominal shear strength of a perforated link with web slits is determined from Equation 5-9.

$$V_{n_s} = \frac{\sigma_y \cdot Z_s}{\frac{1}{2}L_b} = \frac{\sigma_y \cdot t \cdot d^2}{2L_b}$$

Equation 5-8

$$V_{n_T} = \frac{\sigma_y \cdot Z_T}{\frac{1}{2}L_b} = \frac{2\sigma_y \cdot Z_T}{L_b}$$

$$F_y = 2 \cdot V_{n_T} + (n - 1) \cdot V_{n_s}$$

Equation 5-9

where t is link web thickness; d is the strip's depth; L_b is expressed in Equation 5-7; Z_s and Z_T are the plastic section modulus of the inner strip module and the T section module.

5.3. Cast Steel Shear Links with Perforated Circular Holes

5.3.1. Cast Steel Shear Link: Specimen Geometry and Dimensions

Two cast steel link specimens with different web perforation ratios are considered in this study. These two cast steel I-section link beam specimen with circular hole web perforation has a depth (h) of 215 mm and a length (L) of 600 mm and was tested under quasi-static loading protocol by researchers (Zhang 2015) at Tongji University, Shanghai, China. The cast steel link specimens. The experiment test setup for quasi-static loading of cast steel link beams is shown in Figure 5-41. The flange width (b_f), flange thickness (t_f), web thickness (t_w), and stiffener thickness (t_s) of the perforated cast steel link beams are 180mm, 15mm, 12 mm, and 14 mm respectively. The specimens' are 180mm, 15mm, 12

mm, and 14 mm respectively. Circular holes of a diameter (D) of 20 mm are perforated over the link web. Geometry and dimensions of the two perforated cast steel links are shown in Figure 5-39. The cast steel specimen referred to as design 1 has the horizontally aligned circular holes spaced 60 mm ($S_{diag}=60$ mm) apart; while the cast steel link specimen referred to as design 2 has diagonally aligned circular holes spaced 42.4 mm ($S_{diag}=42.4$ mm) apart. Details of design 1 and design 2 are listed in Table 5-12.

5.3.2. Finite Element Modeling

FE analysis is conducted on the two perforated cast steel link specimens shown in Figure 5-39. The finite element model is created by using shell element 181 in ANSYS Academic version 15.0. The meshed finite element models are plotted in Figure 5-40. Boundary constraints of the FE models of the cast steel link beams are the same as that of the FE models of the stainless steel link beams. The stress strain relationship of cast steel is obtained from the material experiment conducted by Zhang (2015). The plasticity hardening parameters of cast steel for FE models are listed in Table 5-13.

Cyclic reversal displacement prescribed by AISC Seismic Provisions (2010) was adopted for loading protocol in FE analysis to simulate the quasi-static load test on the link beam. The prescribed loading protocol in terms of link rotation γ is shown in Figure 5-3.

The ductile fracture initiation under cyclic loading is set as the controlling limit state for the perforated cast steel links with circular holes, as observed in experimental tests. The

shear force vs. link rotation angle hysteresis curves from FE analysis are truncated after the estimated fracture initiation point based on the CVGM criteria for ductile fracture.

5.3.4. Results and Discussions

Comparative study are conducted on the elastic stiffness, nominal shear strength, and ultimate strength of the two cast steel link beams with perforated web circular holes, based on the FEM simulation and experimental data. Analytical calculation of the elastic stiffness and nominal shear strength of the perforated cast steel links with circular holes is presented next.

Analytical Calculation Results

Based on the cast steel coupon test results from Zhang (2015), the yield stress and modulus of elasticity of cast steel are 483 MPa and 206 GPa respectively. Using Equation 5-6 and Equation 5-9, the analytical results are listed in Table 5-14.

Numerical Simulation and Experiment Results

The hysteresis loops from the FEM simulation results and the experiment results are plotted in Figure 5-42. The fracture initiation point predicted by the CVGM method is indicated in the hysteresis curve from the FEM simulation. After the predicted fracture initiation point, the FEM hysteresis curve is changed to dashed line to distinguish from the curve before fracture. It is observed that the hysteresis loops from the FEM simulation results and the experiment results match very well over the entire loading

process. As crack propagation is not explicitly modeled in the FEM simulation, the FEM simulated hysteresis curve start to deviate from the experimental curve when severe cracking occurred in the last loading cycle. The FEM derived hysteresis curve is terminated finally due to numerical convergence failure.

The elastic stiffness, nominal shear strength, and ultimate shear strength of the perforated cast steel link beams are determined from the backbone curves shown in Figure 5-43. The V_n and V_u values from the FEM simulation and the experimental results are indicated in Figure 5-43. Detailed values of V_n and V_u are listed in Table 5-14.

5.3.5. Discussion

A summary of the elastic stiffness K_0 , nominal shear strength V_n , and ultimate shear strength V_u given by three methods for the two perforated cast steel link beams is listed in Table 5-16. Though with different web area perforation ratios, the strength and stiffness of the two perforated cast steel links are very close, as reflected by the experiment results. This observation is contradicting with the hypothesis in the analytical method, that the stiffness and strength of the perforated links with circular holes are reduced proportional to increasing web area perforation ratio. On the other hand, the analytical results generally match well with the FEM results and the experiment results for the link beam specimen of design 2, but not for the specimen of design 1. Hence it can be concluded that for the perforated cast steel links, the strength and stiffness properties are affected by both the web area perforation ratio and the perforation pattern.

As illustrated in Figure 5-43, ductility ratio μ is defined as the ratio of γ_u (the link rotation angle corresponding to the fracture initiation estimated from the FEM simulation or the link rotation angle corresponding to 15% drop in load capacity from the experiment results) to γ_y ($\gamma_y = V_u / K_0$). Detailed values of γ_y , γ_u , and μ are listed in Table 5-15. It can be observed that the ductility values from the FEM simulation and the experiment generally match well with each other for design 2; yet for design 1, the FEM simulation results underestimate γ_u value compared with experimental results. Moreover, the experiment results shown in Figure 5-43 reveal that strength degradation occurred later for the link beam specimen of design 2 (at link rotation of 0.09 radians) compared with design 1 specimen (at link rotation of 0.07 radians). The cast steel links with diagonally aligned circular holes generally have better ductility.

Hysteretic energy dissipation capacity is another important factor in evaluating the seismic performance of a link beam. The energy dissipation of the perforated cast steel link in each loading cycle after the initial yielding is normalized with the dissipated hysteretic energy of the corresponding imperforated link with an idealized elasto-plastic stress-strain constitutive relationship. The normalized hysteretic energy dissipation and link rotation angles for the two perforated cast steel links are plotted in Figure 5-44.

Von Mises plastic strain contours obtained from the FEM simulations at the link rotation angles of 0.02, 0.05, 0.07, and 0.09 radians are shown in Figure 5-45. High Von Mises plastic strain zones occurred between the holes aligned in the same row and the holes aligned in the same column. Thereby, cracks are expected to initiate within these zones.

The deformed shapes of the test specimens are shown in Figure 5-47. Paints of the specimens flaked off at large plastic deformation locations, which match with the high Von Mises plastic strain zones shown in Figure 5-45. In the experiment test, cracks were first observed during the loading cycle of 0.03 radians for both specimens, and connected into a large crack during the loading cycle of ± 0.07 radians for the specimen of design 1 and did so during the loading cycle of ± 0.11 radians for the specimen of design 2. The test specimens after fracture are shown in Figure 5-47. Cracks formed within the high Von Mises plastic strain zones in Figure 5-45, as expected.

The fracture initiation occurrence predicted with the CVGM criteria is compared with the crack observations from the experiment. The evolution of the damage variable with the loading cycle is shown in Figure 5-48. Ductile fracture would take place whenever the damage variable exceeds the unity value in the FEM simulation. The crack occurrence observed in the experiment is also indicated in Figure 5-48. For the link specimen of design 1, fracture initiation is predicted in the 33rd loading cycle with the link rotation angle amplitude of ± 0.03 radians in the FEM simulation; and crack was first observed in the experiment during the same loading cycle. For the specimen of design 2, fracture initiation is predicted to first happen in the 34th loading cycle with a link rotation angle amplitude of ± 0.04 radians; and crack initiation was observed in the experiment in the 33rd loading cycle with the amplitude of ± 0.03 radians, which corresponds to a damage variable value around 0.6. Generally speaking, CVGM provides reasonably good predictions to the crack initiation of the perforated cast steel link beams with circular holes.

5.4. Cast Steel Link Beams with Perforated Slits

5.4.1. Finite Element Modeling

Finite element (FE) analysis was conducted on one specimen of cast steel link beam with perforated web slits. The cast steel I-section link beam specimen has a depth of 215 mm and a length of 600 mm and was tested under quasi-static loading protocol by researchers (Zhang 2015) at Tongji University, Shanghai, China. The flange width, flange thickness, web thickness, and stiffener thickness of the perforated cast steel link are 180mm, 15mm, 12 mm, and 14 mm respectively. Longitudinal slits are perforated on the web, with a length of 120 mm, width of 10 mm, and center-to-center distance of 35 mm from each other. Detailed geometry and dimensions of the perforated cast steel link beam are shown in Figure 5-49.

The accuracy of the FE model is verified by comparing the FE analysis (FEA) results with the experimental test data of the perforated cast steel link beam specimen. The shear force vs. link rotation hysteresis loops from FEA and experimental test are plotted in Figure 5-50. It is seen that up to link rotation angle of 0.06 the FEA-derived hysteresis curve matches well with the experimental curve. At large link rotation angles (>0.06), the FEA curve becomes less accurate as fracture growth could not be simulated in FE modeling.

5.4.2. Results and Discussions

The following parameters are used for performance evaluation of the perforated cast steel link beam: elastic stiffness K_0 , nominal shear strength V_n , ultimate strength V_u , ductility ratio μ , and the energy dissipation capacity.

The elastic stiffness K_0 (unit: kN/mm) is calculated from the initial linear portion of the backbone curve shown in Figure 5-51. Detailed values of K_0 determined from the backbone curves of the hysteresis loops from the FE analysis results and experimental test results are listed in Table 5-16. The accuracy of the FE analysis is verified by comparing the stiffness values. Strength degradation is observed in the hysteresis curves. The primary factor contributing to the strength degradation is fracture in the web.

Two strength values are recorded: nominal shear strength V_n and ultimate strength V_u . The V_n and V_u of the perforated cast steel link beam are determined both from the FEM simulation results and experimental test data, as shown in Figure 5-51. The over-strength factor Ω is defined as the ratio of V_u to V_n . Detailed values of V_n , V_u , and Ω are listed in Table 5-16.

Ductility ratio μ of the cast steel link is defined as the ratio of γ_u to γ_y . The definitions of γ_y and γ_u are illustrated in Figure 5-51. Detailed values of γ_y , γ_u , and μ are listed in Table 5-17. Since crack initiation and propagation mechanisms are not incorporated in the FEM simulation, FE analysis overestimates the γ_u and μ values.

Hysteretic energy dissipation of a link beam in a loading cycle is equal to the area enclosed by the corresponding hysteresis loop of that load cycle. The energy dissipated by the perforated cast steel link with web slits in each loading cycle is normalized in the same way as before. The normalized hysteretic energy dissipation evolution and link rotation angle of the perforated cast steel link with web slits are shown in Figure 5-52. The general trend of the hysteretic energy dissipation is increasing with load cycle numbers.

5.4.3. Fracture Initiation and Growth

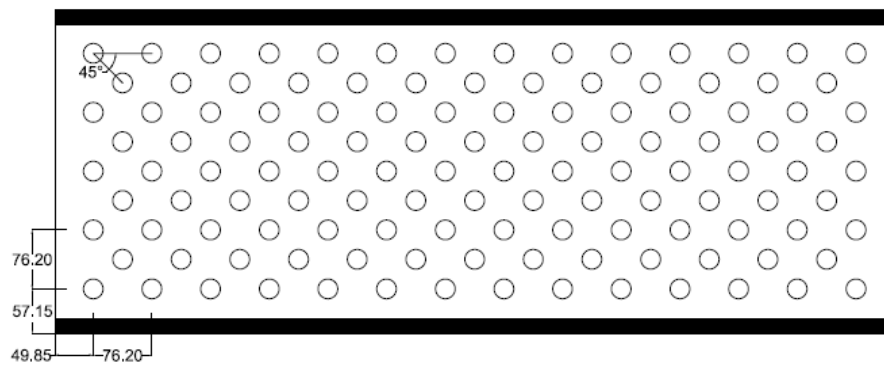
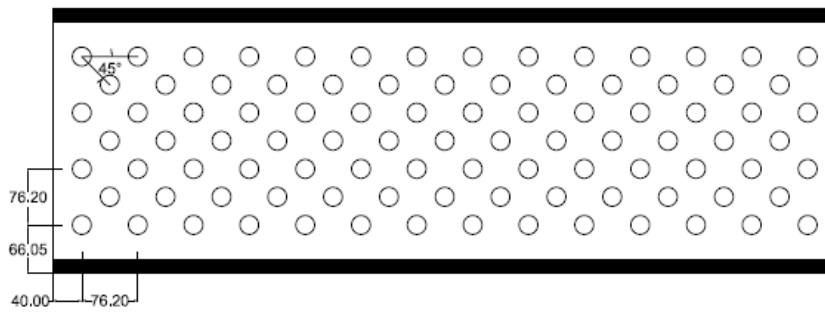
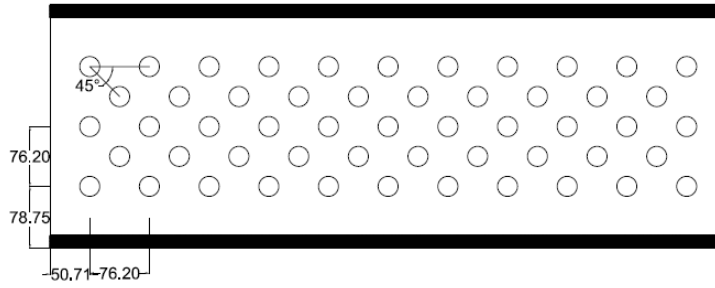
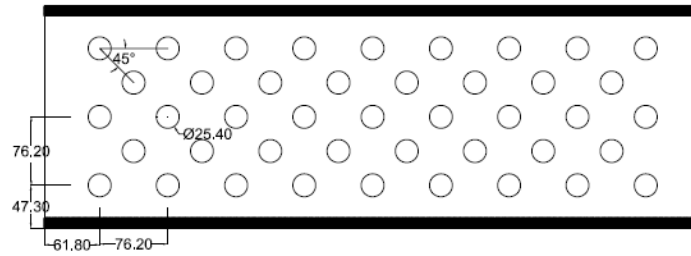
Von Mises plastic strain contours are recorded from the FE simulation at the link rotation angles of 0.02, 0.05, 0.07, 0.09, and 0.11 radians respectively, as shown in Figure 5-53. It is seen that plastic strain first occurred at the slit corners close to the flanges, followed by occurrence at the slit corners close to the mid-section-height of the link. This finding suggests that slit corners near the flanges are more susceptible to severe plastic deformation and thus low-cycle fatigue induced fracture under cyclic loading. It is also observed that with increasing link rotation angles, plastic strain zone near flange slit corner extends towards the flanges along a 45 degrees angle direction, while the plastic strain zone near mid-section-height expands to the nearby slits along the depth direction of the link. Thereby, cracks are expected to form at the corner ends of the perforated slits and propagate in the link's depth direction for those interior cracks or in 45 degree angle direction for those near the flange.

During the experimental test, crack was first found at the loading cycle of 0.03 radians, which formed an approximate 45 degree angle with the loading direction (perpendicular to the longitudinal axis of the link beam). During the loading cycle of ± 0.09 radians, neighboring cracks were connected together and the experiment testing was terminated due to significant load capacity drop. The fractured specimen after the experiment testing is shown in Figure 5-54. Compared to the Von Mises plastic strain contour shown in Figure 5-53, it is seen that fracture locations coincide with the high plastic strain regions indicated in FE analysis derived von Mises plastic strain contour plots, and the crack propagation directions are generally the same as the Von Mises plastic strain propagation directions.

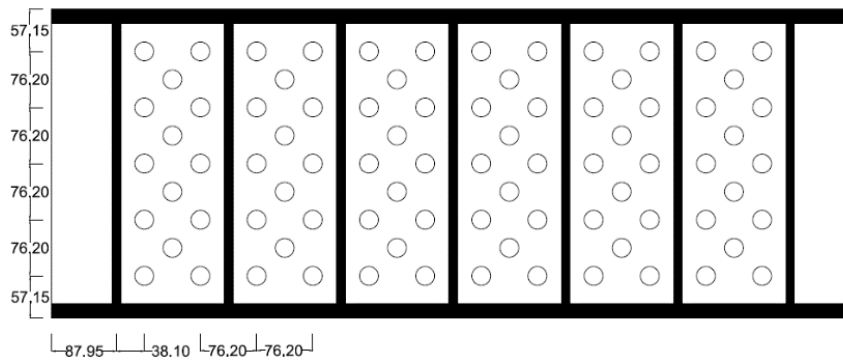
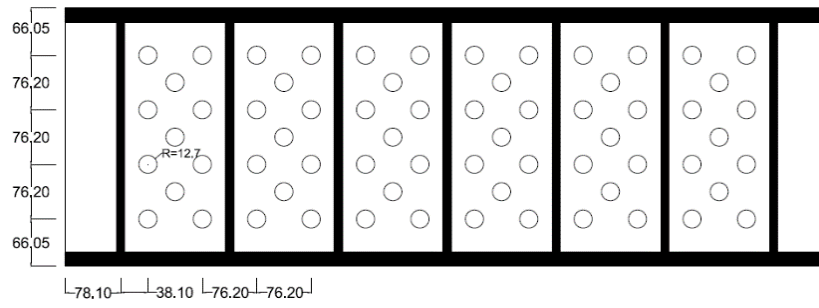
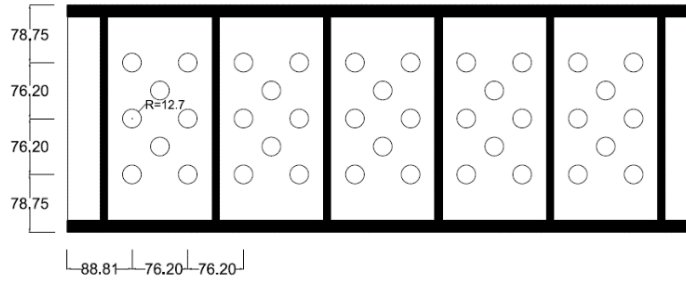
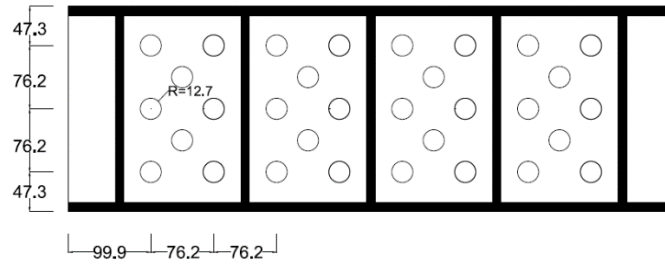
The fracture initiation point predicted using the CVGM criteria in the FE analysis of the perforated cast steel link is compared with the experiment observations, as Figure 5-55. Based on the CVGM fracture criterion (see Chapter 3 for details), fracture initiates whenever the damage variable in any hot spot area exceeds one. Shown in Figure 5-55, fracture initiation is predicted to occur during the 34th loading cycle, which is at the link rotation angle of ± 0.04 radians. For the test specimen, fracture was observed at the 33rd loading cycle, corresponding to the link rotation angle of ± 0.03 radians; and the experiment testing was terminated when the cracks were connected over the web section during the 37th loading cycle, at the link rotation angle of ± 0.09 radians. Accuracy of the fracture initiation predicted using CVGM is further verified here.

5.5. Relation to the Next Chapter

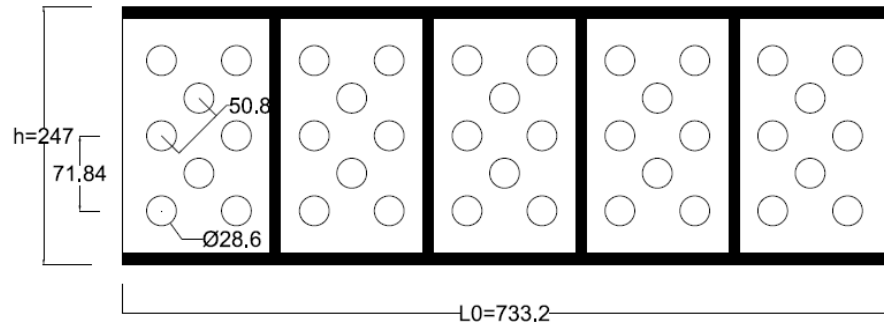
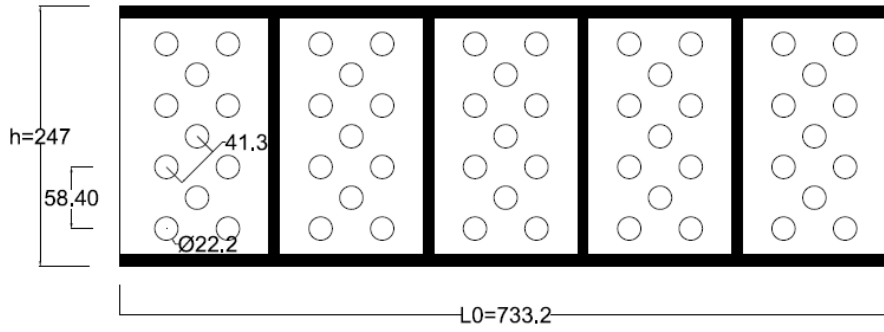
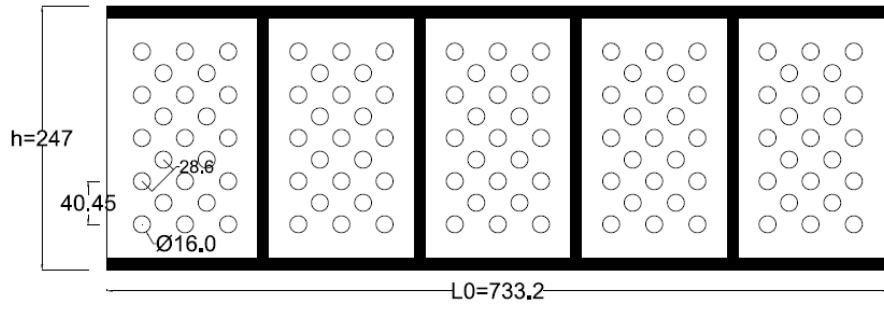
In this chapter, nonlinear FE analysis results are presented for AISI 316L stainless steel links with web perforations; both FE analysis and experimental testing results are presented for cast steel link beams with web perforations. Web perforation is shown to be a cost-effective approach to tune the mechanical properties of link beams. Based on the FEM simulation results of AISI 316L stainless steel links and the experimental test results of the cast steel links, the use of slit perforation allows the links to be tuned for strength and stiffness to a greater degree. From the experiment test results of the cast steel links, the ductility of the cast steel links with perforated slits is lower than the ductility of the cast steel links with circular holes and severe fracture occurred in the perforated cast steel links with slits during the link rotation amplitude of 0.07 radians. This might be explained by the specific configuration of the slit pattern design of the test cast steel link beam and its ductility is likely to be improved if more slender strips are used. Since AISI 316L stainless steel is much ductile than cast steel, the fracture initiation of the perforated AISI 316L stainless steel links is believed to happen at much larger link rotation angle values if properly designed. In Chapter 6, AISI 316L stainless steel links with perforated slits are selected as the fuse members for the self-centering EBF systems.



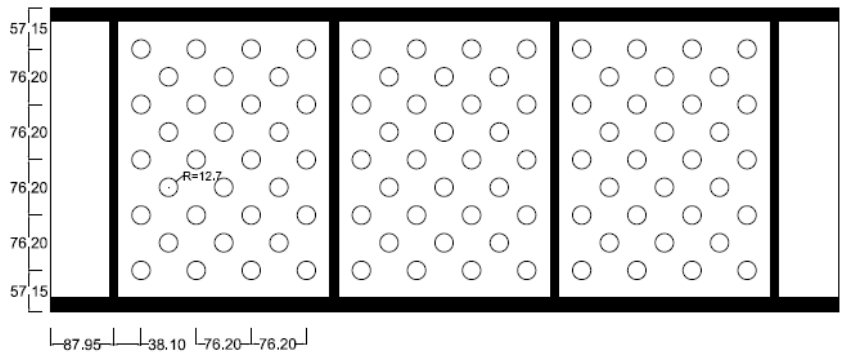
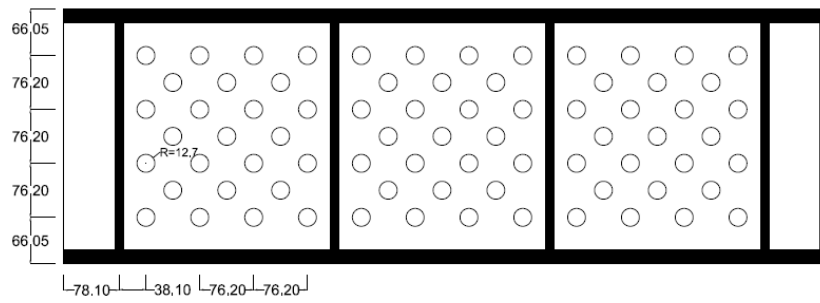
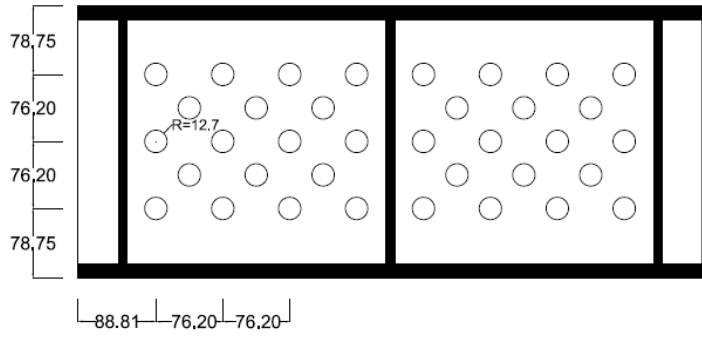
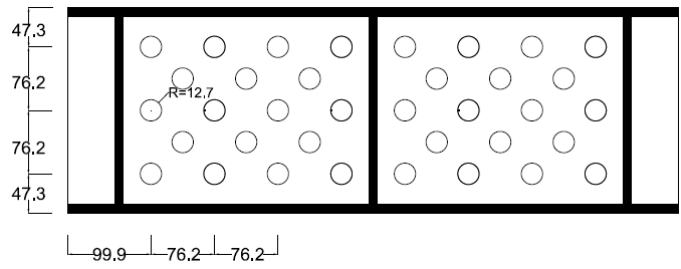
(a) Group I Links



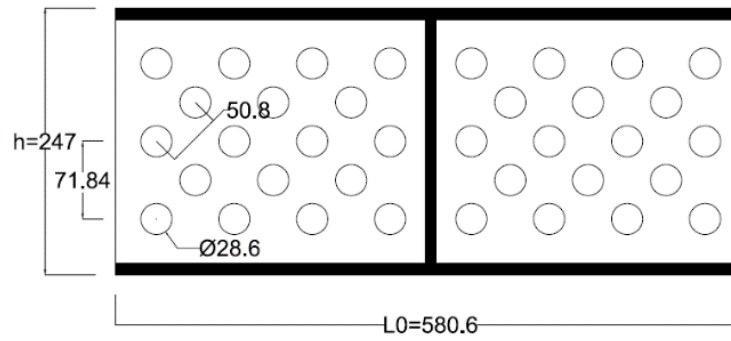
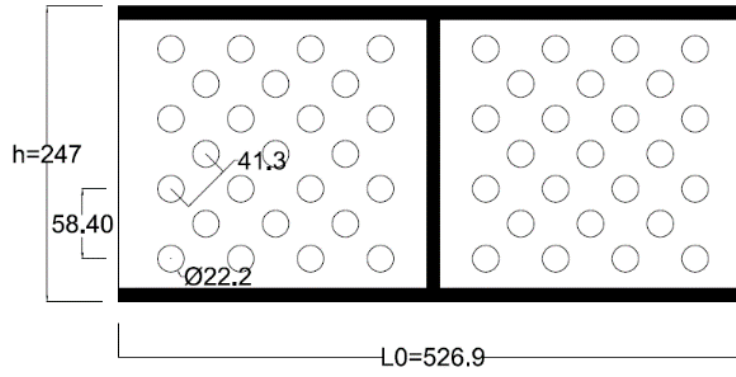
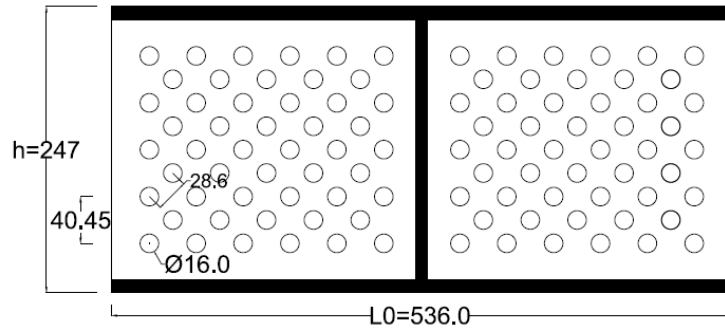
(b) Group II Links

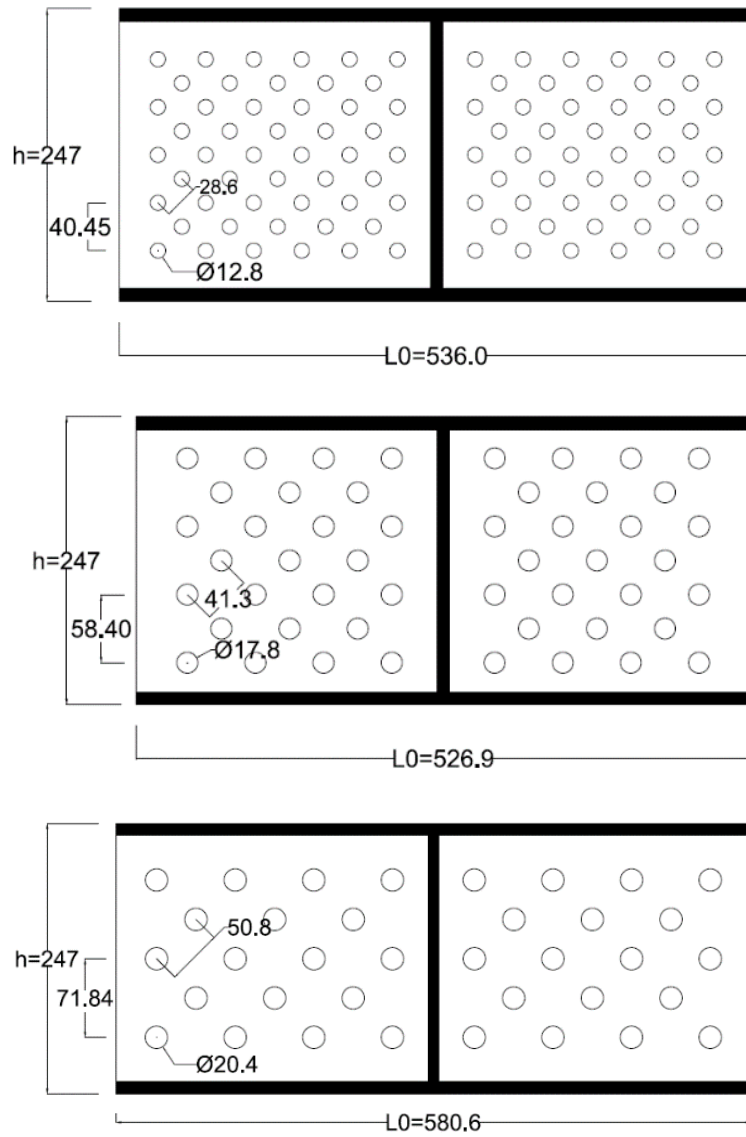


(c) Group III Links



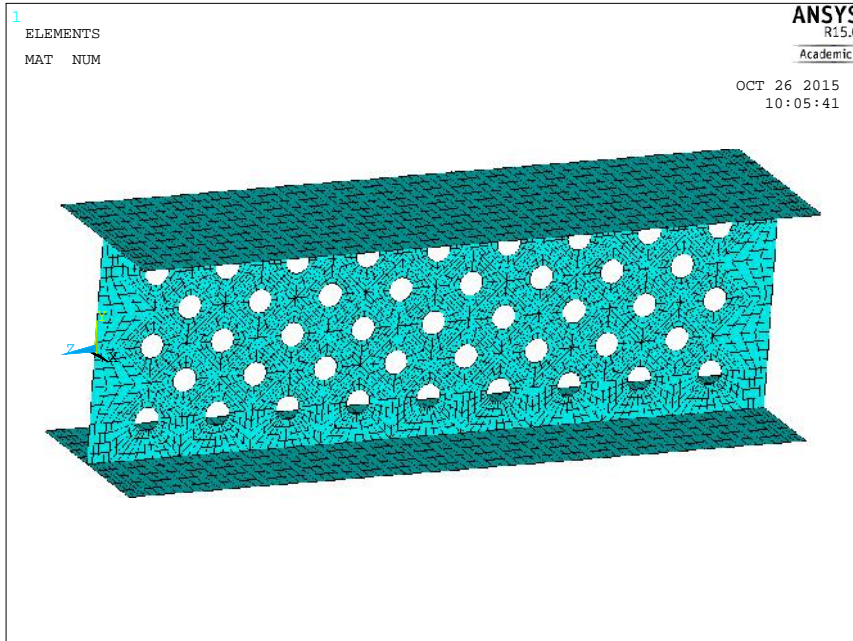
(d) Group IV Links



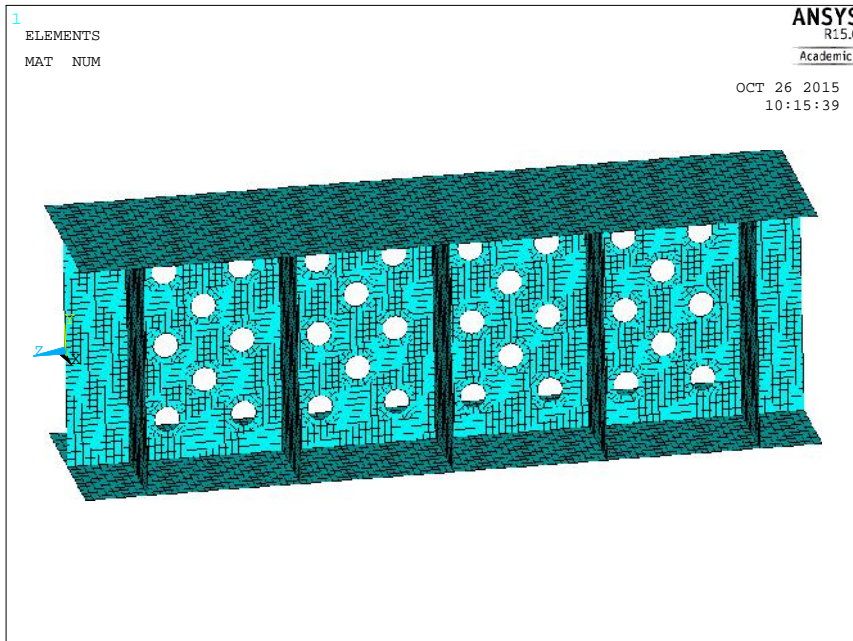


(e) Group V Links

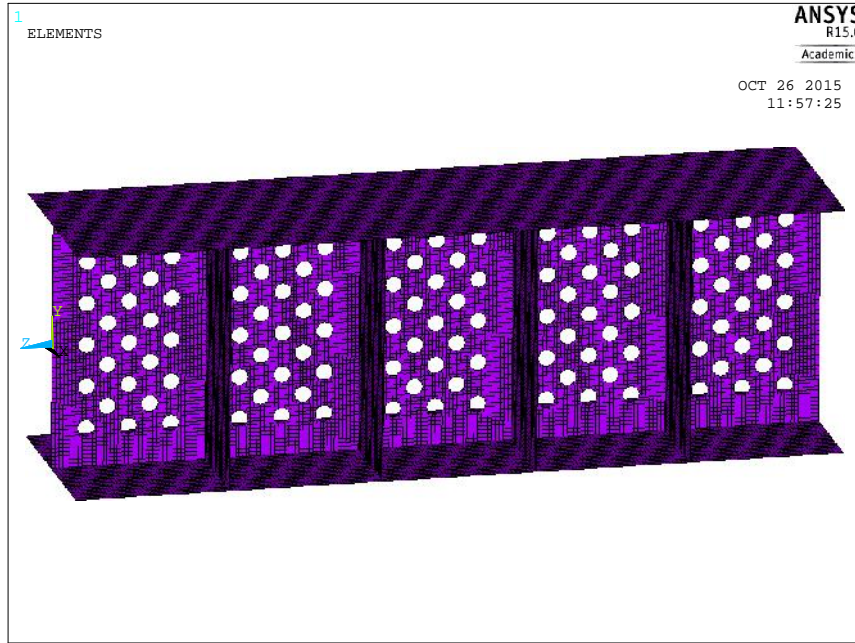
Figure 5-1 AISI 316L stainless steel perforated links with circular holes



(a) Meshed finite element model for Group I-1



(b) Meshed finite element model for Group II-1



(c) Meshed finite element model for Group III-1

Figure 5-2 Meshed models of AISI 316L stainless steel perforated links with circular holes

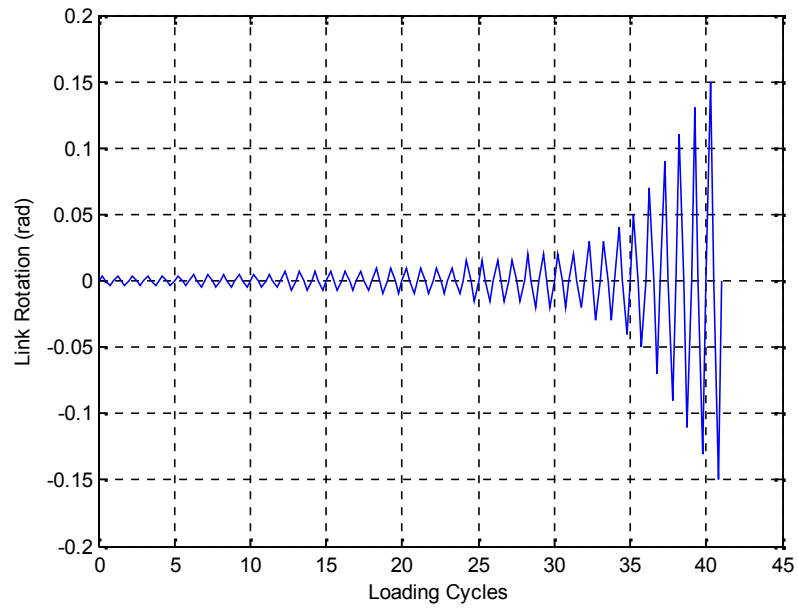
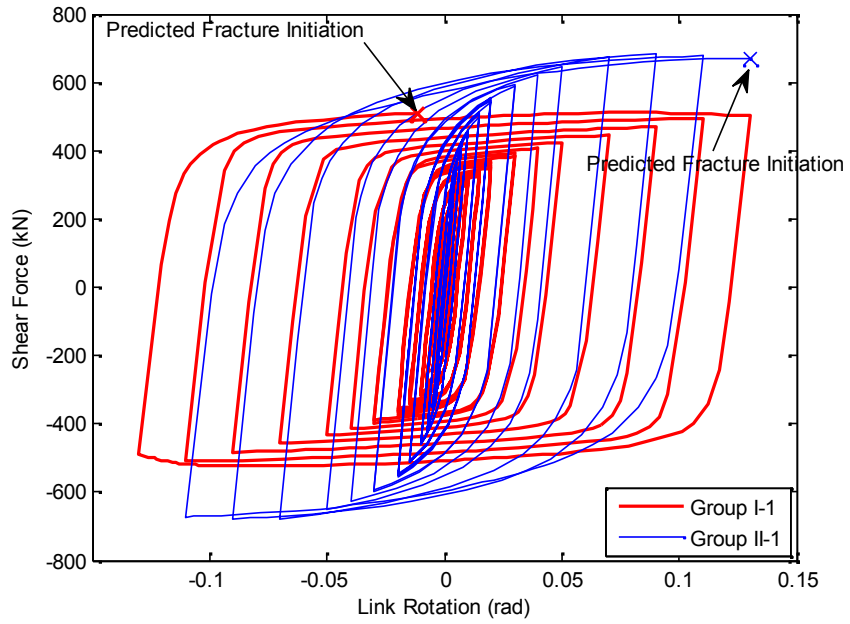
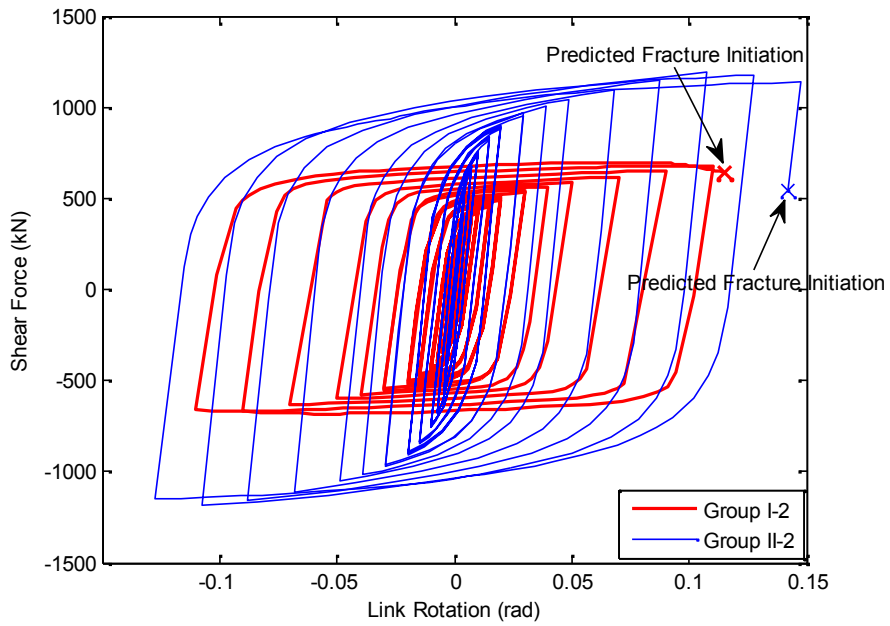


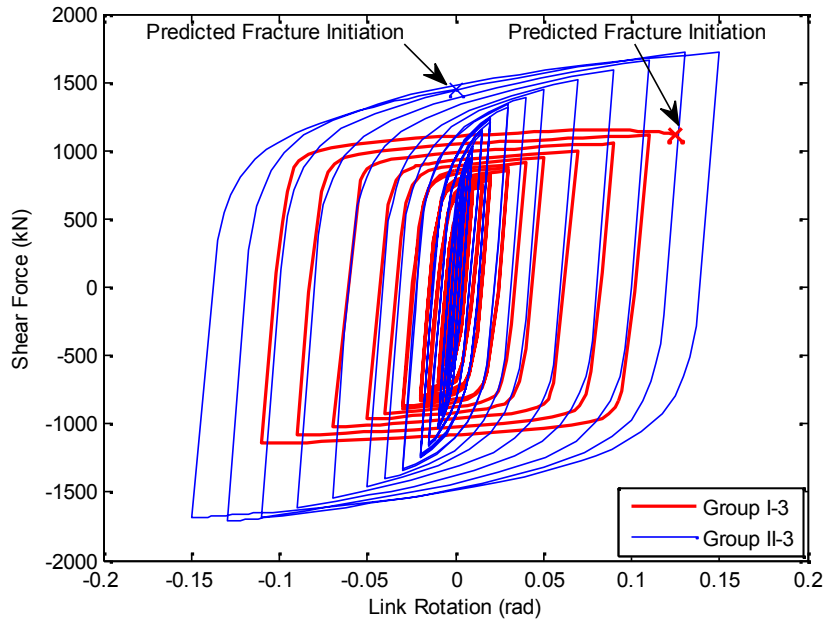
Figure 5-3 Cyclic loading protocol prescribed by AISC 2010



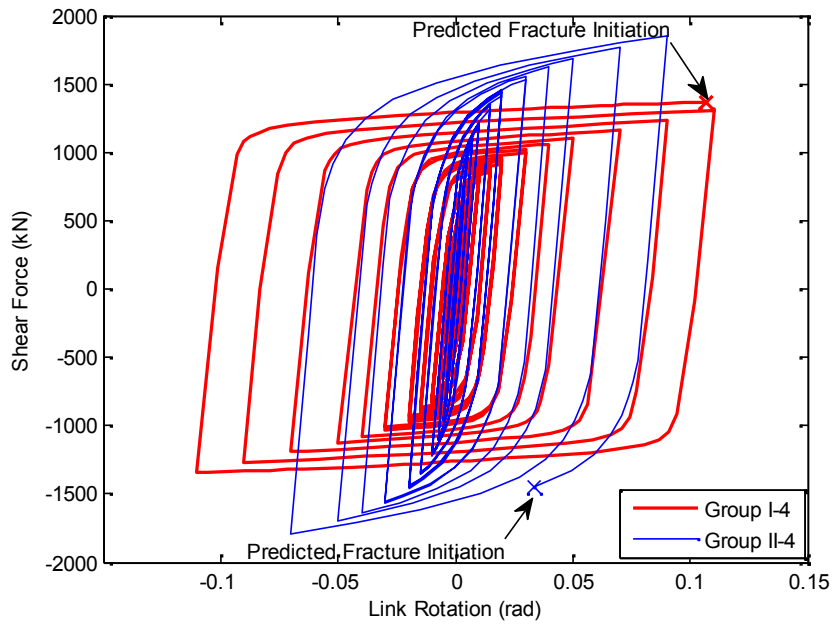
(a) W10x33 section



(b) W12x50 section



(c) W14x74 section



(d) W16x77 section

Figure 5-4 Hysteresis loops for Group I & Group II

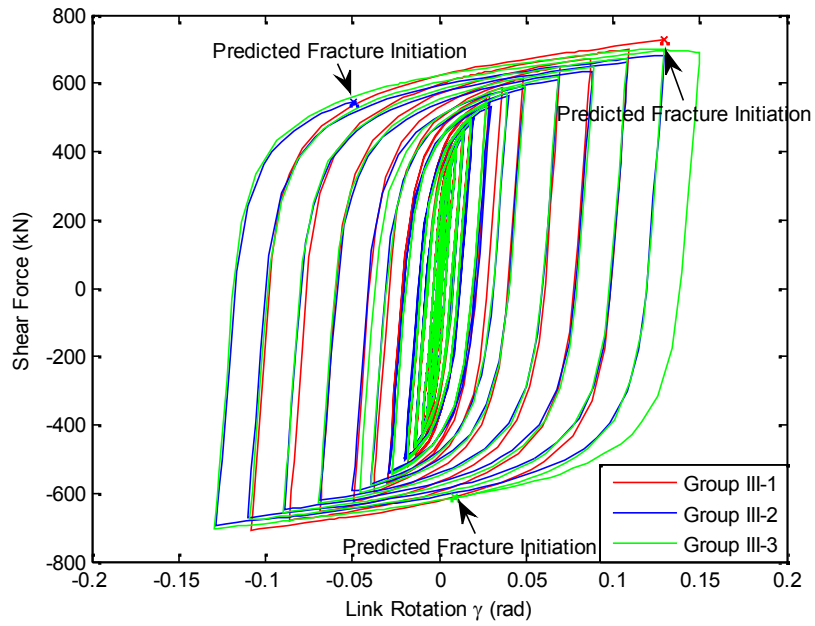


Figure 5-5 Hysteresis loops for Group III

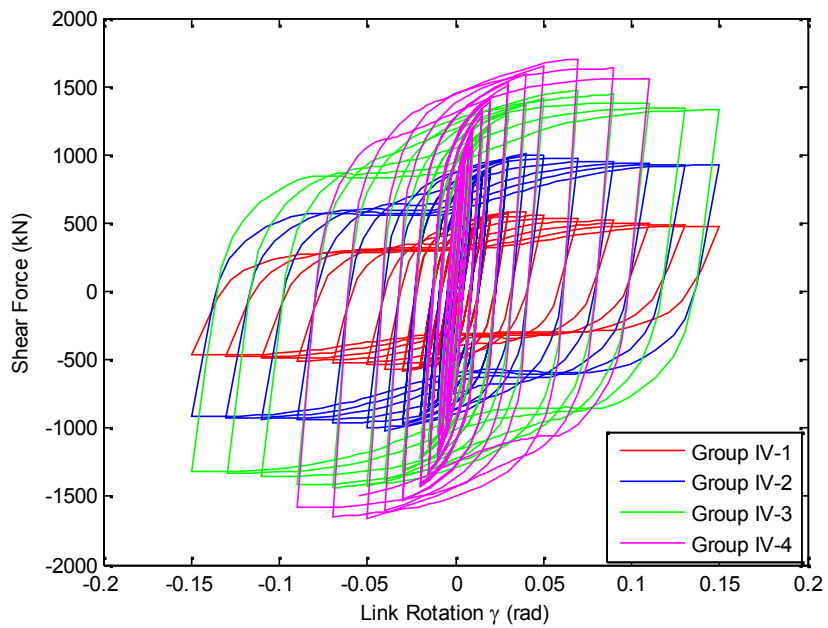


Figure 5-6 Hysteresis loops for Group IV

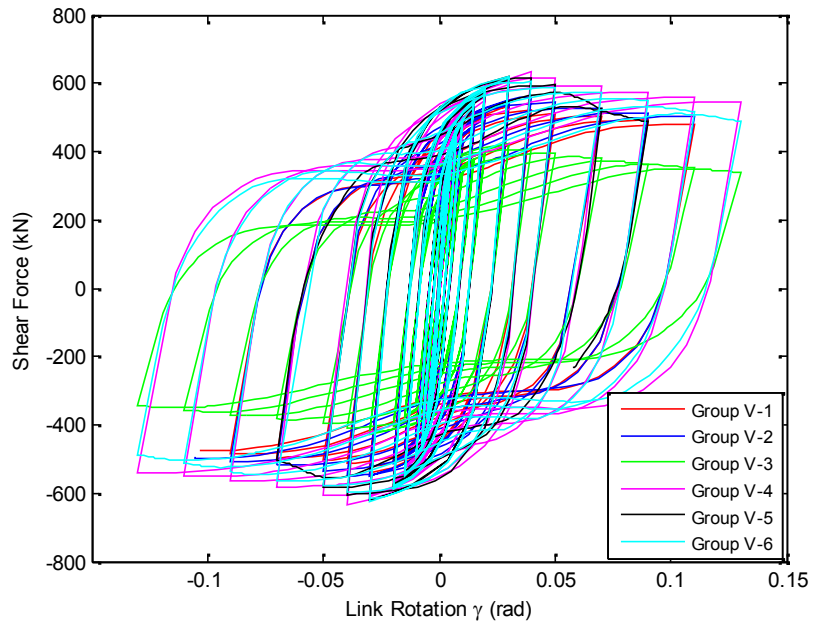
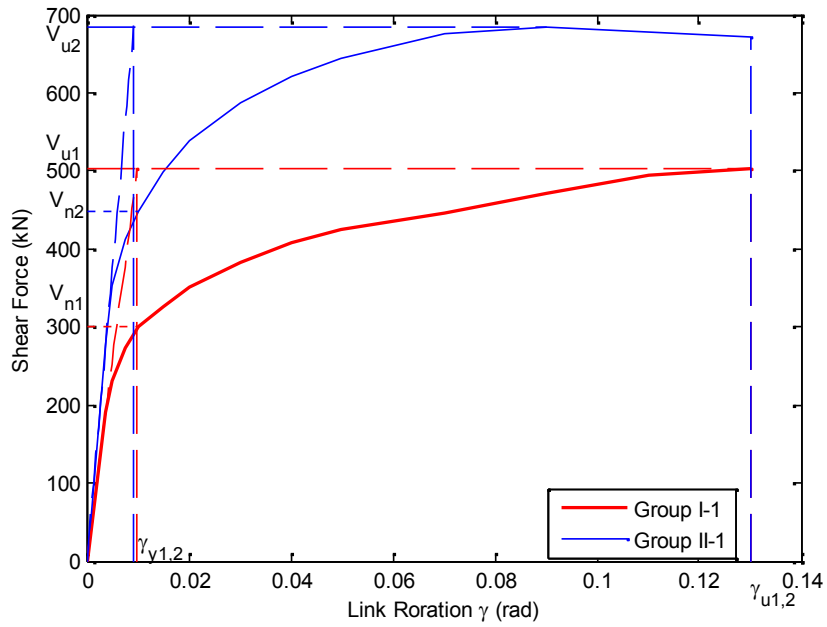
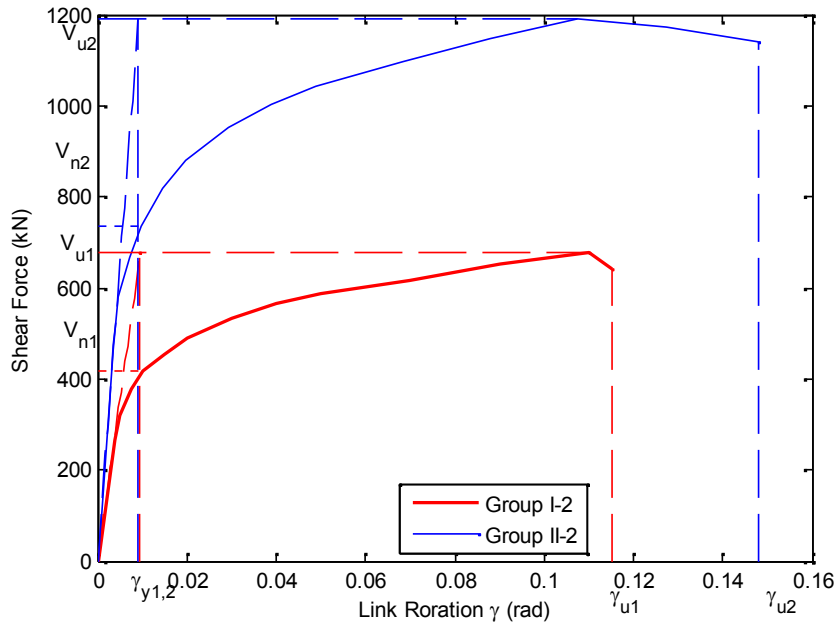


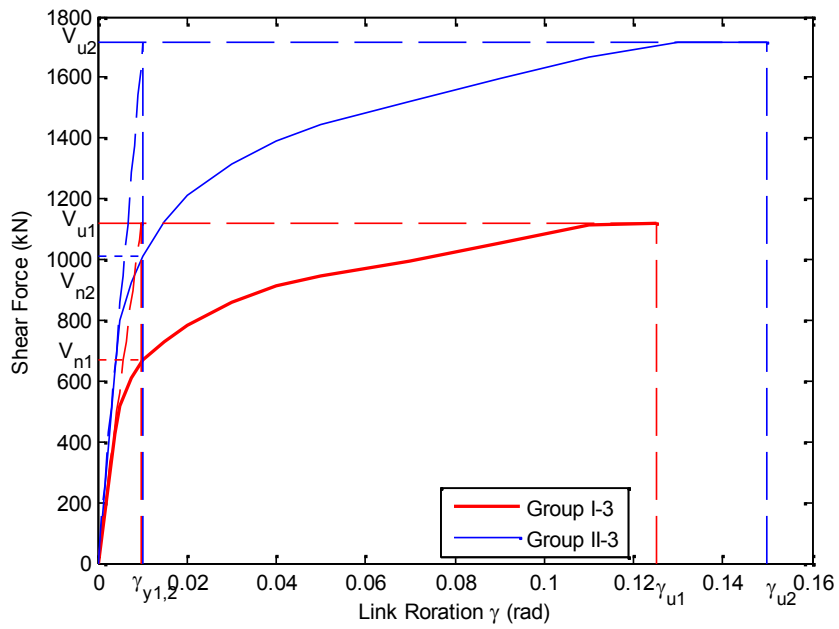
Figure 5-7 Hysteresis loops for Group V



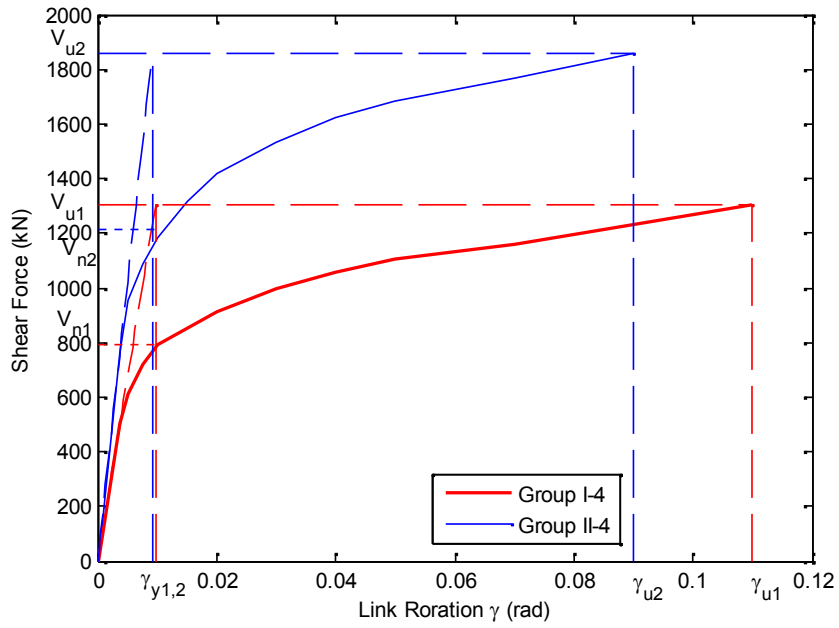
(a) W10x33 section



(b) W12x50 section

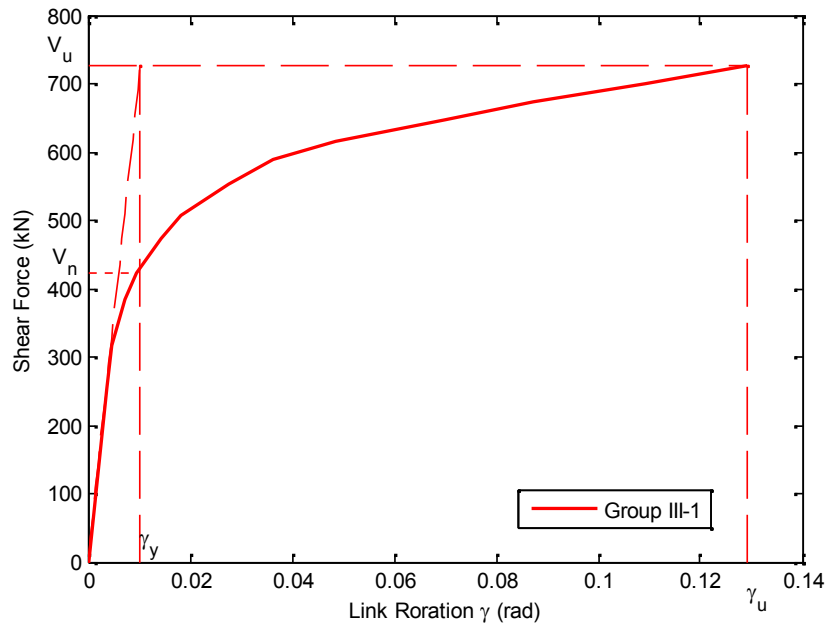


(c) W14x74 section

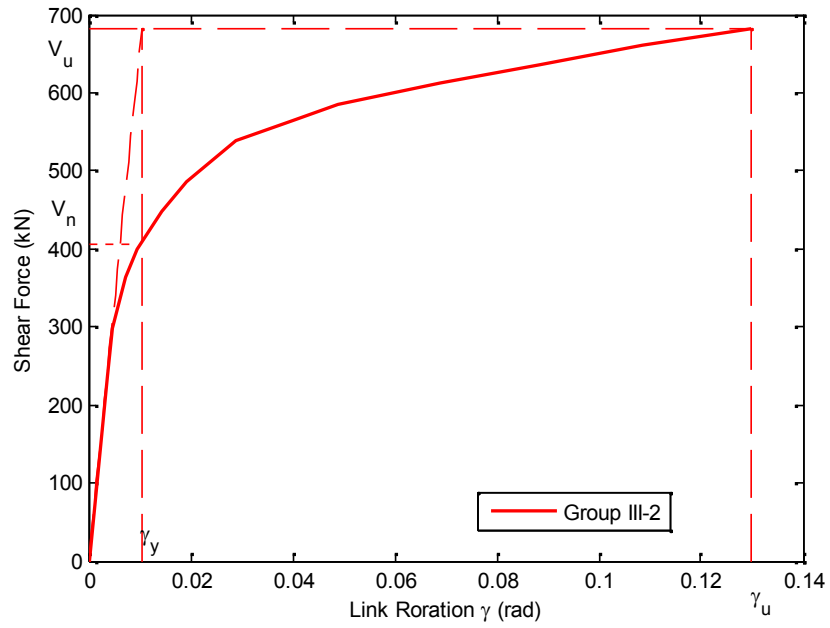


(d) W16x77 section

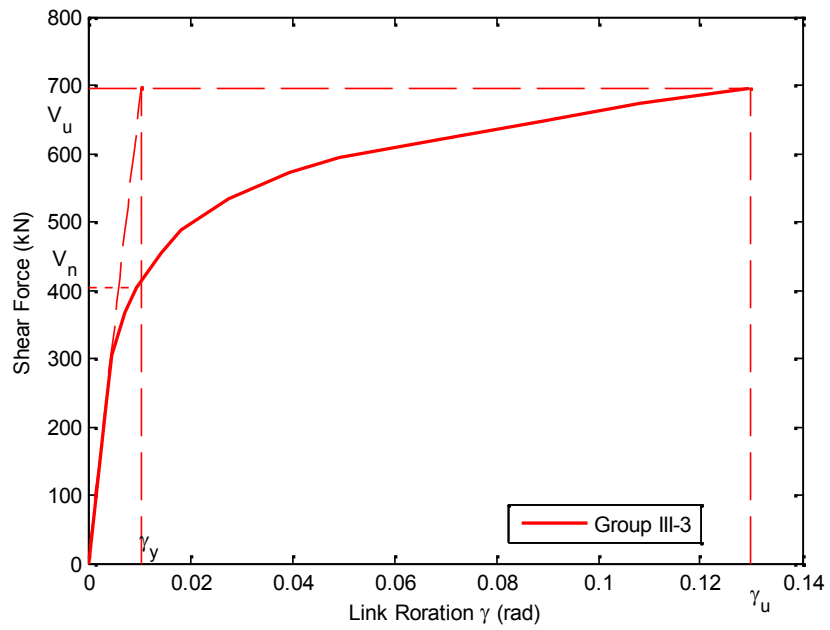
Figure 5-8 Backbone curves for Group I&II



(a)

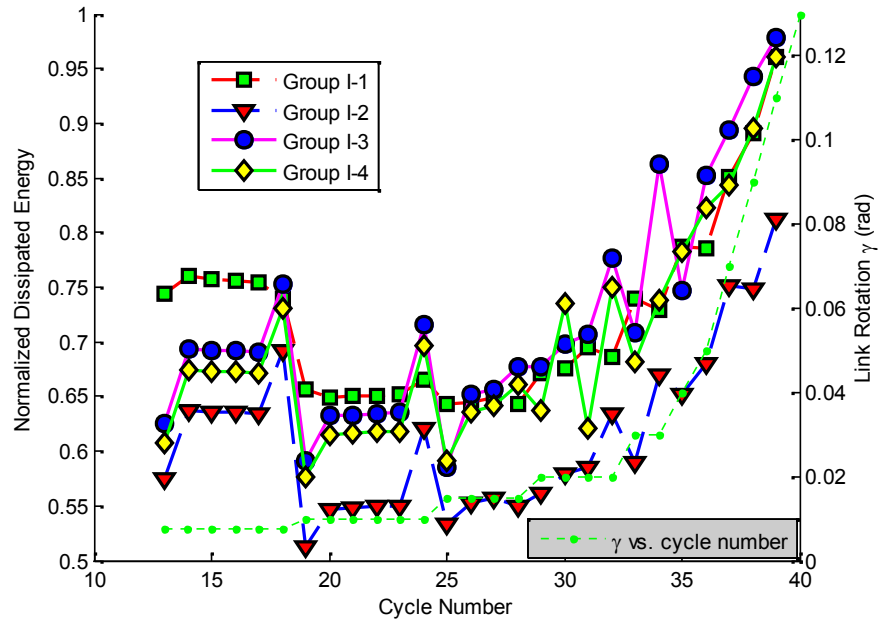


(b)

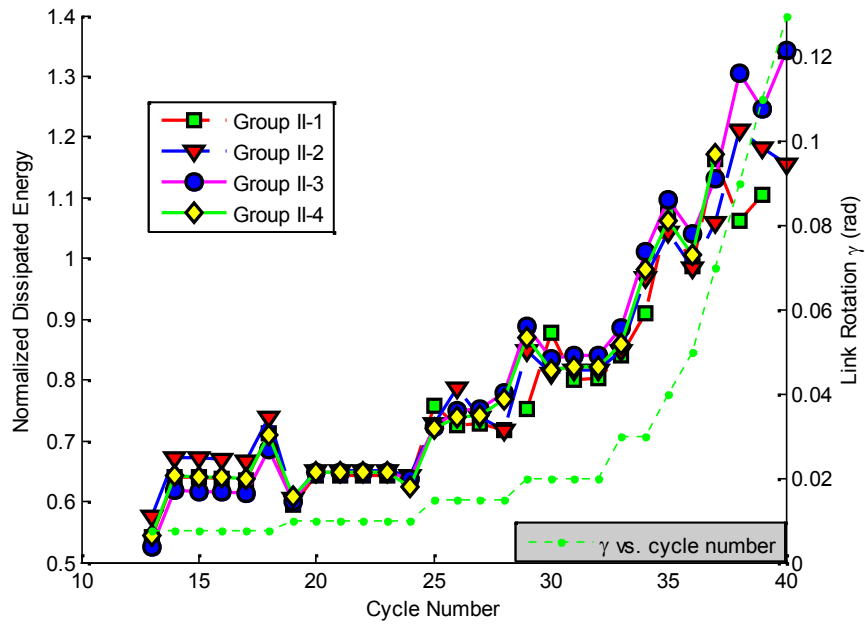


(c)

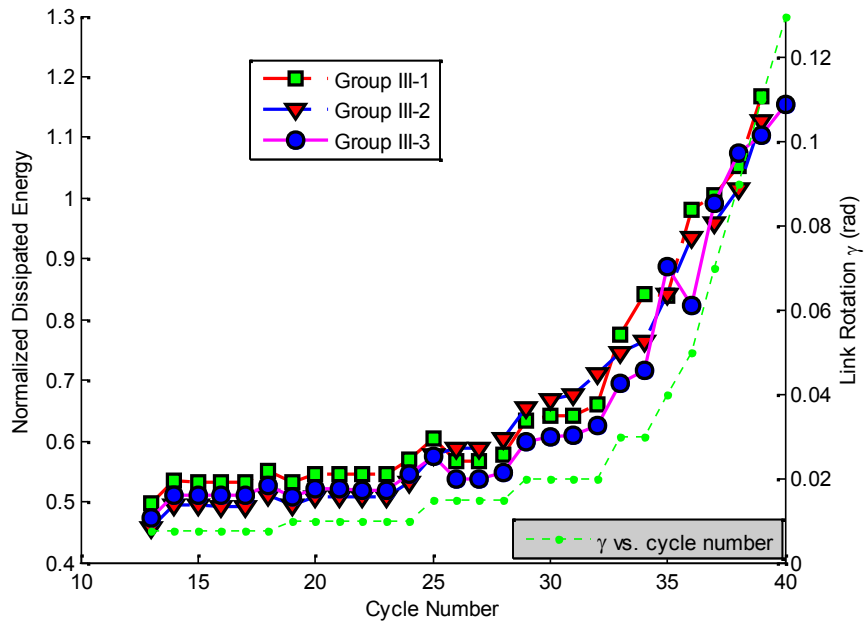
Figure 5-9 Backbone curves for Group III



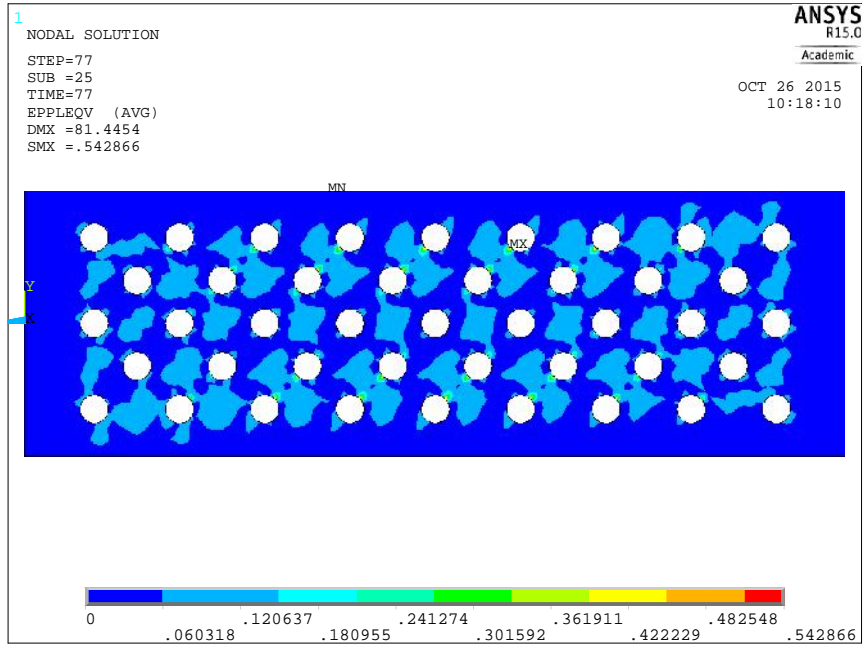
(a)



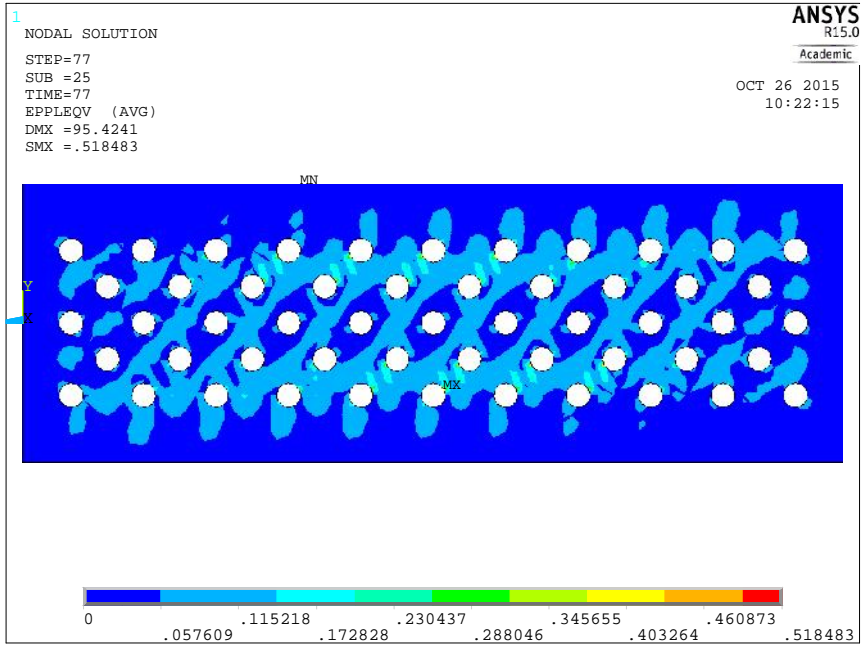
(b)



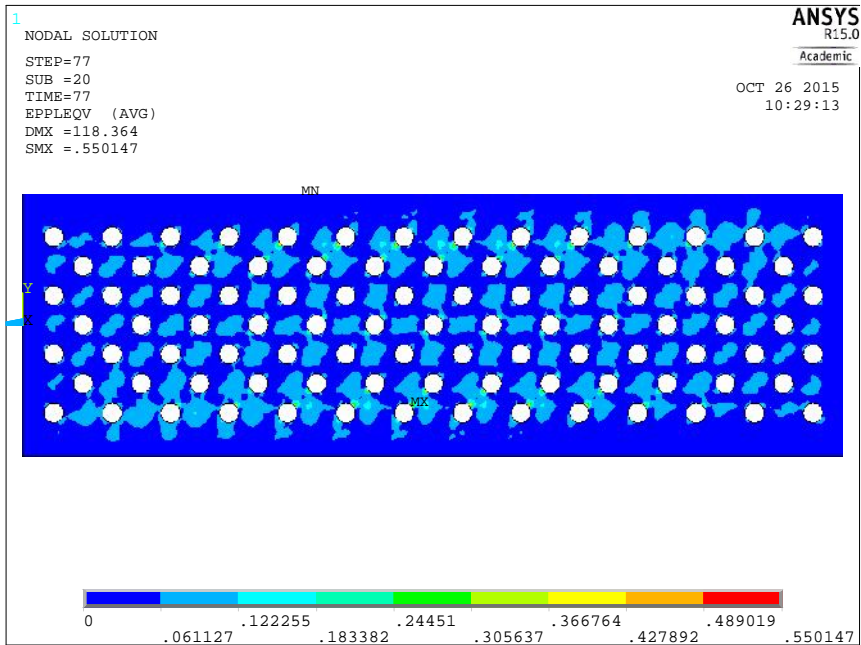
(c) **Figure 5-10** Hysteretic energy dissipation for Group I, Group II, and Group III



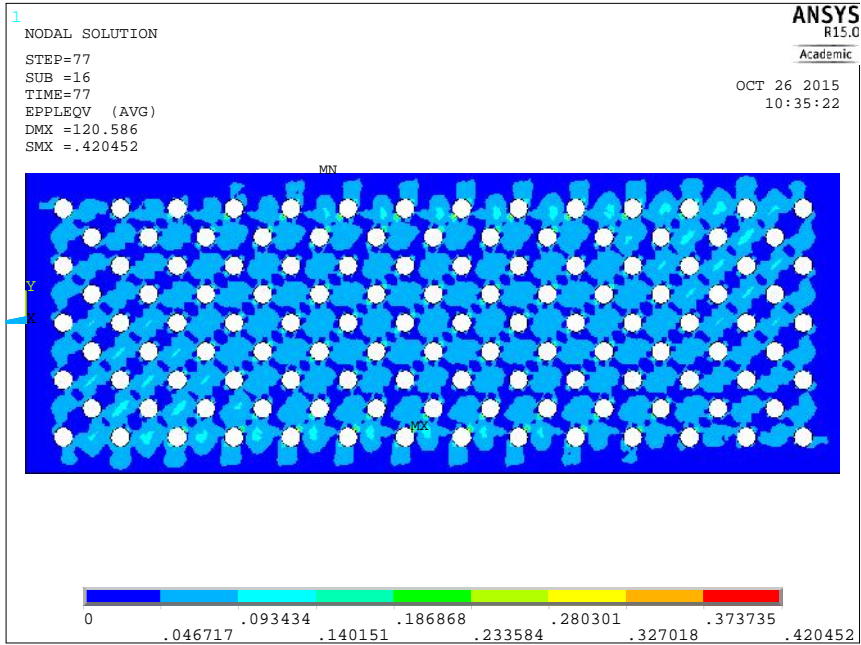
(a1) Von Mises plastic strain contour of Group I-1 at $\gamma = 0.11$ radians



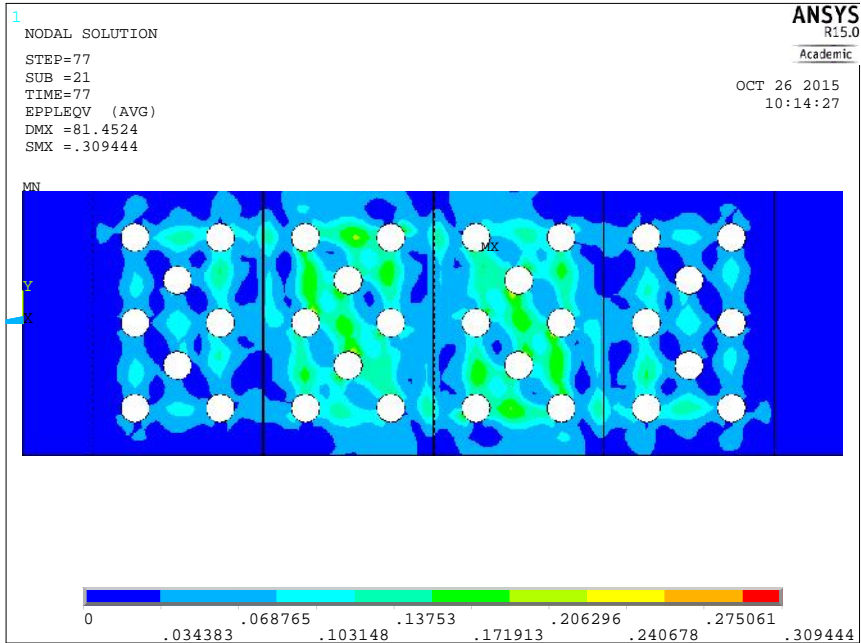
(a2) Von Mises plastic strain contour of Group I-2 at $\theta = 0.11$ radians



(a3) Von Mises plastic strain contour of Group I-3 at $\theta = 0.11$ radians



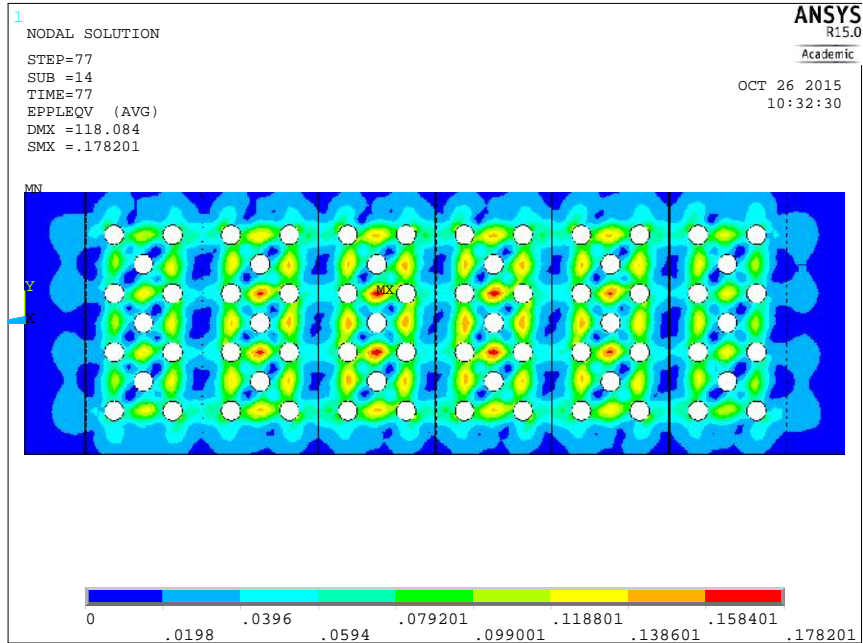
(a4) Von Mises plastic strain contour of Group I-4 at $\theta = 0.11$ radians



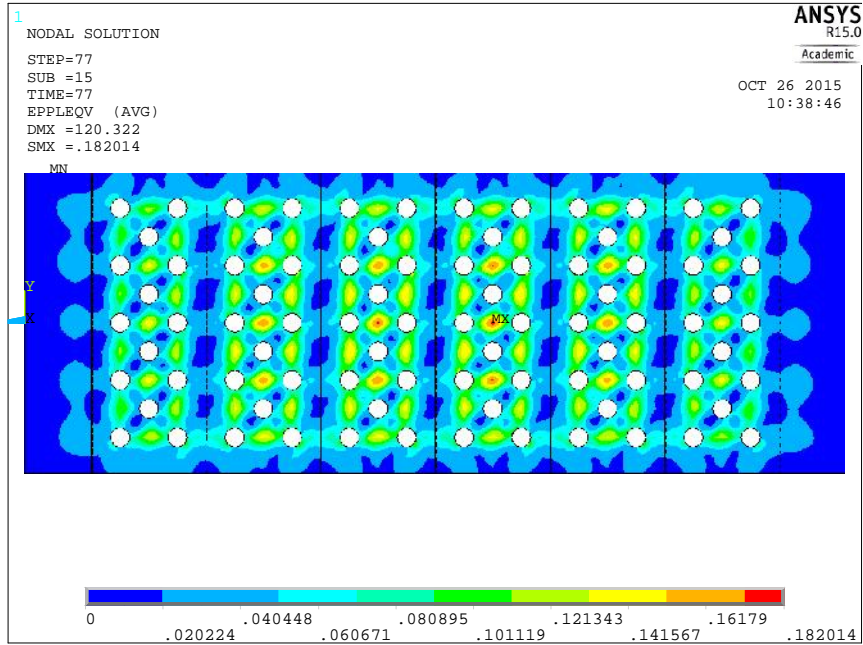
(b1) Von Mises plastic strain contour of Group II-1 at $\theta = 0.11$ radians



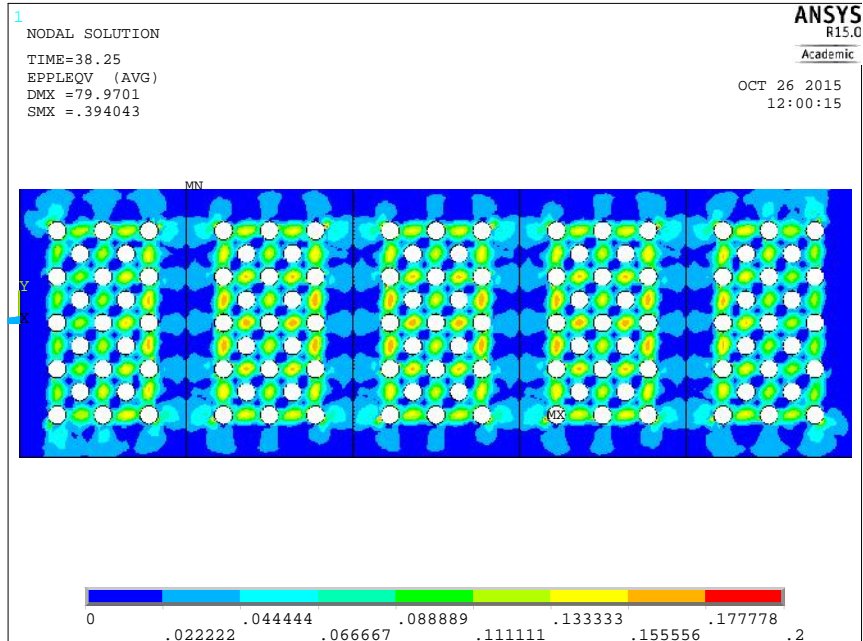
(b2) Von Mises plastic strain contour of Group II-2 at $\theta = 0.11$ radians



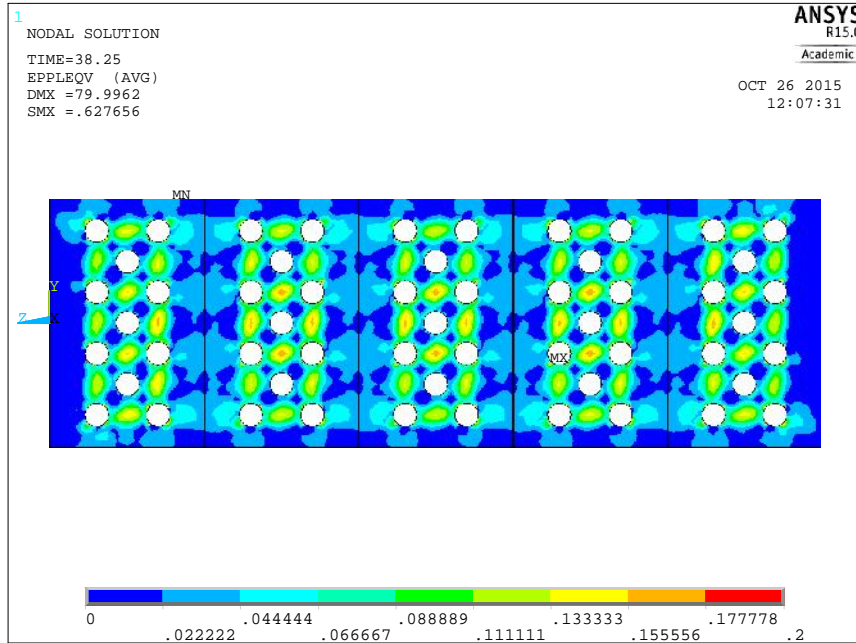
(b3) Von Mises plastic strain contour of Group II-3 at $\theta = 0.11$ radians



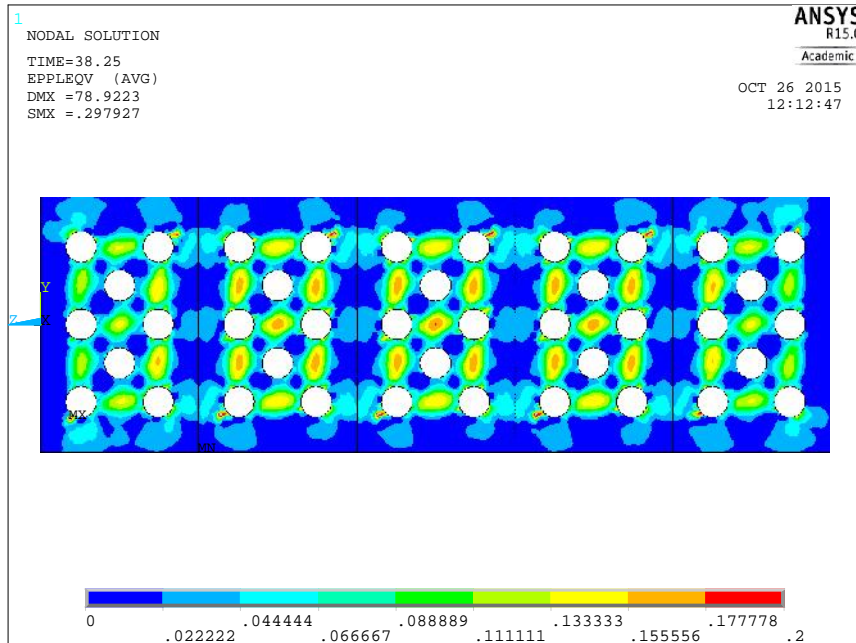
(b4) Von Mises plastic strain contour of Group II-4 at $\theta = 0.11$ radians



(c1) Von Mises plastic strain contour of Group III-1 at $\theta = 0.11$ radians

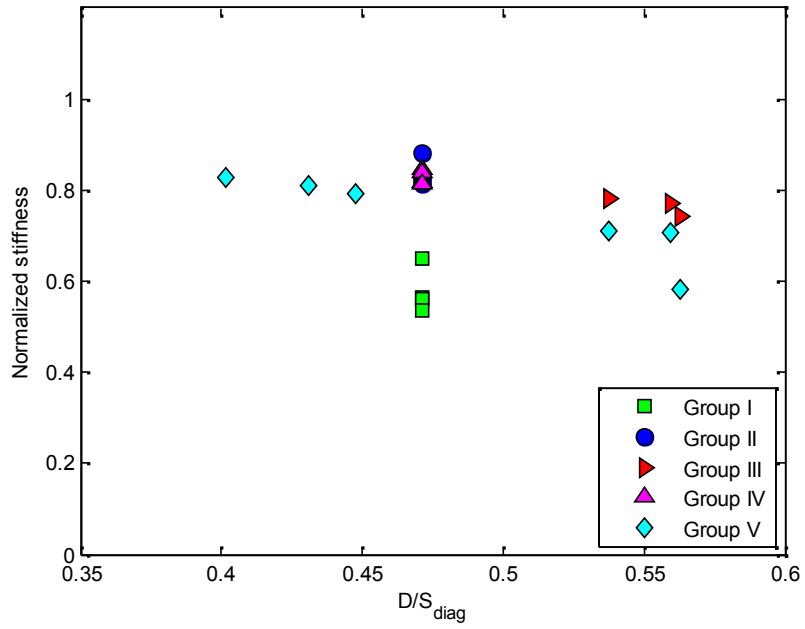


(c2) Von Mises plastic strain contour of Group III-2 at $\theta = 0.11$ radians

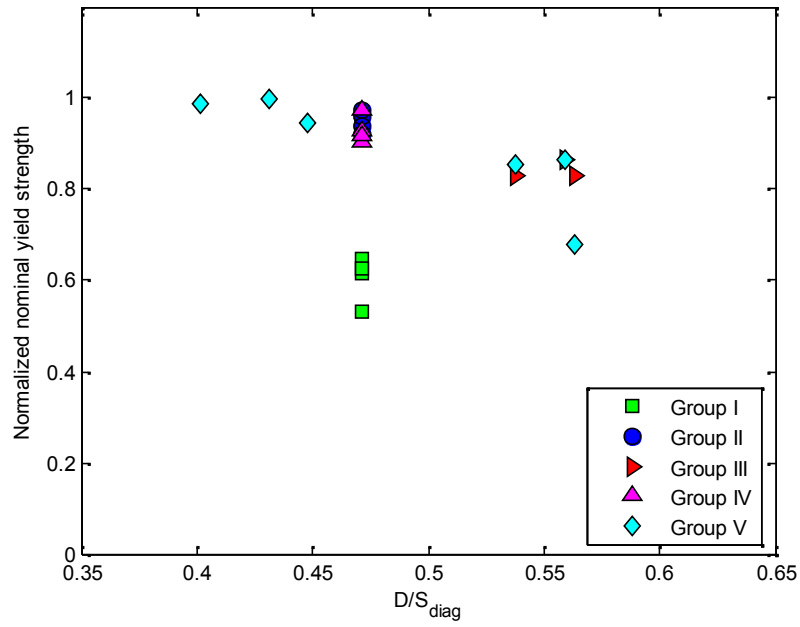


(c3) Von Mises plastic strain contour of Group III-3 at $\theta = 0.11$ radians

Figure 5-11 Von Mises plastic strain contours of stainless steel links with circular holes at $\theta = 0.11$ radians

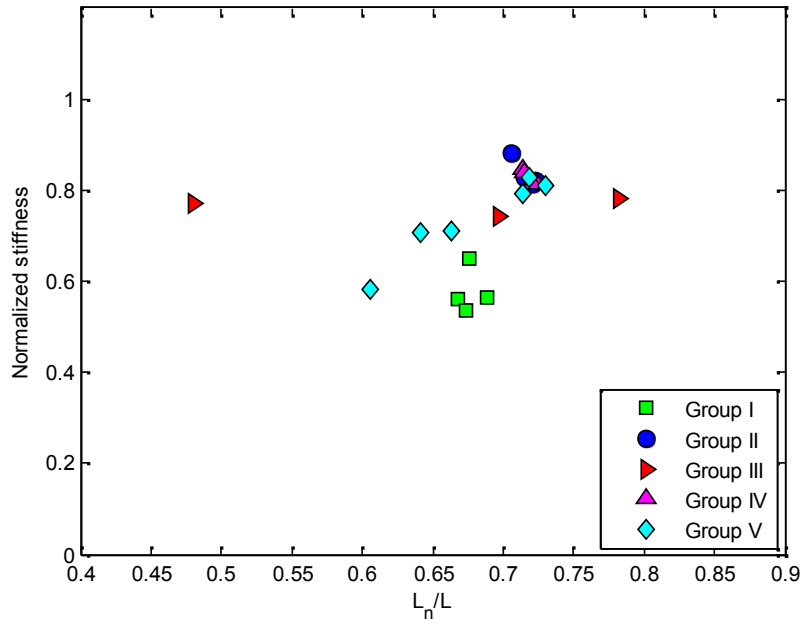


(a)

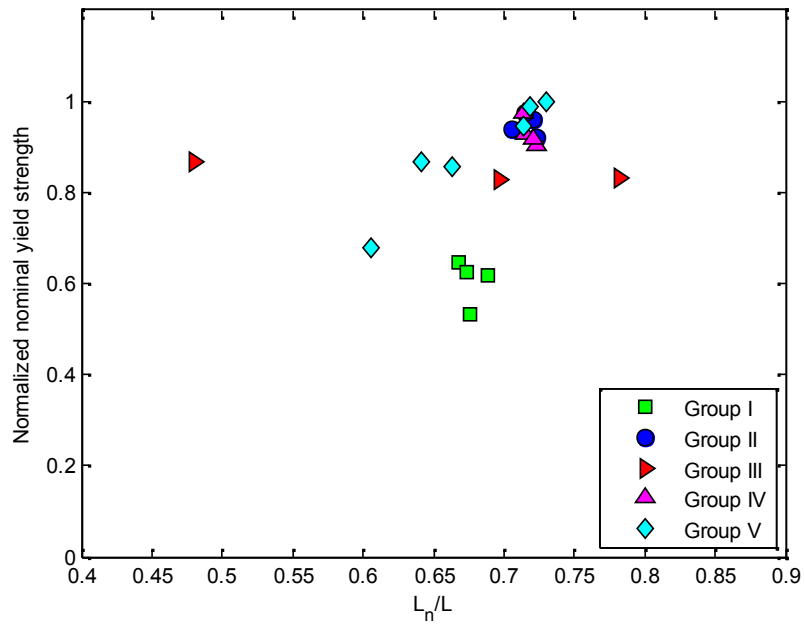


(b)

Figure 5-12 Normalized stiffness and strength values versus D/S_{diag}

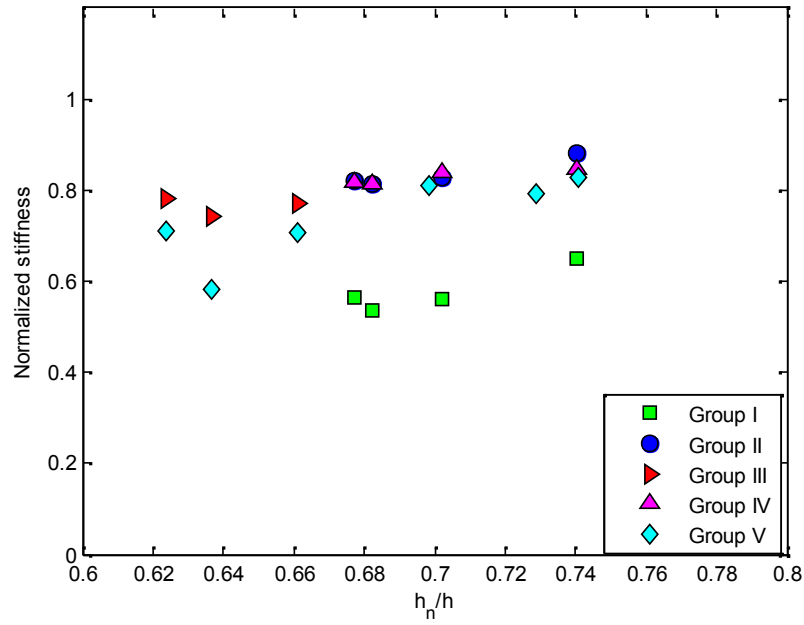


(a)

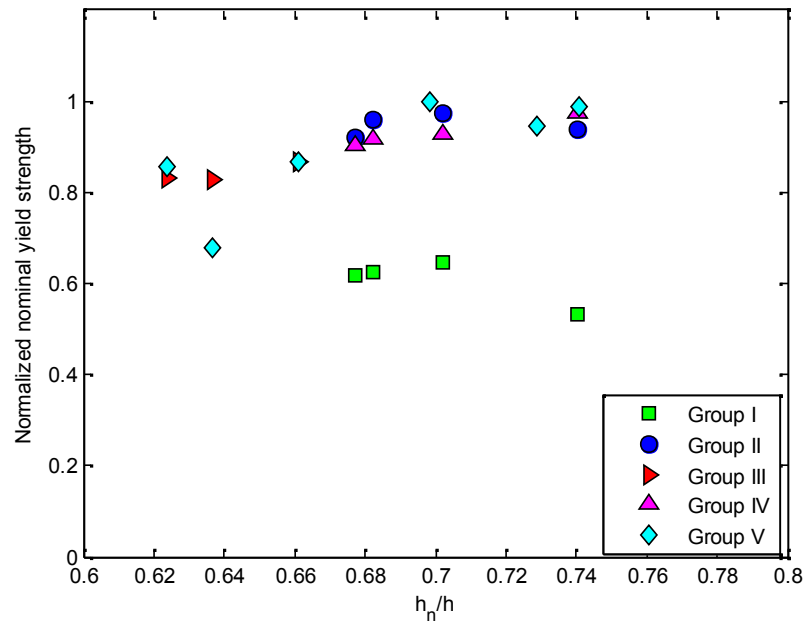


(b)

Figure 5-13 Normalized stiffness and strength values versus L_n/L

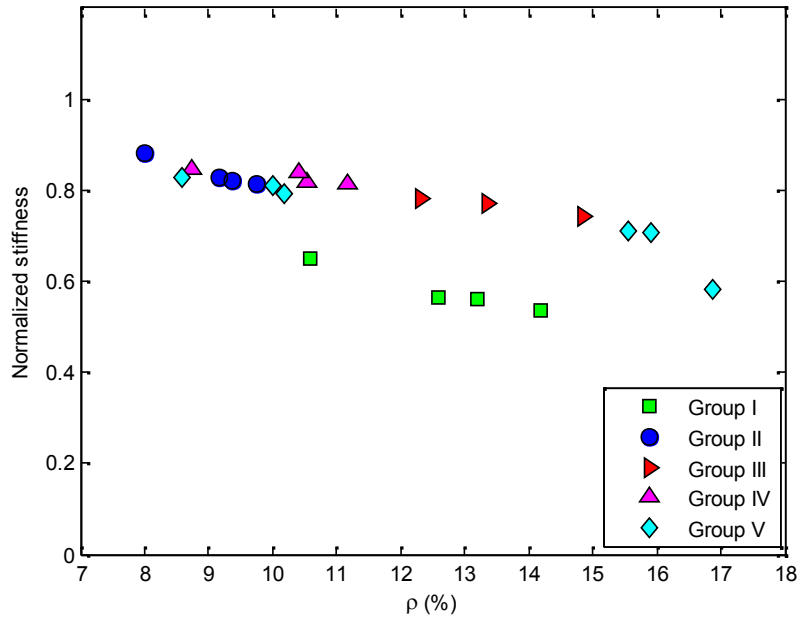


(a)

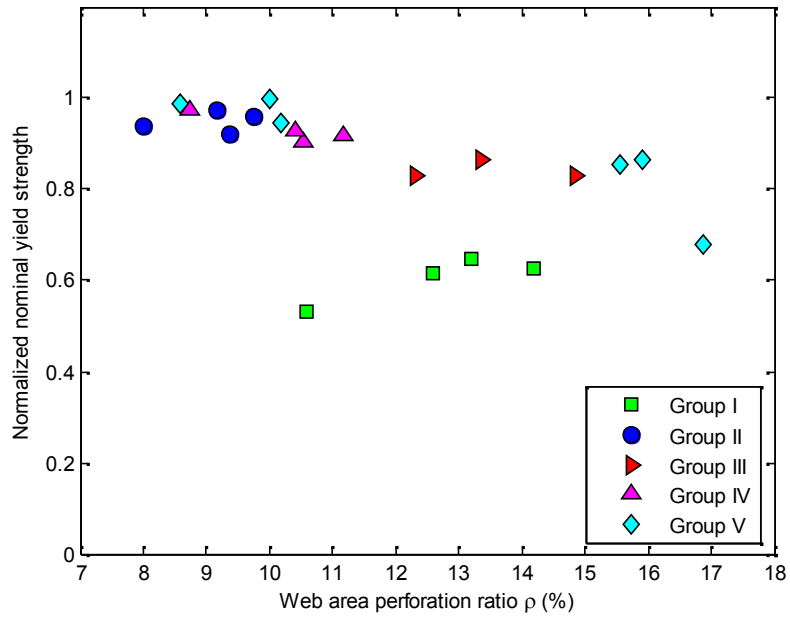


(b)

Figure 5-14 Normalized stiffness and strength values h_n/h



(a)



(b)

Figure 5-15 Normalized stiffness and strength values versus perforation ratio (%)

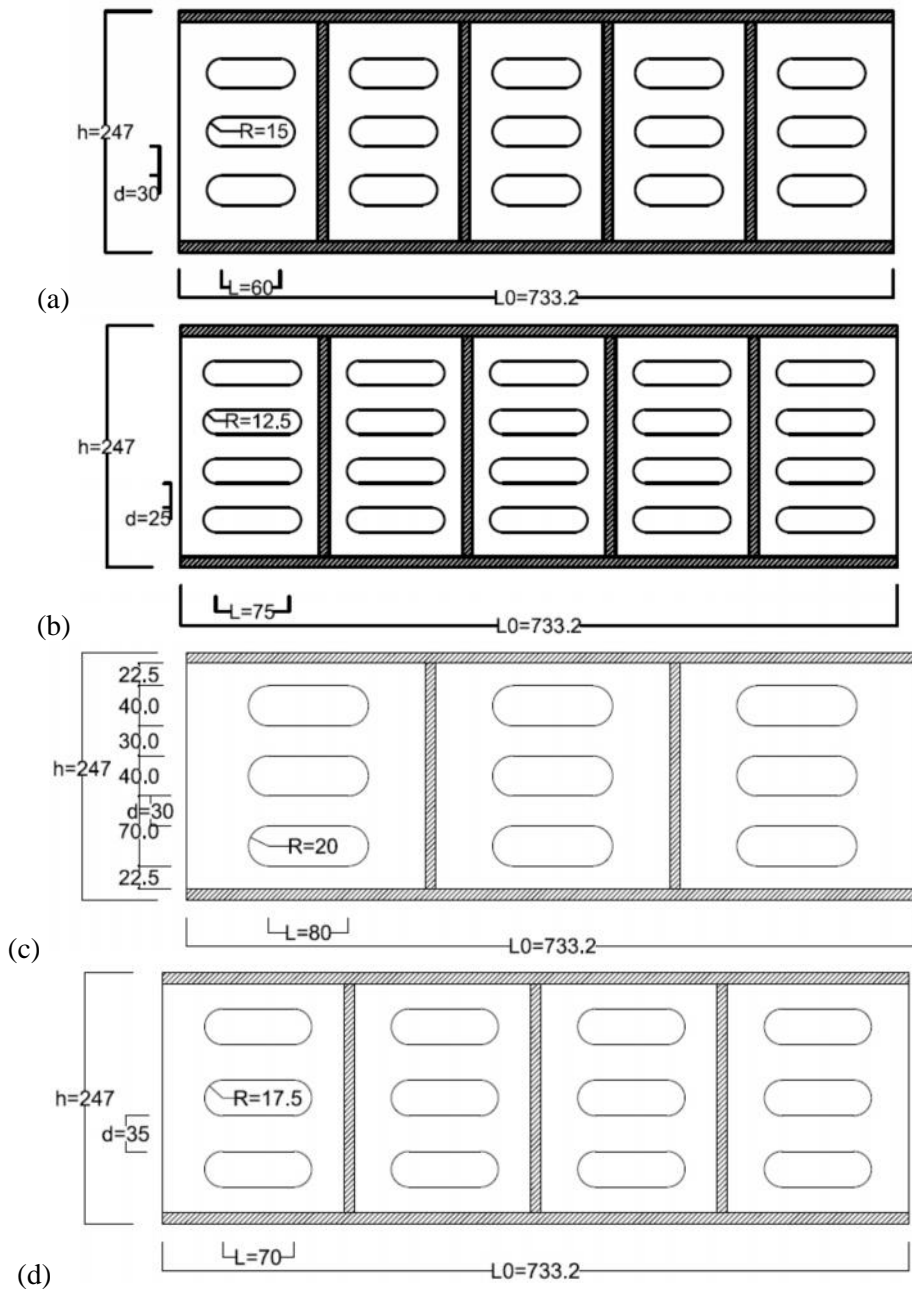


Figure 5-16 Section Sketches for the Perforated Links (Case 1 to Case 4)

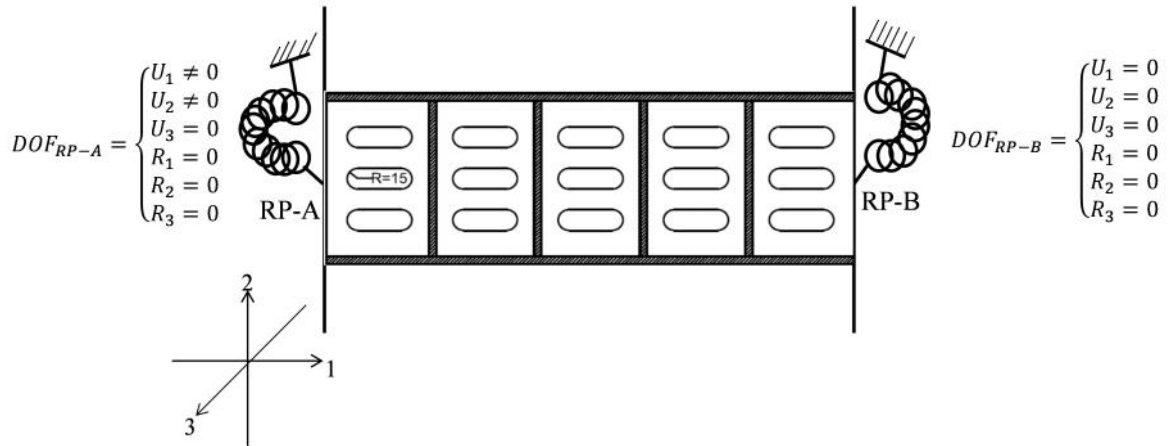
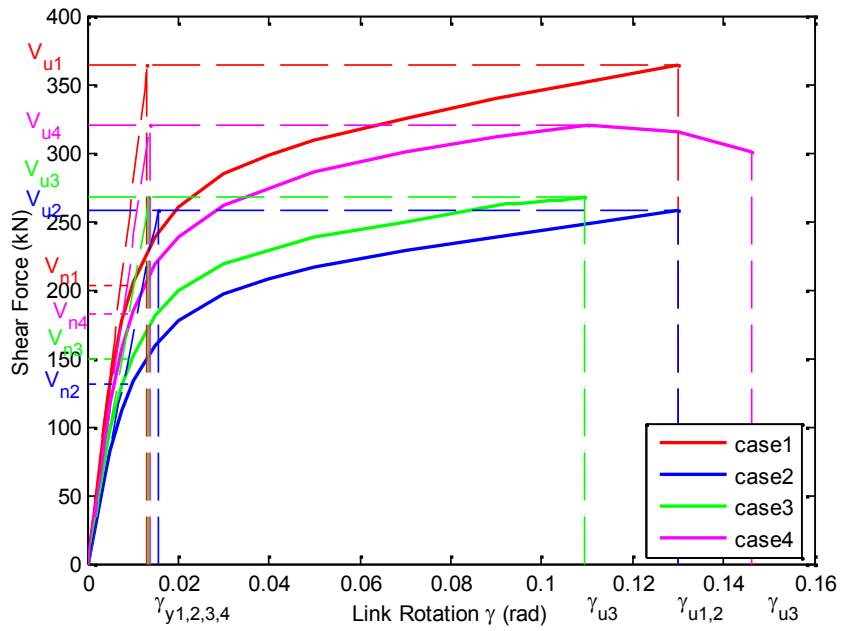
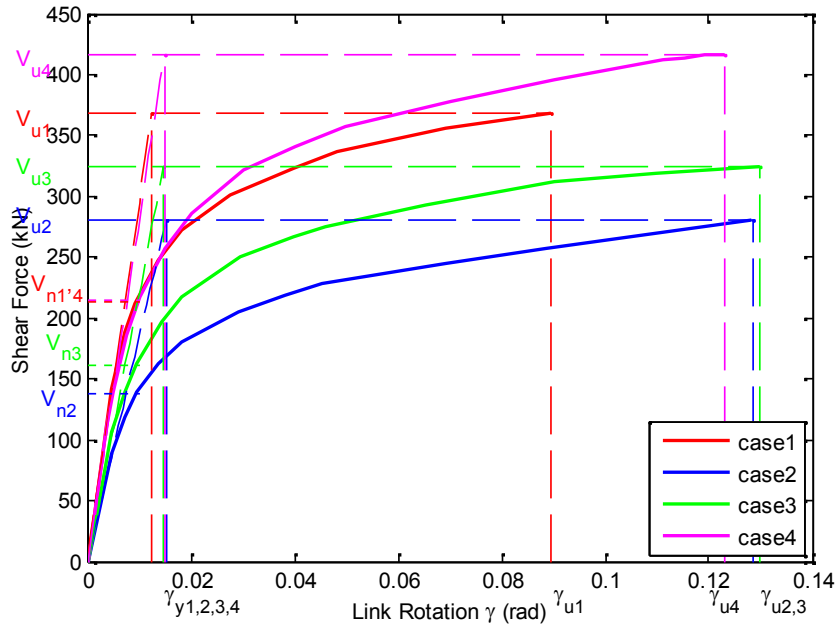


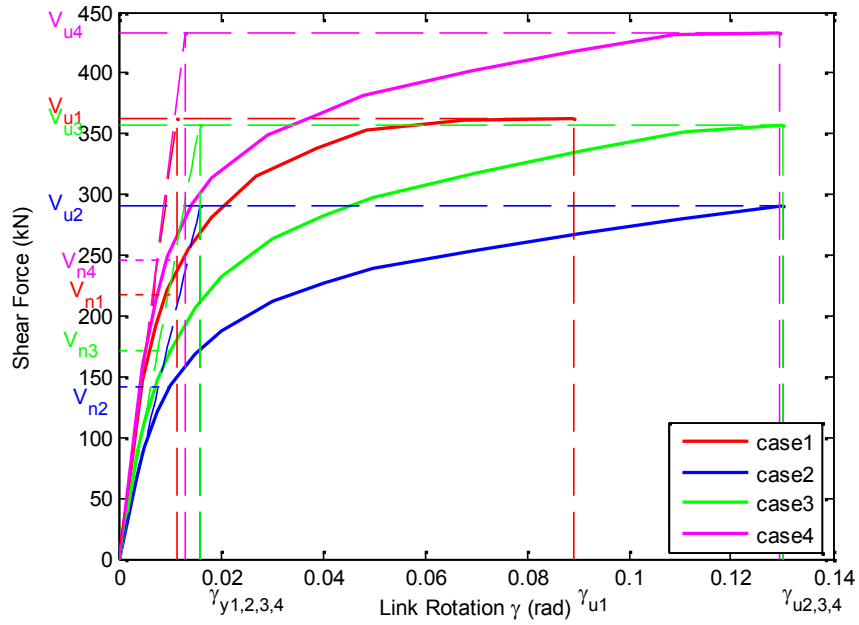
Figure 5-17 Boundary Restraints Applied to Each Perforated Link under Transverse Shear Force



(a) 80 mm flange width case



(b) 150 mm flange width case



(c) 202 mm flange width case

Figure 5-18 Backbone curves for the perforated stainless steel links with horizontal slits

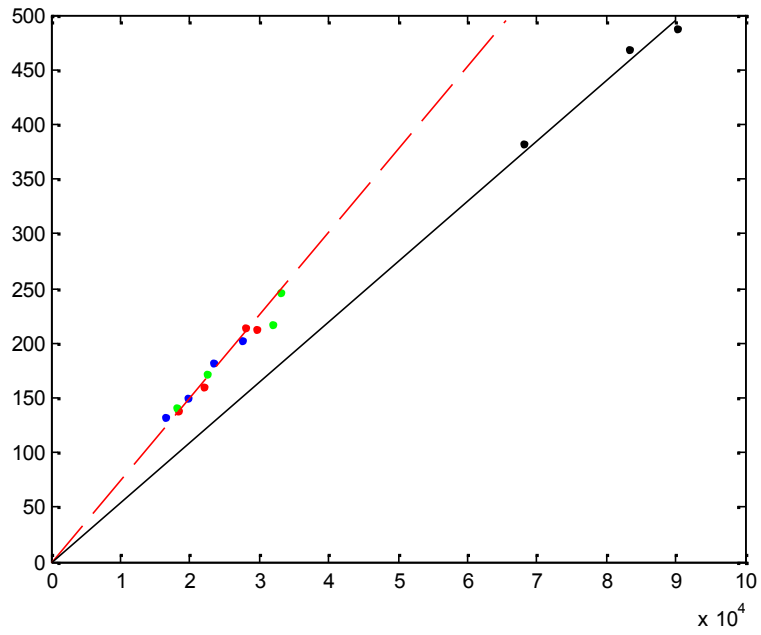
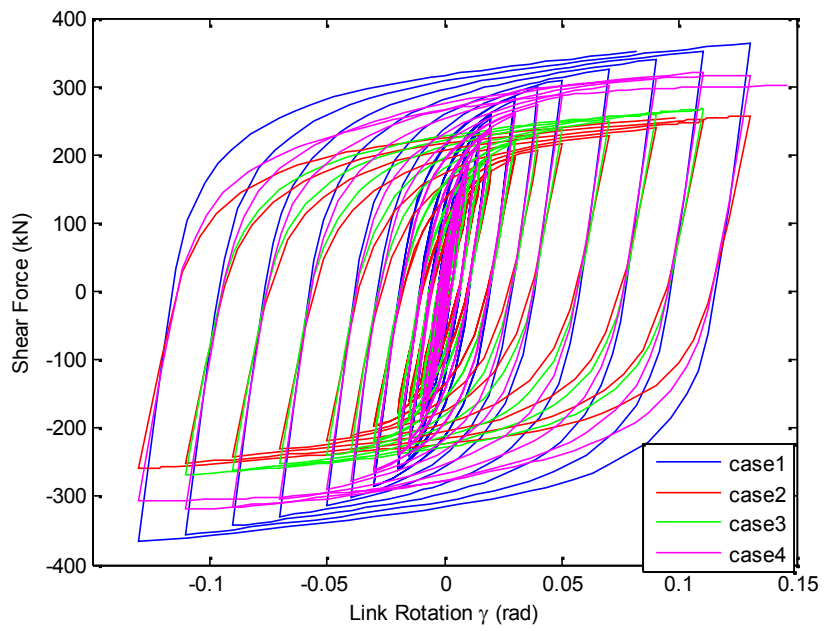
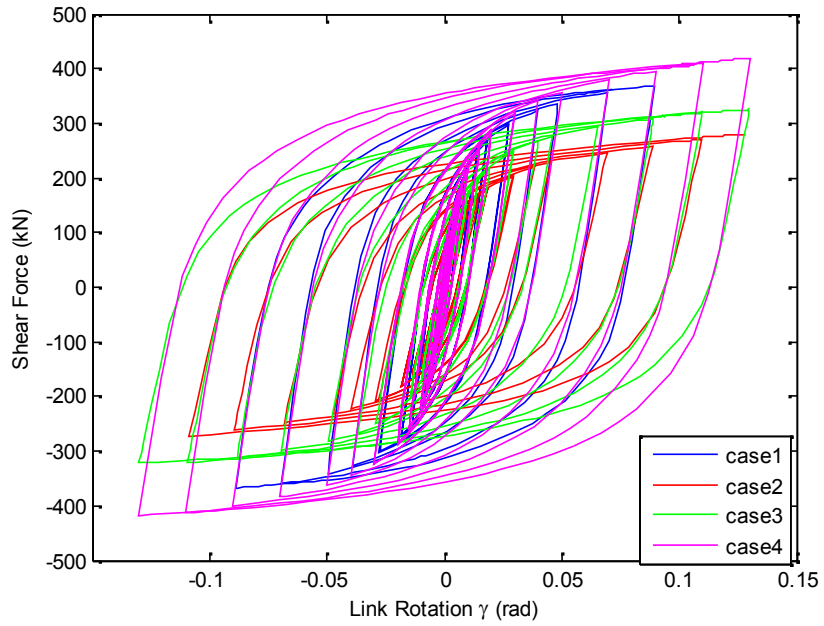


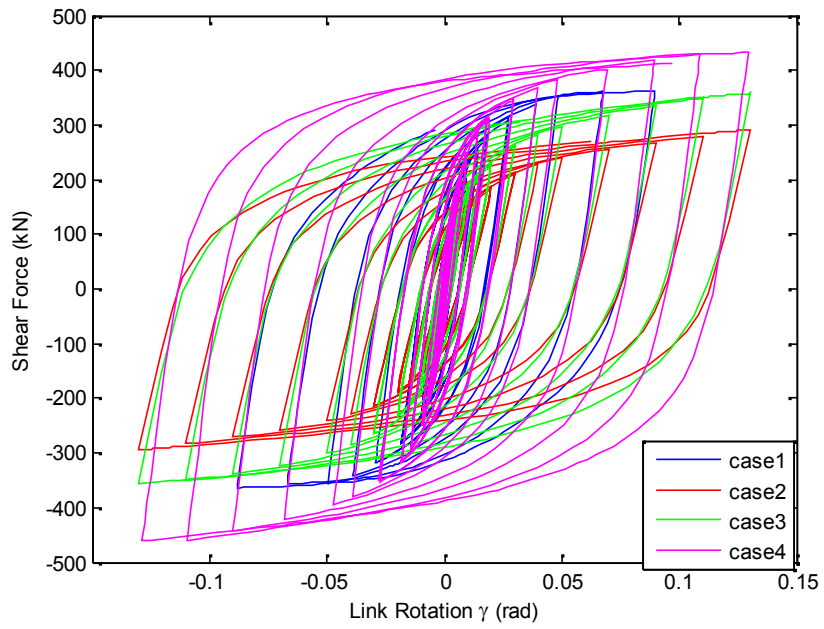
Figure 5-19 V_n vs. K_0 Relationships for the Perforated and Imperforated Links



(a) 80 mm flange width case

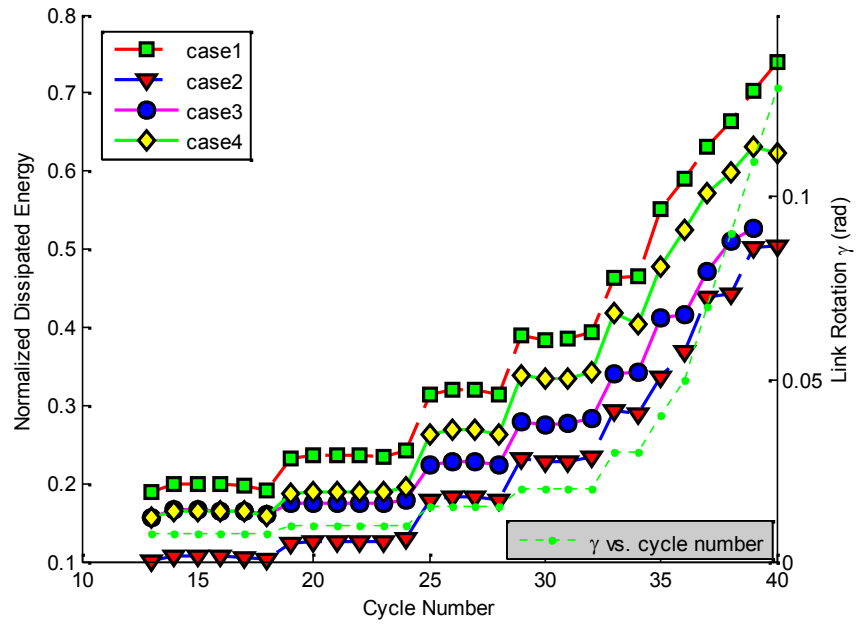


(b) 150 mm flange width case

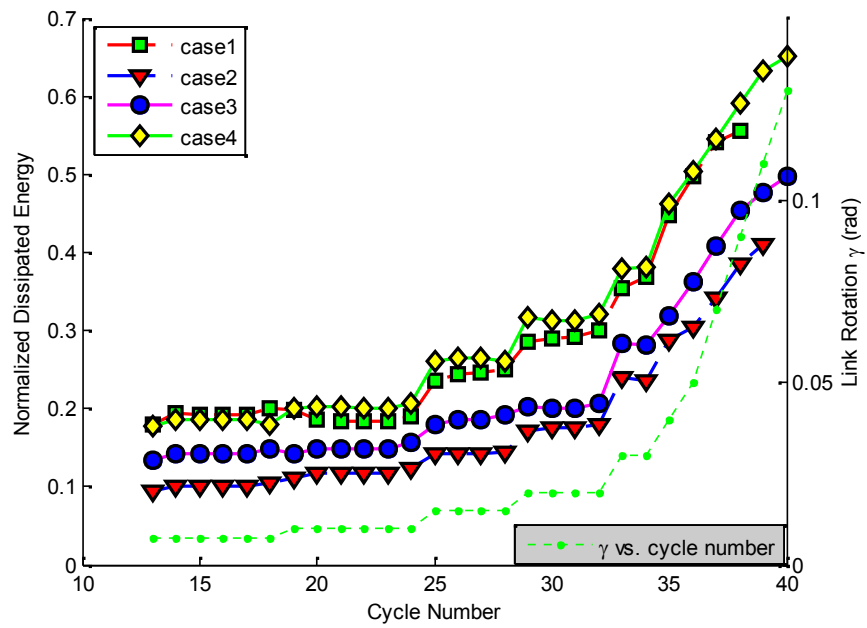


(c) 202 mm flange width case

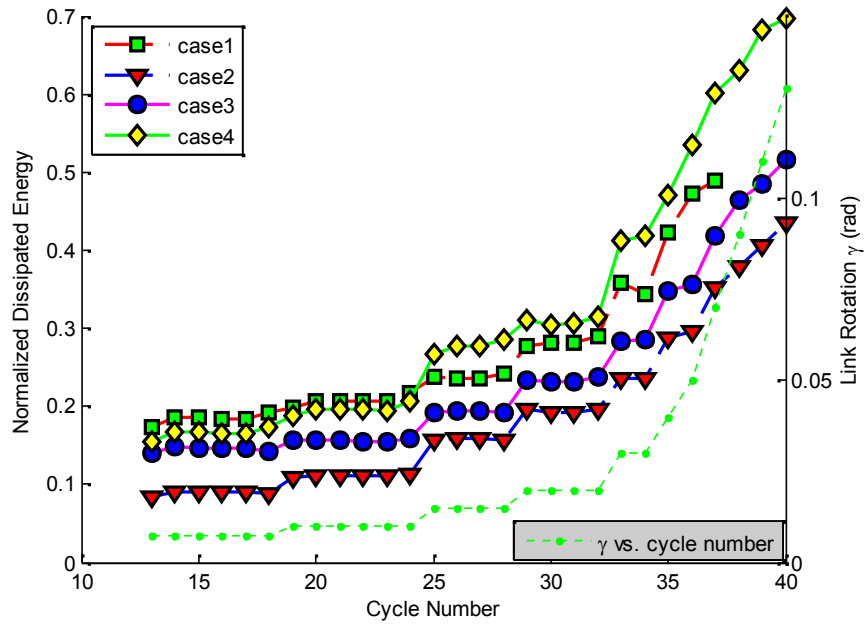
Figure 5-20 Hysteresis loops of the perforated stainless steel links with horizontal slits



(a) 80 mm flange width case

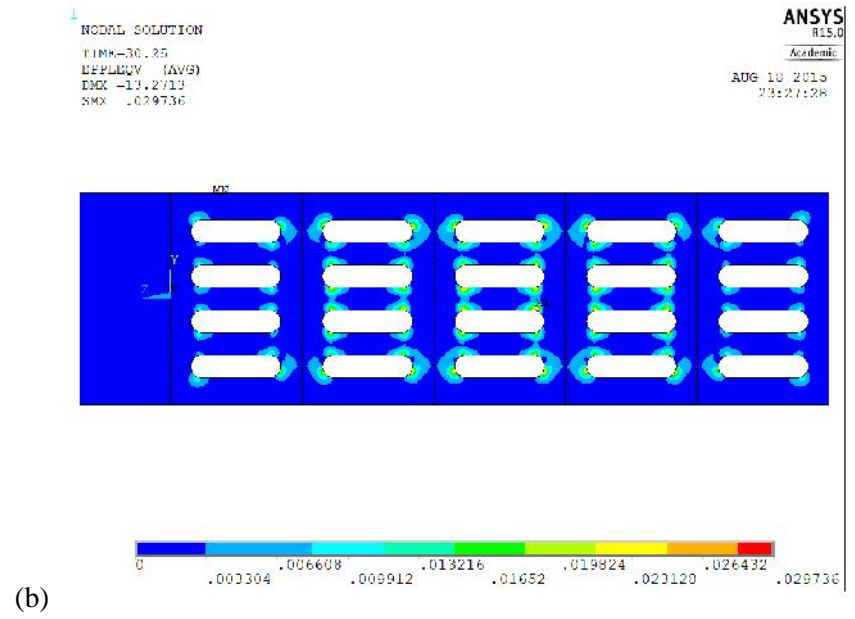
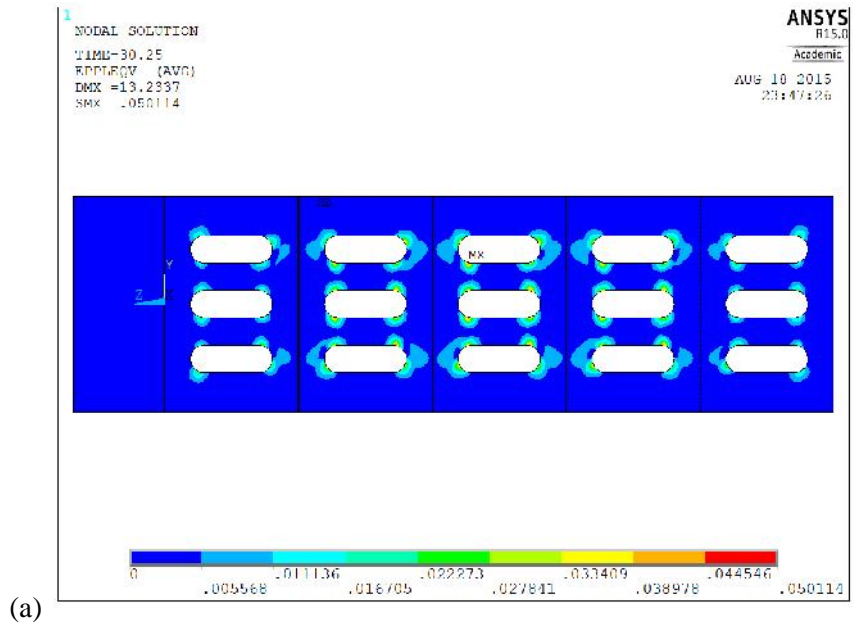


(b) 150 mm flange width case



(c) 202 mm flange width case

Figure 5-21 Hysteretic energy dissipation of the perforated stainless steel links with horizontal slits



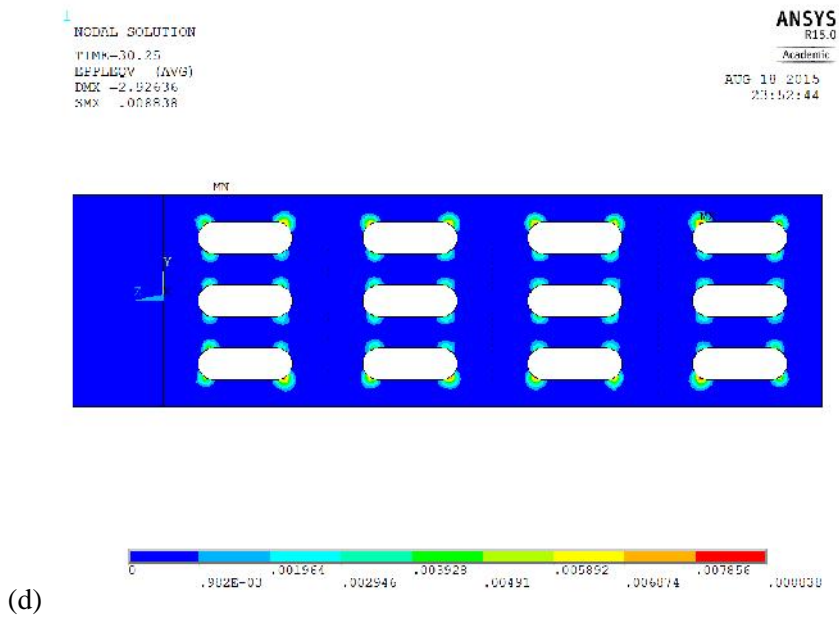
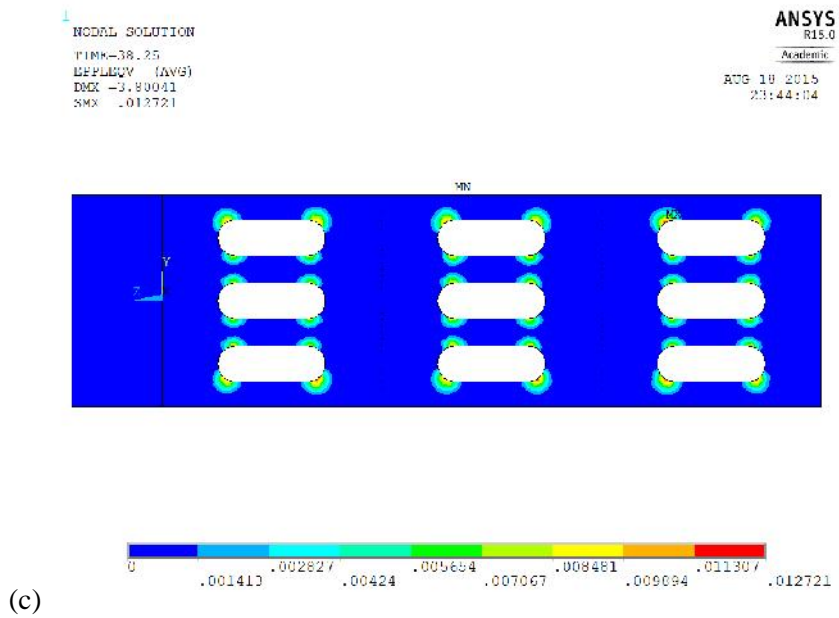
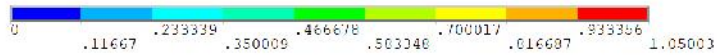
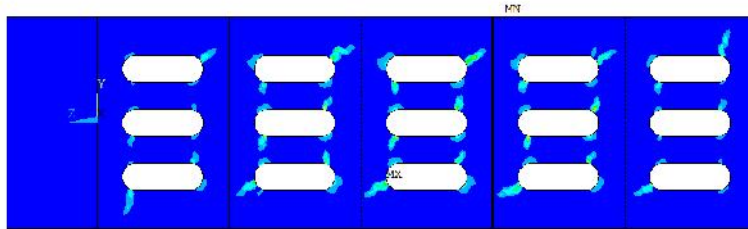


Figure 5-22 Von Mises plastic strain contour at $\theta = 0.02$ radians for perforated links in Group 3

MODAL SOLUTION
TIME=38.25
DEPLEVY (AVG)
DMX =78.6218
SMX = 1.05003

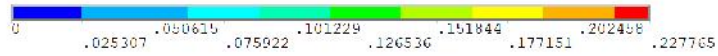
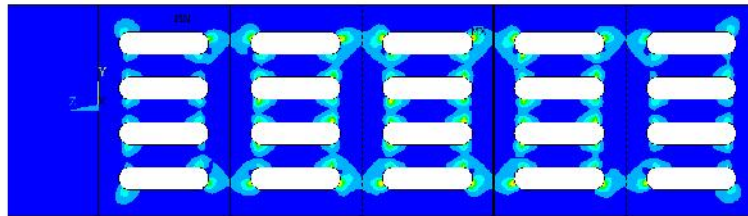
ANSYS
R15.0
Academic
R09 18 2015
23:48:23



(a)

MODAL SOLUTION
TIME=38.25
DEPLEVY (AVG)
DMX =64.7341
SMX = 1.227765

ANSYS
R15.0
Academic
R09 18 2015
23:28:47



(b)

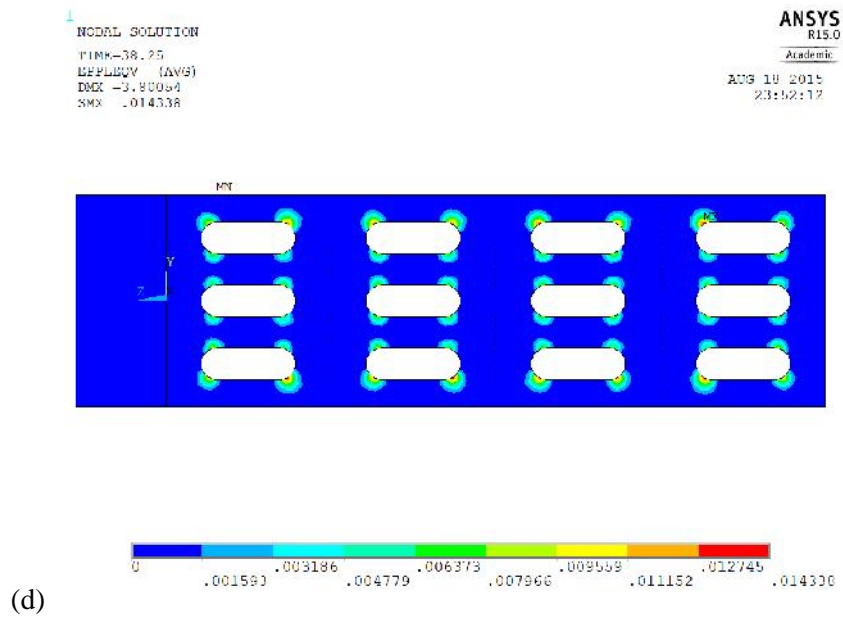
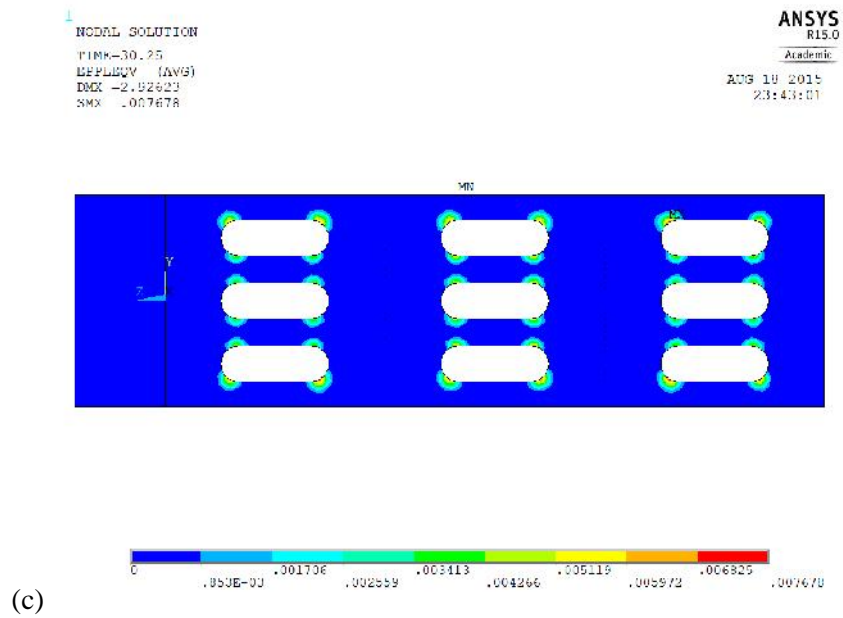


Figure 5-23 Von Mises plastic strain contour at $\theta = 0.11$ radians for perforated links in Group 3

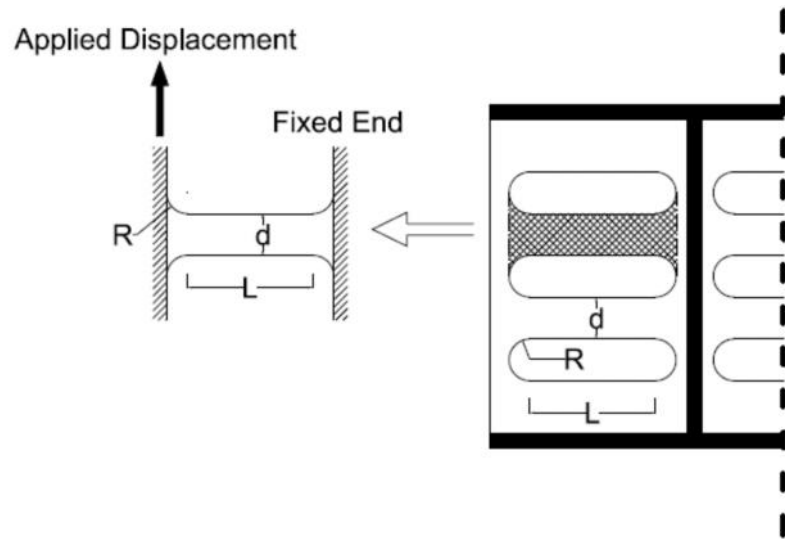


Figure 5-24 Module strip configuration

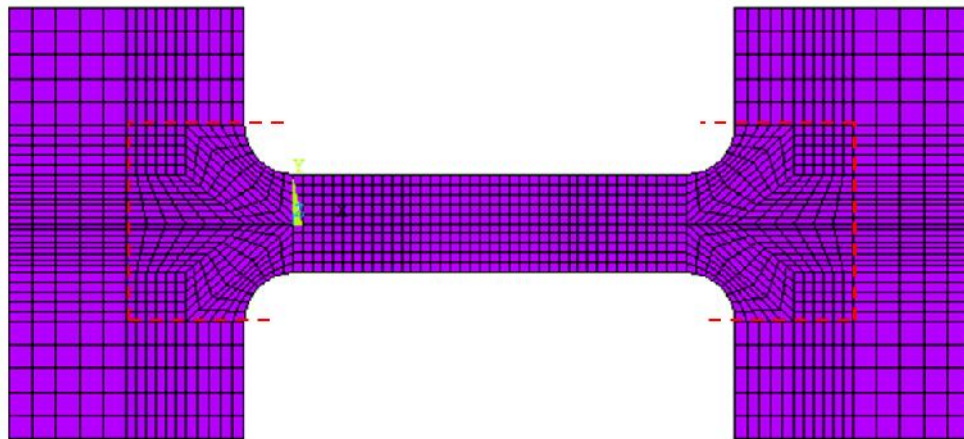


Figure 5-25 Finite element model of an investigated module case (case 2)

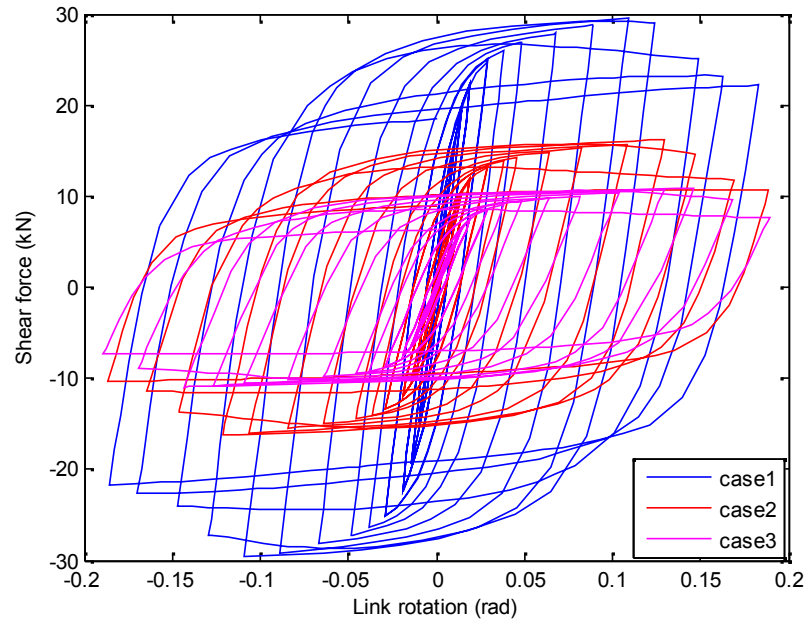


Figure 5-26 Hysteresis force displacement relationship for module cases 1 through 3

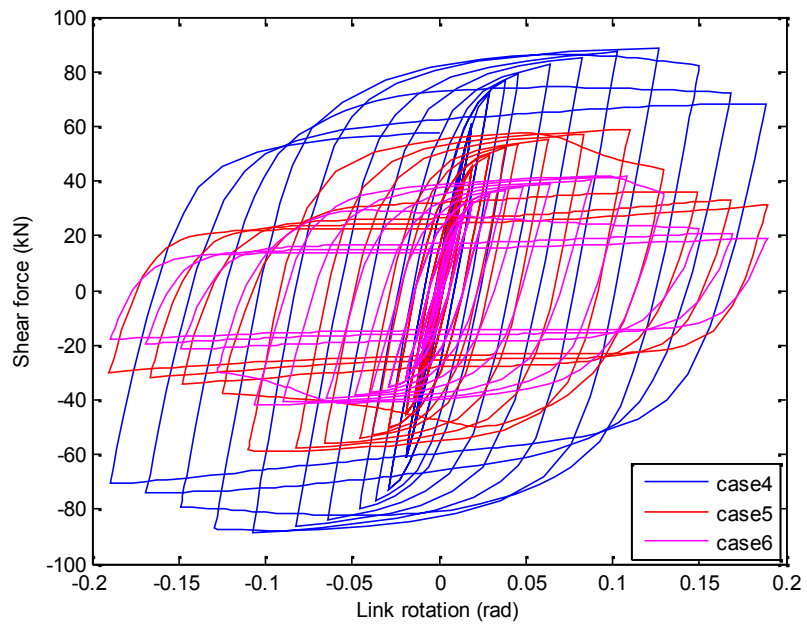


Figure 5-27 Hysteresis force displacement relationship for module cases 4 through 6

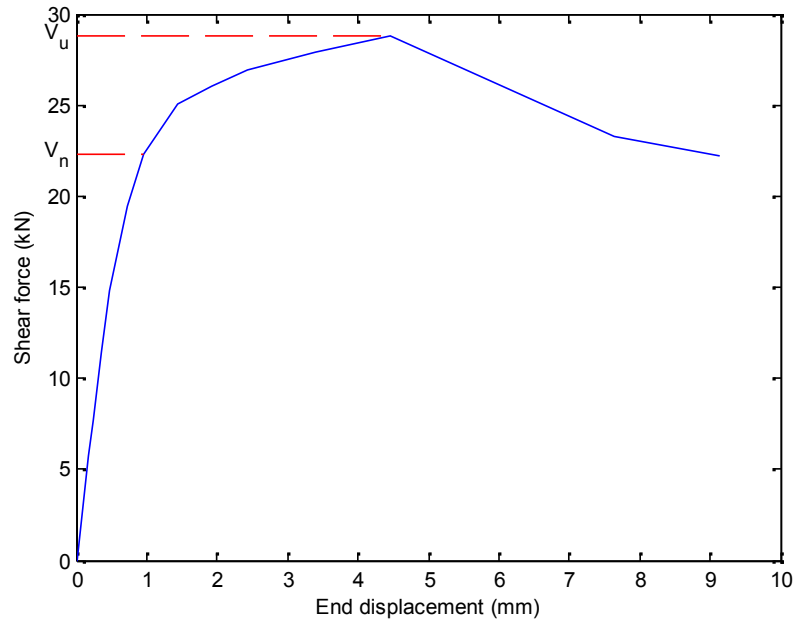


Figure 5-28 Backbone curve for module case 1

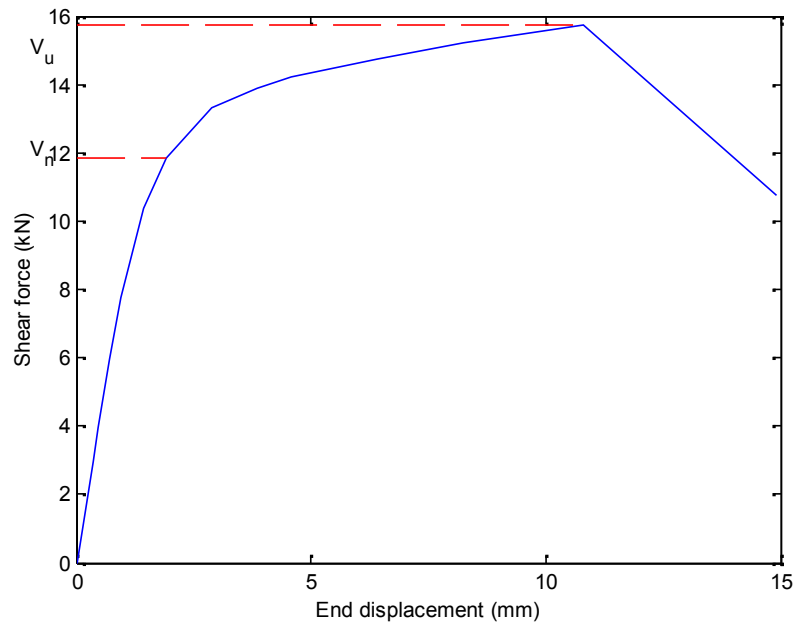


Figure 5-29 Backbone curve for module case 2

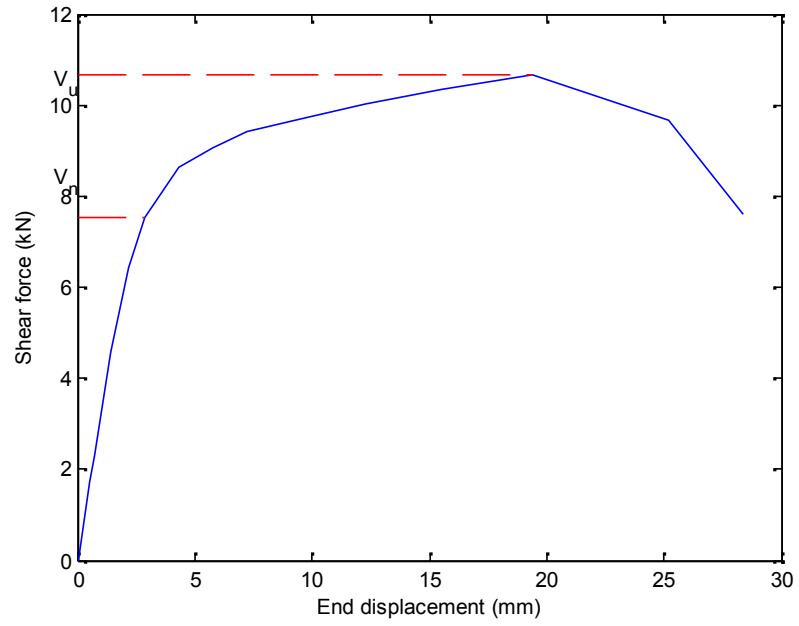


Figure 5-30 Backbone curve for module case 3

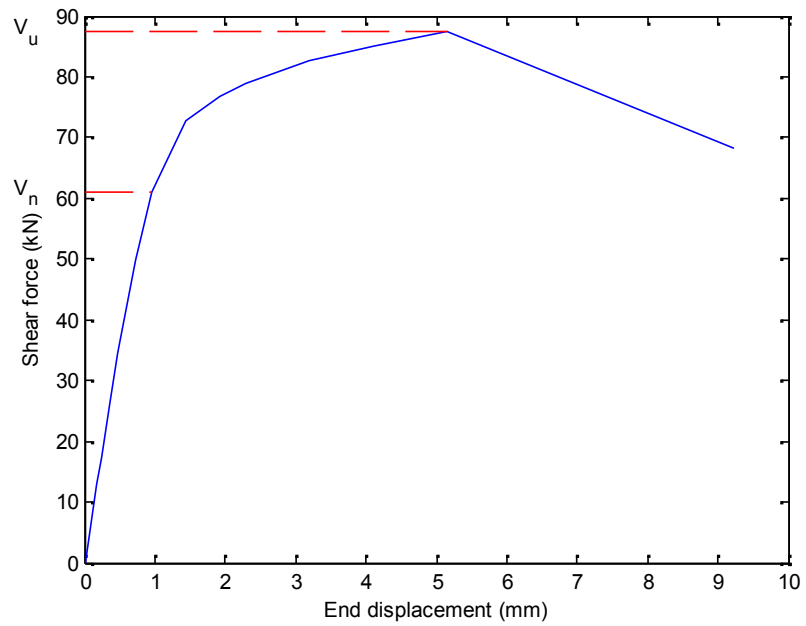


Figure 5-31 Backbone curve for module case 4

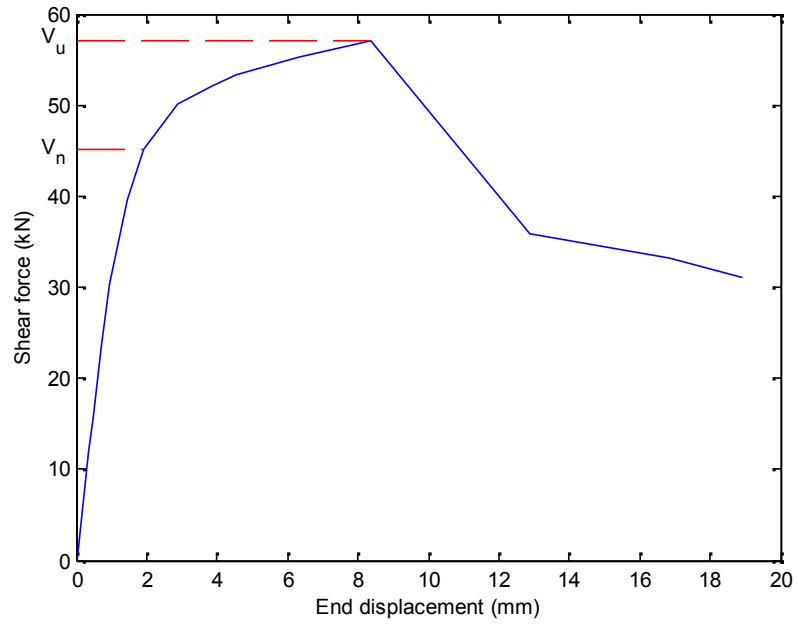


Figure 5-32 Backbone curve for module case 5

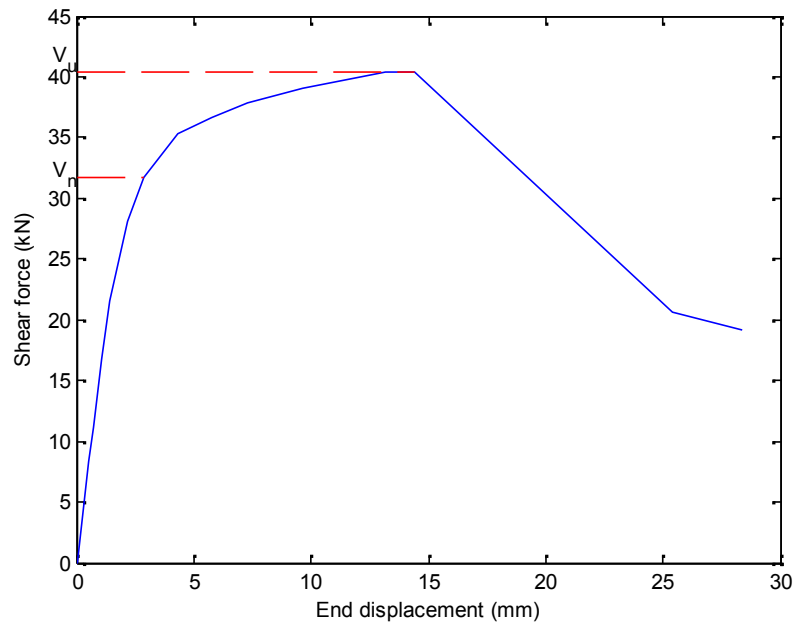
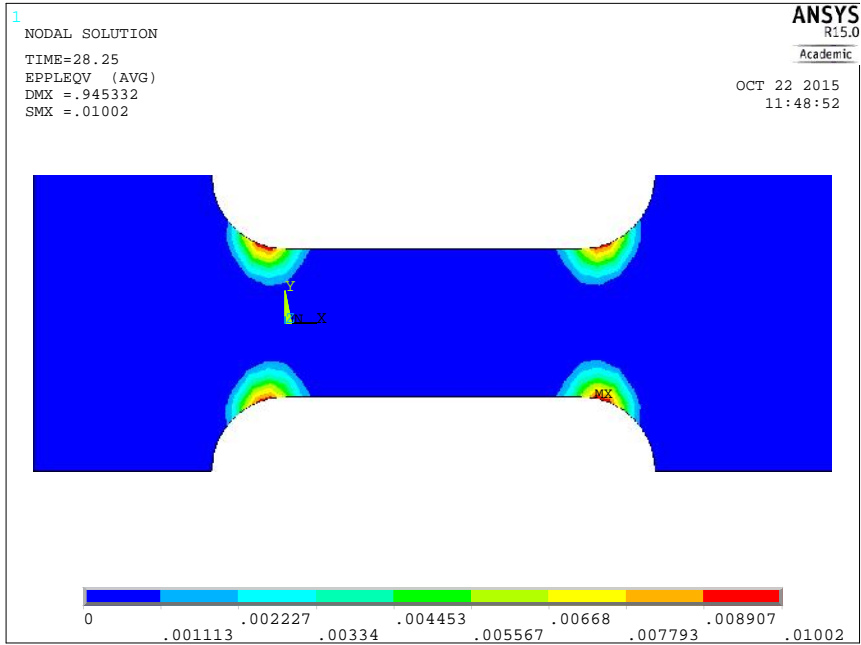
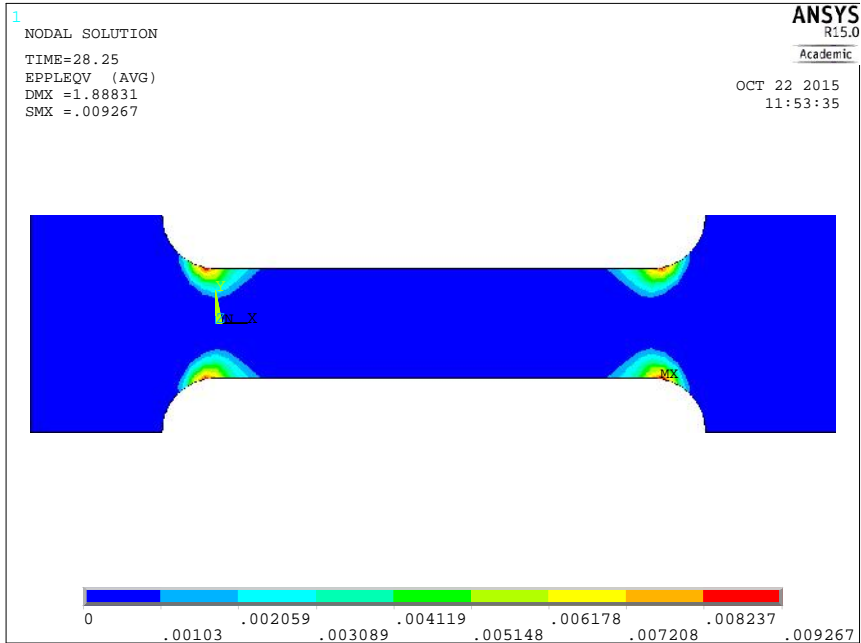


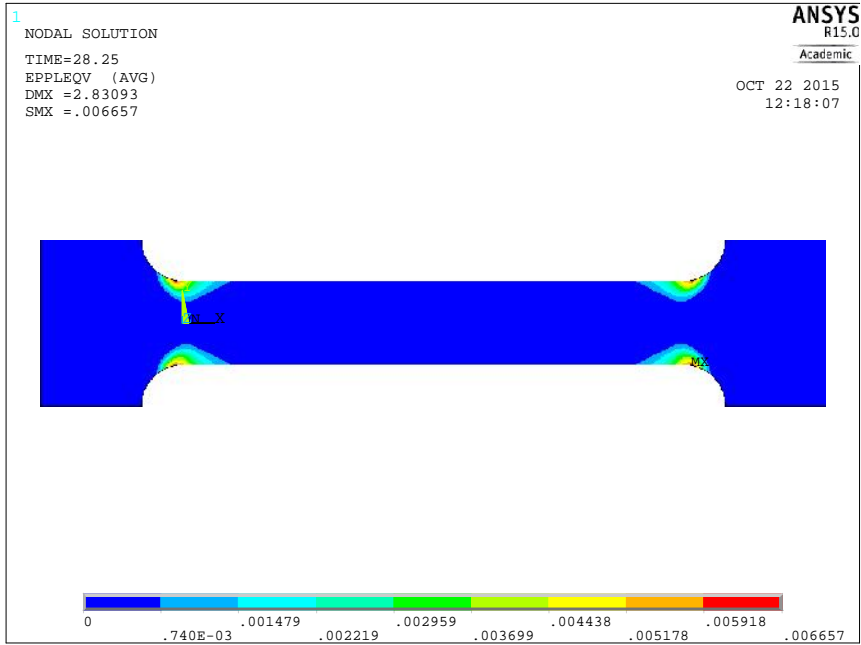
Figure 5-33 Backbone curve for module case 6



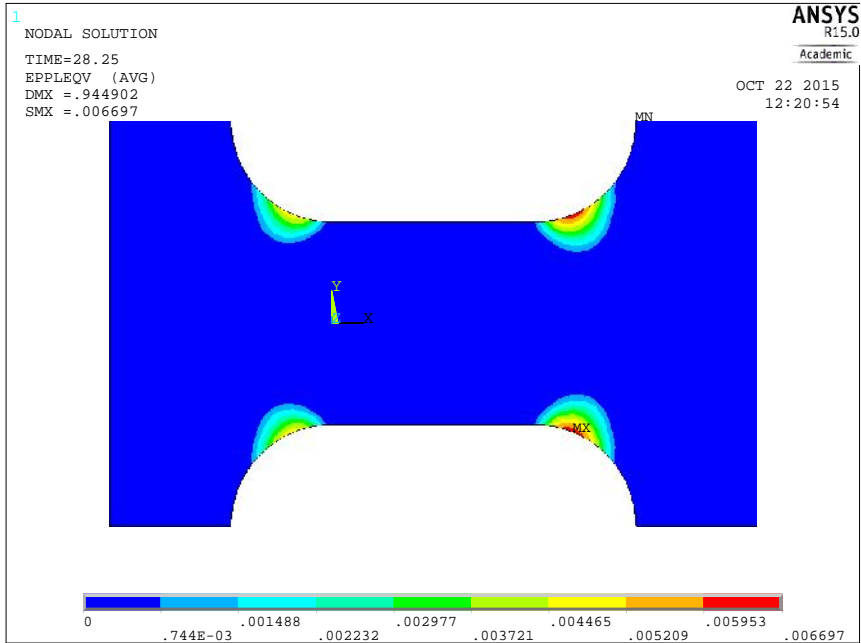
(a) Von Mises plastic strain distribution of module strip case 1



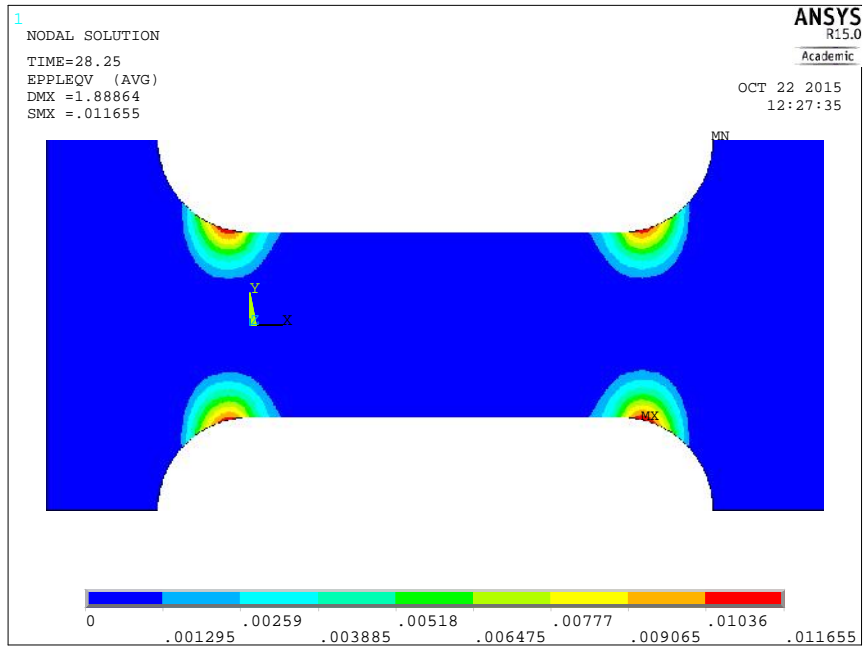
(b) Von Mises plastic strain distribution of module strip case 2



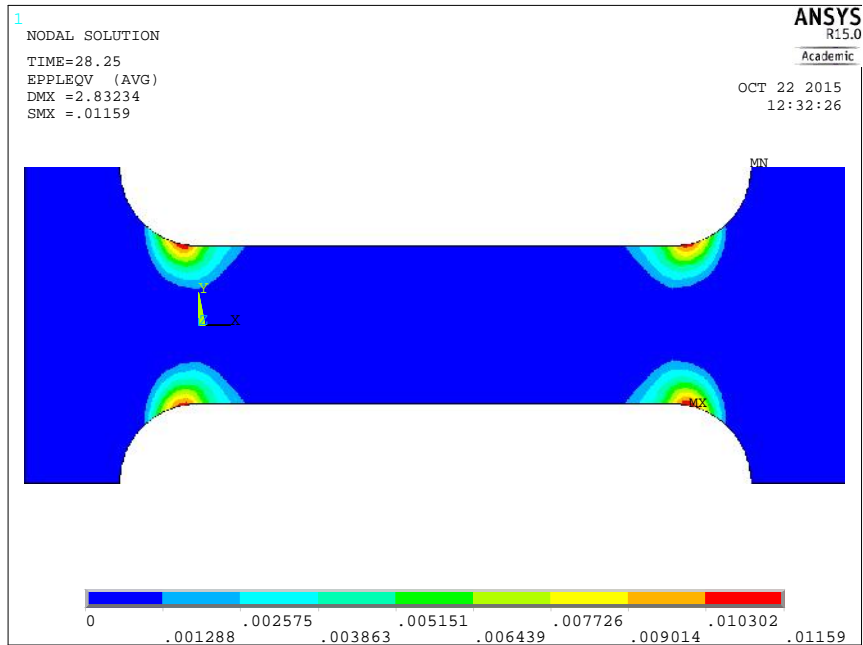
(c) Von Mises plastic strain distribution of module strip case 3



(d) Von Mises plastic strain distribution of module strip case 4

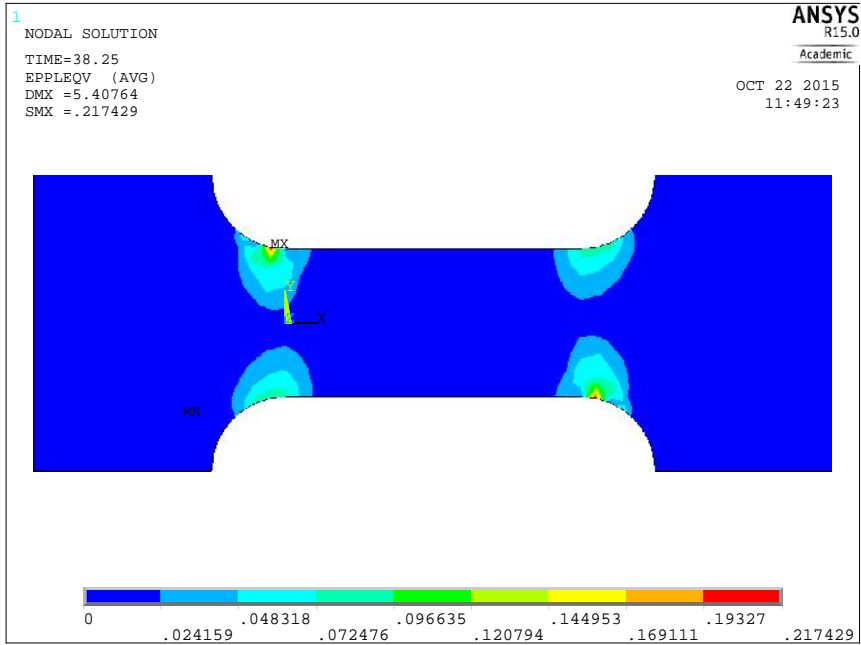


(e) Von Mises plastic strain distribution of module strip case 5

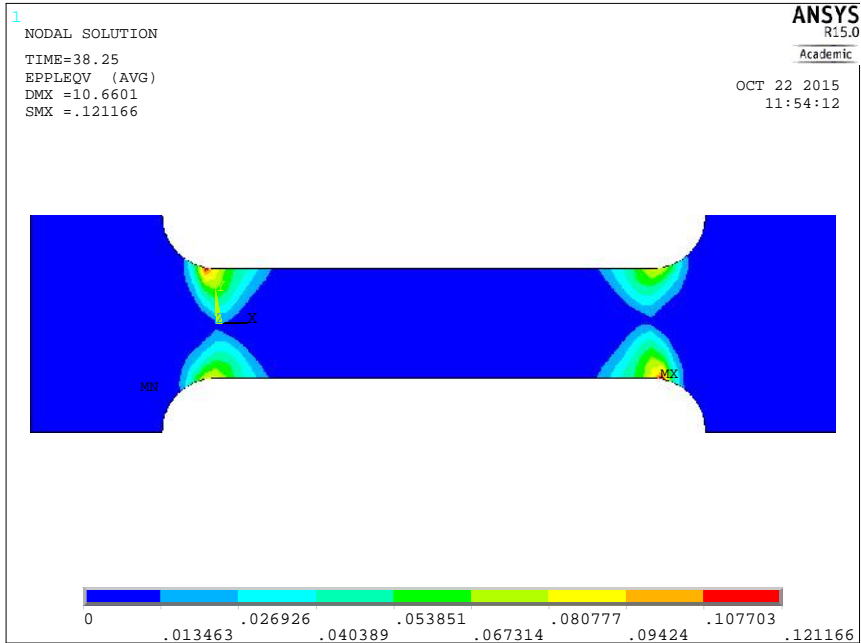


(f) Von Mises plastic strain distribution of module strip case 6

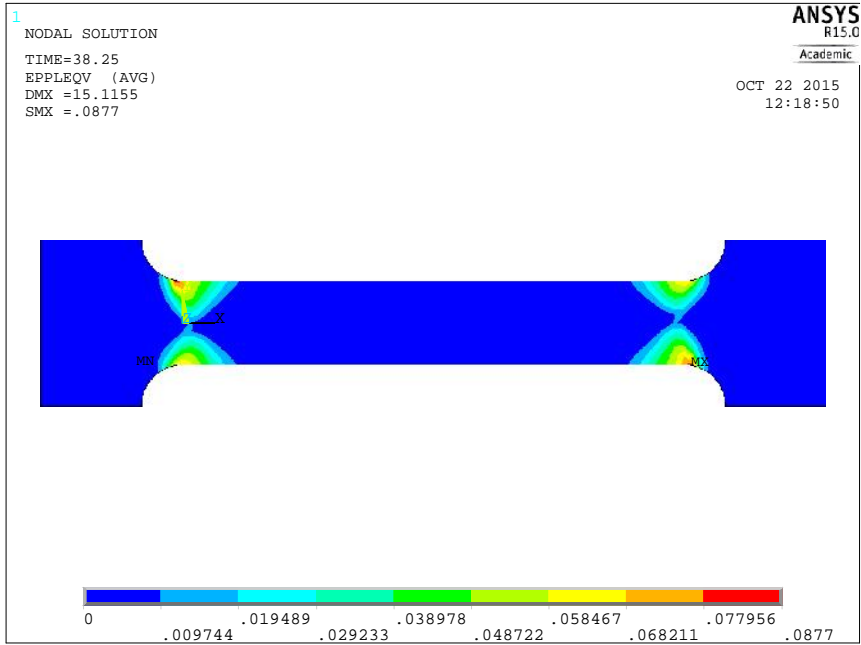
Figure 5-34 Von Mises plastic strain contours for module strip case 1 to 6 at $\theta = 0.02$ radians



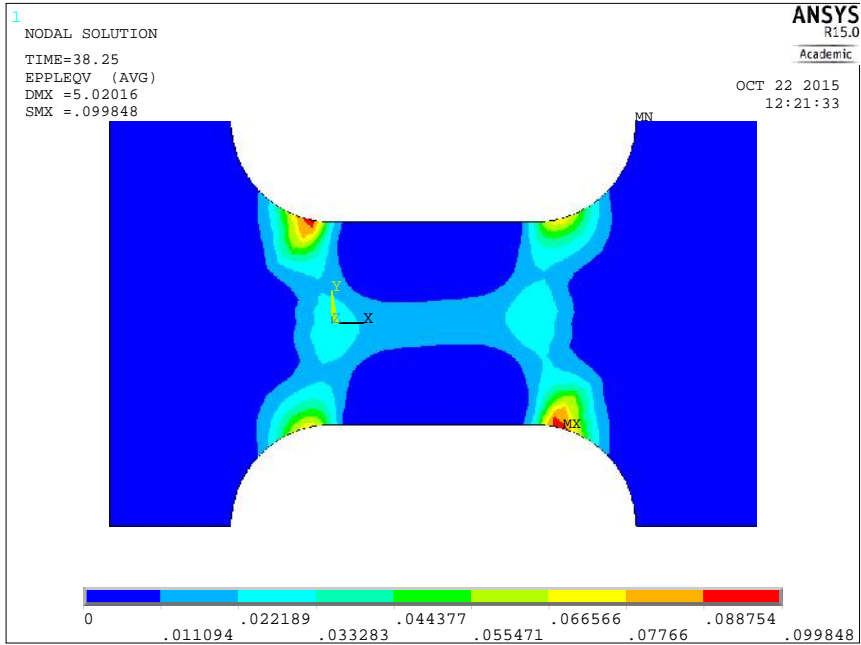
(a) Von Mises plastic strain distribution of module strip case 1



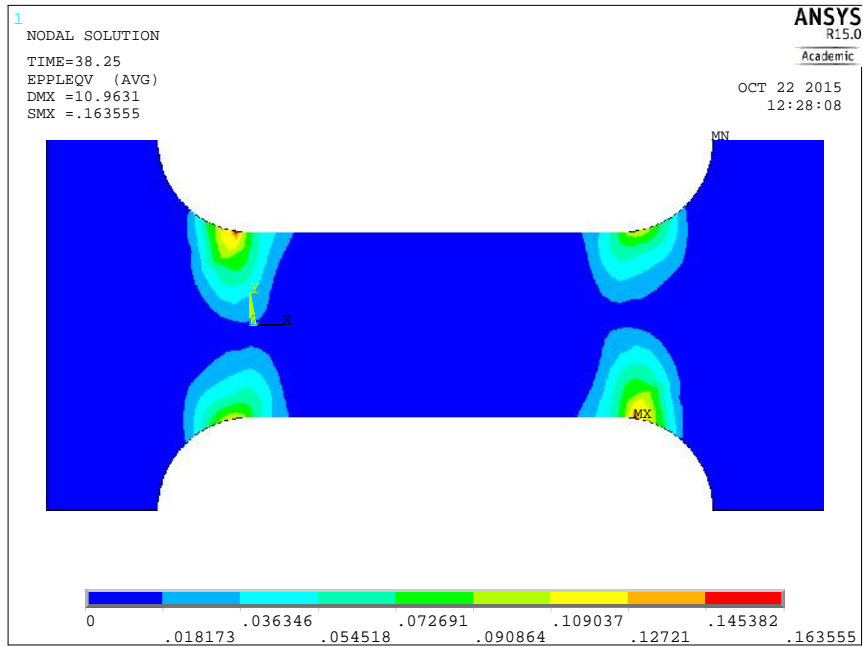
(b) Von Mises plastic strain distribution of module strip case 2



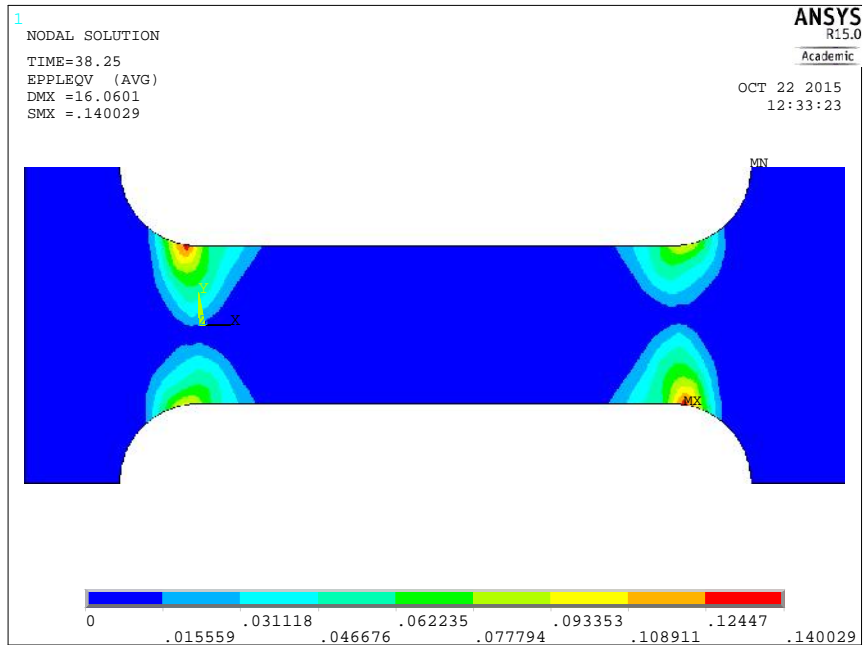
(c) Von Mises plastic strain distribution of module strip case 3



(d) Von Mises plastic strain distribution of module strip case 4



(e) Von Mises plastic strain distribution of module strip case 5



(f) Von Mises plastic strain distribution of module strip case 6

Figure 5-35 Von Mises plastic strain contours for module strip case 1 to 6 at $\theta = 0.11$ radians



Figure 5-36 Simplified model of each module case

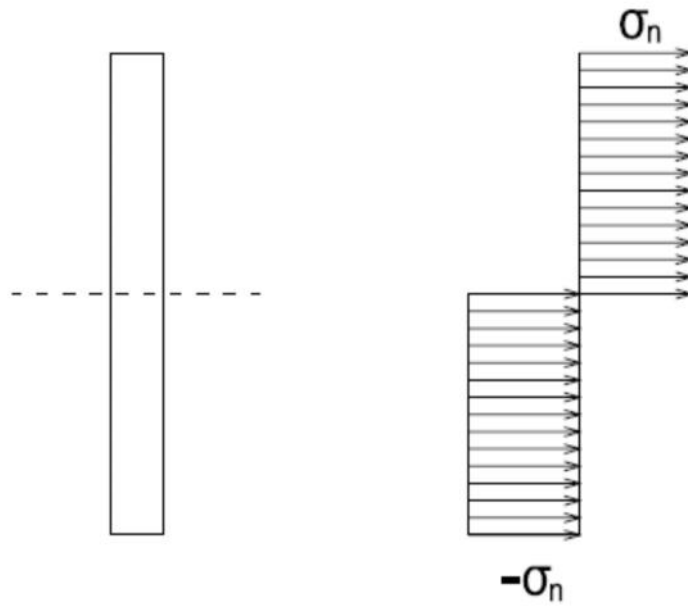


Figure 5-37 Theoretical normal stress distribution at the module end

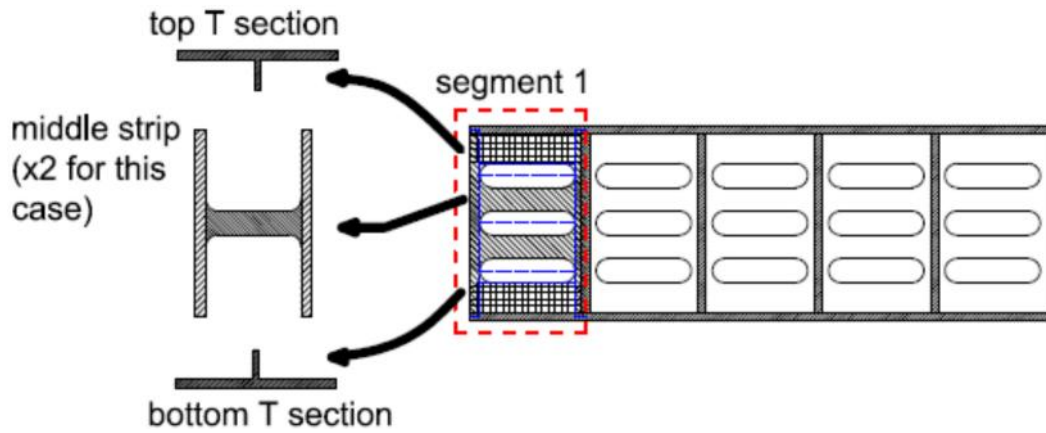


Figure 5-38 T Section Module and the Inner Strip Module Discretization

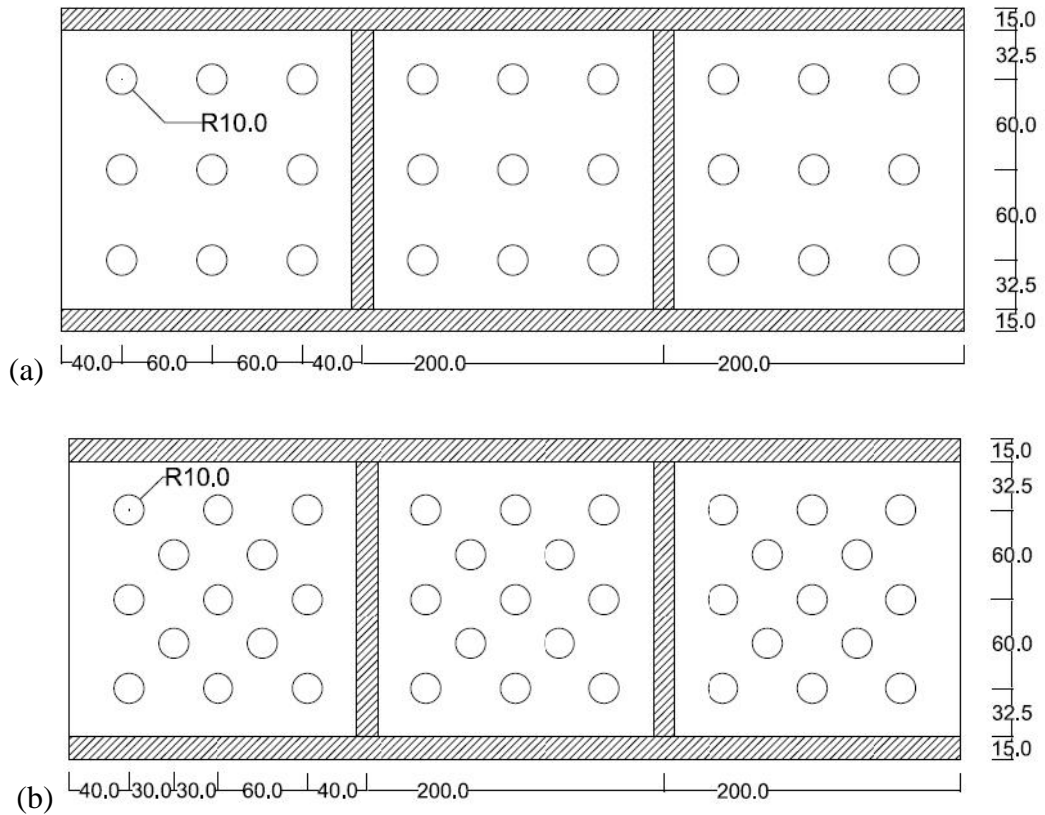
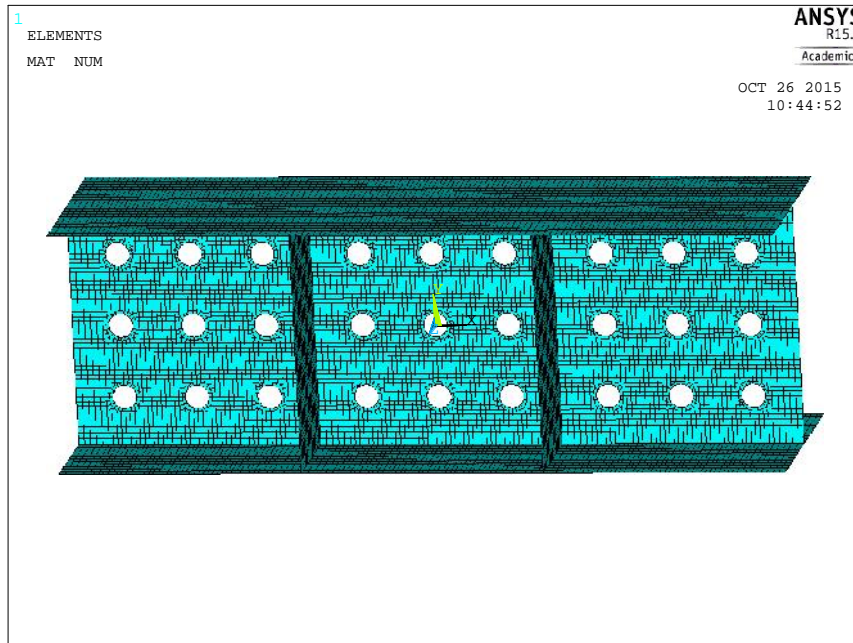
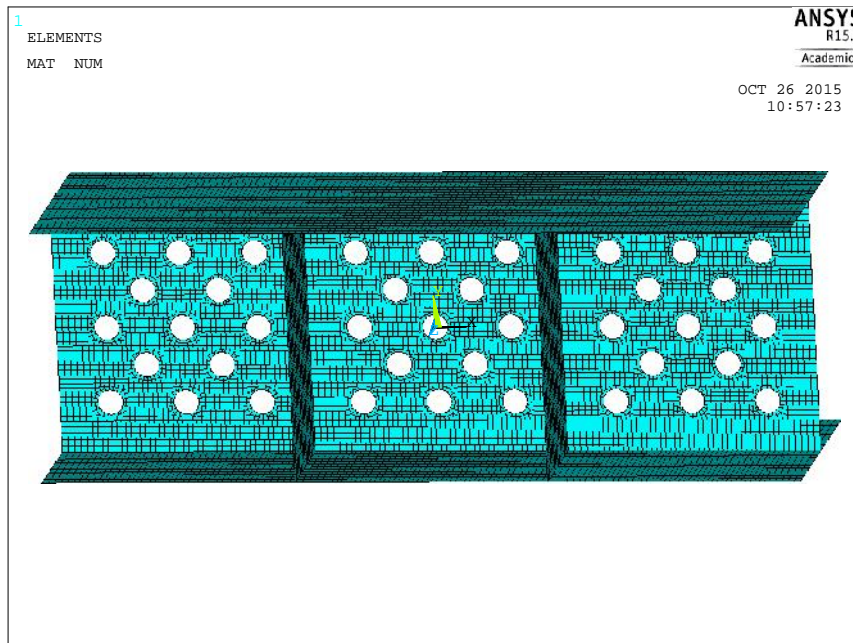


Figure 5-39 Section Sketch for the Perforated Cast Steel Links: (a) Design 1, (b) Design 2

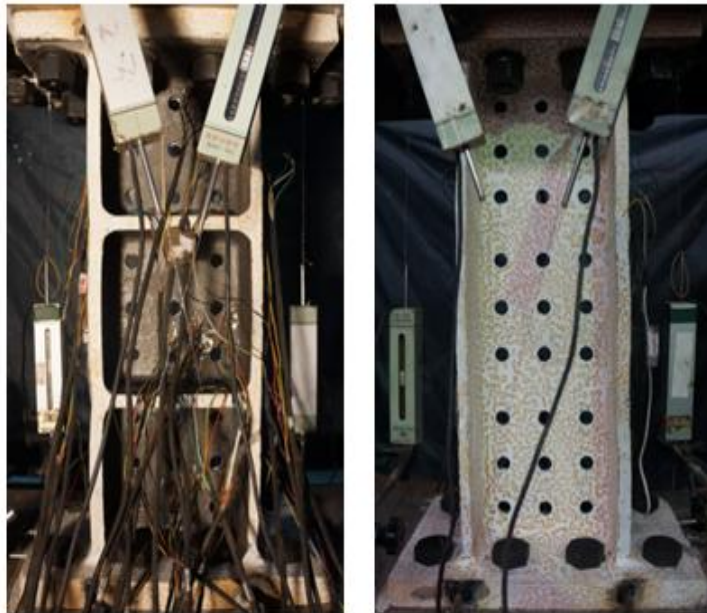


(a) Perforated cast steel link with circular holes (design 1)



(b) Perforated cast steel link with circular holes (design 2)

Figure 5-40 Meshed Models of the Cast Steel Link Specimens

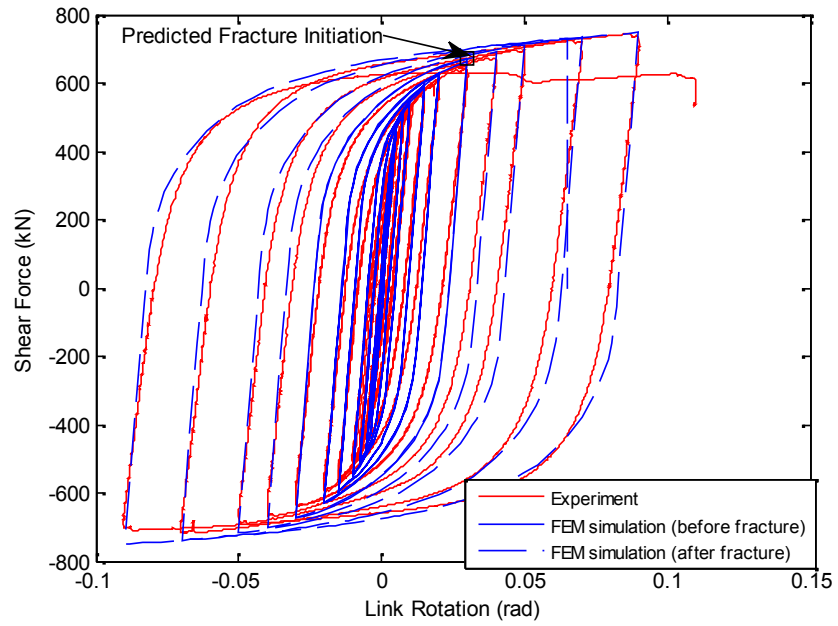


Design 1

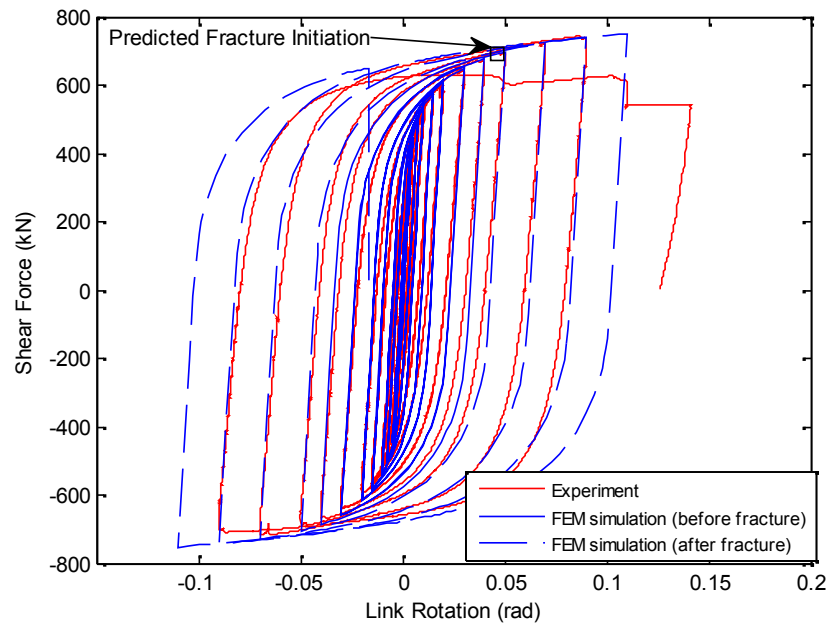


Design 2

Figure 5-41 Experiment Setup for the Cast Steel Link Specimens (Zhang 2015)

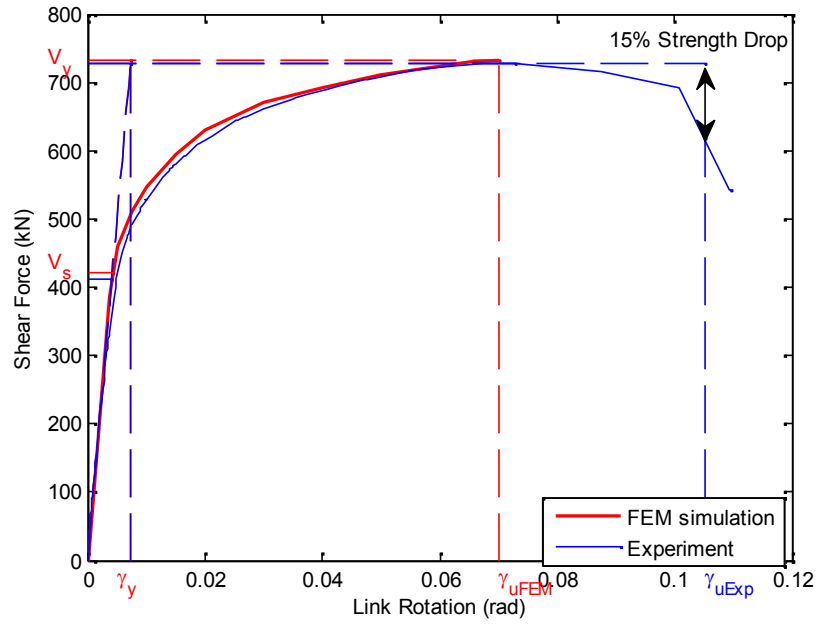


(a)

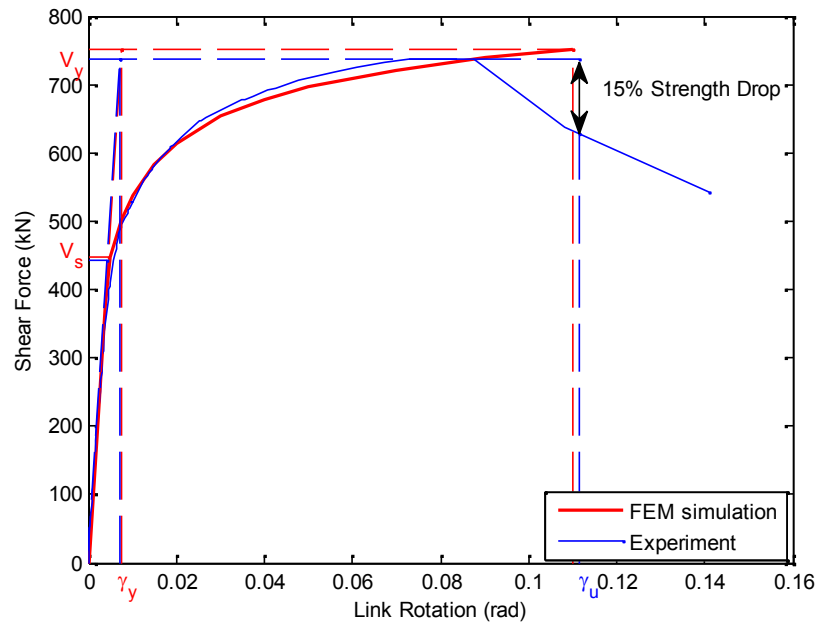


(b)

Figure 5-42 Hysteresis Loop: (a) Design 1, (b) Design 2

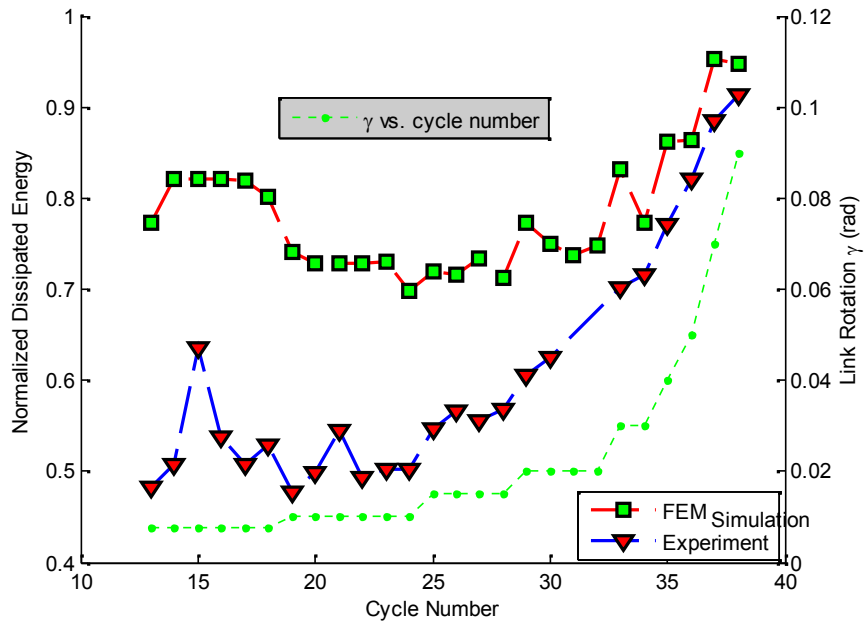


(a)

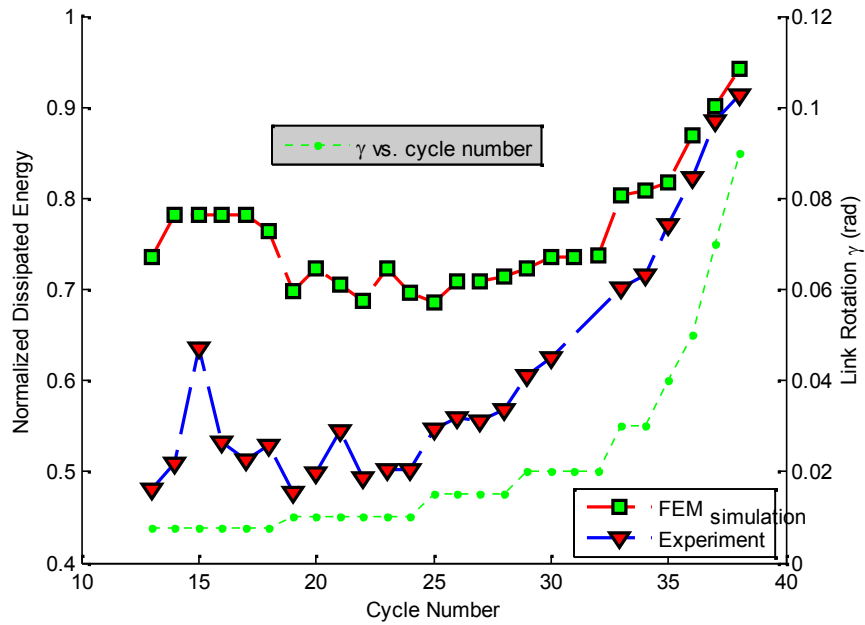


(b)

Figure 5-43 Backbone Curve: (a) Design 1, (b) Design 2

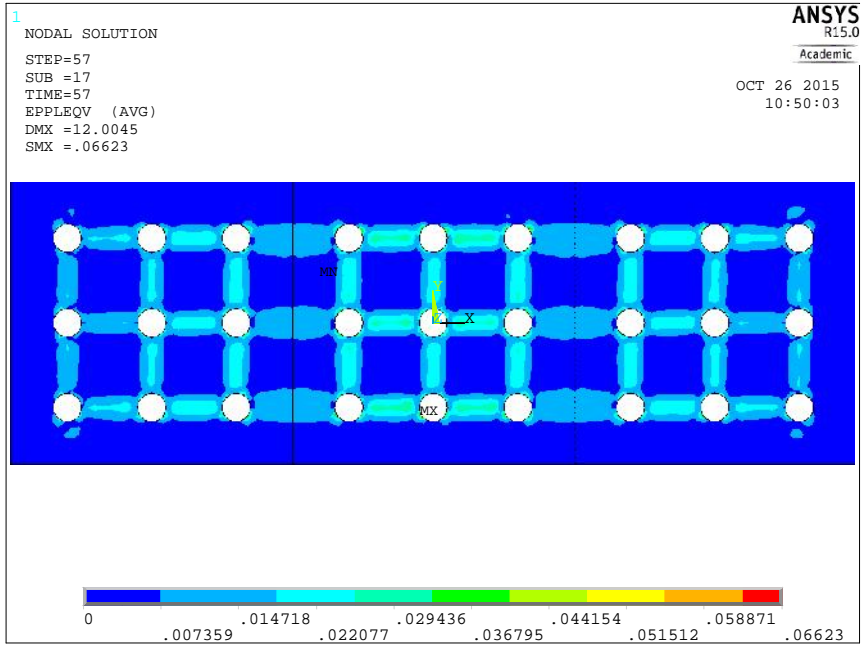


(a)

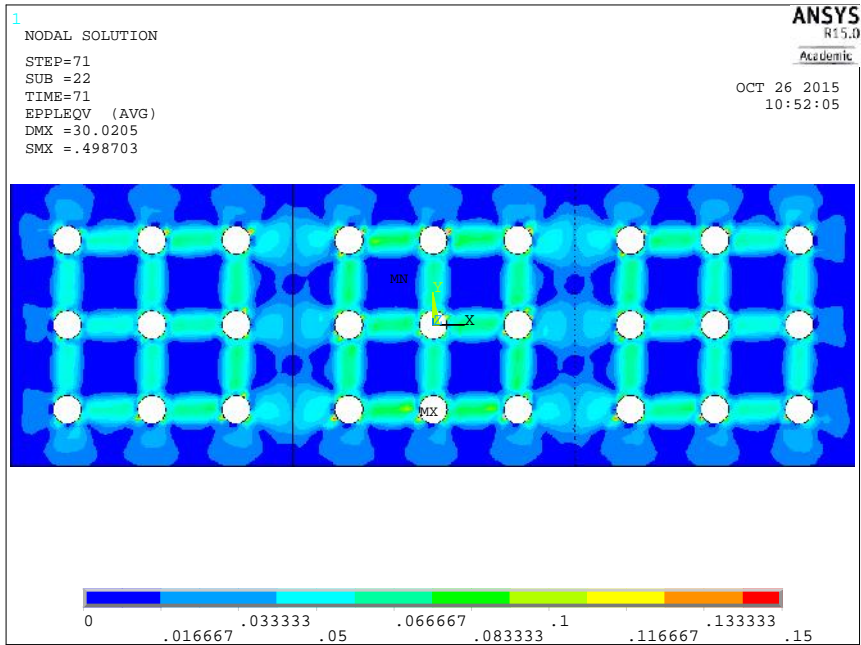


(b)

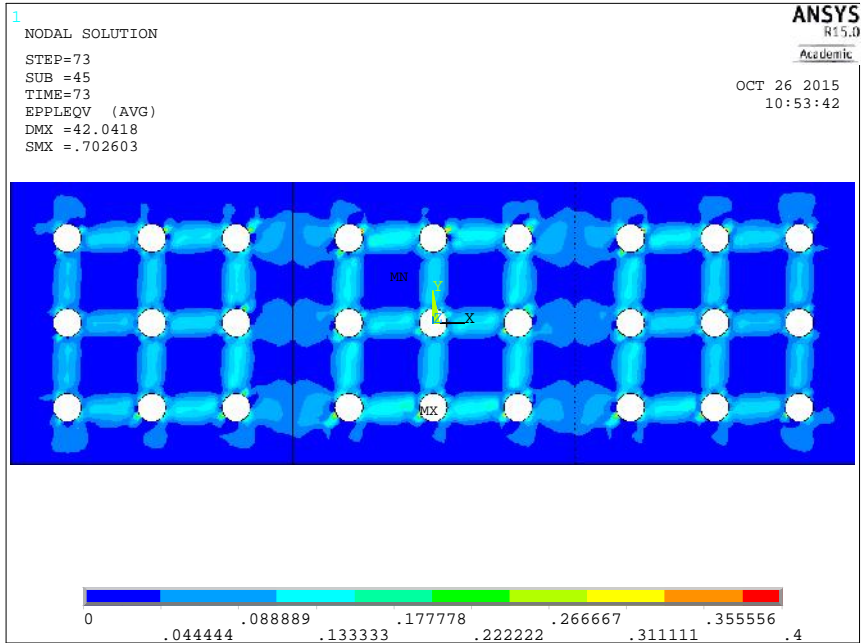
Figure 5-44 Energy Dissipation: (a) Design 1, (b) Design 2



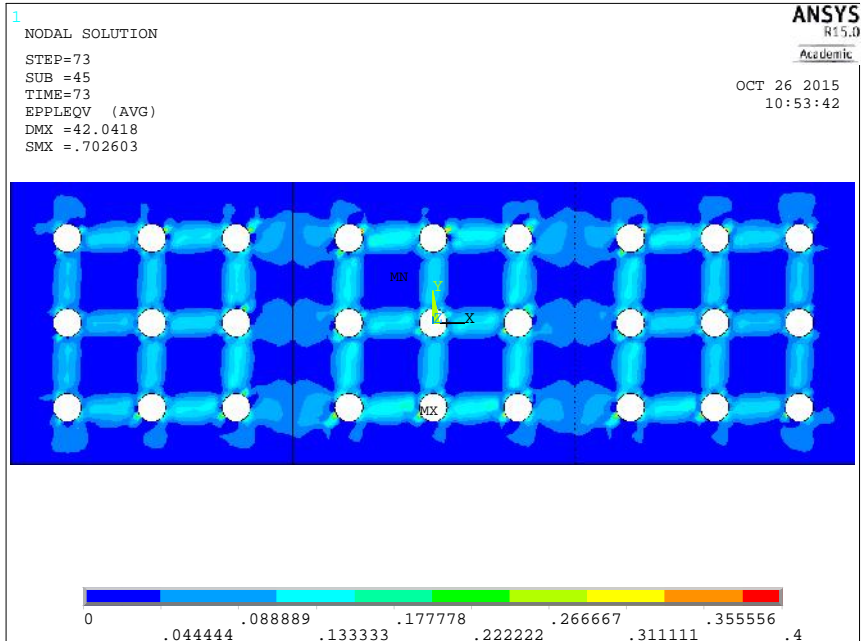
(a) Perforated cast steel link design 1 at $\theta = 0.02$ radians



(b) Perforated cast steel link design 1 at $\theta = 0.05$ radians

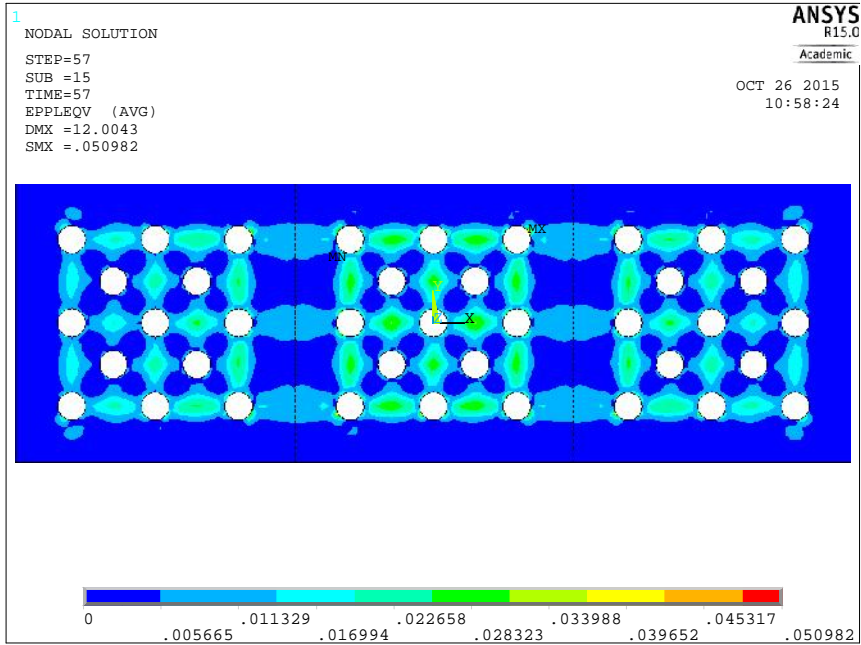


(c) Perforated cast steel link design 1 at $\theta = -0.07$ radians

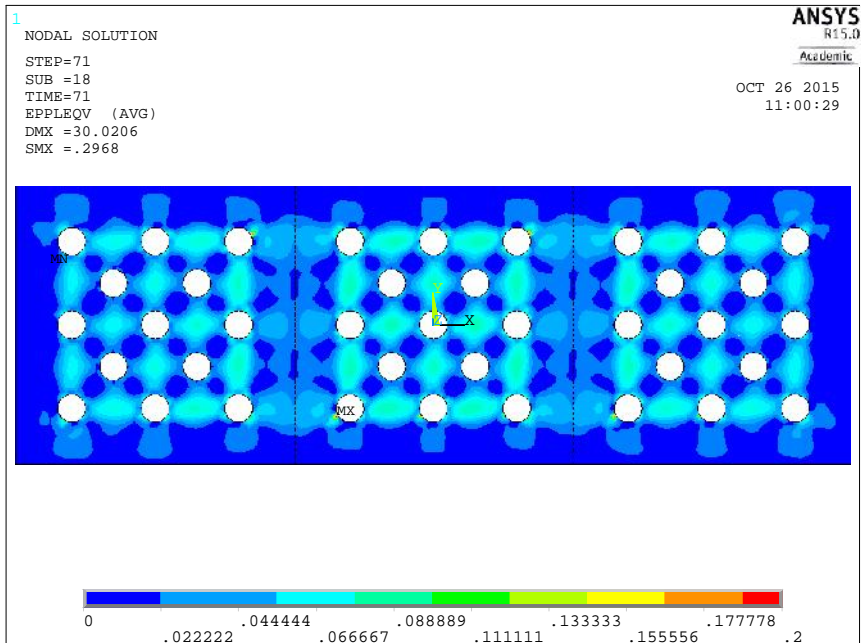


(d) Perforated cast steel link design 1 at $\theta = -0.09$ radians

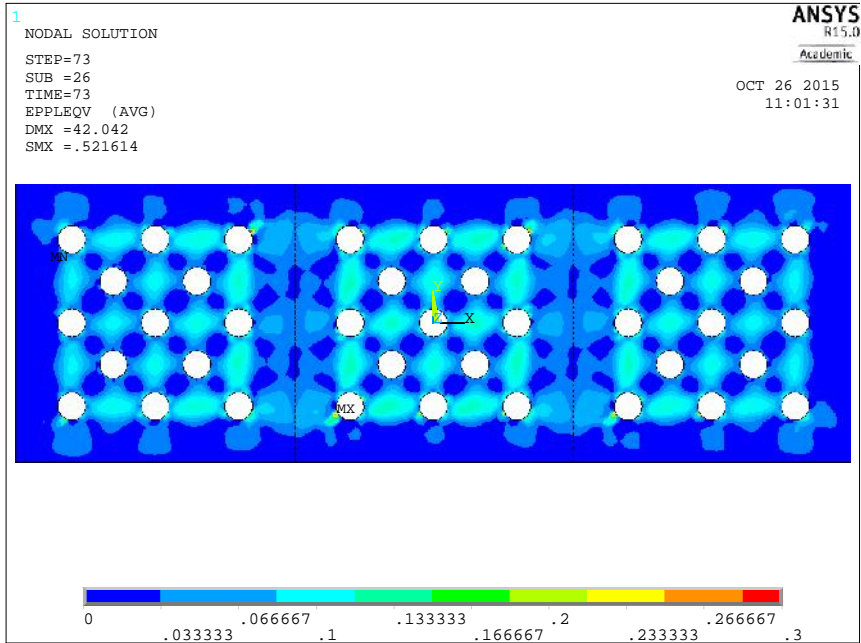
Figure 5-45 Von Mises plastic strain contours of design 1



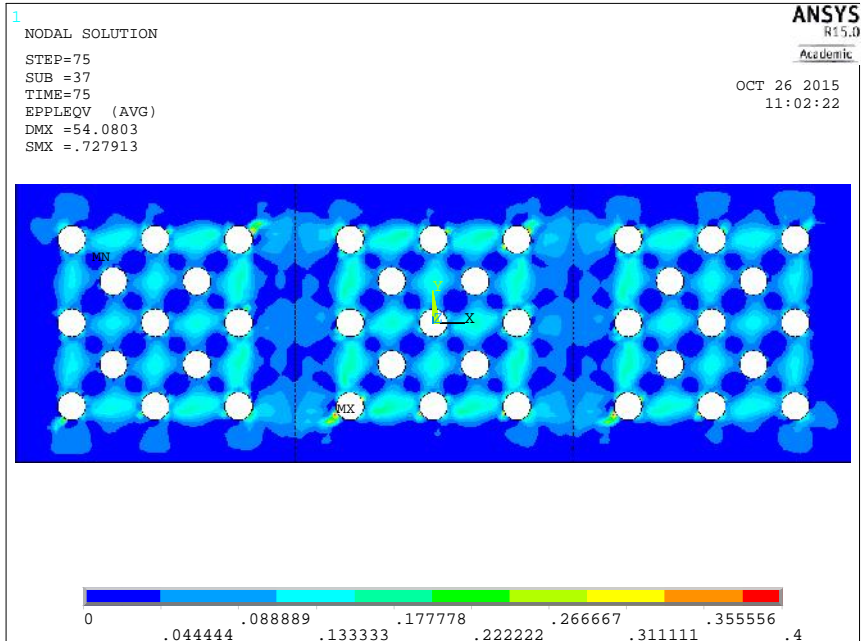
(a) Perforated cast steel link design 2 at $\theta = -0.02$ radians



(b) Perforated cast steel link design 2 at $\theta = -0.05$ radians



(c) Perforated cast steel link design 2 at $\theta = -0.07$ radians



(d) Perforated cast steel link design 2 at $\theta = -0.09$ radians

Figure 5-46 Von Mises plastic strain contours of design 2

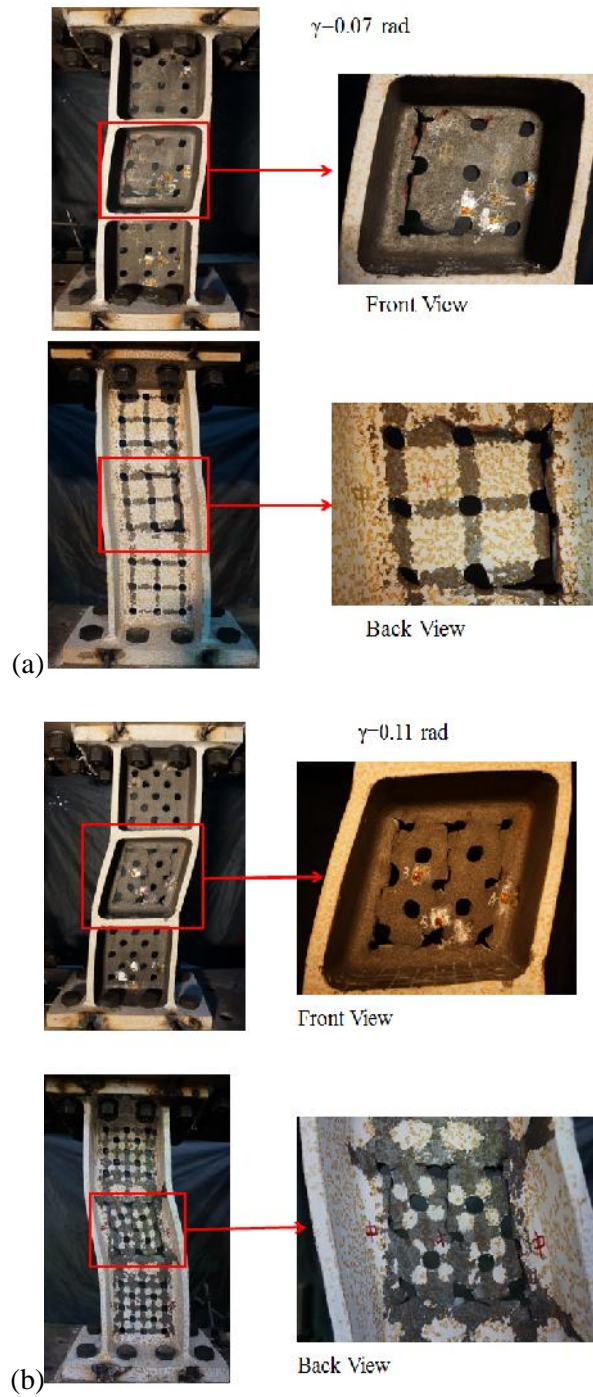
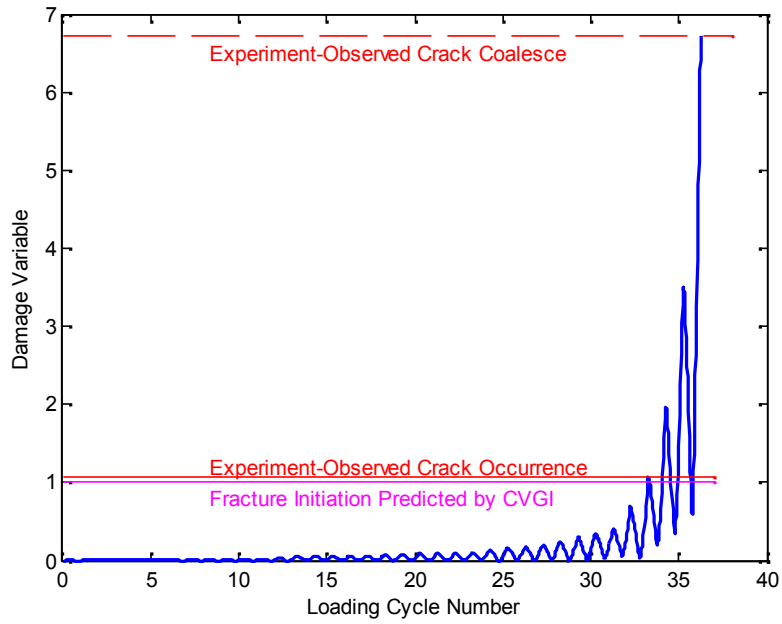
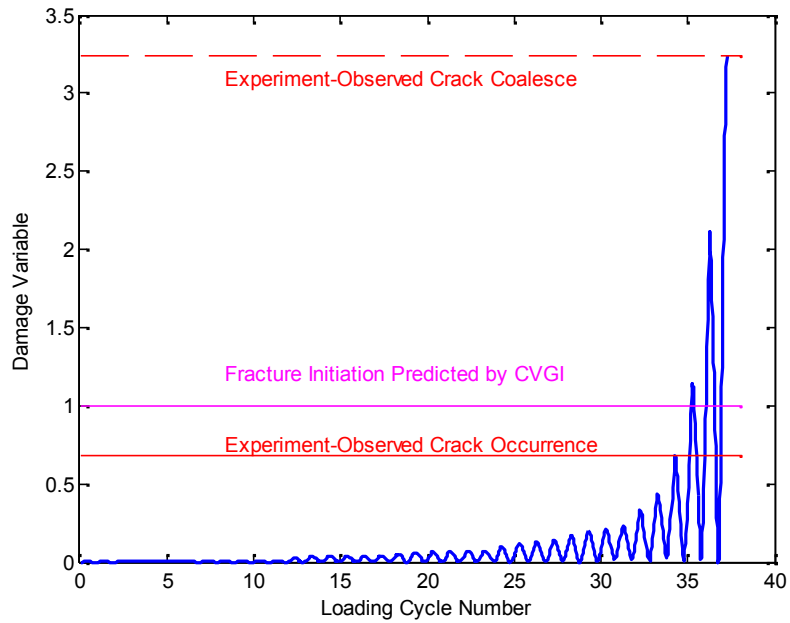


Figure 5-47 Cracks of the test specimens: (a) Design 1, (b) Design 2 (Zhang 2015)



(a)



(b)

Figure 5-48 CVGM fracture initiation prediction: (a) Design 1, (b) Design 2

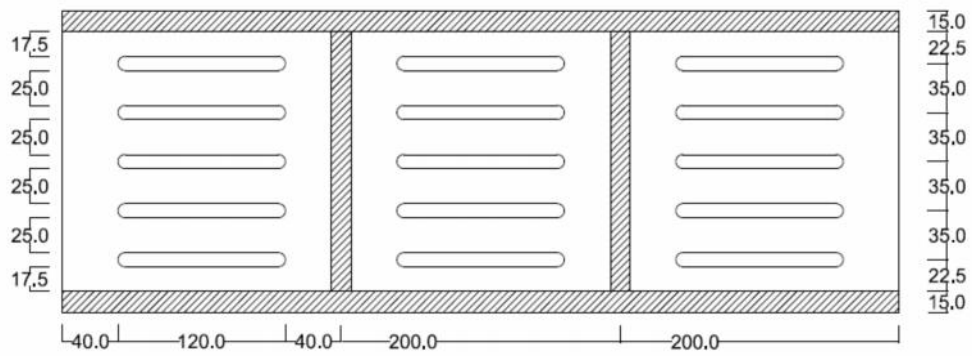


Figure 5-49 Section sketch for the perforated cast steel link with horizontal slits

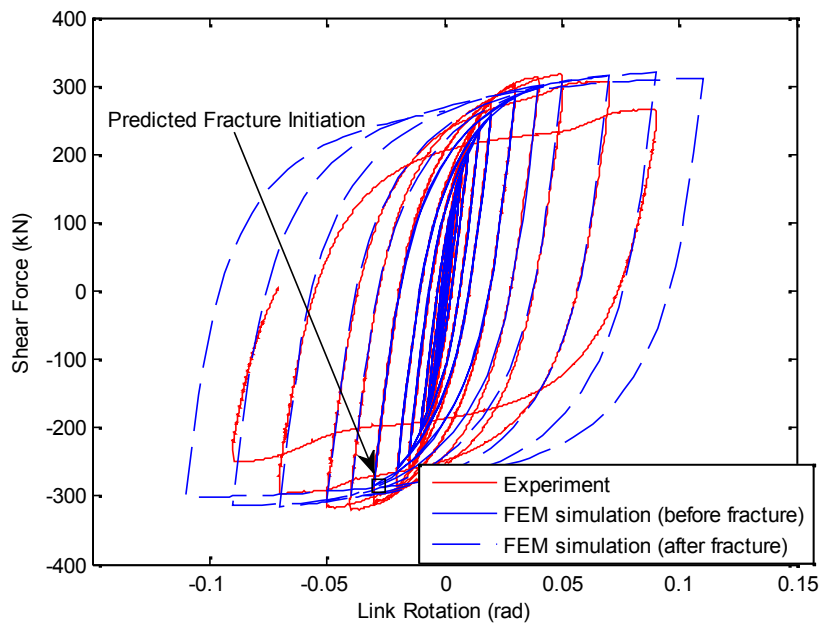


Figure 5-50 Hysteresis loop comparison for slit cast steel link (Experiment by Zhang 2015)

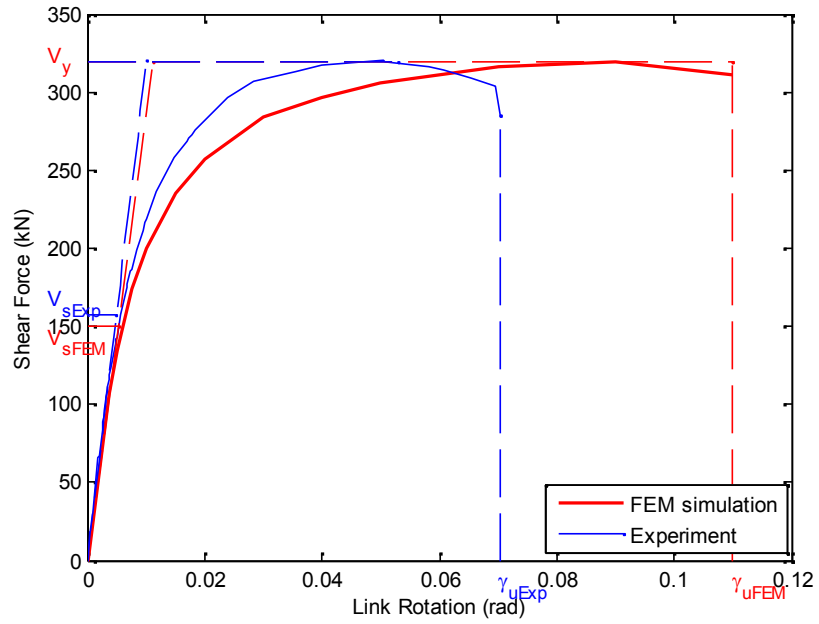


Figure 5-51 Backbone curve comparison for slit cast steel link (Experiment by Zhang 2015)

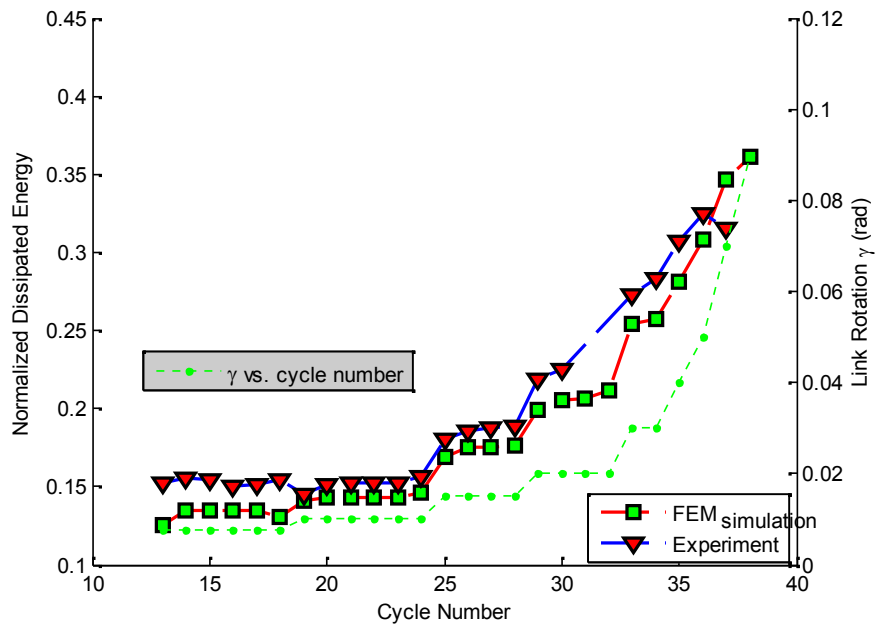
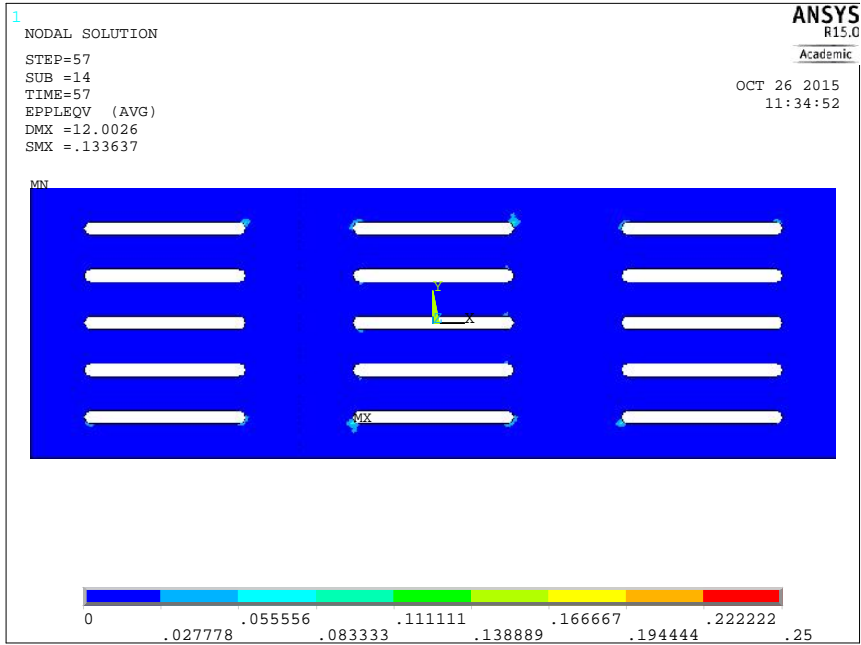
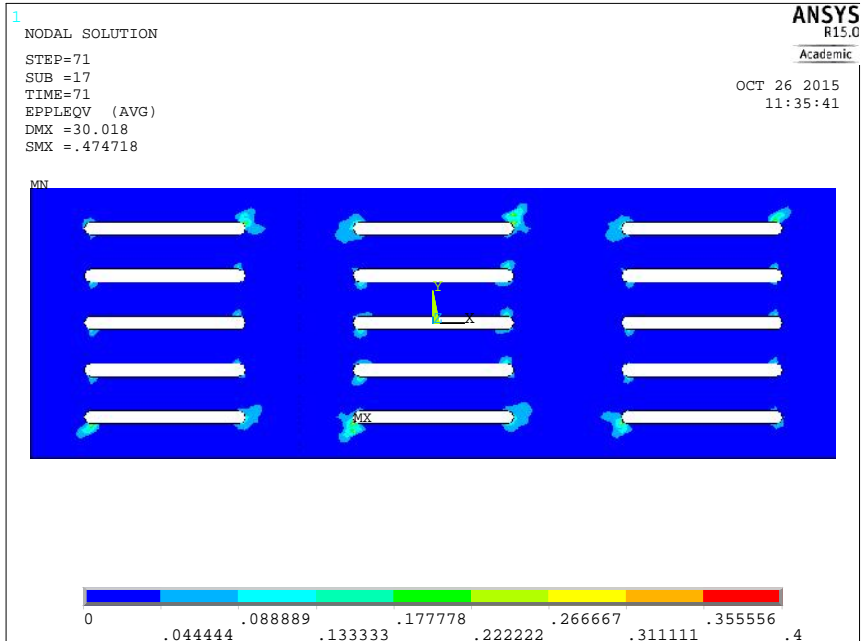


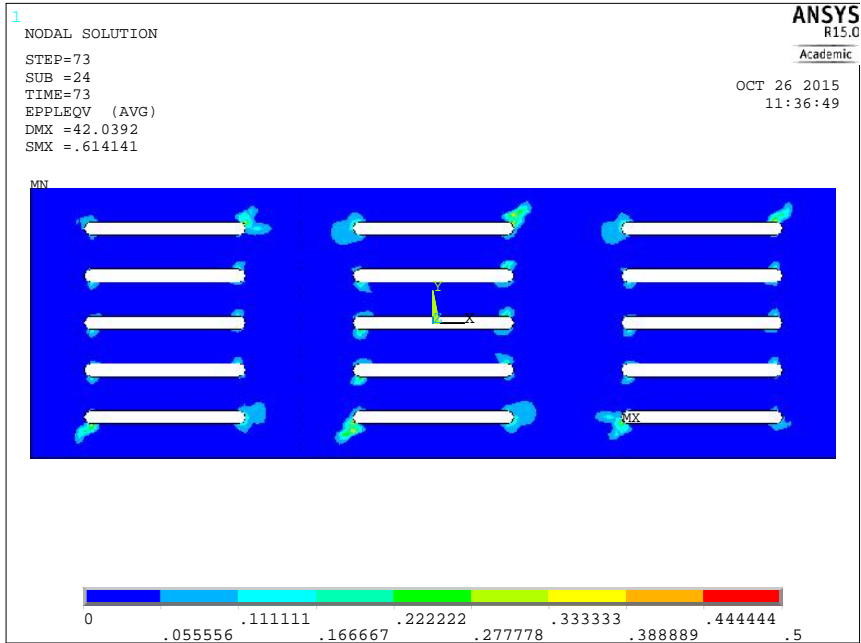
Figure 5-52 Energy dissipation for the perforated cast steel link with slits



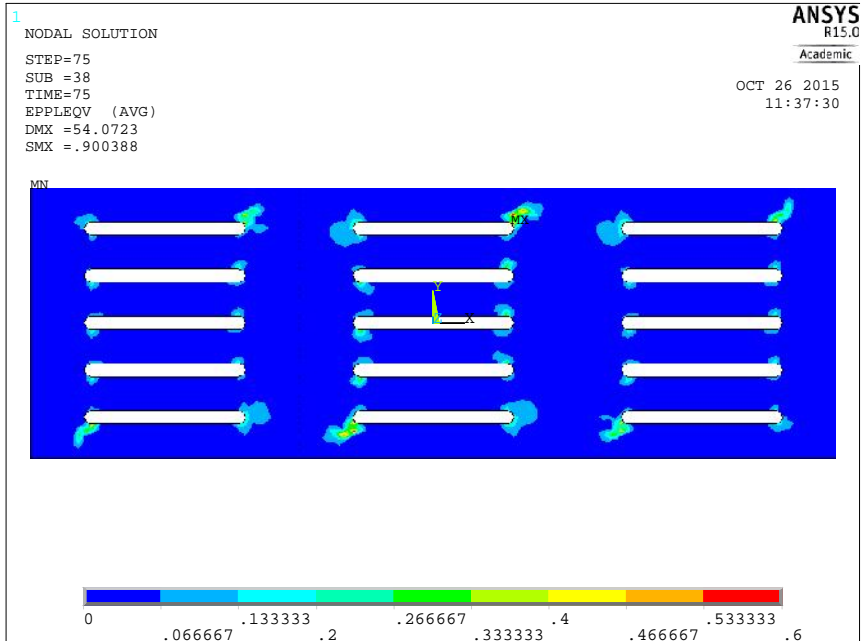
(a) Perforated cast steel link with horizontal slits at $\theta = 0.02$ radians



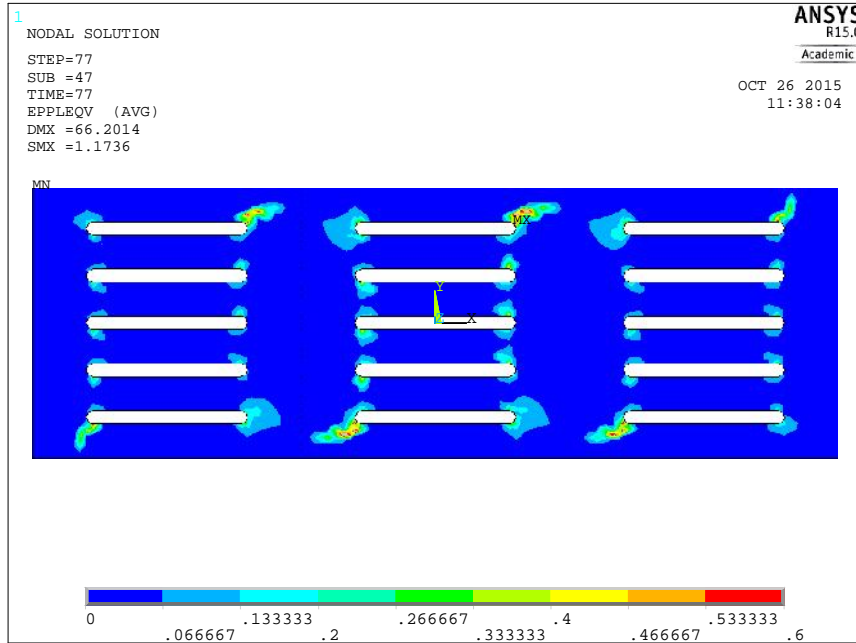
(b) Perforated cast steel link with horizontal slits at $\theta = 0.05$ radians



(c) Perforated cast steel link with horizontal slits at $\theta = 0.07$ radians



(d) Perforated cast steel link with horizontal slits at $\theta = 0.09$ radians



(e) Perforated cast steel link with horizontal slits at $\theta = 0.11$ radians

Figure 5-53 Von Mises plastic strain contours for the perforated cast steel link with horizontal slits

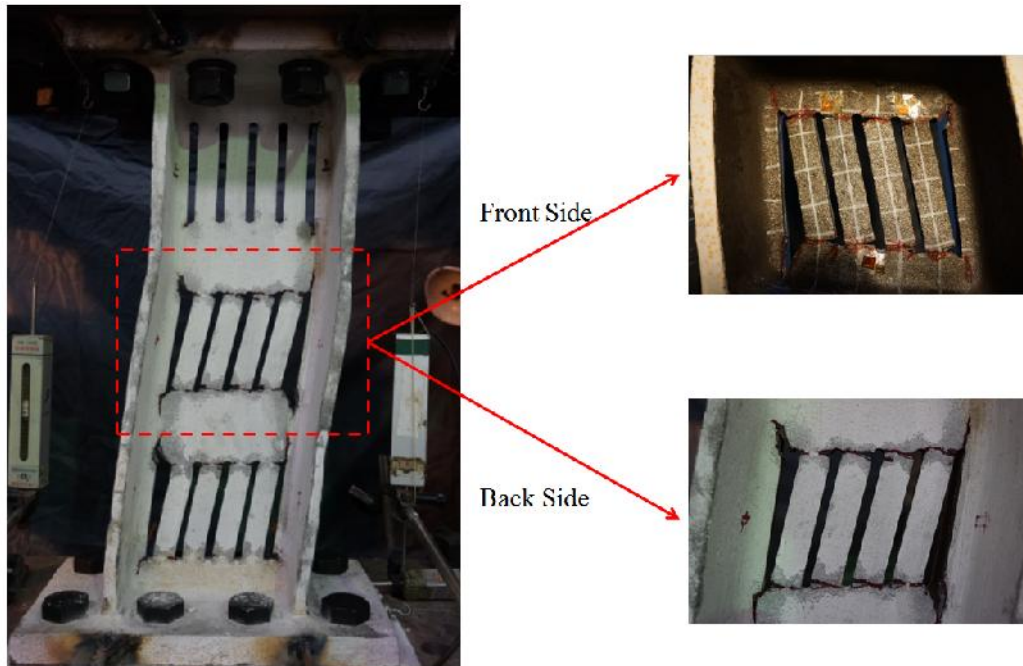


Figure 5-54 Crack of cast steel slit link beam (Zhang 2015)

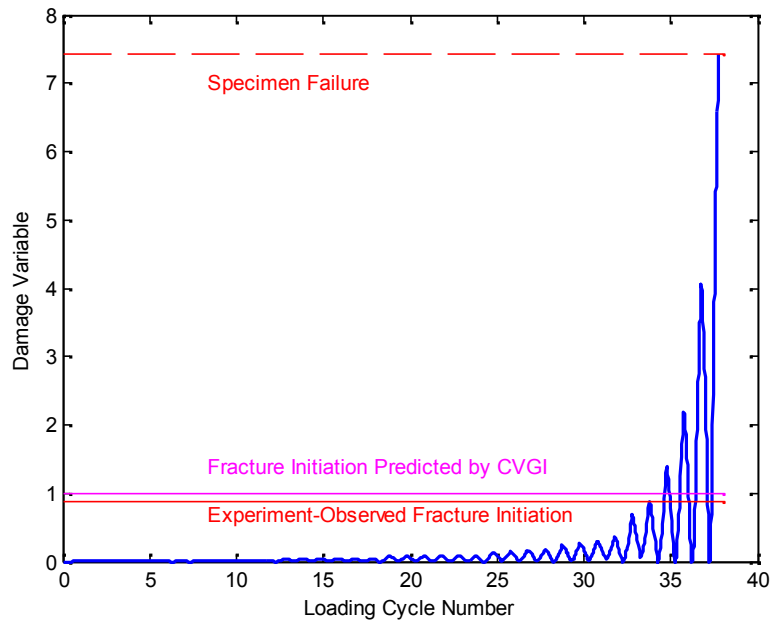


Figure 5-55 Fracture Initiation Prediction by CVGM

Table 5-1 Section details of the perforated link specimens (unit: mm)

Group	#	Label	Section	b_f	t_f	t_w	h	L	t_s	D	S_{diag}	ρ (%)
I	1	Group-I-1	W10x33	202.2	11.0	7.4	247.0	733.2	10.0	25.4	53.9	12.59
	2	Group-I-2	W12x50	205.2	16.3	9.4	309.9	863.3	10.0	25.4	53.9	10.59
	3	Group-I-3	W14x74	256.5	19.9	11.4	360.7	1070.6	11.4	25.4	53.9	13.20
	4	Group-I-4	W16x77	261.6	19.3	11.6	419.1	1090.3	11.6	25.4	53.9	14.18
II	1	Group-II-1	W10x33	202.2	11.0	7.4	247.0	733.2	10.0	25.4	53.9	9.37
	2	Group-II-2	W12x50	205.2	16.3	9.4	309.9	863.3	10.0	25.4	53.9	8.00
	3	Group-II-3	W14x74	256.5	19.9	11.4	360.7	1070.6	11.4	25.4	53.9	9.17
	4	Group-II-4	W16x77	261.6	19.3	11.6	419.1	1090.3	11.6	25.4	53.9	9.76
III	1	Group-III-1	W10x33	202.2	11.0	7.4	247.0	733.2	10.0	16.0	28.6	13.36
	2	Group-III-2	W10x33	202.2	11.0	7.4	247.0	733.2	10.0	22.2	41.3	12.30
	3	Group-III-3	W10x33	202.2	11.0	7.4	247.0	733.2	10.0	28.6	50.8	14.85
IV	1	Group-IV-1	W10x33	202.2	11.0	7.4	247.0	733.2	10.0	25.4	53.9	10.54
	2	Group-IV-2	W12x50	205.2	16.3	9.4	309.9	710.9	10.0	25.4	53.9	8.74
	3	Group-IV-3	W14x74	256.5	19.9	11.4	360.7	1070.6	11.4	25.4	53.9	10.42
	4	Group-IV-4	W16x77	261.6	19.3	11.6	419.1	1090.3	11.6	25.4	53.9	11.16
V	1	Group-V-1	W10x33	202.2	11.0	7.4	247.0	535.98	10.0	16.0	28.6	15.90
	2	Group-V-2	W10x33	202.2	11.0	7.4	247.0	526.88	10.0	22.2	41.3	15.56
	3	Group-V-3	W10x33	202.2	11.0	7.4	247.0	580.64	10.0	28.6	50.8	16.88
	4	Group-V-4	W10x33	202.2	11.0	7.4	247.0	535.98	10.0	12.8	28.6	10.17
	5	Group-V-5	W10x33	202.2	11.0	7.4	247.0	526.88	10.0	17.8	41.3	10.01
	6	Group-V-6	W10x33	202.2	11.0	7.4	247.0	580.64	10.0	20.4	50.8	8.59

Table 5-2 Strength properties of the perforated stainless steel link beams with circular holes

Group	Specimen	K_0 (kN/rad)	\bar{K}_0	V_n (kN)	\bar{V}_n	Ω
I	I-1	50769.28	0.563	300.2	0.616	2.05
	I-2	95448.12	0.650	417.1	0.533	1.98
	I-3	113881.80	0.560	671.5	0.648	2.04
	I-4	134244.80	0.537	790.6	0.625	2.01
II	II-1	74088.53	0.821	449	0.921	1.92
	II-2	129686.90	0.883	734.8	0.938	1.90
	II-3	168140.60	0.827	1009	0.974	2.12
	II-4	203060.40	0.812	1215	0.961	1.90
III	III-1	69690.67	0.772	422.3	0.866	2.20
	III-2	70667.15	0.783	405.3	0.831	2.04
	III-3	67094.46	0.743	404.1	0.830	2.19
IV	IV-1	73231.44	0.818	439.9	0.904	1.66
	IV-2	133180.37	0.847	742.9	0.975	1.70
	IV-3	165777.63	0.838	991.2	0.927	1.85
	IV-4	199739.09	0.813	1185	0.919	1.80
V	V-1	73355.36	0.708	421.3	0.865	1.66
	V-2	73987.39	0.710	415.8	0.855	1.73
	V-3	58374.86	0.581	330.7	0.679	1.64
	V-4	81959.17	0.791	460.5	0.945	1.78
	V-5	84274.96	0.809	486.2	0.999	1.65
	V-6	83270.61	0.829	481.1	0.773	1.63

Table 5-3 Ductility of the perforated stainless steel link beams with circular holes

Group	Specimen	γ_v (rad)	γ_u (rad)	μ
I	I-1	0.0099	0.130	13.13
	I-2	0.0093	0.115	12.45
	I-3	0.0096	0.125	13.08
	I-4	0.0092	0.110	11.98
II	II-1	0.0098	0.130	13.22
	II-2	0.0102	0.148	14.49
	II-3	0.0097	0.150	15.45
	II-4	0.0092	0.090	9.84
III	III-1	0.0103	0.129	12.53
	III-2	0.0104	0.130	12.47
	III-3	0.0104	0.130	12.45

Table 5-4 Section dimensions of perforated stainless steel link beams with slits

	t_f (mm)	h (mm)	t_w (mm)	t_s (mm)	L_0 (mm)	d (mm)	L (mm)	R (mm)
case 1	11.0	247.0	7.4	10.0	733.2	30	60	15.0
case 2	11.0	247.0	7.4	10.0	733.2	25	75	12.5
case 3	11.0	247.0	7.4	10.0	733.2	30	80	20.0
case 4	11.0	247.0	7.4	10.0	733.2	35	70	17.5

Table 5-5 Initial stiffness values K_0 (kN/rad) of the perforated stainless steel link beams with slits

	Group I	Group II	Group III
case 1	27518.95	29543.36	31961.62
case 2	16557.99	18406.16	18200.89
case 3	19707.72	21913.64	22480.60
case 4	23322.86	27954.75	33069.18

Table 5-6 Properties of the conventional stainless steel link beams

	K_0 (kN/rad)	V_p (kN)	V_u (kN)	Ω
flange=80mm	68007.23	382.6	655	1.71
flange=150mm	83378.77	469.1	841	1.79
flange=202mm	90253.99	487.4	962	1.97

Table 5-7 Strength values of the perforated stainless steel link beams with slits

Group	case#	V_n (kN)	V_u (kN)	Ω
I	case 1	202.5	363.99	2.75
	case 2	131.6	257.46	3.11
	case 3	149.8	267.14	2.71
	case 4	182.7	320.36	2.75
II	case 1	213.3	368.62	2.59
	case 2	137.7	280.11	3.15
	case 3	160.7	324.94	3.07
	case 4	214.1	417.04	2.98
III	case 1	217.8	362.09	2.47
	case 2	141.4	291.30	3.20
	case 3	171.6	357.62	3.18
	case 4	245.8	433.07	2.71

Table 5-8 Ductility properties of the perforated stainless steel links with slits

Group No.	Perforation Type	γ_u (rad)	γ_v (rad)	μ
I	case 1	0.13	0.0132	9.83
	case 2	0.13	0.0155	8.36
	case 3	0.1096	0.0136	8.09
	case 4	0.1462	0.0137	10.64
II	case 1	0.0894	0.0125	7.17
	case 2	0.1284	0.0152	8.44
	case 3	0.1298	0.0148	8.75
	case 4	0.1231	0.0149	8.25
III	case 1	0.0892	0.0113	7.87
	case 2	0.13	0.0160	8.12
	case 3	0.13	0.0159	8.17
	case 4	0.1295	0.0131	9.89

Table 5-9 Section details of the module strip cases

	d (mm)	t (mm)	L (mm)	R (mm)
case 1	25	6	50	12.5
case 2	25	6	100	12.5
case 3	25	6	150	12.5
case 4	50	6	50	25
case 5	50	6	100	25
case 6	50	6	150	25

Table 5-10 FEM simulation results of the module strip cases

	K_0 (kN/mm)	V_n (kN)	V_u (kN)
case 1	31.77	22.30	28.31
case 2	8.23	11.87	15.13
case 3	3.18	7.61	10.04
case 4	71.88	62.33	85.77
case 5	32.89	44.88	56.19
case 6	15.48	31.62	38.84

Table 5-11 Comparisons on the analytical and FEM simulation results of the module strip cases

	Analytical		FEM Simulation	
	K_0 (kN/mm)	V_n (kN)	K_0 (kN/mm)	V_n (kN)
case 1	33.98	22.30	31.77	20.89
case 2	8.57	11.85	8.23	10.44
case 3	3.27	7.83	3.18	6.96
case 4	89.59	63.58	71.88	83.54
case 5	33.98	44.60	32.89	41.77
case 6	15.90	31.41	15.48	27.85

Table 5-12 Section dimensions of the cast steel link specimens with circular holes (Zhang 2015)

	L (mm)	h (mm)	b_f (mm)	t_f (mm)	t_w (mm)	t_s (mm)	D (mm)	S_{diag} (mm)	ρ (%)
Design 1	600	215	180	15	12	14	20	60	7.09
Design 2	600	215	180	15	12	14	20	42.4	10.21

Table 5-13 Calibrated material strain hardening constants for cast steel

C_1	γ_1	k	R_0	R_∞	b
5872.7	31.51	483	0	21	1.2

Table 5-14 Strength properties of perforated cast steel link beams with circular holes
(Experiment by Zhang 2015)

		K_0 (kN/mm)	V_n (kN)	V_u (kN)
Design 1	Analytical	181.7	511.5	/
	FEM	171.3	458.5	736.8
	Experiment	153.09	441.8	718.13
Design 2	Analytical	170.3	472.8	/
	FEM	166.9	450.3	742.5
	Experiment	151.76	452.7	739

Table 5-15 Ductility properties of cast steel link beams with circular holes (Experiment by Zhang 2015)

		γ_v (rad)	γ_u (rad)	μ
Design 1	FEM	0.0072	0.07	9.72
	Experiment	0.0078	0.1051	13.47
Design 2	FEM	0.0074	0.11	14.86
	Experiment	0.0081	0.1117	13.79

Table 5-16 Comparisons on the strength properties of the slit cast steel link (Experiment by Zhang 2015)

Parameters	Analytical	FEM	Experiment
K_0 (kN/mm)	42.12	48.89	47.54
V_n (kN)	244.2	199.7	218.2
V_u (kN)	/	319.3	317.6

Table 5-17 Ductility properties of slit cast steel link (Experiment by Zhang 2015)

	γ_v (rad)	γ_u (rad)	μ
FEM Simulation	0.0113	0.11	9.73
Experiment	0.0101	0.0703	6.96

Chapter 6 : Nonlinear FE Analysis of Self-Centering Eccentrically Braced Frames under Cyclic Loading

Post-tensioned self-centering eccentrically braced frame (SC-EBF) structure has been recently proposed as a new type of seismic resistant structural system with enhanced resilience. Compared to conventional EBF structures, the residual drifts of the SC-EBF structures are negligibly small under design basis earthquake. In this chapter, nonlinear FE analysis results of the cyclic load behaviors of one-bay one-story prototype SC-EBF structure are presented and discussed. Two types of EBF configurations - K-type SC-EBF and D-type SC-EBF, are considered in this study. For each configuration of the SC-EBF structure, four different designs for the rocking link beam length and posttensioned (PT) tendon area are considered. For the investigated SC-EBF structures, the dominant ultimate failure mode is found to be the PT tendon yielding. The fuse devices for the SC-EBF structures are designed from perforated AISI 316L stainless steel link beams with web slits. Analytical base shear-drift relationships for the investigated SC-EBF structures are formulated and verified by comparing with the FE analysis results, which are useful for the design analysis of the SC-EBF structures.

6.1. Introduction

EBFs are widely used in North America as a seismic resistant structural system in buildings. Conventional EBF structure possesses high initial stiffness and ductility, yet under design basis earthquake, plastic deformation would occur in the link beams and

residual drift might thus result. Seismic retrofit of EBFs can be costly and time-consuming, as evidenced by the 2011 New Zealand earthquake in Christchurch.

As an alternative to control seismic damage, self-centering mechanism is introduced to conventional structural frames, such as moment resisting frames (MRF). Experiments conducted by Christopoulos et al. (2002), Ricles et al. (2002), Garlock et al. (2007), and Kim and Christopoulos (2008) verified the self-centering behavior of posttensioned MRFs without composite beam-slab effect. It was experimentally verified that the MRF structures can generally return to the original positions from the maximum inter-story drift ratio of 2% to 3%. Friction devices or steel angles were installed at the beam-to-column joints in the MRFs for seismic energy dissipation. The design procedures for the SC-MRF structures were proposed by Garlock et al. (2007) and Kim and Christopoulos (2009).

Similar to the low-damage design objective of the SC-MRF structures, the SC-EBF is expected to behave the same way as the conventional EBF structures under the low to moderate seismic load while it will have no or very little residual drift after the design basis earthquake. As reported in Chapter 2, currently very little research has been conducted on SC-EBF structures. The single experimental study of the quasi-static behaviors of the SC-EBF structure was conducted by Cheng et al. (2012).

Although the experiments on the SC-MRF structures with only one bay and one story exhibited promising self-centering behaviors (Christopoulos et al. 2002, Ricles et al. 2002, Garlock et al. 2007, and Kim and Christopoulos 2008), MacRae and Clifton (2013)

pointed out that in SC-MRF structures with multiple bays and stories, beam deformation discontinuities existed between the beams at different floor levels, rendering the beams in the upper story levels susceptible of losing contact with columns. Furthermore, MacRae and Clifton (2013) pointed out that the deformation incompatibilities existed between the beams and the slabs when the composite beam-slab sections formed. As a result, either severe cracking was induced to floor slabs due to gap opening at the beam-to-column joints; or the gaps at the beam-to-column joints were restrained from opening due to floor slabs, resulting in damage to the beams or columns.

The solutions to the identified problems in the SC-MRF structures by MacRae and Clifton (2013) can be very costly, which offsets the benefits brought by the SC-MRF structures. The deformation discontinuities of beams between different stories are related to the section depth differences of beams, as smaller sections are generally assigned to the beams in the upper stories of a MRF. The deformation discontinuities at the beam-to-column joints at upper stories would be completely eliminated if all beams were assigned with the same section size; yet this approach is not economical in the design of MRF since beams are generally long. On the other hand, MacRae and Clifton (2013) suggested two approaches in solving the deformation incompatibility between the floor slabs and the beams; however, both approaches required complicated design of the collector beams and the interfaces between slabs and beams, which significantly increases the construction cost.

SC-EBF is proposed with the hope of overcoming the above identified problems in the SC-MRF structures. Compared to the main girders in the SC-MRF structures, the link beams in the SC-EBF structures are much shorter and can be designed to have the same depth along building height without significantly increasing the design budget, in order to eliminate the gap opening discrepancy at different floor levels. Furthermore, instead of providing special design for the entire floor slab and collector beams proposed for the SC-MRF structures, only the floor slab in the vicinity of the link beam needs special design in the SC-EBF, which substantially reduces the work for floor design and construction.

Compared to conventional EBF structures, the SC-EBF structures are believed to outperform with the following advantages: 1) self-centering mechanism is introduced so that no or little residual drift exists after an earthquake; 2) damage in the structural structure is concentrated to the fuse devices that can be inspected and replaced more easily. Other structural components are designed to remain elastic during a design basis earthquake; 3) the strength, stiffness, ductility and energy dissipation properties of the SC-EBF can be tuned with more flexibility than conventional ductile design would allow for.

6.2. Case Study on K-type SC-EBF Structures

A total of four cases of the K-type SC-EBF structures with varying rocking link beam lengths and PT tendon areas were investigated in this study. The general configuration of the K-type SC-EBF structure is schematically illustrated in Figure 6-1, which was

adapted from the SC-EBF structure experimentally tested by Cheng et.al (2012). In case 1, the rocking link beam length is 980 mm and the PT tendon area on each side of the beam is 420 mm^2 from three 7-wires 0.6 inch nominal diameter PT strands (nominal area of one PT strand = 140 mm^2) strain respectively (i.e., total PT tendon area = 840 mm^2). In case 2, the rocking link beam length is 980 mm and the PT tendon area at each side of the beam is reduced to 280 mm^2 from two 7-wires 0.6 inch nominal diameter PT strands. In case 3, the rocking link beam length is increased twice to 2,060 mm and the PT tendon area at each side of the beam is 700 mm^2 from five 7-wires 0.6 inch nominal diameter PT strands. In case 4, the rocking link beam length is 2060 mm and the PT tendon area at each side of the beam is 462 mm^2 from three 7-wires 0.5 inch nominal diameter PT strands and three 7-wires 0.375 inch nominal diameter PT strands (nominal area of one 0.5 inch PT strand = 99 mm^2 and nominal area of one 0.375 inch PT strand = 99 mm^2). The PT tendon area is determined in such a way that the effective linear limit force values of the SC-EBF case 1 and case 3 are close to each other and that the effective linear limit force values of the SC-EBF case 2 are similar to that of case 4. PT tendons are post-tensioned between the beam-to-column joints in all the K-type SC-EBF cases. For all the K-type SC-EBF cases, the initial post-tensioning stress in the PT tendons is designated to have the same value. Gap openings are triggered at the pre-compressed joints once the lateral load exceeds the pre-set gap opening threshold value. The post-gap-opening stiffness of the SC-EBF is contributed by the force couple formed at the contact surface; and is generally made much lower than the SC-EBF's initial stiffness. Yielding of the PT tendon is set as one of the controlling limiting state of the K-type SC-

EBF structures, which would significantly reduce the SC-EBF's load carrying capacity due to imminent tendon fracture shortly after yielding. Replaceable fuse devices are installed on both sides of the rocking link beam for seismic energy dissipation.

6.2.1. Prototype K-type SC-EBF Structure

The prototype K-type SC-EBF structure under concern is adapted from the one-bay one-story SC-EBF test specimen designed by Cheng et al. (2012). Section sizes of the beams, columns, braces, and the rocking link beam are all increased to have increased stiffness and strength that is suitable for SC-EBF structures. Steel plates with a thickness of 50 mm were attached to the beam ends at the PT connections. To evaluate the effect of the rocking link beam length on the SC-EBF's performance, a shorter rocking link beam length of 980 mm is used in case 1 and case 2; while in case 3 and case 4, the rocking link beam length is increased twice to 2,060 mm. To evaluate the effects of the PT tendon area on the cyclic load behaviors of the SC-EBF structures, the PT tendon area in case 2 was reduced to two-thirds that of case 1; and the PT tendon area in case 4 was also made approximately two-thirds that of case 3. The beam length in all the SC-EBF cases was fixed at 2,700 mm; the column height was fixed at 3,367 mm; and the inclination angle between the brace and the column in each SC-EBF case was fixed at 40°. Beam sections in case 3 and case 4 were enlarged to keep the initial axial compression stress in the beams from PT tendons approximately the same as that of case 1 and case 2. Section dimensions for the beams, columns, braces, and rocking link beam of the four SC-EBF cases are listed in Table 6-1.

Specially detailed fuse devices were connected between the beams' end plates on the two sides of the rocking link beam in the SC-EBF structures. The fuse devices were fabricated using hot-rolled AISI 316L stainless steel I-section beam. The section sizes of the fuse devices were S 6x12 in case 1 and case 2 (hereafter referred to as "short fuse") and S 5x10 in case 3 and case 4 (hereafter referred to as "long fuse"). Horizontal slits were perforated over the web area of the stainless steel fuse beams to achieve the desired properties. For the short fuse, the perforated slits had the constant length of 60 mm and width of 16 mm, and were spaced at the fixed distance of 16 mm in the vertical direction. For the long fuse, the perforated slits had the constant length of 40 mm and width of 10.8 mm, and were spaced at the fixed distance of 10.8 mm in the vertical direction. As the axial deformation induced by the gap opening was significantly large, a "finger" joint was created at the middle of the fuse devices to prevent axial stress due to longitudinal expansion associated with link beam rocking after gap opening. The "finger" joint was capable of transferring shear force but would slide freely in longitudinal direction. Hence the axial force within the fuse devices was substantially reduced to the amount caused only by the friction force developing over the contact surfaces of the "finger" joint; and the transfer of transverse shear force in the fuse devices was not disrupted. Section details of the two perforated AISI 316L fuse beams are schematically shown in Figure 6-2 and Figure 6-3 respectively. The "finger" section in both fuses measures 140 mm long with a thickness of 30 mm. The friction coefficient μ at the contact interfaces at the "finger" section was set as 0.3.

6.2.2. Finite Element Simulation Study

Nonlinear finite element analysis of the four cases of K-type SC-EBF structures were performed using ANSYS Academic ver. 15.0. The primary EBF frame members of the SC-EBF structures use A992 steel and the fuse devices were made of AISI 316L stainless steel. The combined plasticity hardening model was employed to characterize the stress strain relationship for both materials under cyclic loading. The calibrated material parameters of the combined hardening models for A992 steel and AISI 316L stainless steel can be found in Chapter 2.

With regard to the finite element model establishment for the EBF structures installed with replaceable link beams (Mago 2013), the structural components of the K-type SC-EBF structures were represented by different elements in ANSYS Academic ver. 15.0. Beam elements were adopted for modeling the SC-EBF's columns, and portions of the beams and braces away from the rocking link beam. Shell elements were used for the middle portion of the rocking link beam, the fuse beams, and portions of the beams and braces that are near the rocking link beam. Solid elements were employed to model the beam end plates and the two end portions of the rocking link beam to ensure exact compression zone size over the contact surface. Link elements were utilized for modeling the PT tendons. As the SC-EBF structure is symmetric about the web plane of the EBF beam, only half model was built to represent the SC-EBF structure in ANSYS. The meshed model of a typical prototype SC-EBF structure is shown in Figure 6-4.

Loading procedure adopted for the FE analysis of the SC-EBF structure involves two quasi static steps.

Step 1: Starting from time zero, the initial post-tensioning force was gradually applied to the PT tendons and completed at time equal to one. At time equal to one, the post-tensioning stress in the PT tendons was 741 MPa. This step corresponds to the physical post-tensioning process of the PT tendons.

Step 2: From time equal to one, a cyclic loading protocol was applied to the SC-EBF structure. The cyclic loading protocol expressed in terms of the SC-EBF's story drift ratio is adapted from the experiment loading protocol by Ricles et al. (2006). This loading protocol includes first three cycles with an amplitude of 0.005, and the following every three cycles with an amplitude increment of 0.005. The loading protocol applied to the SC-EBF structures is plotted in Figure 6-5. This step represented the cyclic loading process of the SC-EBF structure and was terminated once the PT tendons yielded.

6.2.3. Analytical Force-Displacement Relations of K-type SC-EBF Structures

6.2.3.1. General view

The gradual gap opening process of the SC-EBF is schematically illustrated in Figure 6-6, which can be divided into five distinct phases. In phase I, the EBF beams are in full contact with the rocking link beam and the compression stress is uniformly distributed over the contact surface. In phase II, the contact stress at the bottom flange reduces to zero while maximum contact stress occurs at the top flange at the left side of the link

beam. In phase III, the compression zone shrinks and the zero contact stress location moves upward to the mid-height of the rocking link beam; the PT tendons are on the verge of being elongated. In phase IV, the zero contact stress point continues to move upwards at the left side of the link beam. PT tendons are elongated due to gap opening. In phase V, zero contact strain location is near the top flange of the left side of the link beam. Based on the research conducted by Christopoulos (2002), the transition between phase II and phase III is very swift.

Usually the fuse device is designed to be much weaker than the primary frame of the SC-EBF. Hence the interaction effect between the fuse device and the SC-EBF's frame is assumed to be negligible so that the mechanical properties of the SC-EBF structure can be decoupled, i.e., the force displacement relationship of the SC-EBF structure can be calculated by superimposing that of the SC-EBF's frame and fuse devices. This calculation strategy which greatly simplifies the analytical formulation process is schematically illustrated in Figure 6-7.

6.2.3.2. Force-Displacement Relationship

The force displacement relationship of the SC-EBF frame is governed by three key parameters: the initial stiffness K_1 , the effective linear limit force F_y (which is equal to the applied lateral force at gap opening), and the post-gap-opening stiffness K_2 . The internal force distribution of the rocking link beam in the SC-EBF frame under the applied lateral load is shown in Figure 6-8.

Referring to the relationship proposed by Richards (2010), the elastic deformation of an EBF is comprised of four parts: the axial deformation of the braces, the axial deformation of the beam, the shear deformation of the beam, and the bending deformation of the beam. Before gap opening, the lateral elastic stiffness of the SC-EBF is identical to that of conventional EBFs. Therefore, the initial stiffness K_1 of the SC-EBF frame is calculated using the equation proposed by Richards (2010), which is expressed in Equation 6-1:

$$K_1 = \frac{1}{\frac{1}{2E} \left(\frac{L_d}{A_d} \right) \left(\frac{L_d}{a} \right)^2 + \frac{1}{2E} \left(\frac{a}{A_b} \right) + \frac{1}{G} \left(\frac{H^2 e}{A_{bv} L^2} \right) + \frac{H^2 e^2}{12EI L}} \quad \text{Equation 6-1}$$

Where: terms L , L_d , e , a , and H are the SC-EBF's full bay width, brace length, rocking link beam length, beam length, and bay height shown in Figure 6-8; terms E and G are the elastic modulus and shear modulus of A992 steel; terms A_d , A_b , and A_{bv} are the brace's section area, beam's section area, and the beam's web area respectively.

The PT tendons are further stretched after the gap opens between the beam end plates and the rocking link beam ends. The bending moments at the end sections of the rocking link beam are equal to the force couple formed by the PT tendon force and the compression force resultant over the contact surfaces. From the research work by Christopoulos (2002), the compression contact stress is assumed to be linearly distributed over the flange thickness of the link beam. Therefore, the effective linear limit force F_y of the bare SC-EBF frame without fuse devices can be calculated as Equation 6-2:

$$F_y = 2P = 2 \cdot \frac{M \cdot L}{H \cdot e} = \frac{2 \cdot F_{PT_0} \cdot \left(\frac{1}{2}h - \frac{1}{3}t_f\right) \cdot L}{H \cdot e} = \frac{F_{PT_0} \cdot (h - t_f) \cdot L}{H \cdot e} \quad \text{Equation 6-2}$$

Where F_y is the effective linear limit force of the bare SC-EBF frame; h and t_f are the depth and flange thickness of the rocking link beam.

After gap opening, the increment of the PT tendon force is proportional to the gap opening distance at the mid-height of the link beam, which is calculated from Equation 6-3.

$$F_{PT} = \beta \cdot E_{PT} \cdot A_{PT} \cdot \frac{\Delta_{PT}}{L} + F_{PT_0} = F_{PT_0} + \beta \cdot E_{PT} \cdot A_{PT} \cdot \frac{\gamma_{gap} \cdot (h - t_f)}{L} \quad \text{Equation 6-3}$$

$$\Delta_{PT} = \frac{h_w}{2} \cdot \gamma_{gap} \cdot 2 = (h - t_f) \cdot \gamma_{gap}$$

The relationship among the link rotation angle γ , the gap opening angle γ_{gap} , and the lateral displacement Δ_{push} is expressed in Equation 6-4:

$$\theta \cdot L = \frac{\Delta_{push}}{H} \cdot L = \gamma \cdot e = (\gamma_{gap} + \gamma_0) \cdot e \quad \text{Equation 6-4}$$

Considering the force equilibrium relation for the SC-EBF frame, the relationship between the lateral force P and the PT tendon force F_{PT} is expressed in Equation 6-5:

$$P = \frac{V \cdot \frac{1}{2}L}{H} = \frac{M \cdot L}{H \cdot e} = \frac{F_{PT} \cdot \left(\frac{1}{2}h - \frac{1}{2}t_f\right) \cdot L}{H \cdot e} \quad \text{Equation 6-5}$$

Take derivatives of both sides of Equation 6-5, the post-gap-opening stiffness K_2 of the SC-EBF frame is expressed in Equation 6-6.

$$K_2 = \frac{dV_{base}}{d\Delta_{push}} = \frac{2 \cdot dP}{d\Delta_{push}} = \frac{\beta \cdot E_{PT} \cdot A_{PT} \cdot (h - t_f)^2 \cdot L}{H^2 \cdot e^2} \quad \text{Equation 6-6}$$

Where: term E_{PT} is the elastic modulus of the PT tendons; A_{PT} is the section area of the PT tendons; F_{PT0} is the initially applied tension force in the PT tendons; γ_0 is the critical link rotation angle at gap opening; β is the parameter to account for the stress loss of the PT tendons due to the axial elastic compressive deformation of the SC-EBF during the loading process as a result of the increased axial compression force from PT tendons. The meaning of β is illustrated in the following paragraph.

The displaced configuration of the SC-EBF frame is plotted in Figure 6-9. Under the lateral load, the the SC-EBF frame is first deformed to the shape which is represented by the solid black line in Figure 6-9. However, the axial compression force applied to the beams and the rocking link beam of the SC-EBF frame by the PT tendons is also increased due to the additional gap opening at the interface between the rocking link beam and the beams. As a result, the beams and the rocking link beam are further compressed to the deformed shape represented by the red dashed line in Figure 6-9. Thereby, the tension stress of the PT tendons is decreased due to the additional elastic deformation of the SC-EBF frame. The real instantaneous tension stress in the PT tendons is computed by multiplying the parameter β to the tension stress of the PT tendon when the additional elastic deformation of the SC-EBF is not considered. Parameter β is

related to the stiffness of the SC-EBF frame and the PT tendon, expressed in Equation 6-7.

$$\beta = \frac{(A_{beam} + A_{brace} \cdot \cos^3 \alpha) \cdot A_{link} \cdot L}{(A_{beam} + A_{brace} \cdot \cos^3 \alpha)A_{link}L + 2A_{link}A_{PT}a + A_{PT}(A_{beam} + A_{brace} \cdot \cos^3 \alpha)e} \quad \text{Equation 6-7}$$

Where: A_{beam} , A_{link} , and A_{brace} are the section area of the beams, rocking link beam, and braces of the SC-EBF frame; L , a , and e are the SC-EBF frame length, beam length, and rocking link beam length respectively shown in Figure 6-8; α is the angle between the brace and the horizontal direction.

6.2.3.3. Contribution from Fuse Device

In the initial configuration of the SC-EBF shown in Figure 6-10, the corner points of the rocking link beam are coinciding with points A_1 and B_1 on the left-side beam end plate and points A_2 and B_2 on the right-side beam plate. The end points of the fuse link's centerline are located at points O_1 and O_2 at the mid-height of the beam. Unit vectors \vec{e}_1 (i.e., \mathbf{i}) and \vec{e}_2 (i.e., \mathbf{j}) are defined to be parallel and perpendicular to the longitudinal axis of the beam respectively in the initial configuration of the SC-EBF. In the displaced configuration of the SC-EBF shown in Figure 6-11, when the SC-EBF is pushed to the right by a lateral load, points A_1 , A_2 , B_1 , B_2 , O_1 , and O_2 move to the new locations of A_1' , A_2' , B_1' , B_2' , O_1' , and O_2' respectively and the angle between the displaced beam's longitudinal axis and the horizontal direction is defined as θ . As the elastic deformation of the rocking link beam is negligible, the length of the rocking link beam's diagonal line is assumed to be unchanged, i.e., $B_1A_2=B_1'A_2'$. The fuse's relative end displacement Δ_{fuse}

is equal to the projected length of vector $\overrightarrow{O'_1O'_2}$ to the directional vector $\overrightarrow{e'_2}$. The relationship of Δ_{fuse} with respect to θ is calculated in Equation 6-8:

$$\begin{aligned}\overrightarrow{O'_1O'_2} &= \overrightarrow{O'_1B'_1} + \overrightarrow{B'_1A'_2} + \overrightarrow{A'_2O'_2} = \overrightarrow{B'_1A'_2} + h \cdot (\sin\theta \cdot \mathbf{i} + \cos\theta \cdot \mathbf{j}) \\ \overrightarrow{B'_1A'_2} &= e' \cdot \cos[\alpha_0 - (\gamma - \theta)] \cdot \mathbf{i} - e' \cdot \sin[\alpha_0 - (\gamma - \theta)] \cdot \mathbf{j} \\ \overrightarrow{O'_1O'_2} &= e' \cdot \cos[\alpha_0 - (\gamma - \theta)] \cdot \mathbf{i} - e' \cdot \sin[\alpha_0 - (\gamma - \theta)] \cdot \mathbf{j} + h \cdot \sin\theta \cdot \mathbf{i} + h \cdot \cos\theta \cdot \mathbf{j} \\ \overrightarrow{e'_2} &= \sin\theta \cdot \mathbf{i} + \cos\theta \cdot \mathbf{j} \\ \Delta_{fuse} &= [e' \cdot \cos(\alpha_0 - \gamma + \theta) + h \cdot \sin\theta] \sin\theta \\ &\quad + [h \cdot \cos\theta - e' \cdot \sin(\alpha_0 - \gamma + \theta)] \cos\theta\end{aligned}\tag{Equation 6-8}$$

Where: e' is the length of B_1A_2 ; α_0 is the angle between the diagonal direction and the longitudinal axis of the rocking link beam; θ is the angle formed between the longitudinal axis of the beam and the horizontal direction in the displaced configuration; and γ is the link rotation angle corresponding to θ .

The calculation of the critical link rotation angle γ_0 at gap opening is illustrated in Figure 6-12. The maximum contact stress occurs at the top flange of the rocking link beam. The link rotation angle γ_0 is equal to the shortening of the top flange divided by the distance from the neutral axis to the center of the top flange of the rocking link beam before gap opening. The compression force applied to the link beam by the PT tendons is equal to the compression force at the contact interface. Thereby, the critical link rotation γ_0 can be calculated based on Equation 6-9:

$$F_{PT_0} = F_C = \frac{1}{2} E \cdot t_f \cdot b_f \cdot \varepsilon_0$$

$$\gamma_0 = \frac{\varepsilon_0 \cdot e}{\frac{1}{2}(h - t_f)} = \frac{2F_{PT_0} \cdot e}{E \cdot t_f \cdot b_f \cdot (h - t_f)}$$

Equation 6-9

Where: terms t_f , b_f , e , and h are the rocking link beam's flange thickness, flange width, link length and depth respectively; ε_0 is the compression strain at the top flange center.

The angle θ_0 formed by the beam's longitudinal axis to the horizontal axis at gap opening is calculated from Equation 6-10.

$$\theta_0 = \frac{\Delta}{H} = \frac{F_y}{K_1 H} = \frac{F_{PT_0} \cdot L \cdot (h - t_f)}{K_1 \cdot H^2 \cdot e}$$

Equation 6-10

After gap opening, the link rotation angle γ is equal to the sum of the gap opening angle γ_{gap} and the critical link rotation angle γ_0 at gap opening. The tension force of the PT tendons is proportionally increased with gap opening. Based on the force equilibrium of the SC-EBF frame, the relationship between the gap opening angle γ_{gap} and the lateral load P applied at the EBF beam-column joint is expressed in Equation 6-11.

$$F_{PT} = F_{PT_0} + 2 \cdot \beta \cdot E_{PT} \cdot A_{PT} \cdot \frac{\Delta_{PT}}{L} = F_{PT_0} + \beta \cdot E_{PT} \cdot A_{PT} \cdot \frac{\gamma_{gap} \cdot (h - t_f)}{L}$$

Equation 6-11

$$P = \frac{M \cdot L}{H \cdot e} = \frac{F_{PT} \cdot \left(\frac{1}{2}h - \frac{1}{2}t_f\right) \cdot L}{H \cdot e}$$

From the force displacement relationship of the SC-EBF frame, the relationship between P and θ is expressed in Equation 6-12:

$$\theta = \theta_0 + \frac{2P - F_y}{K_2 \cdot H} \quad \text{Equation 6-12}$$

It is assumed that the link rotation angle γ is linearly related to θ before gap opening as the deformation of the SC-EBF structure is very small. Therefore, the relationship of γ with respect to θ is expressed in Equation 6-13:

$$\gamma = \begin{cases} \gamma_{gap} + \gamma_0 = \frac{K_2 \cdot H^2 \cdot e \cdot \theta + (K_1 - K_2)H^2 \cdot e \cdot \theta_0 - F_{PT_0} \cdot L \cdot (h - t_f)}{2\beta \cdot E_{PT} \cdot A_{PT} \cdot (h - t_f)^2} + \gamma_0 & \text{for } \theta \\ \frac{\theta}{\theta_0} \gamma_0 = \frac{4K_1 \cdot H^2 \cdot e^2}{E \cdot t_f \cdot b_f \cdot (h - t_f)^2 \cdot L} \theta & \text{for } \theta \end{cases} \quad \text{Equation 6-13}$$

The relative end displacement of the fuse device can be related to the drift of the SC-EBF by combining Equation 6-8 and Equation 6-13.

6.2.3.4. Force Displacement Relationship of Fuse Members

Fuse members were also modeled in ANSYS ver. 15. From the FEM simulation results, the cyclic shear force versus end displacement relationships of the short fuse and the long fuse used for the SC-EBF structures in this study are plotted in Figure 6-13.

6.2.3.5. Contribution of Fuse Shear to SC-EBF Structure

The additional base shear force ΔV_b of the SC-EBF structure required to balance the shear force of the fuse devices is calculated from Equation 6-14. The base shear force on the SC-EBF structure with fuse devices is equal to the sum of the lateral force applied to

the SC-EBF frame and the additional lateral force due to the fuse members (two fuse members total were used, one on each side of the rocking link beam).

$$\Delta V_b = 2 \cdot \frac{V_{fuse} \cdot \frac{1}{2}L}{H} - f = \frac{V_{fuse} \cdot L}{H} - \mu \cdot V_{fuse} \quad \text{Equation 6-14}$$

6.2.3.6. Validation of the Analytical Force Displacement Formulation for the SC-EBF Structure

The accuracy of the analytical formulation on the force displacement relationship of the SC-EBF structure is verified by comparing with the FEM analysis results. For the investigated four cases of the K-type SC-EBF structures, the hysteresis lateral force vs. drift curves obtained from FEM simulation and analytical derivation are plotted in Figure 6-14 through Figure 6-17. Tensile stress in the PT tendons was recorded during the cyclic loading process in the FEM analysis. Yielding of the PT tendons occurred in the 7th load cycle for case 1 and case 2 when the drift ratio reached approximately 1.4%; while PT tendon yielding occurred in the 15th loading cycle for case 3 and case 4 when the drift ratio reached little over 2.5%. Accordingly, the hysteresis lateral force vs. drift curves of case 1 and case 2 were truncated after the first occurrence of the drift ratio of 1.4%; and the hysteresis lateral force vs. drift curves of case 3 and case 4 were truncated at the end of the 15th loading cycle.

It can be observed that the analytically derived curves match well with the corresponding FEM simulation curves for the investigated four cases of the SC-EBF structures. The

analytical derivations on the lateral force vs. drift curves for the SC-EBF case 3 and case 4 slightly deviate from the FEM curves. It is concluded that as the rocking link beam is less rigid in case 3 and case 4, the assumption made in Equation 6-8 that the rocking link beam behaves as a rigid body is less accurate. Reflected in Figure 6-14 through Figure 6-17, the analytical derived curves are seen to generally over-estimate the residual drift of the SC-EBF structures.

6.2.4. Numerical Simulation Results and Discussion

A total of seven sections were selected from the K-type SC-EBF cases for evaluating the internal force responses in this study. Internal forces including the axial force, the shear force, and the bending moment were recorded at the selected locations during FE simulation. The selected key locations are marked in Figure 6-18, including the left side (section A-A), middle (section B-B), and the right side (section C-C) of the beam on the left, the middle (section D-D) and bottom (section E-E) of the column on the left, the middle section (section F-F) of the bracing on the left, and the left section (section G-G) of the rocking link beam. Similar to the above treatment for the hysteresis loops of the SC-EBF cases, for case 1 and case 2, all recorded internal forces at the seven selected sections were truncated after the first occurrence of the drift ratio of 1.4%; and for case 3 and case 4, all recorded internal forces at the selected sections were truncated at the end of the 15th loading cycle.

6.2.4.1. EBF Beam

The axial force histories at sections A-A, B-B, and C-C for case 1 to case 4 are plotted in Figure 6-19. The axial forces in the beams of the K-type SC-EBF structures were normalized by the beams' axial yield force N_P , which was equal to the product of nominal yield stress of A992 steel and the beams' gross cross-section area. The maximum N/N_P value occurred during the 6th loading cycle for case 1 and case 2 at the drift ratio of 1.5%. And the maximum N/N_P ratio was observed during the 15th loading cycle for case 3 and case 4 at the drift ratio of 2.5%. It can be also observed that N/N_P ratio was significantly lower in case 2 and case 4 compared to case 1 and case 3, as the PT tendon area was reduced by 1/3. As the beam section area is much larger in case 3 than in case 1, the axial force in case 3 at PT tendon yielding was much higher than the axial force in case 1 at PT tendon yielding.

The shear force histories of these three beam sections (section A-A, section B-B, and section C-C) for the four cases of the K-type SC-EBF structures are plotted in Figure 6-20 through Figure 6-22. The shear forces in the beams of the K-type SC-EBF structures were normalized by the beams' shear strength V_P , which was equal to the product of the material's nominal shear yield stress ($=0.6f_y$) and web area for wide-flange steel shapes. It can be observed that at these three sections the V/V_P ratio was very small and barely changed with the increasing drift. The V/V_P ratio was slightly lower in the SC-EBF cases with reduced PT tendon area. For each K-type SC-EBF case, the V/V_P ratio at the three

selected sections of the beam was identical, since there is no other transverse external force acting over the beam.

The bending moment histories at these three sections of the EBF beam in the four cases of the SC-EBF structures are plotted in Figure 6-23 through Figure 6-25. The bending moments in the beams of the SC-EBF structures were normalized by the beams' plastic moment M_P , which was equal to the nominal yield stress multiplied by the beam's plastic section modulus. It can be observed that the M/M_P ratio was smallest near the beam-to-column joint and largest near the beam-to-link joint, which is consistent with the moment distribution pattern in the EBF subjected to lateral load. It can also be observed that the M/M_P ratio was lower in the SC-EBF cases with reduced PT tendon area, as expected. During the loading process, it can be observed that M/M_P ratio increased much more rapidly in the SC-EBF cases with short link beam length. As the plastic moments of the EBF beams in case 3 and case 4 are much higher than those in case 1 and case 2, the actual beam end bending moments in case 3 and case 4 were much higher than the beam end bending moments in case 1 and case 2 respectively.

6.2.4.2. EBF Column

The shear force histories at the middle-length section (section D-D) and the bottom section (section E-E) of the column for the four cases of the K-type SC-EBF structures under cyclic loading are plotted in Figure 6-26 and Figure 6-27. The shear forces were normalized by the column's shear strength V_P , which was equal to the product of the material's nominal shear yield stress ($=0.6f_y$) and web area for I-section steel shape. It

can be observed that at the V/V_P ratio was fairly small in the column up to the maximum drift ratio. This phenomenon is in agreement with theoretical analysis, as column is primarily subjected to axial force. The V/V_P ratios at the two selected sections in each K-type SC-EBF case were generally identical, which is in agreement with the theoretical analysis, as no lateral force was acting along the column. Shown in Figure 6-26 and Figure 6-27, the column shear forces in the SC-EBF cases with long rocking link beam (case 3 and case 4) were generally higher than that of the SC-EBF cases with short link beam (case 1 and case 2).

6.2.4.3. EBF Bracing

The axial force history of the middle-length section (section F-F) of the brace for the four investigated cases of the SC-EBF structures are plotted in Figure 6-28. Similar to the afore-mentioned beam axial force normalization procedure, the bracing axial force of the SC-EBF structures was normalized by the bracing's axial yield strength N_P , which was equal to the nominal yield stress multiplied by the brace's gross section area. Shown in Figure 6-28, the brace's maximum N/N_P ratio was 0.3 in case 3 at the peak drift ratio. Similar to the observation made on the N/N_P ratio in the beams of the K-type SC-EBF cases, the N/N_P ratios of case 2 and case 4 were smaller than the N/N_P ratios of case 1 and case 3, as the PT tendon areas were smaller. However, when yielding of the PT tendons occurred, the axial forces in case 1 and case 3 were very close.

6.2.4.4. Rocking Link Beam

The axial force history of the left end section (section G-G) of the rocking link beam for the four investigated cases of the SC-EBF structures is plotted in Figure 6-29. The axial force in the rocking link beam of the SC-EBF structures were normalized by the rocking link beam's axial yield strength N_P , which was equal to the nominal yield stress multiplied by the link beam's gross section area. It can be observed that the N/N_P ratio was substantially lower in the K-type SC-EBF cases with reduced PT tendon area.

The shear force history of the left end section of the rocking link beam for the four investigated cases of the SC-EBF structures is plotted in Figure 6-30. The shear force in the rocking link beam of the SC-EBF structures were normalized by the rocking link beam's plastic shear strength V_P . Upon yielding of PT tendons, the V/V_P ratios for case 1 and case 3 were close to each other; yet as the link beam's plastic shear strength V_P is higher in case 1, the actual shear force is higher in the K-type SC-EBF cases with short link beam length at PT tendon yielding.

The bending moment history of the left end section of the rocking link beam for the four investigated cases of the K-type SC-EBF structures is plotted in Figure 6-31. The shear force in the rocking link beam of the SC-EBF structures were normalized by the rocking link beam's plastic moment M_P . It can be observed that the M/M_P ratio was significantly larger in case 3 than in case 1 at PT tendon yielding; hence the link end moment is larger in the K-type SC-EBF cases with long rocking link beam.

6.2.4.5. PT Tendon

The tensile stress in the PT tendons versus the drift ratio of each SC-EBF case is plotted in Figure 6-32. The minimum nominal yield stress of the G270 PT tendon is 1670 MPa, which is also indicated in Figure 6-32. The occurrence of the PT tendon yielding is set as one of the ultimate limit state for the SC-EBF structures, as the ultimate fracture stress of the PT tendon is very close to its yield stress. Shown in Figure 6-32, the tensile stress in the PT tendons of the SC-EBF cases with short link beam length increases much more rapidly with the increasing lateral drift ratio than the SC-EBF cases with the long link beam length.

6.2.4.6. Damage Index for Fuse Members

Fracture of the fuse members should be avoided by all means in the SC-EBF design, since the lateral drift ratio of the SC-EBF would be significantly increased so that the frame can take over the additional force carried out by the fuse devices. With reference to the research conducted by Kanvinde and Deierlein (2007) on the cyclic void growth model (CVGM) for predicting the ductile fracture initiation of structural steel, the damage index is defined as the ratio of the cyclic void growth index (CVGI) to the critical cyclic void growth index ($CVGI_{critical}$), which is expressed in Equation 6-15. The damage index should be controlled less than 1 to ensure the prevention of the ductile fracture initiation.

$$Damage = \frac{CVGI}{CVGI_{critical}} \quad \text{Equation 6-15}$$

The definition of CVGI and $CVGI_{critical}$ can be found in Chapter 2.

FE analysis was conducted on the fuse members of S6x12.5 link (short fuse) and S5x10 link (long fuse) that were treated as the substructures. The end displacements of the fuse members retrieved from the finite element models of the SC-EBF cases were substituted to the substructures for the fuse members. Meshing was further refined for the substructures. The damage index history was calculated from the identified critical locations of the substructure models of the fuse members, as shown in Figure 6-33. It can be observed that when the PT tendons started to yield, the damage index in the fuse members is still far below 1, indicating fracture of fuse members is not a controlling limit state here. The Von Mises plastic strain contour for the short fuse at the maximum lateral drift ratio of 1.4% for case 1 and the Von Mises plastic strain contour for the long fuse at the maximum lateral drift ratio of 2.5% for case 3 are plotted in Figure 6-34 and Figure 6-35 respectively. As observed in Figure 6-35, severe flange and web buckling is triggered at the right-side end of the long fuse.

6.2.4.7. Cyclic Loading Behavior of K-type SC-EBF Structures

The cyclic loading behaviors of the K-type SC-EBF cases were assessed in terms of the following structural parameters: the initial stiffness of the SC-EBF frame (K_1), the post-gap-opening stiffness of the SC-EBF frame (K_2), the effective linear limit force (F_y), which is equal to the required lateral force at gap opening of the SC-EBF frame, the

ultimate strength (F_u), which is equal to the maximum allowable lateral force corresponding to the ultimate limit state, and the energy dissipation capacity. Parameter α is defined as the ratio of K_1 to K_2 . The hysteretic energy dissipation capacity is quantified with the hysteretic energy dissipation ratio β_E , which is defined as the ratio of the hysteresis loop area of a self-centering structure to the area of a bilinear elastoplastic system under cyclic loading to the same maximum displacement (Seo and Sause 2005). The ductility of the SC-EBF structures is represented by the ultimate drift ratio δ_u , which is the drift ratio at the ultimate limit state. Detailed data of the cyclic loading behavior of the K-type SC-EBF structures in this study are listed in Table 6-2.

6.3. Case Study on D-type SC-EBF Structures

Self-centering behaviors were also investigated for the D-type SC-EBF structures. For comparison purpose, the four investigated cases of D-type SC-EBF structures were modified on the basis of the four cases of the K-type SC-EBF structures respectively. The general configuration of the D-shape SC-EBF structure is schematically illustrated in Figure 6-36. The D-type SC-EBF structures in this study were labeled as case I, case II, case III, and case IV, which correspond to case 1 through case 4 of the K-type SC-EBF structures. The PT tendon size, initial PT stress, rocking link beam length, and section sizes of the beam, the column connecting the beam, the rocking link beam, and the brace of the D-type SC-EBF structures are the same as the corresponding K-type SC-EBF case. The beam length in the D-type SC-EBF case is twice that of the corresponding K-type SC-EBF case as the beam was installed on one side only. The inclination angle between

the brace and the column in the D-type SC-EBF was adjusted accordingly for the beam length increase and a larger section than the column section in the K-type SC-EBF is used for the right side column adjacent to the rocking link beam. Replaceable fuse devices of the same section sizes as that in the corresponding K-type SC-EBF cases are installed on both sides of the rocking link beam of the D-type SC-EBF cases for energy dissipation. Similarly, yielding of the PT tendon is set as one of the controlling limit states of the D-type SC-EBF structures.

6.3.1. Prototype D-type SC-EBF Structure

For the investigated D-type SC-EBF structures, a short rocking link beam with a length of 980 mm is used in case I and case II; while in case III and case IV, the rocking link beam length is doubled to 2,060 mm. Steel plates with a thickness of 50 mm are welded to the beam end next to the link beam. To evaluate the effects of PT tendon area on the cyclic load behaviors of the D-type SC-EBF structures, the PT tendon area in case II was reduced to two-thirds that of case I; and the PT tendon area in case IV was also made approximately two-thirds that of case III. The EBF beam length in all four D-type SC-EBF cases is fixed at 5,400 mm; the column length is fixed at 3,367 mm; and the inclination angle between the brace and the column in each D-type SC-EBF case is 62.3° . Section dimensions of the beam, the column connecting the beam, the brace, the rocking link beam, and the column connecting the rocking link beam of the four D-type SC-EBF cases are listed in Table 6-3.

Similarly, the section sizes of the fuse devices were S 6x12 in case I and case II (hereafter referred to as “short fuse”) and S 5x10 in case III and case IV (hereafter referred to as “long fuse”). Perforation designs and the finger joint designs of the fuse devices are the same as those for the K-type SC-EBF cases.

6.3.2. Finite Element Simulation Study

Nonlinear finite element analysis of the four cases of the D-type SC-EBF structures were performed in ANSYS Academic ver. 15.0. The primary EBF frame members of the SC-EBF structures were made of A992 steel and the fuse devices were made of AISI 316L stainless steel. The combined plasticity hardening model was employed to characterize the stress strain relationship for both materials under cyclic loading. The calibrated material parameters of the combined hardening models for A992 steel and AISI 316L stainless steel can be found in Chapter 2.

Finite element models were built for the D-type SC-EBF structures in a similar approach as the K-type SC-EBF structures. Beam elements were adopted for modeling the SC-EBF’s columns, and portions of the beams and braces away from the rocking link beam. Shell elements were used for the rocking link beam, the fuse beams, and portions of the beams and braces that are near the rocking link beam. Link elements were utilized for modeling the PT tendons. As the SC-EBF structure is symmetric about the web planes of the EBF beam, only half model was built to represent the SC-EBF structure in the ANSYS. The meshed model of a typical D-type SC-EBF structure is shown in Figure 6-37.

Loading procedure adopted for the FE analysis of the D-type SC-EBF structure involves two steps as below:

- Step 1 (applying PT force): Starting from time zero, the initial PT force was gradually applied to the PT tendons and completed at time equal to one. At time equal to one, the pre-tensioning stress in the PT tendons was 741 MPa. This step corresponds to the physical post-tensioning process of the PT tendons.
- Step 2 (cyclic loading test): From time equal to 1, a cyclic loading protocol was applied to the D-type SC-EBF structure. The cyclic loading protocol applied to each D-type SC-EBF case was the same as that of the corresponding K-type SC-EBF case.

6.3.3. Analytical Force-Displacement Relations of D-type SC-EBF Structures

For the four cases of the D-type SC-EBF structures, the hysteresis lateral force vs. drift curves obtained from FEM simulations are plotted in Figure 6-39. For case I and case II, the force displacement hysteresis loops were truncated after PT tendon yielding in the 7th loading cycle when the drift ratio reached approximately 1.5%. For case III and case IV, the force displacement hysteresis loops were truncated after the end of the 15th load cycle when the drift ratio reached 2.5%. The tension stress in the PT tendons in case III and case IV is slightly below its yield strength at that time point.

A total of eight sections were selected from the D-type SC-EBF cases for evaluating the internal force responses in this study. Internal forces including the axial force, the shear

force, and the bending moment were recorded at the selected locations during FE simulation. The selected key locations are marked in Figure 6-38, including the left side (section A-A), middle (section B-B), and the right side (section C-C) of the beam, the middle (section D-D) and bottom (section E-E) of the column connecting the beam, the middle section (section F-F) of the brace, and the middle section (section G-G) of the column connecting the rocking link beam, and the right side (section H-H) of the rocking link beam. Similar to the above treatment for the hysteresis loops of the SC-EBF cases, for case I and case II, all recorded internal forces at the eight selected sections were truncated after the first occurrence of the drift ratio of 1.5%; and for case III and case IV, all recorded internal forces at the selected sections were truncated at the end of the 15th loading cycle.

6.3.4.1. EBF Beam

The axial force histories at section A-A in case I through case IV are plotted in Figure 6-40. The axial forces in the beam of the D-type SC-EBF structures were normalized by the beams' axial yield force N_P . The maximum N/N_P value occurred during the 9th loading cycle for case I and case II at the drift ratio of 1.5%. And the maximum N/N_P ratio was observed during the 15th loading cycle for case III and case IV at the drift ratio of 2.5%. It is also observed that N/N_P ratio in case II and case IV was lower than case I and case III, as the PT tendon area was reduced by 1/3.

The shear force histories of these three beam sections (section A-A, section B-B, and section C-C) for the four cases of the D-type SC-EBF structures are plotted in Figure

6-41 through Figure 6-43. The shear forces in the beams of the D-type SC-EBF structures were normalized by the beams' shear strength V_p . It can be observed that at these three sections the V/V_p ratio was fairly small. The V/V_p ratio was slightly lower in the D-type SC-EBF cases with reduced PT tendon area. For each D-type SC-EBF case, the V/V_p ratio at the three selected sections of the beam was identical, since there is no other transverse external force acting along the beam.

The bending moment histories at these three sections of the EBF beam in the four cases of the D-type SC-EBF structures are plotted in Figure 6-44 through Figure 6-46. The bending moments in the beams of the SC-EBF structures were normalized by the beams' plastic moment M_p . It can be observed that the M/M_p ratio was smallest near the beam-to-column joint and largest near the beam-to-link joint, which is consistent with the moment distribution pattern in the EBF subjected to lateral load. It can also be observed that the M/M_p ratio was lower in the SC-EBF cases with reduced PT tendon area, as expected. During the loading process, it can be observed that M/M_p ratio increased much more rapidly in the SC-EBF cases with short link beam length. As the plastic moments of the EBF beams in case III and case IV are much higher than those in case I and case II, the actual beam end bending moments in case III and case IV were much higher than the beam end bending moments in case I and case II respectively.

6.3.4.2. EBF Column

The shear force histories at the middle-length section (section D-D) and the bottom section (section E-E) of the column connecting the beam for the four cases of the D-type SC-EBF structures are plotted in Figure 6-47 and Figure 6-48. The shear forces were normalized by the column's shear strength V_p . It can be observed that at the V/V_p ratio was fairly small in the column up to the maximum drift ratio. This observation is in agreement with theoretical analysis, as the column is primarily subjected to axial force. The V/V_p ratios at the two selected sections in each D-type SC-EBF case were generally identical, since no lateral force was acting along the column. Shown in Figure 6-47 and Figure 6-48, the column shear forces in the D-type SC-EBF cases with long rocking link beam (case III and case IV) were generally higher than that of the D-type SC-EBF cases with short link beam (case I and case II).

The shear force and the axial force histories at the middle-length section (section G-G) of the column connecting the rocking link beam for the four cases of the D-type SC-EBF structures under cyclic loading are plotted in Figure 6-49 and Figure 6-50 respectively. The shear forces and the axial forces were normalized by the column's shear strength V_p and axial yield force N_p . Both V/V_p ratio and N/N_p ratio were fairly small in the column adjacent to the rocking link beams of the D-type SC-EBF cases up to the maximum drift ratio. The V/V_p ratio and the N/N_p ratio were smaller in case II and case IV, as the PT tendon area was smaller accordingly.

6.3.4.3. EBF Bracing

The axial force history at the middle-length section of the brace (section F-F) for the four investigated cases of the D-type SC-EBF structures are plotted in Figure 6-51. Similar to the afore-mentioned beam axial force normalization procedure, the bracing axial force of the SC-EBF structures was normalized by the brace's axial yield strength N_p . Shown in Figure 6-51, the brace's maximum N/N_p ratio was 0.4 in case I at the peak drift ratio. Similar to the observation on the N/N_p ratio in the beams of the D-type SC-EBF cases, the N/N_p ratios of case II and case IV were smaller than the N/N_p ratios of case I and case III, as the PT tendon areas were smaller.

6.3.4.4. Rocking Link Beam

The axial force, shear force, and the bending moment histories at the right side (section H-H) of the rocking link beam for the four investigated cases of the D-type SC-EBF structures are plotted in Figure 6-52, Figure 6-53, and Figure 6-54 respectively. The axial force, shear force, and bending moment are normalized in the same procedure as for the beam.

6.3.4.5. PT Tendon

The tensile stress in the PT tendons versus the drift ratio of each D-type SC-EBF cases is plotted in Figure 6-55. The minimum nominal yield stress of G270 PT tendon is 1,670 MPa, which is also indicated in Figure 6-55. The yielding of the PT tendon is set as one of the controlling limit states for the D-type SC-EBF structures. Shown in Figure 6-55,

the tensile stress in the PT tendons increases much more rapidly with increasing drift ratio values in case I and case II than in case III and case IV.

6.4. Limit States of the SC-EBF Structure

As illustrated in Figure 6-56, the target lateral force response of the SC-EBF structure subjected to seismically induced cyclic loading involves the limit states related to the PT tendons, fuse devices, and other structural components such as beams, columns, and braces. The important limit states to consider in the performance based design of the SC-EBF structure include: 1) gap opening between the beams and the rocking link beam; 2) yielding of the fuse devices; 3) yielding of the SC-EBF frame members, such as beams, rocking link beam, braces, and columns; 4) yielding of the PT tendons; 5) ultimate failure of the SC-EBF frame members, such as fuse fracture. The design objective for the SC-EBF structure is to ensure immediate occupancy (IO) performance under the design basis earthquake and collapse prevention (CP) performance at the maximum considered earthquake.

The performance goals of the SC-EBF structures relating to the above-mentioned limit states are summarized as follows,

- Under low to moderate lateral loads such as design wind load, SC-EBF structures should be made rigid enough to limit the elastic deformation of the structure, i.e., gap opening should be prevented.

- Under the design basis earthquake, the installed fuse devices should develop large plastic deformation for seismic energy dissipation. No damage such as inelastic action and buckling would occur to the frame members of the SC-EBF structure, such as beams, columns, braces, and the rocking link beam. The building should remain fully operational and be available for immediate occupancy.
- Under the maximum considered earthquake, collapse of the SC-EBF structure should be prevented. Hence slight yielding of the PT tendons would be allowed but fracture should be avoided by all means. Effect of fracture of the fuse devices on PT tendon force should be carefully checked to prevent excessive load on PT tendons. Yielding of the structural members such as beams and columns is likely to happen at pre-determined locations, while collapse or partial collapse caused by failure of these frame members must be avoided.

6.5. Relation to the Next Chapter

In this chapter two types of the SC-EBF configurations are investigated for their seismic behaviors: K-type SC-EBF structures and D-type SC-EBF structures. Four cases with varying PT tendon area and rocking link beam length are evaluated for both K-type SC-EBF structures and D-type SC-EBF structures. The yielding of the PT tendons is set as the controlling limit state for each SC-EBF case. As the PT tendon tension stress increases much more rapidly in the SC-EBF cases with short rocking link beams than in the SC-EBF cases with long rocking link beams when the same PT tendon length is used, the SC-EBF structures with short rocking link beams exhibit lower ultimate drift ratio

corresponding to PT tendon yielding. Reflected in Equation 6-11, PT stress in the PT tendons is related to the gap opening angle and rocking link beam depth. For the SC-EBF structures with short rocking link beams, the gap opening angles are much larger than the SC-EBF structures with long rocking beams at the same drift ratio. Given that the rocking link beam depth is the same for all SC-EBF cases, the SC-EBF structures with short rocking link beams reach the limit state (PT tendon yielding) at much smaller drift ratios than the SC-EBF cases with long rocking link beams when the same PT tendon length is used. To increase the maximum allowable drift ratios for SC-EBF cases with short rocking link beams, one alternative is to reduce the rocking link beam depth. However, to avoid substantial reduction of the strength and the stiffness of the SC-EBF structures, two rocking link beams with reduced depth are proposed and studied Chapter 7.

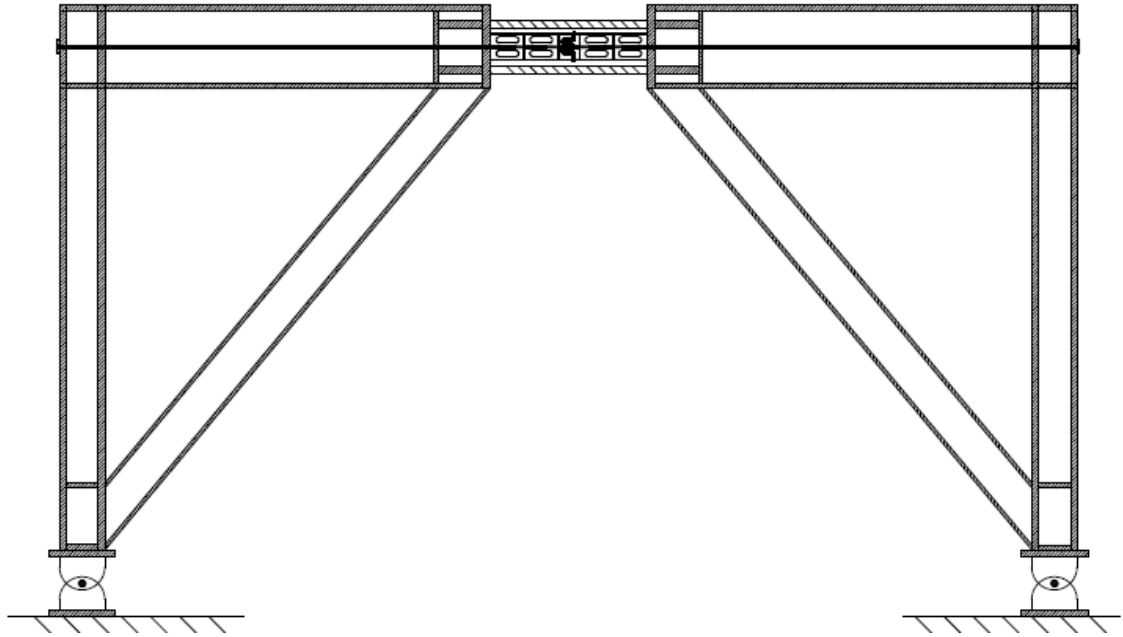


Figure 6-1 General configuration of the K-type SC-EBF structure

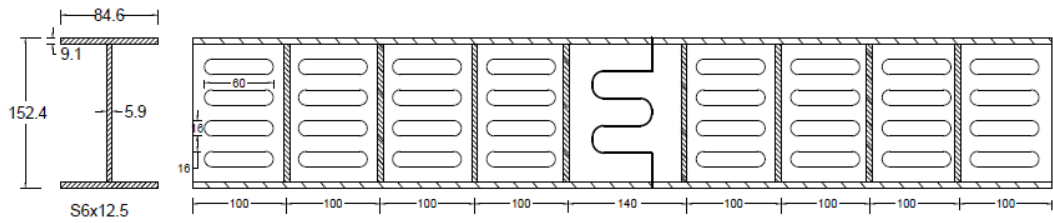


Figure 6-2 Section details of the short fuse

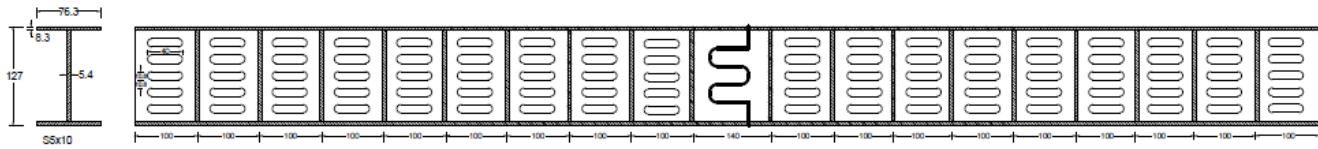


Figure 6-3 Section details for the long fuse

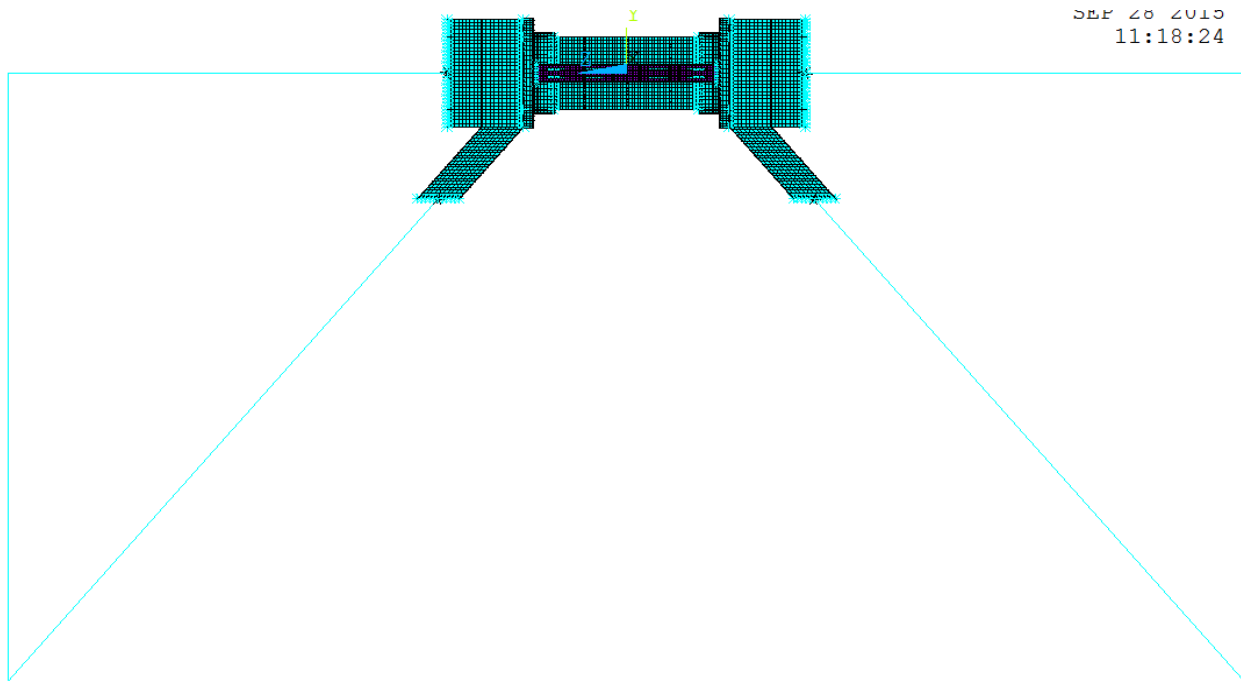


Figure 6-4 Finite element model of the SC-EBF structure with short fuse beam

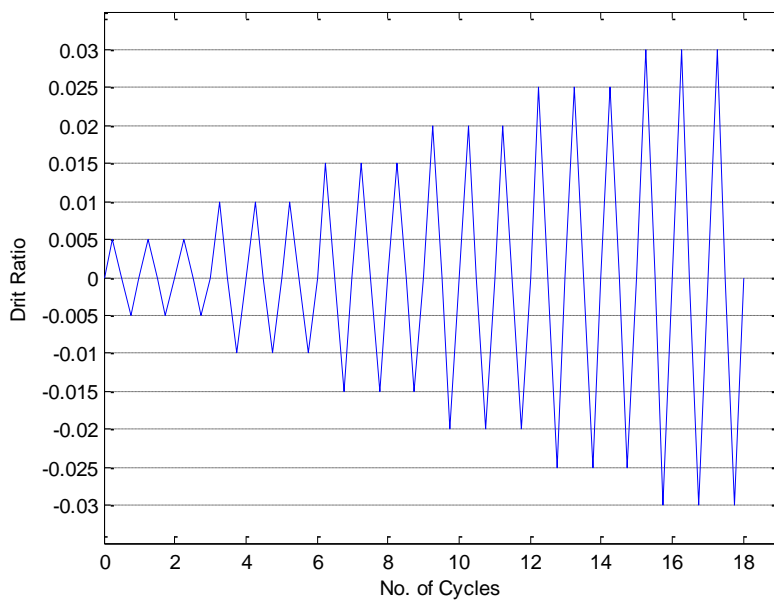
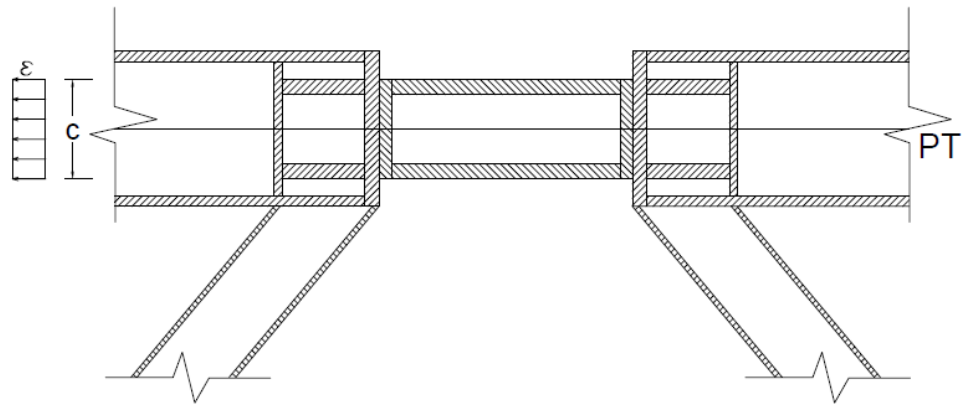
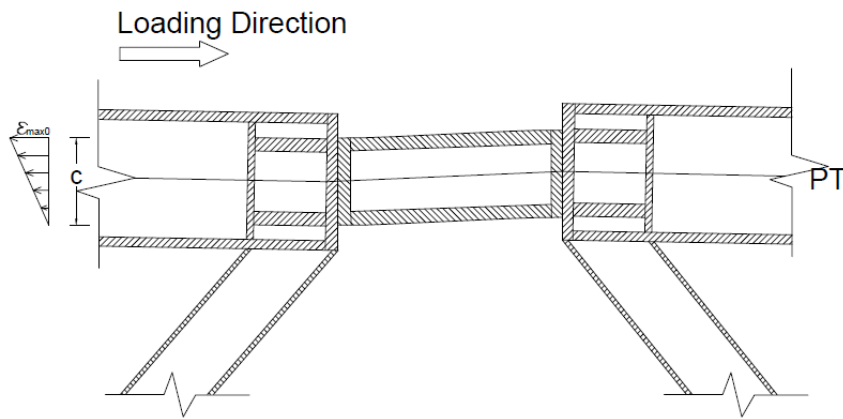


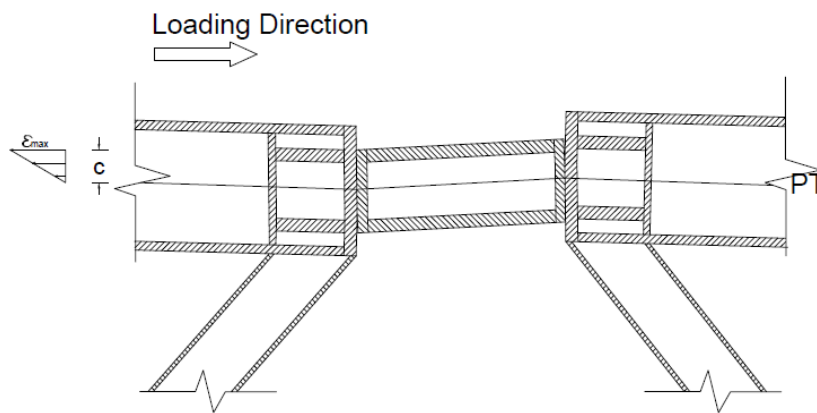
Figure 6-5 Cyclic loading protocol for SC-EBF structures



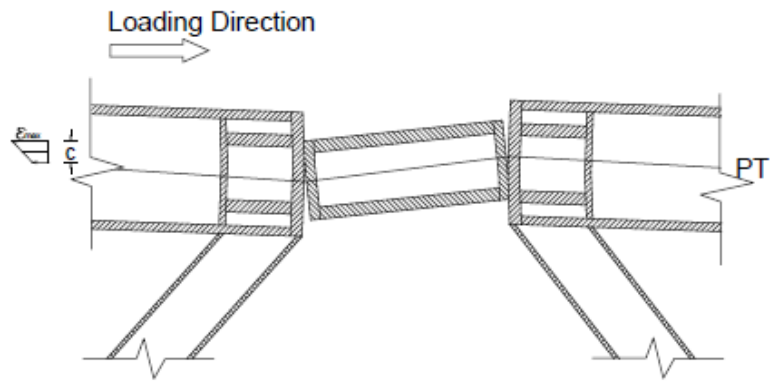
(a) Phase I of the SC-EBF frame



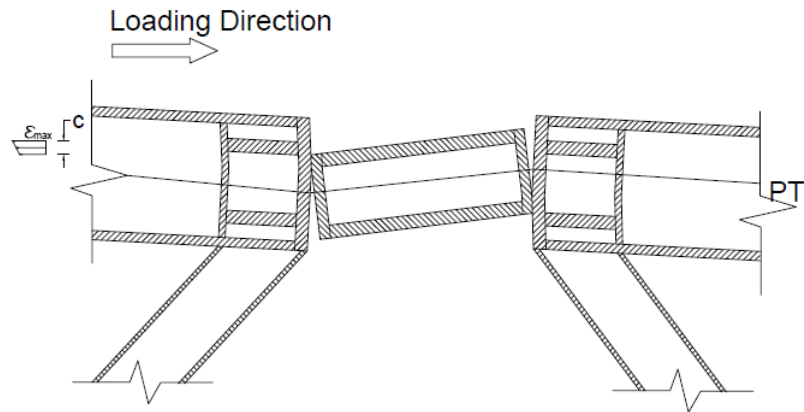
(b) Phase II of the SC-EBF frame



(c) Phase III of the SC-EBF frame



Phase IV of the SC-EBF Frame



Phase V of the SC-EBF Frame

Figure 6-6 Transitions of the contact regions of the SC-EBF under lateral load

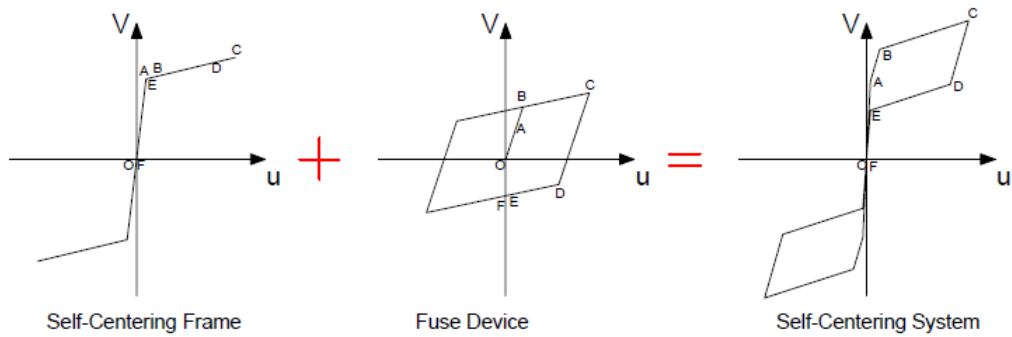


Figure 6-7 Force displacement relationship calculation principle for SC-EBF structure

Points O, A, B, C, D, E, and F correspond to the occurrence of the following affairs:

- O: No external load is applied;
- A: Gap between the rocking link beam and the beam starts to open;
- B: Fuse devices start to yield in the loading direction;
- C: Desired drift is reached;
- D: Fuse devices start to yield in the reversed loading direction;
- E: Gap between the rocking link beam and the beam starts to close;
- F: External load is reduced to zero.

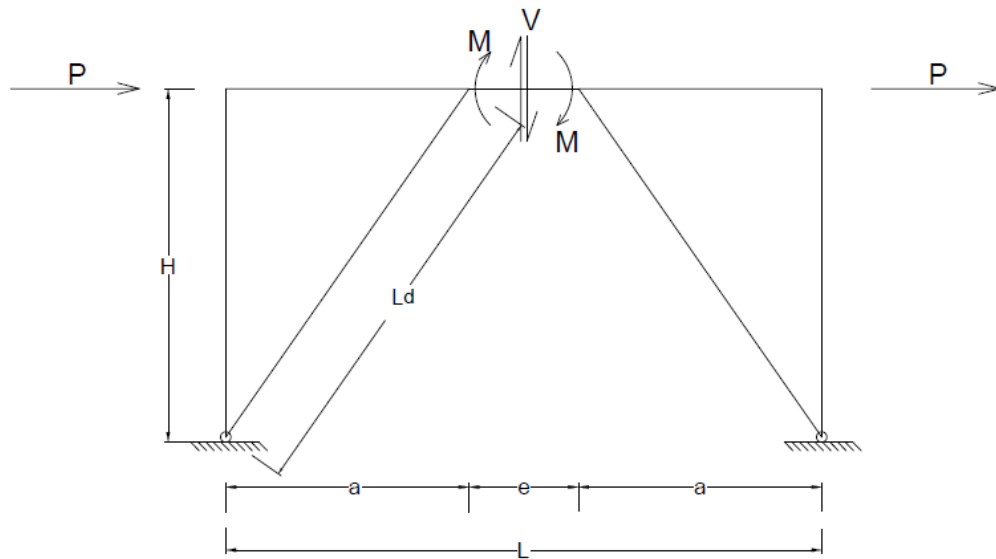


Figure 6-8 Force distribution at the rocking link beam under the lateral load

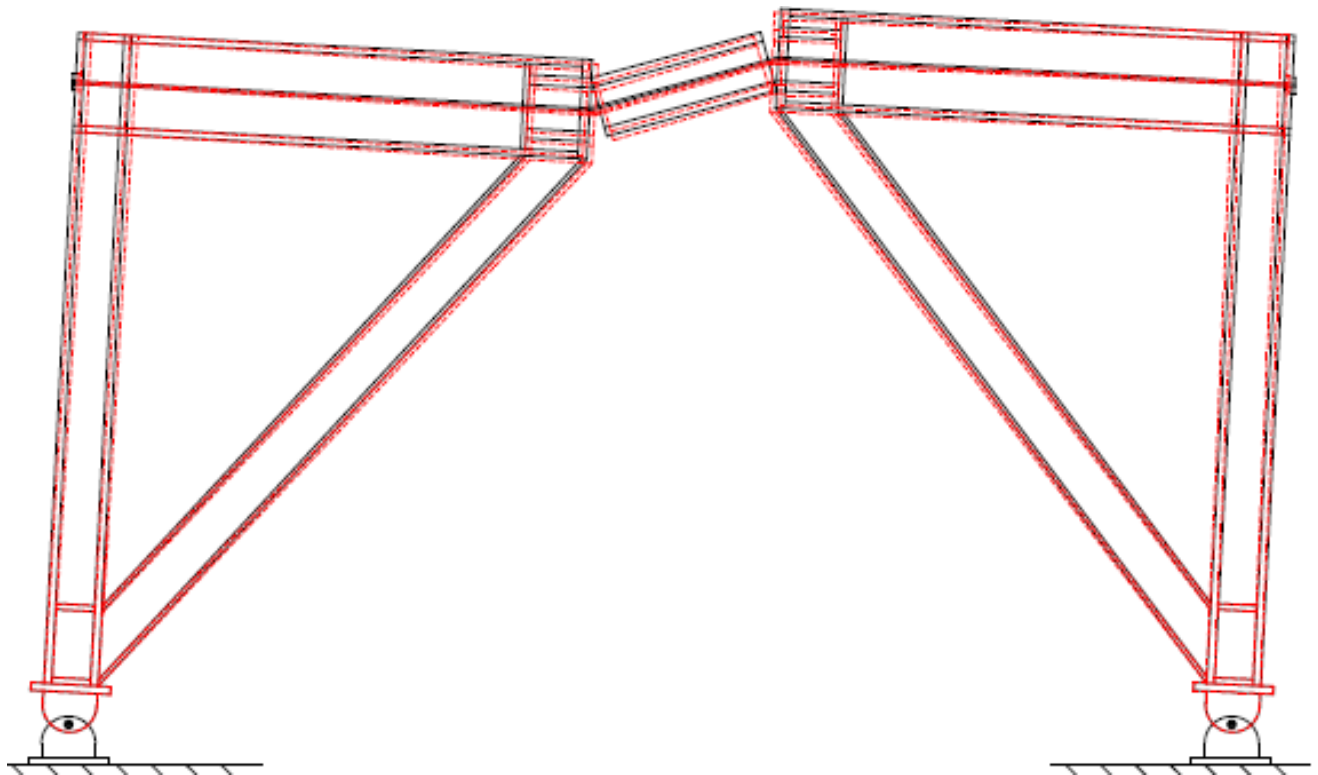


Figure 6-9 Axial compressive deformation of the SC-EBF frame under the increased PT tendon force

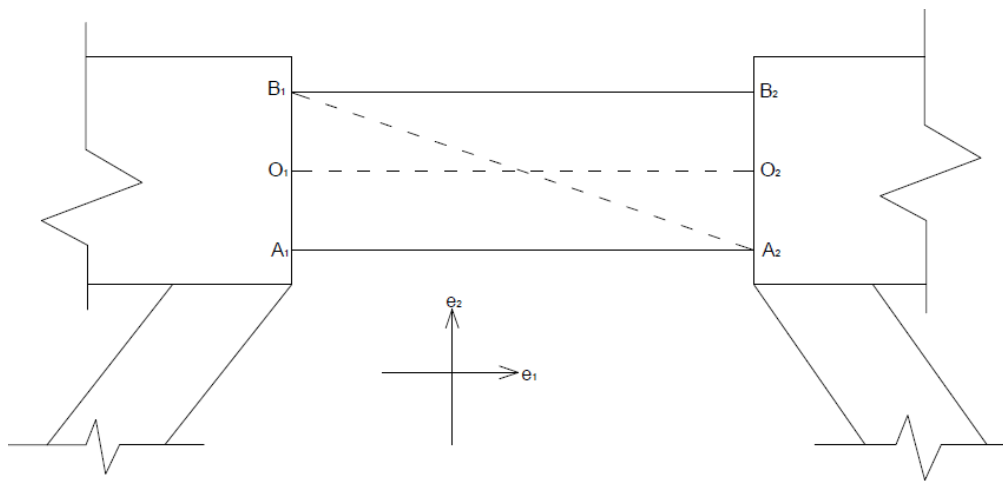


Figure 6-10 Initial configuration of the SC-EBF frame

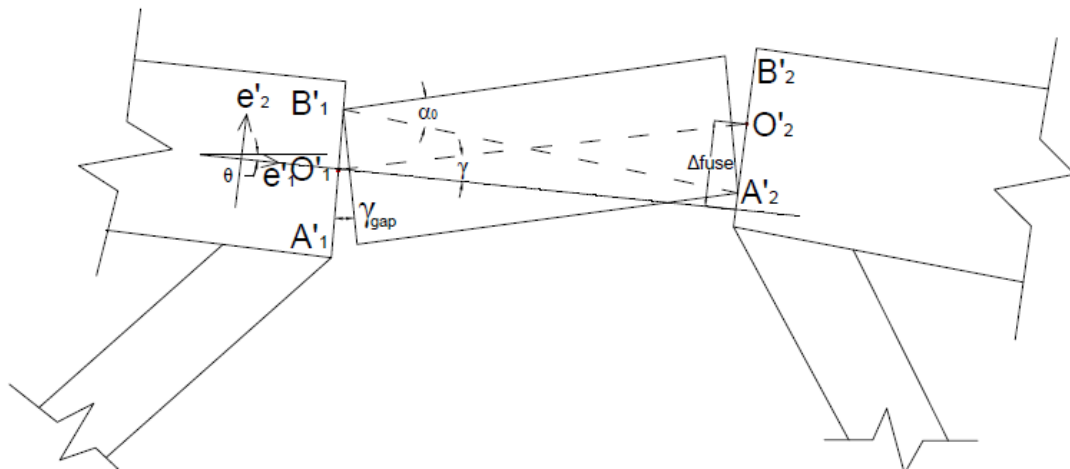


Figure 6-11 Displaced configuration of the SC-EBF frame

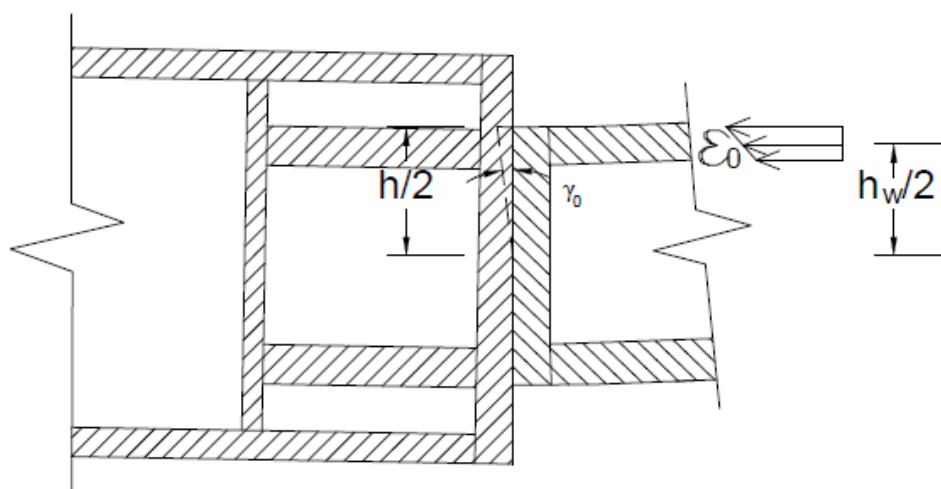


Figure 6-12 Critical link rotation angle determination

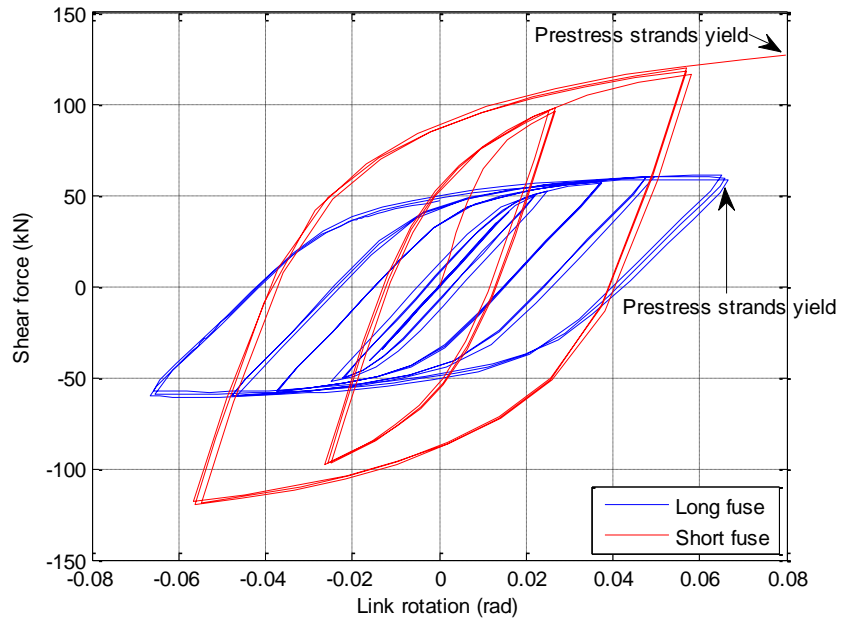


Figure 6-13 Hysteresis force displacement relationship of a single fuse device

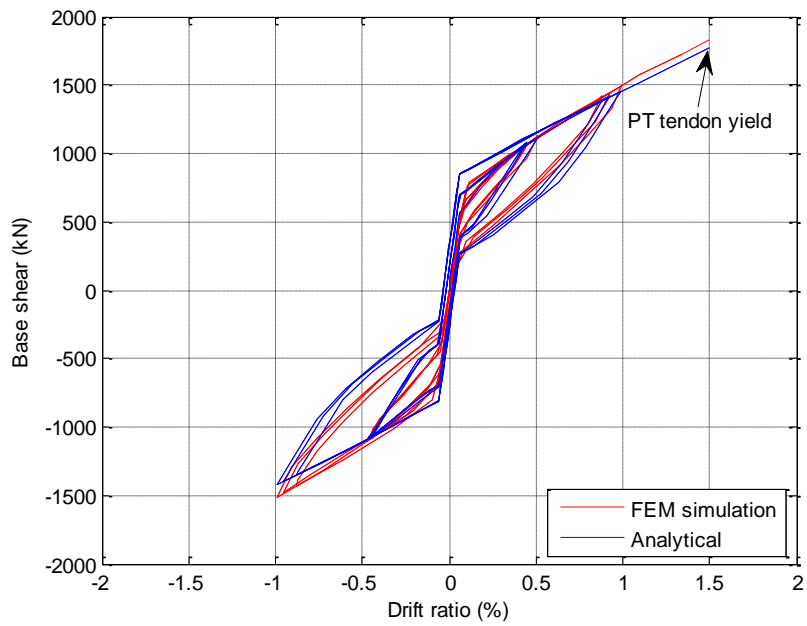


Figure 6-14 Hysteresis force displacement relationship comparison for case 1

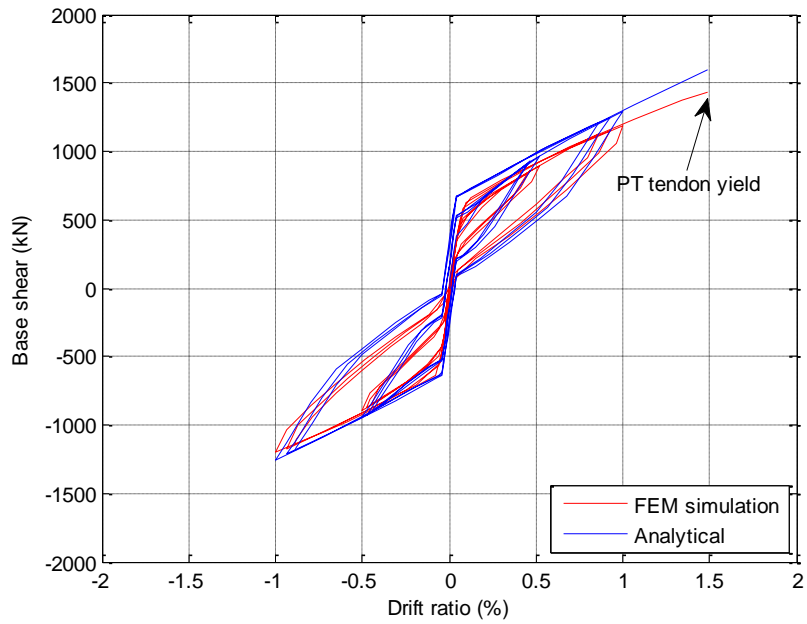


Figure 6-15 Hysteresis force displacement relationship comparison for case 2

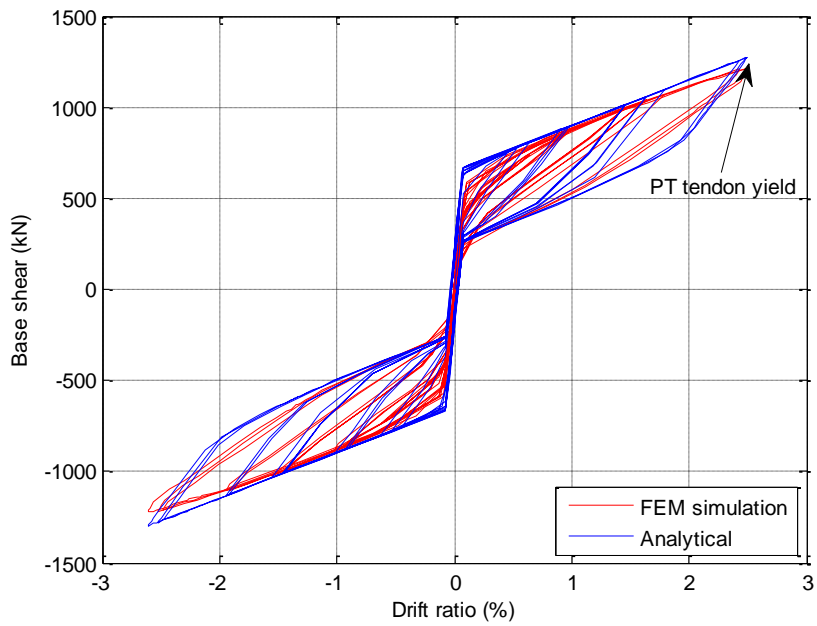


Figure 6-16 Hysteresis force displacement relationship comparison for case 3

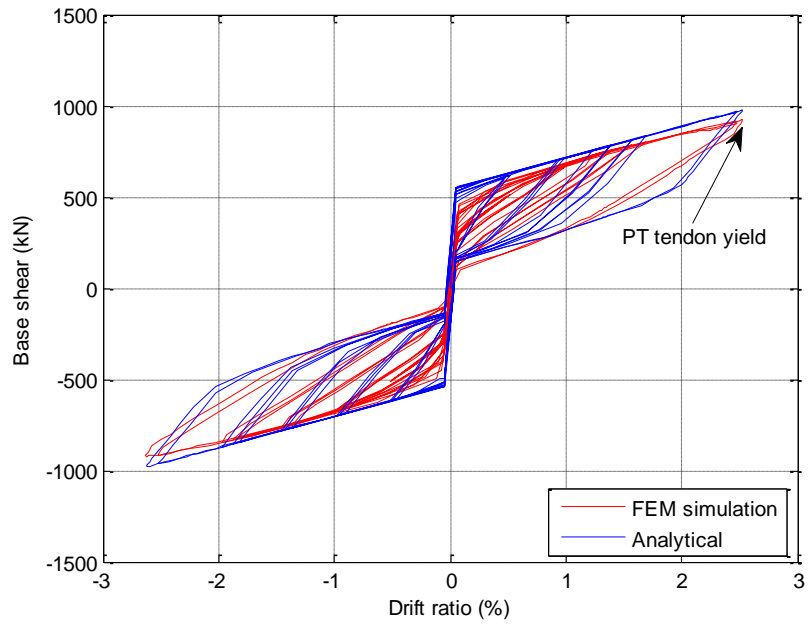


Figure 6-17 Hysteresis force displacement relationship comparison for case 4

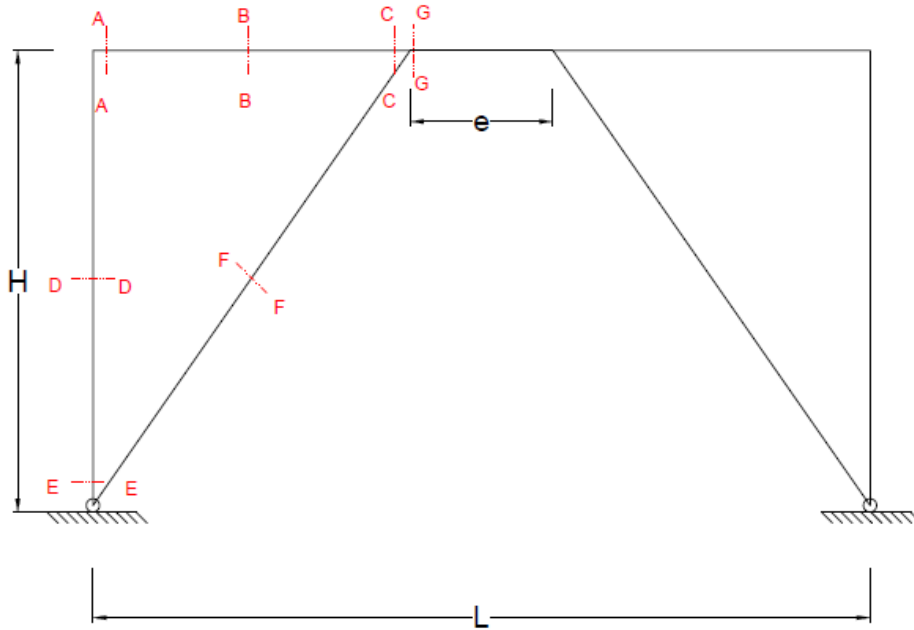


Figure 6-18 Critical locations in the SC-EBF structure

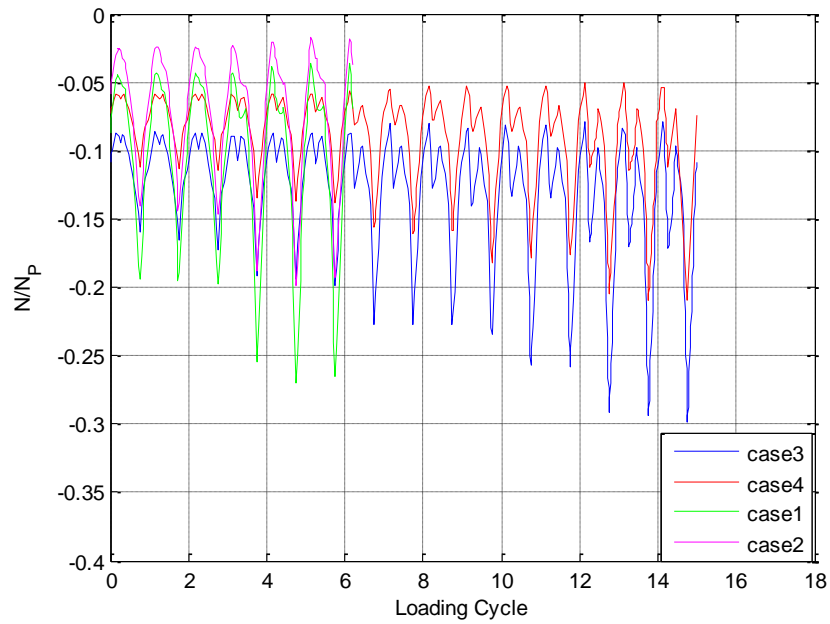


Figure 6-19 Normalized beam axial force at section A-A for K-type SC-EBF cases

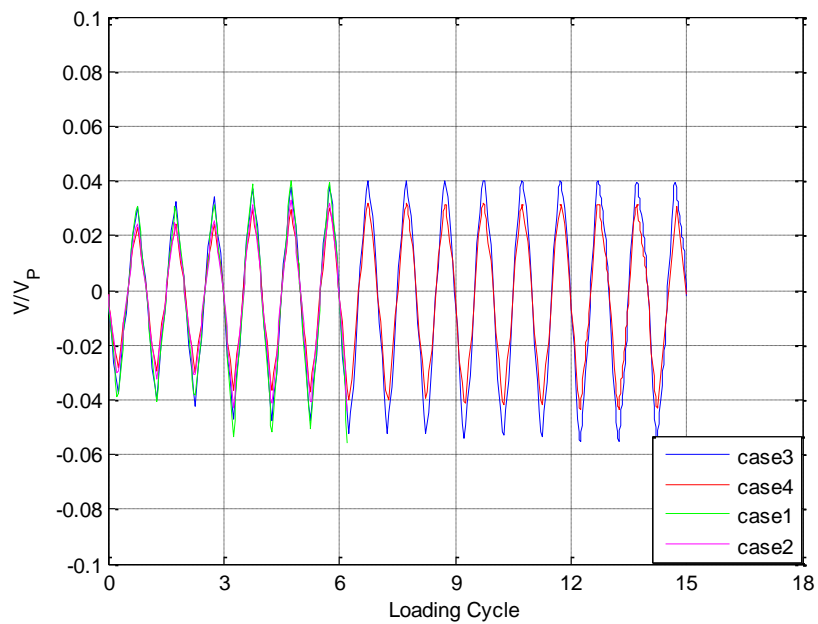


Figure 6-20 Normalized beam shear force at section A-A for K-type SC-EBF cases

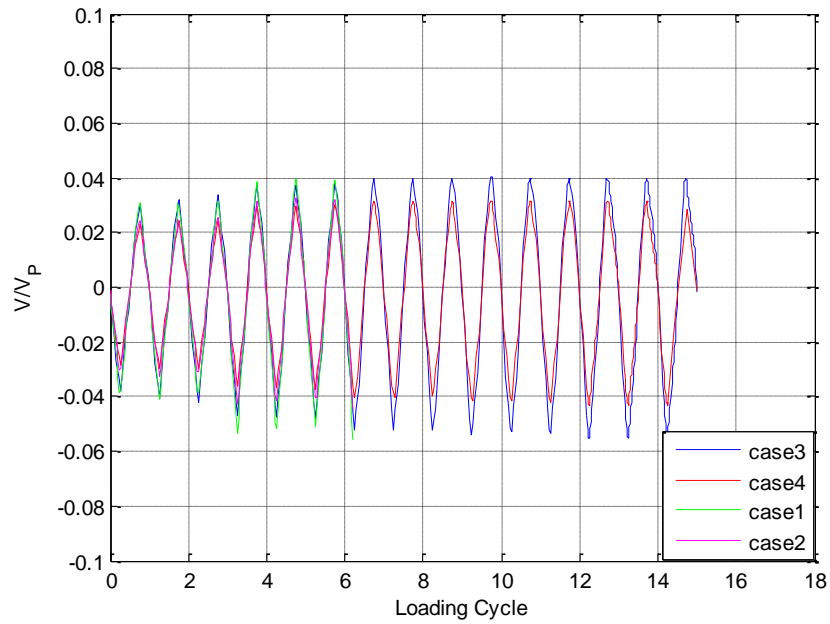


Figure 6-21 Normalized beam shear force at section B-B for K-type SC-EBF cases

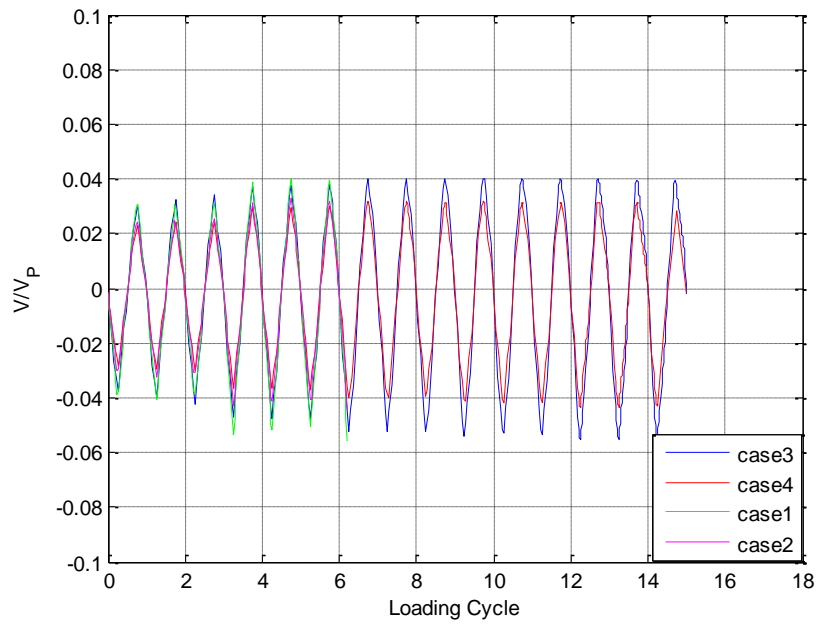


Figure 6-22 Normalized beam shear force at section C-C for K-type SC-EBF cases

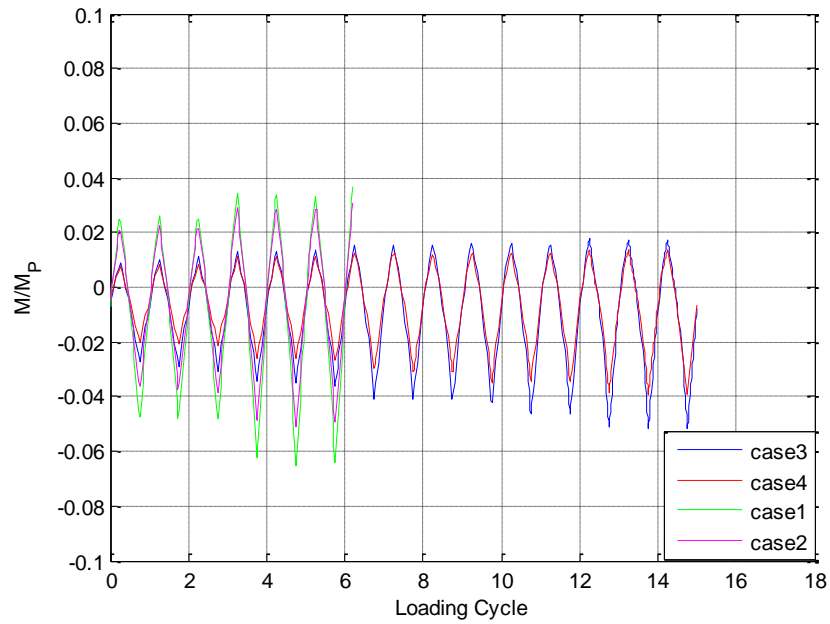


Figure 6-23 Normalized beam bending moment at section A-A for K-type SC-EBF cases

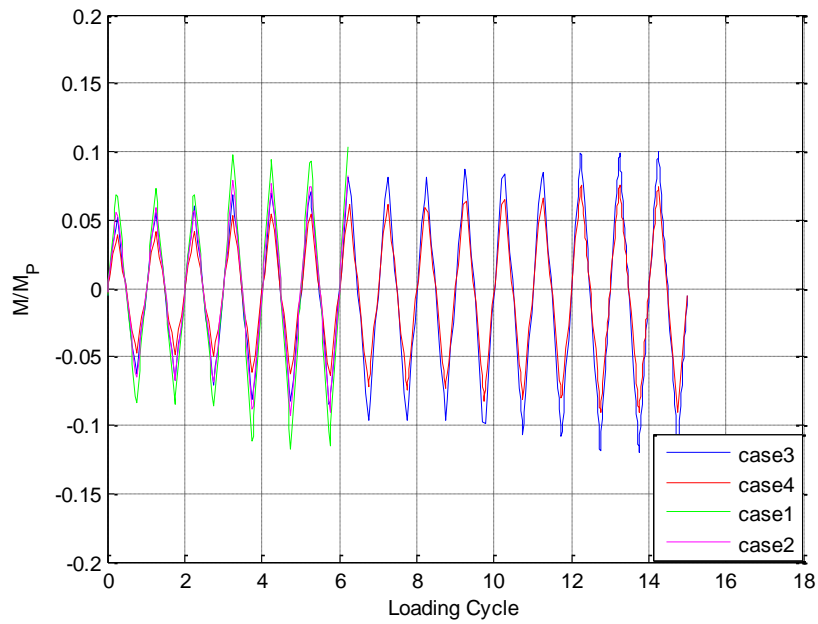


Figure 6-24 Normalized beam bending moment at section B-B for K-type SC-EBF cases

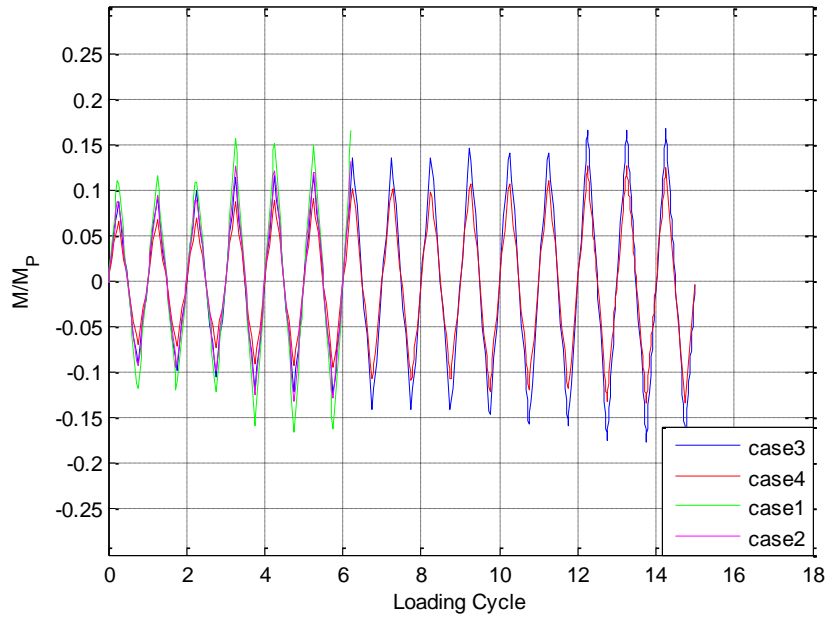


Figure 6-25 Normalized beam bending moment at section C-C for K-type SC-EBF cases

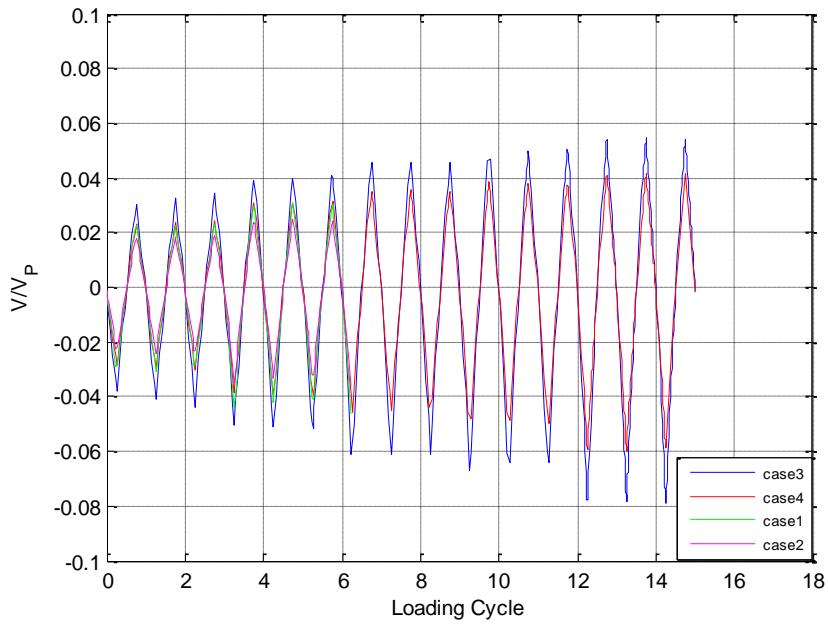


Figure 6-26 Normalized column shear force at section D-D for K-type SC-EBF cases

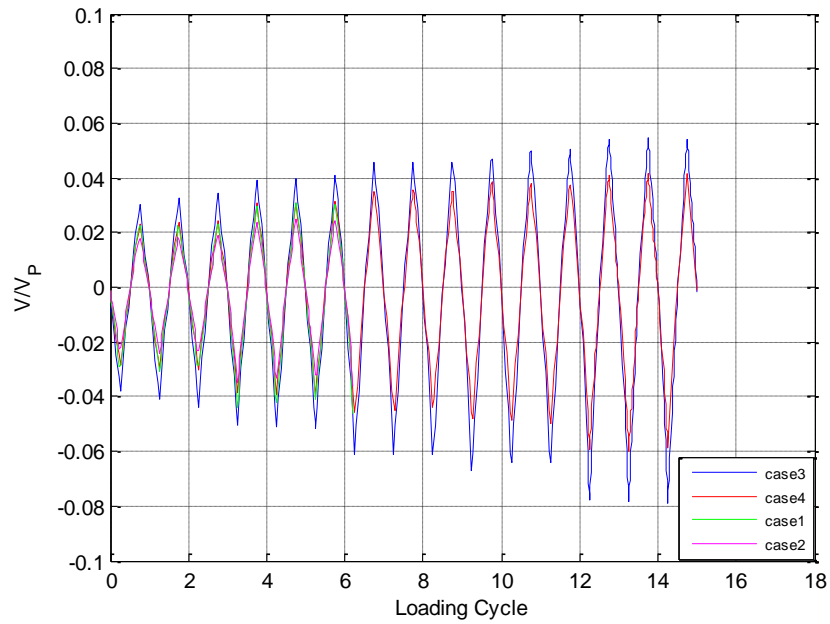


Figure 6-27 Normalized column shear force at section E-E for K-type SC-EBF cases

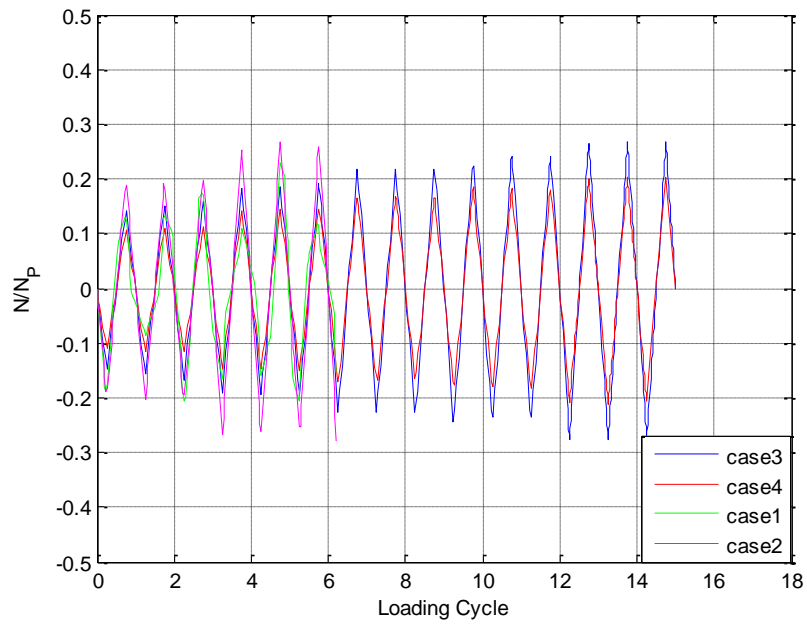


Figure 6-28 Normalized brace axial force at section F-F for K-type SC-EBF cases

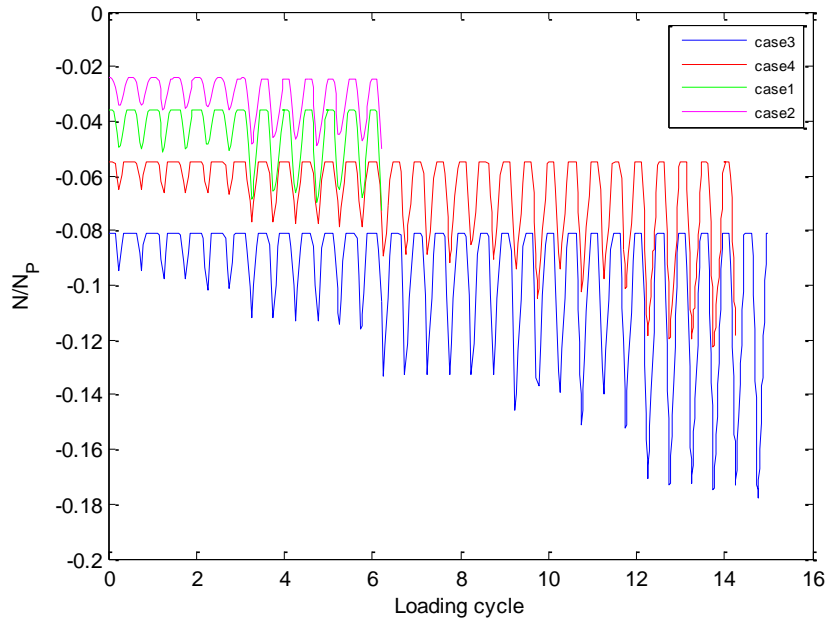


Figure 6-29 Normalized link beam axial force at section G-G for K-type SC-EBF cases

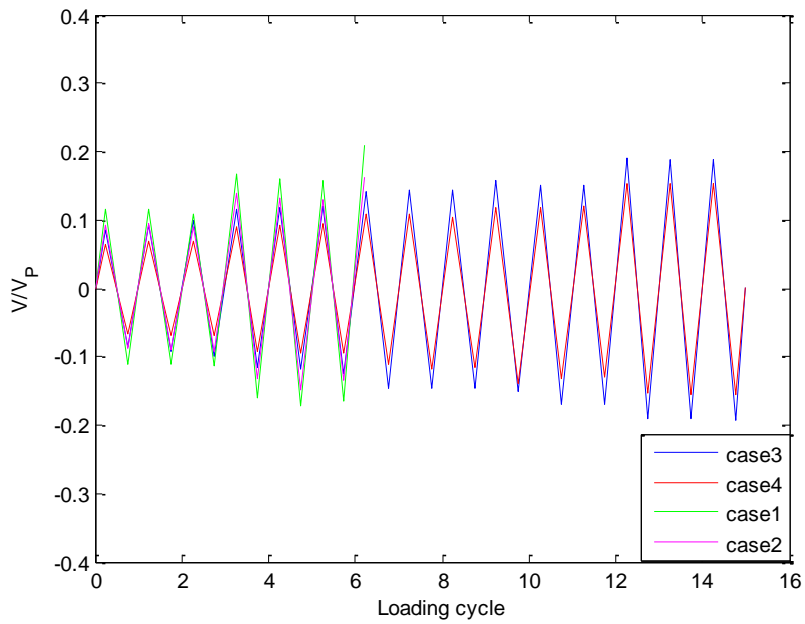


Figure 6-30 Normalized link beam shear force at section G-G for K-type SC-EBF cases

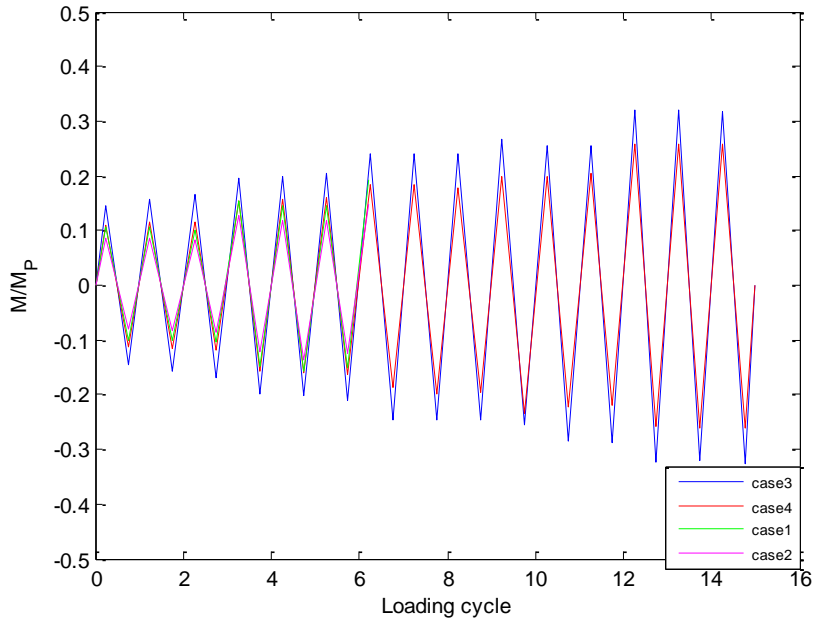


Figure 6-31 Normalized link beam bending moment at section G-G for K-type SC-EBF cases

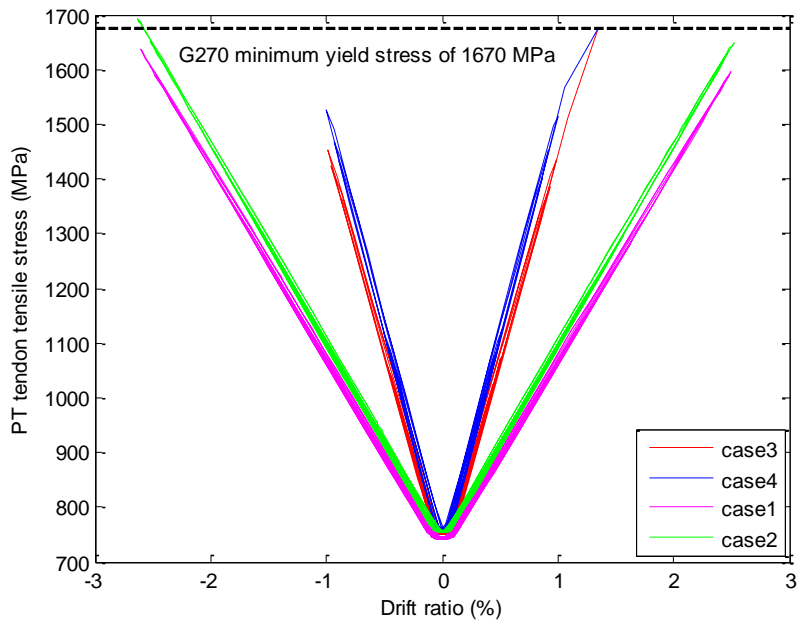


Figure 6-32 Tension stress in PT tendons vs. drift ratio

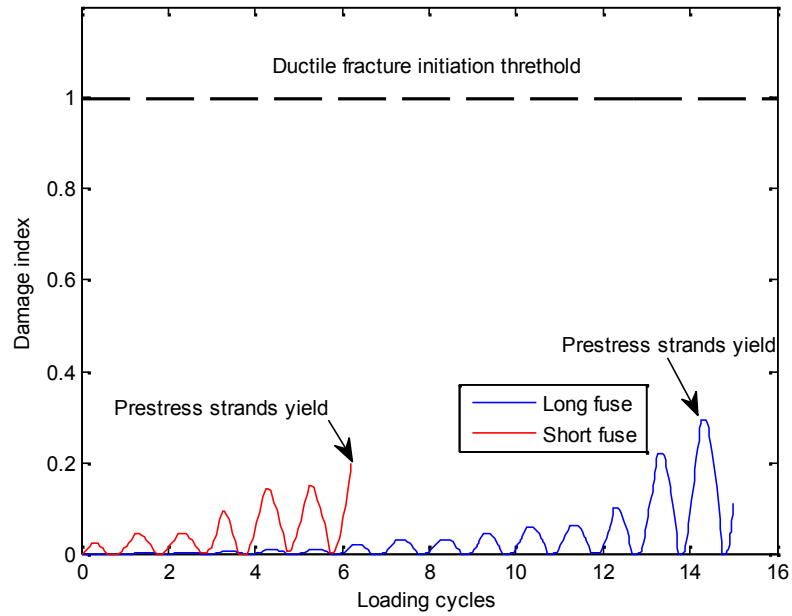


Figure 6-33 Cumulative damage index increment with the loading process

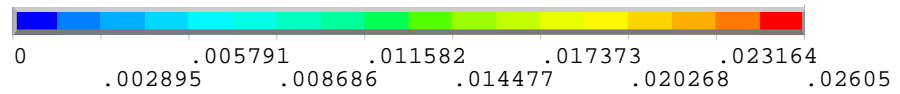
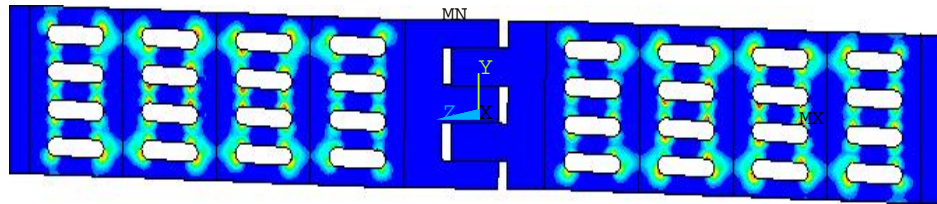


Figure 6-34 Von Mises plastic strain contour of the short fuse at 1.4% lateral drift of case 1

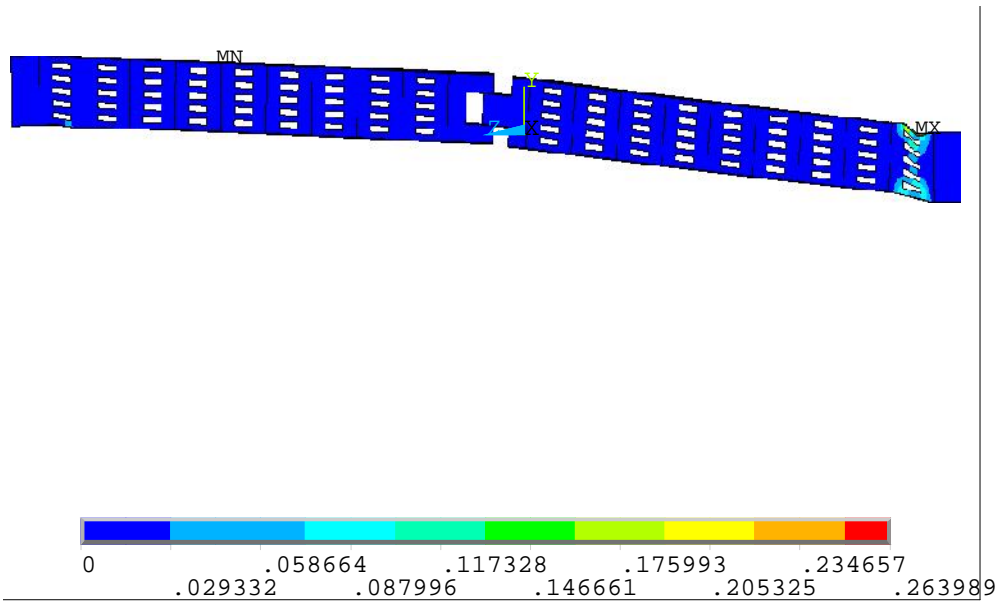


Figure 6-35 Von Mises plastic strain contour of the long fuse at 2.5% lateral drift of case 3

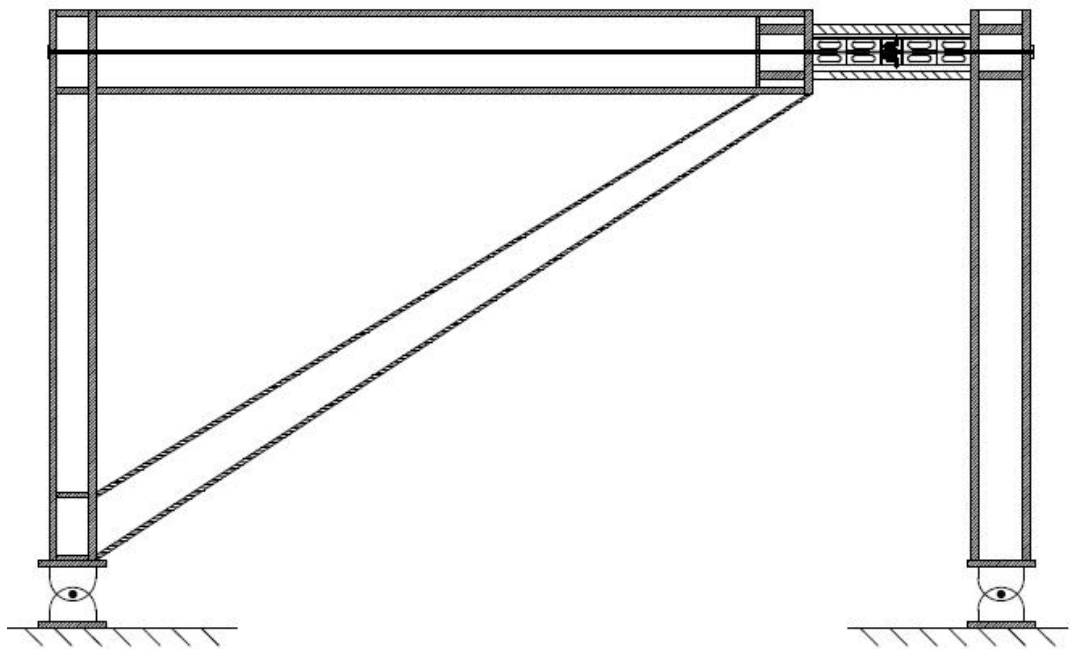


Figure 6-36 Structure Composition of D-type SC-EBF

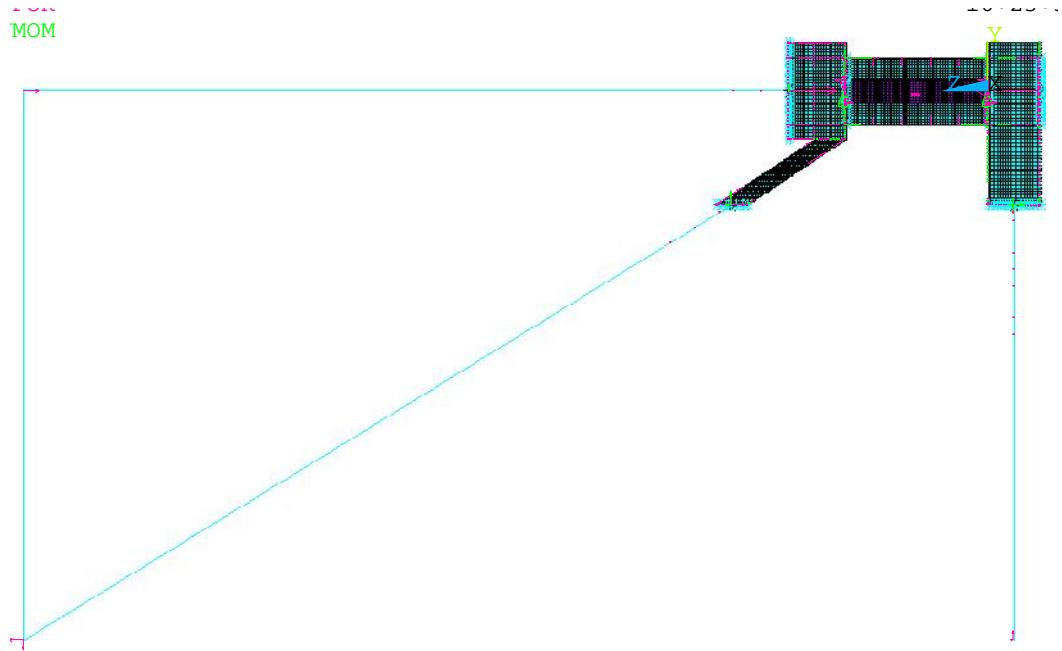


Figure 6-37 Meshed finite element model for a typical D-type SC-EBF

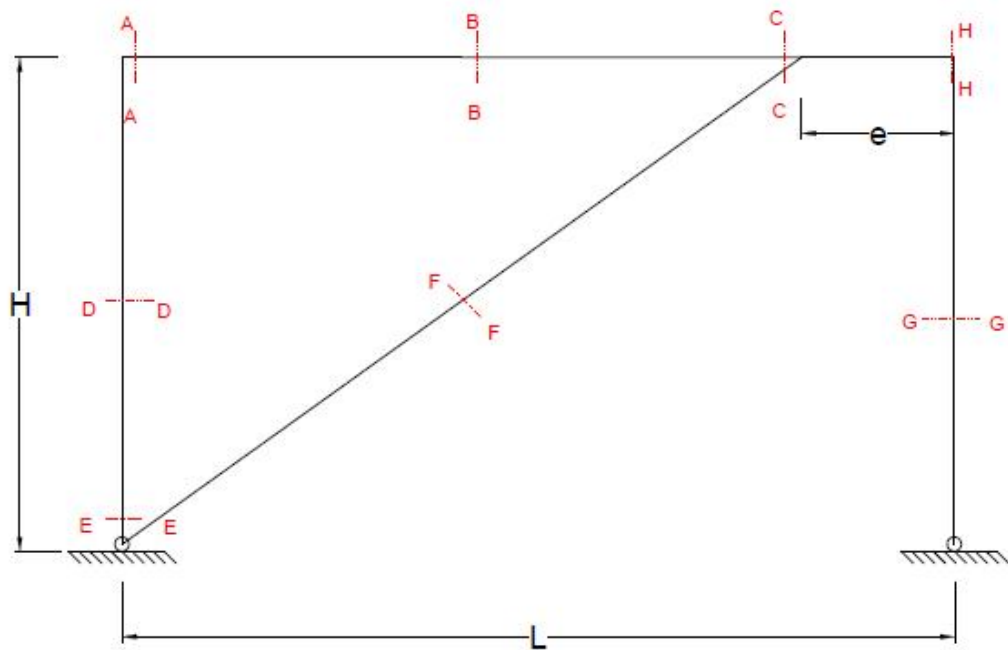


Figure 6-38 Key locations in the D-type SC-EBF

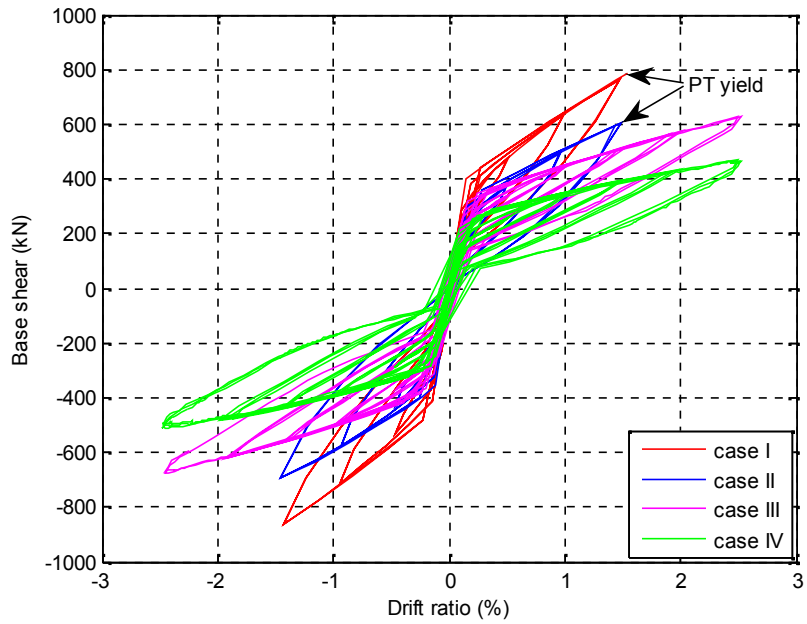


Figure 6-39 Hysteresis force displacement relationships for the D-type SC-EBF cases

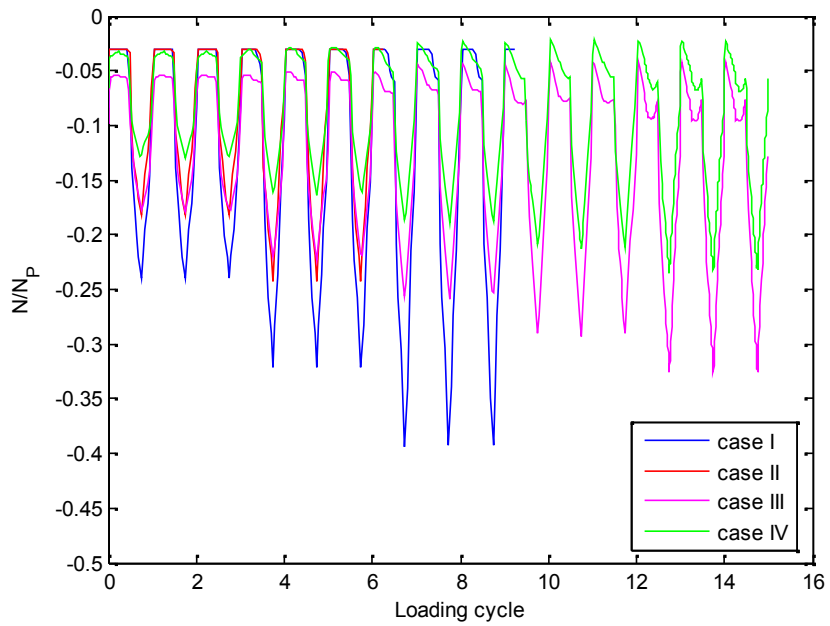


Figure 6-40 Axial force at section B-B

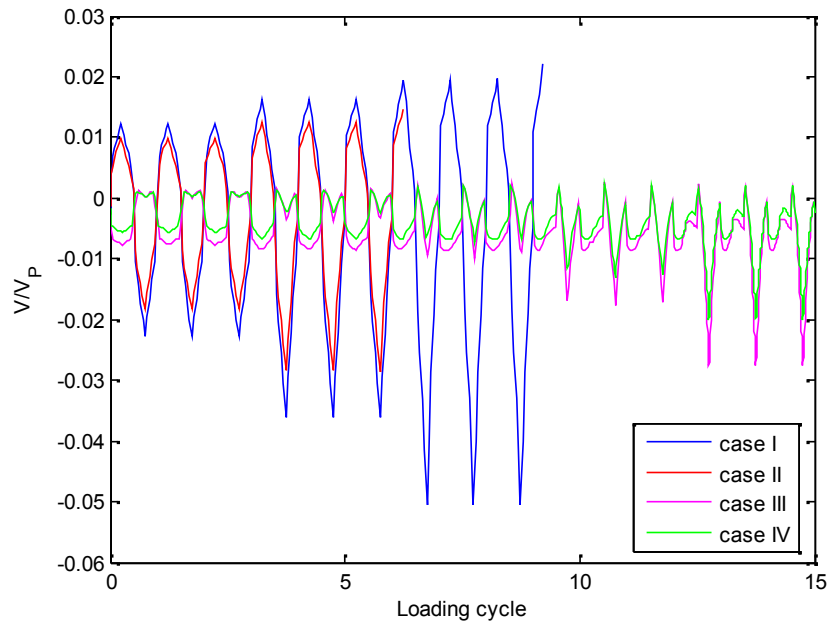


Figure 6-41 Shear at section A-A

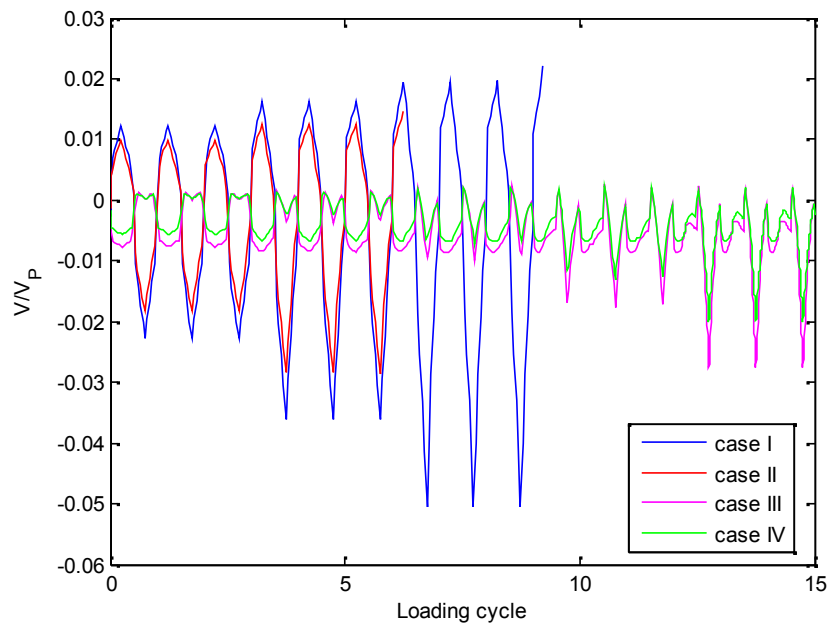


Figure 6-42 Shear at section B-B

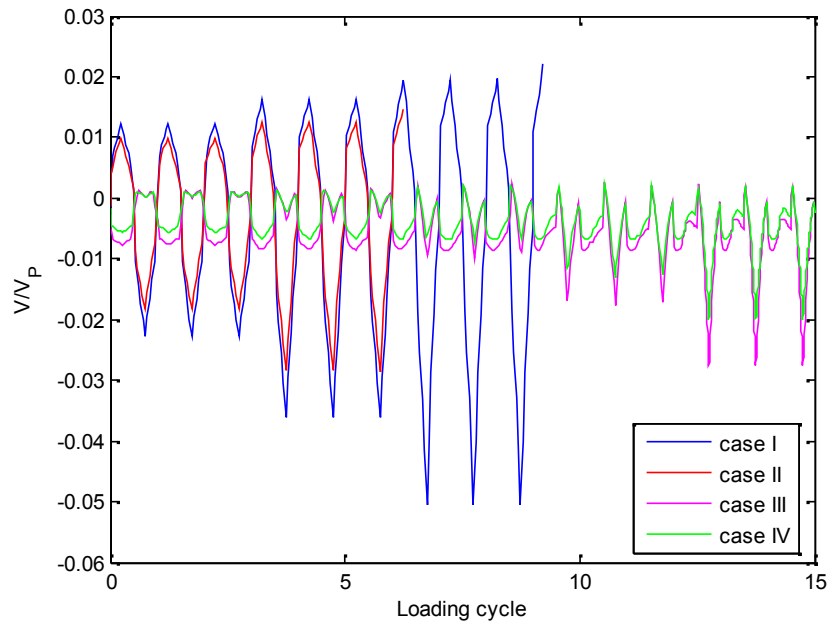


Figure 6-43 Shear at section C-C

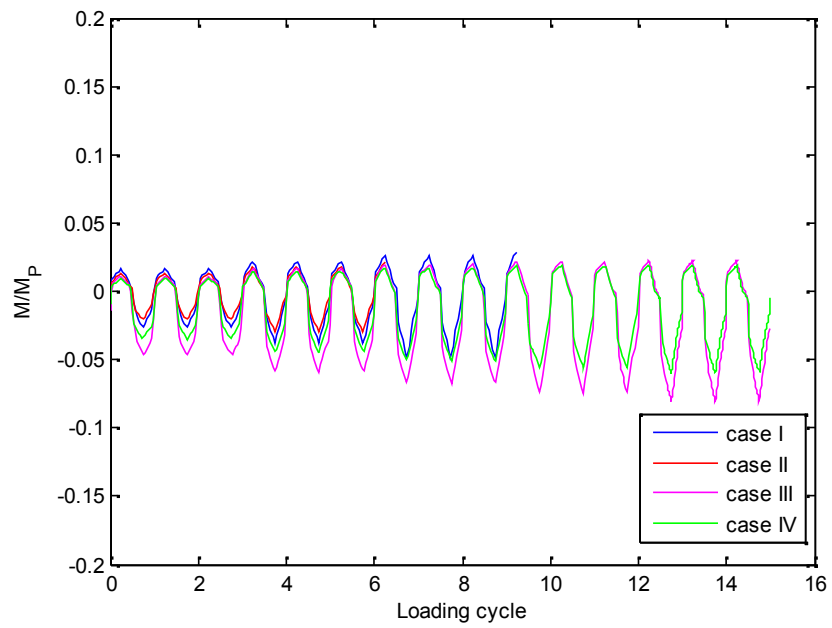


Figure 6-44 Beam bending moment at section A-A

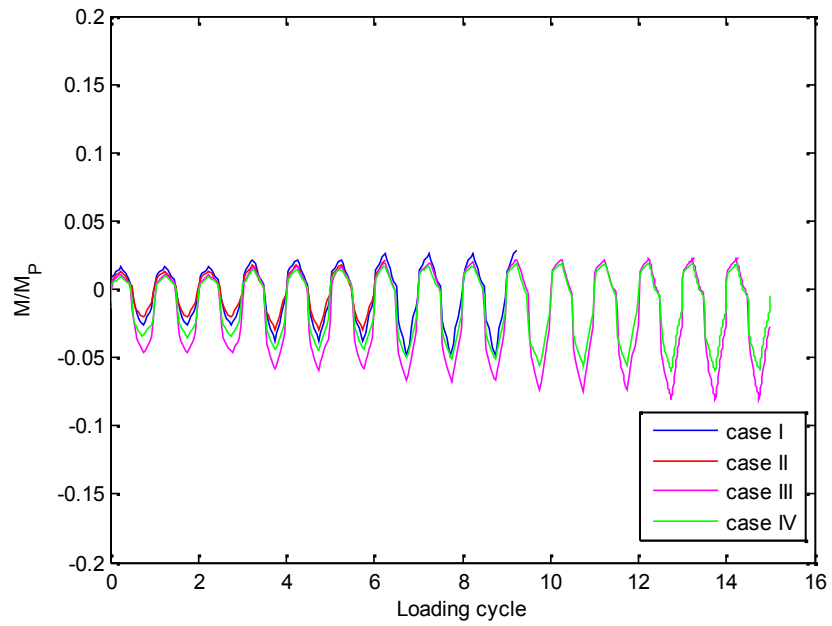


Figure 6-45 Beam bending moment at section B-B

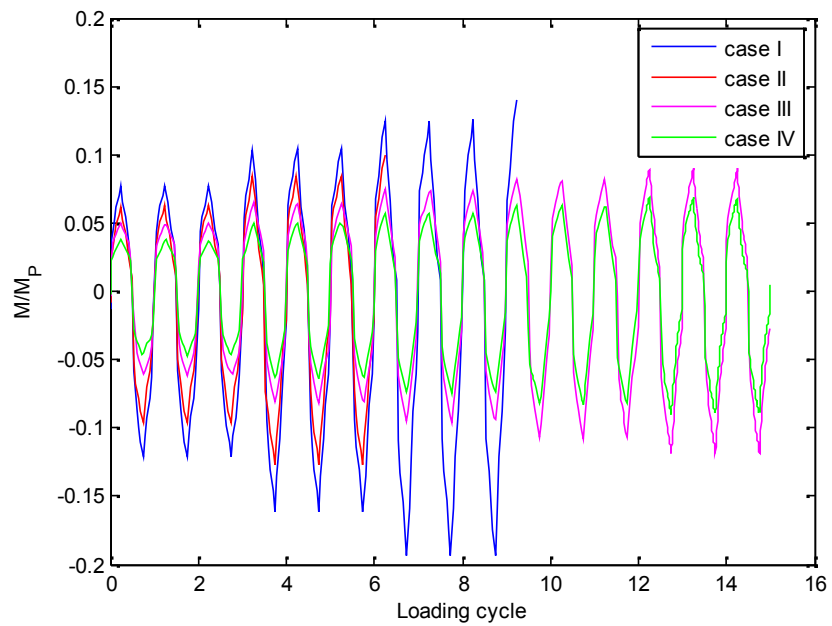


Figure 6-46 Beam bending moment at section C-C

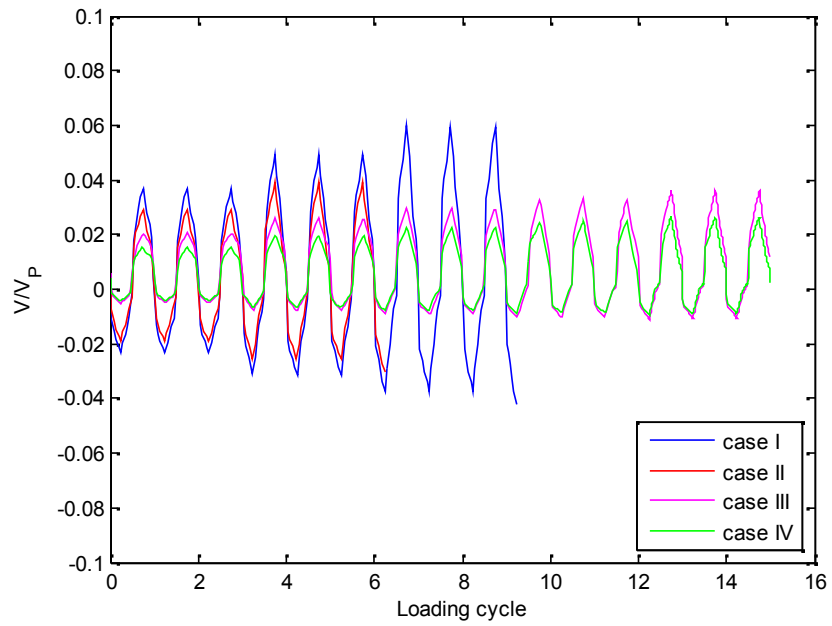


Figure 6-47 Column shear force at section D-D

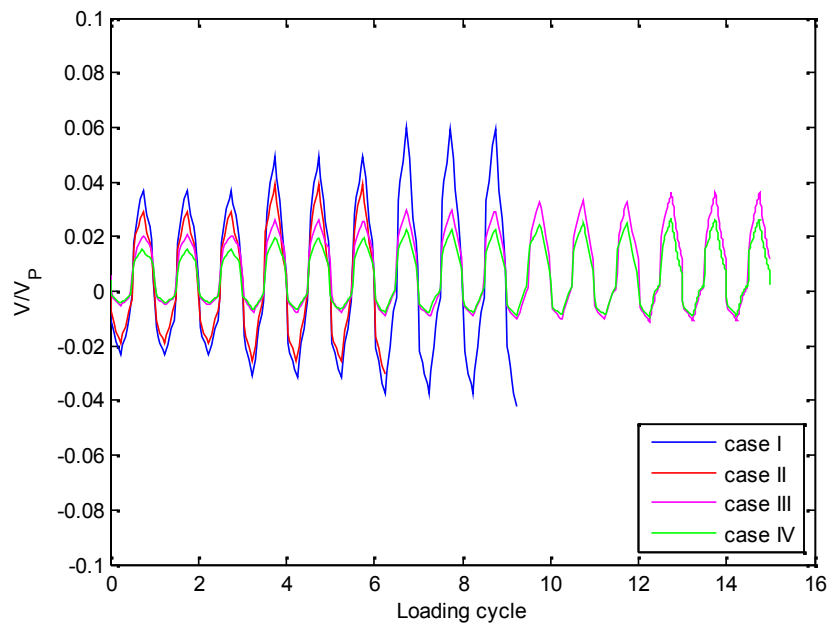


Figure 6-48 Column shear force at section E-E

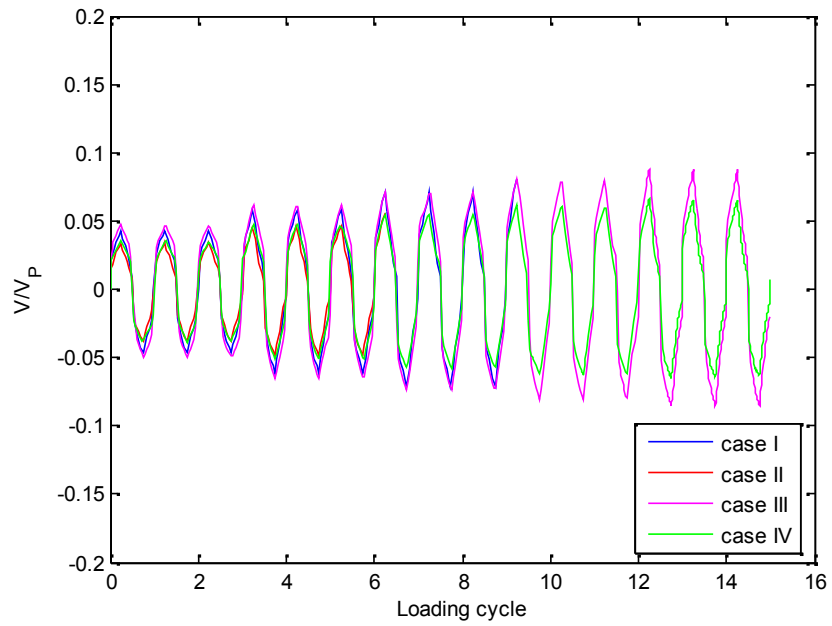


Figure 6-49 Column shear force at section G-G

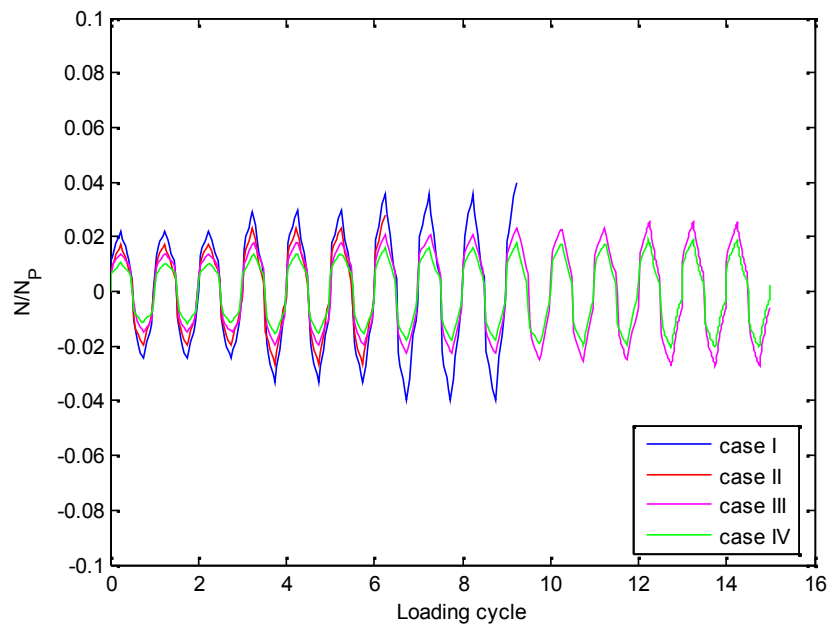


Figure 6-50 Column axial force at section G-G

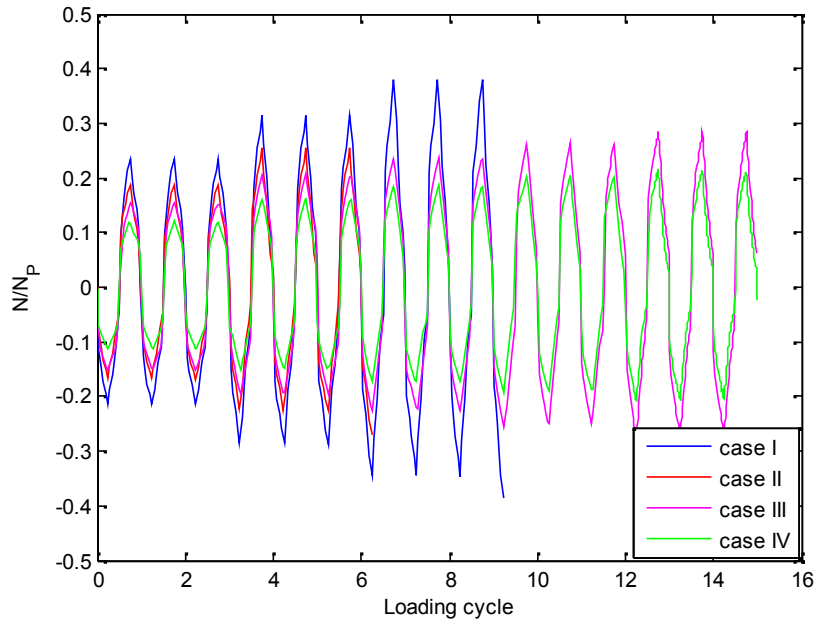


Figure 6-51 Brace axial force at section F-F

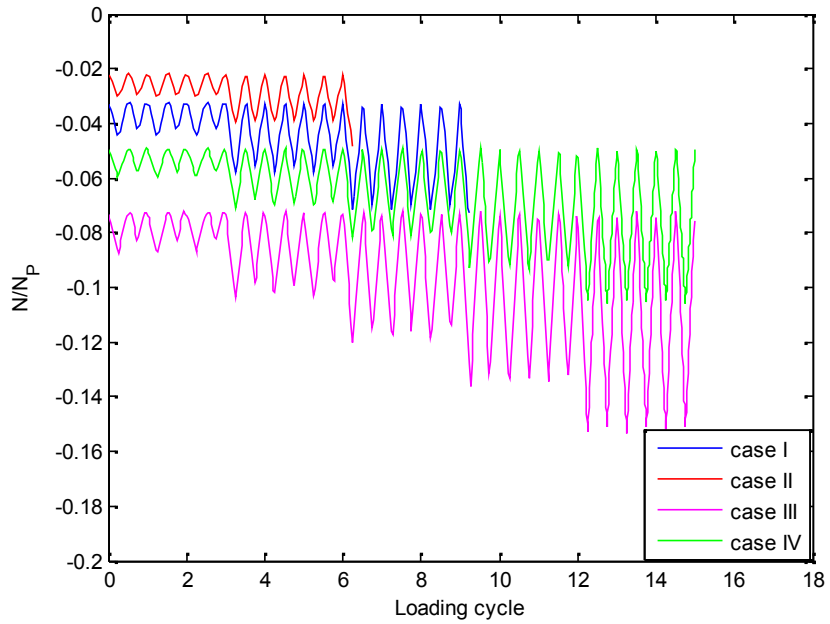


Figure 6-52 Axial force of the rocking link beam at section H-H

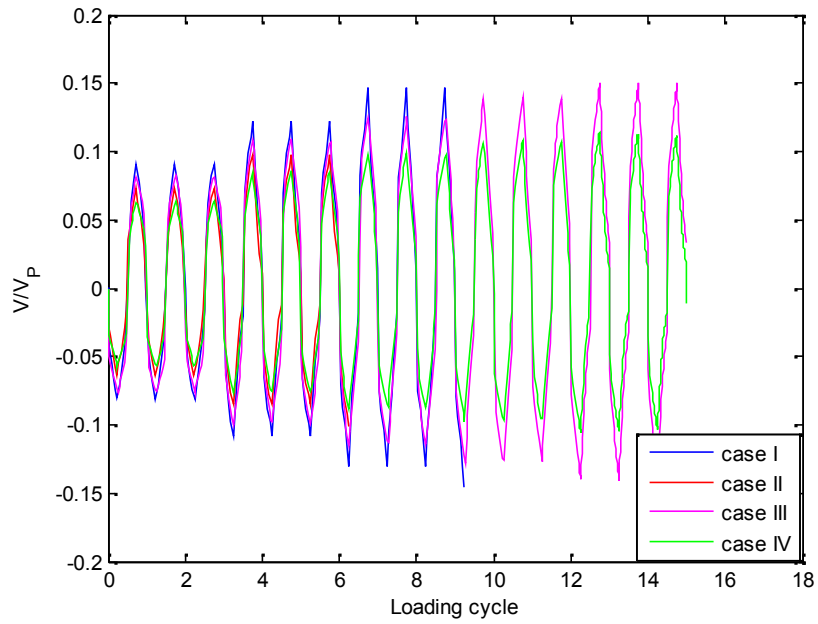


Figure 6-53 Shear force of the rocking link beam at section H-H

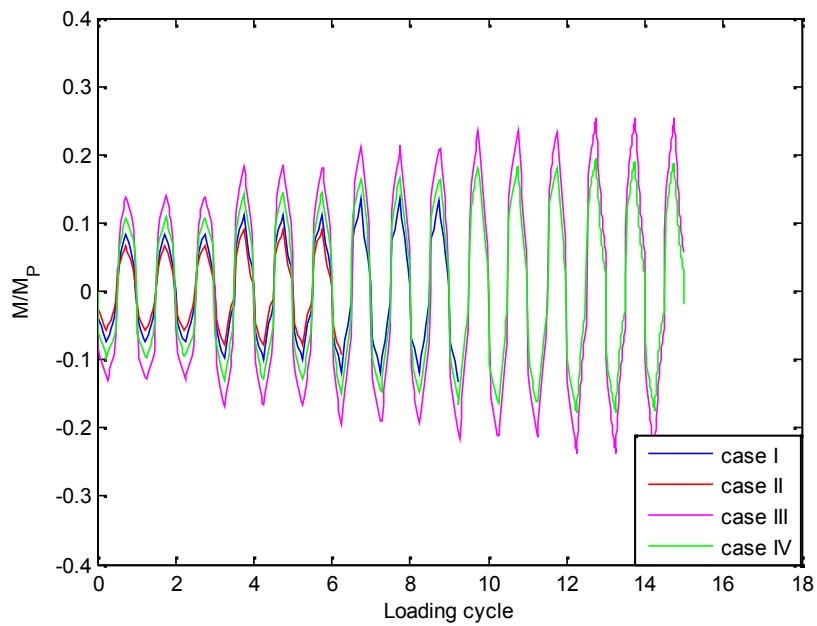


Figure 6-54 End bending moment of the rocking link beam at section H-H

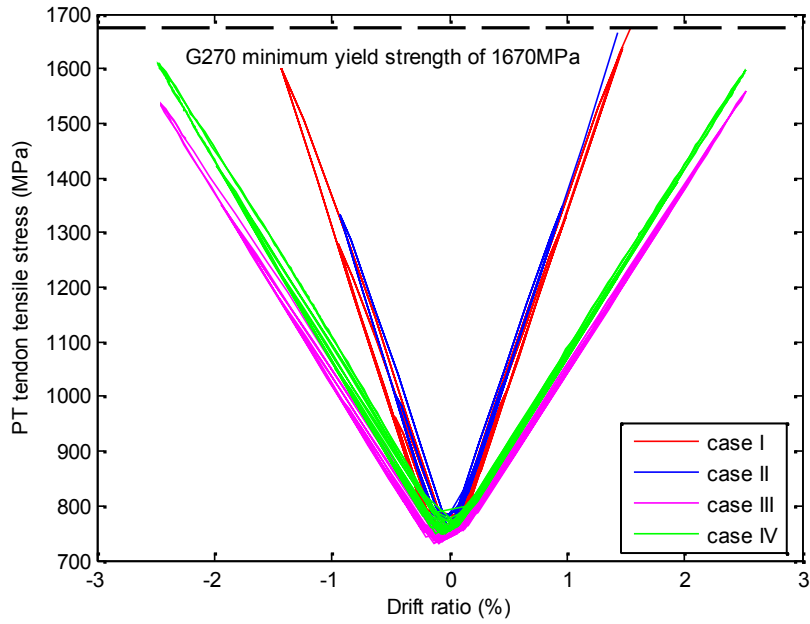


Figure 6-55 PT tendon tension stress of the D-type SC-EBF cases

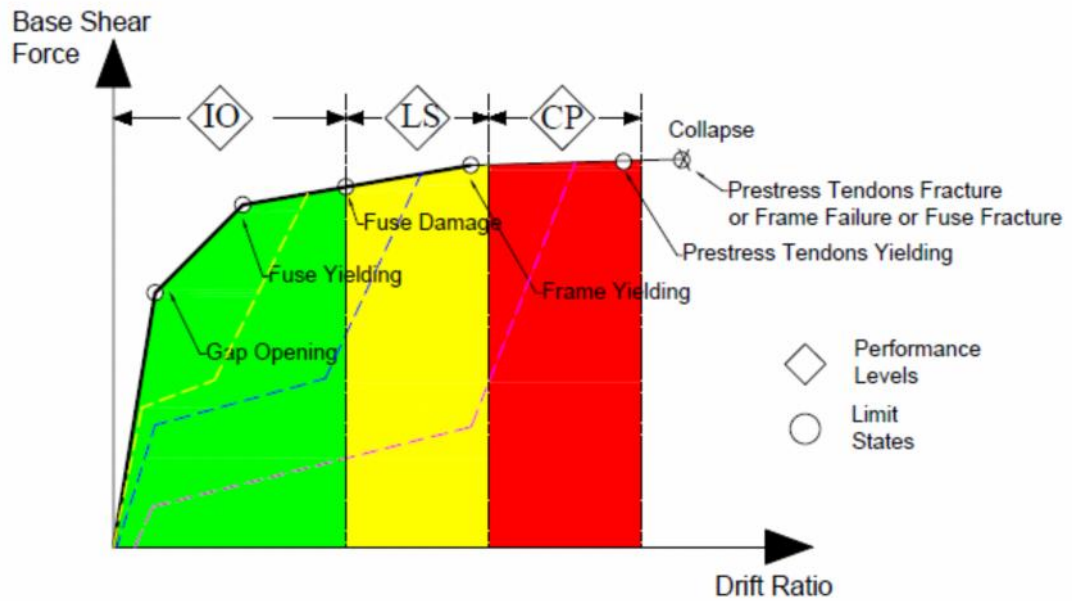


Figure 6-56 Performance goals of the SC-EBF Structure under seismic load (IO = Immediate occupancy; LS = life safety, CP = Collapse prevention)

Table 6-1 Section properties of the structural components for K-type SC-EBF cases

	Structural Member	Section	L (mm)	t_f (mm)	b_f (mm)	t_w (mm)	h (mm)
case1	Beam	W24x104	2700	19.1	325.1	12.7	612.1
	Column	W14x233	3367	43.7	403.9	27.2	406.4
	Brace	W10x60	4395	17.3	256.5	10.7	259.1
	Rocking link beam	welded plate	980	50.0	264.2	60.0	455.8
case2	Beam	W24x104	2700	19.1	325.1	12.7	612.1
	Column	W14x233	3367	43.7	403.9	27.2	406.4
	Brace	W10x60	4395	17.3	256.5	10.7	259.1
	Rocking link beam	welded plate	980	50.0	264.2	60.0	455.8
case3	Beam	W24x146	2700	27.7	327.7	16.5	627.4
	Column	W14x233	3367	43.7	403.9	27.2	406.4
	Brace	W10x60	4395	17.3	256.5	10.7	259.1
	Rocking link beam	welded plate	2060	40.0	264.2	40.0	445.8
case 4	Beam	W24x146	2700	27.7	327.7	16.5	627.4
	Column	W14x233	3367	43.7	403.9	27.2	406.4
	Brace	W10x60	4395	17.3	256.5	10.7	259.1
	Rocking link beam	welded plate	2060	40.0	264.2	40.0	445.8

Table 6-2 Property evaluation for K-type SC-EBF cases

	case1	case2	case3	case4
K_1 (kN/mm)	264.1	264.1	191.1	191.1
K_2 (kN/mm)	16.3	10.9	7.0	4.7
F_v (kN)	533.9	356.0	460.3	341.3
α	6.17%	4.13%	3.66%	2.46%
β_E	21.47%	22.51%	27.45%	26.64%
F_u (kN)	1729	1371	1213	923
δ_u	1.34%	1.34%	2.55%	2.55%

Table 6-3 Section properties of the structural components for D-type SC-EBF cases

	Structural Member	Section	L (mm)	t _f (mm)	b _f (mm)	t _w (mm)	h (mm)
case I	Beam	W24x104	5400	19.1	325.1	12.7	612.1
	Left Column	W14x233	3367	43.7	403.9	27.2	406.4
	Brace	W10x60	6740	17.3	256.5	10.7	259.1
	Rocking link beam	welded plate	980	50.0	264.2	60.0	455.8
	Right Column	W14x257	3367	48.0	406.4	30.0	416.6
case II	Beam	W24x104	5400	19.1	325.1	12.7	612.1
	Column	W14x233	3367	43.7	403.9	27.2	406.4
	Brace	W10x60	6740	17.3	256.5	10.7	259.1
	Rocking link beam	welded plate	980	50.0	264.2	60.0	455.8
	Right Column	W14x257	3367	48.0	406.4	30.0	416.6
case III	Beam	W24x146	5400	27.7	327.7	16.5	627.4
	Column	W14x233	3367	43.7	403.9	27.2	406.4
	Brace	W10x60	6740	17.3	256.5	10.7	259.1
	Rocking link beam	welded plate	2060	40.0	264.2	40.0	445.8
	Right Column	W14x257	3367	48.0	406.4	30.0	416.6
case IV	Beam	W24x146	5400	27.7	327.7	16.5	627.4
	Column	W14x233	3367	43.7	403.9	27.2	406.4
	Brace	W10x60	6740	17.3	256.5	10.7	259.1
	Rocking link beam	welded plate	2060	40.0	264.2	40.0	445.8
	Right Column	W14x257	3367	48.0	406.4	30.0	416.6

Chapter 7 : Nonlinear FE Analysis of the Self-Centering Eccentrically Braced Frames with Two Rocking Link Beams under Cyclic Loading

It is found in Chapter 6 that the ductility of the SC-EBF with short rocking link beams is generally lower than that of SC-EBF with long rocking link beams if PT tendons of the same length are used for both cases. Because the fuse beams are connected between the beams' end plates which are in contact with the rocking link beam in the SC-EBF structures, special design (e.g., "finger joint") is needed for the fuse members to reduce its axial force. For SC-EBF structure with long rocking link beam, it is also difficult to design the fuse link beam to meet the desired energy dissipation capacity because plastic deformation tend to concentrate to narrow regions near the fuse link end. In this chapter, a modified design on the K-type SC-EBF structure with two short rocking link beams is studied, with the aim to achieve a ductility ratio comparable to that of the K-type SC-EBF structure with long rocking link beam and elastic stiffness and gap-opening force similar to those of the K-type SC-EBF structure with short rocking link beam. Additionally, this modified design also allows for the incorporation of fuse devices for enhanced energy dissipation capacity.

7.1. Introduction

As mentioned in Chapter 6, in order to reduce the tensile stress in the PT tendons of the SC-EBF structure with a short rocking link beam under cyclic loading, the depth of the rocking link beam need to be controlled. However, reducing the rocking beam depth would cause decreased values of elastic stiffness K_1 and effective linear limit force V_y of

the SC-EBF structure. Hence a modified design with two parallel rocking link beams are proposed here for the SC-EBF structure to compensate for the elastic stiffness and the effective linear limit force reductions due to decreased rocking link beam depth. Detailed configuration of the K-type SC-EBF structure with two short rocking link beams is schematically shown in Figure 7-1. The section size of each rocking link beam is selected in such a way that its gross section area and web area are approximately half of the rocking link beam in the SC-EBF structure with one short rocking link beam. The composite moment of inertia of the two rocking link beams with reduced section depth is thus equal to that in the SC-EBF structure with one short rocking link beam. Similarly, once the lateral pushover load exceeds a critical value, gap openings are triggered at the pre-compressed joints, as shown in Figure 7-2. Fuse devices are connected between the upper rocking link beam and the lower rocking link beam on both sides, as shown in Figure 7-1. Under the lateral pushover load, the two rocking link beams rotates in parallel to each other, thus causing the fuse devices (a shear panel in this study) to be deformed in shear. Seismic energy is dissipated via the shear yielding of the fuse devices.

7.2. Case Study on the K-type SC-EBF Structure with Two Short Rocking Link Beams

7.2.1. Prototype K-type SC-EBF Structure

For comparison purpose, the prototype K-type SC-EBF structure with two rocking link beams is modified from the K-type SC-EBF structure with one short rocking link beam (i.e., case 1) in Chapter 6. The length and the section sizes of the beams, columns, and

braces of the prototype SC-EBF structure with two rocking link beams are the same as those of case 1. Steel plates with a thickness of 50 mm are welded to the beam ends. The rocking link beams measure 1,030 mm long in the prototype SC-EBF structure with two rocking link beams. Section details of the rocking link beams in the prototype SC-EBF structure are plotted in Figure 7-3. The box shape is selected for ease in installing the fuse devices (perforated AISI 316L stainless steel plates) which are attached to the exterior surfaces of the rocking link beams using high-strength bolts. The PT tendon area is 560 mm² from four 7-wires PT strands (nominal area of one PT strand = 140 mm²) on each side of one rocking link beam (i.e., total PT tendon area is 2,240 mm²). The PT tendons are positioned at the mid-depths of each rocking link beam. Detailed dimensions of the beams, columns, and braces of the prototype SC-EBF structure with two rocking link beams are listed in Table 7-1.

Fuse devices are connected between the upper and the lower rocking link beams on two sides. The fuse devices which resemble the slit steel plate wall panel are fabricated from AISI 316L stainless steel plates. The length, width, and thickness of the stainless steel plate are 296 mm, 200 mm, and 12.7 mm respectively. Slits with round ends were created in the stainless steel plate. The slits measure 120 mm long, 40 mm wide, and have a corner radius of 20 mm, and are spaced 40 mm apart. Section details of the perforated fuse panels are schematically shown in Figure 7-4, where the shaded areas represent the bolted connections of the fuse panel.

7.2.2. Finite Element Simulation Study

Nonlinear finite element analysis of the prototype K-type SC-EBF structure with two short rocking link beams was performed using ANSYS Academic ver. 15.0. The primary EBF frame members of the SC-EBF structure were made of ASTM A992 steel and the fuse devices were made of AISI 316L stainless steel. The combined plasticity hardening model was employed to characterize the stress-strain relationship for both materials under cyclic loading. The calibrated material parameters of the combined hardening models for A992 steel and AISI 316L stainless steel can be found in Chapter 2.

Finite element modeling of the SC-EBF structure with two short rocking link beams is similar to that of the SC-EBF structure with one rocking link beam. Beam elements were adopted for modeling the SC-EBF's columns, and portions of the beams and braces away from the rocking link beams. Shell elements were used for the rocking link beams, the fuse panels, and the portions of the beams and braces near the rocking link beams. Link elements were used for modeling the PT tendons. The half model was built to represent the SC-EBF system in ANSYS. The meshed model of the prototype SC-EBF structure is shown in Figure 7-5.

Loading procedure adopted for the FE analysis of the SC-EBF system involves the following two steps:

- Step 1 (Applying initial PT force): Starting from time zero, the initial postensioned (PT) force was gradually applied to the PT tendons and completed at

time equal to one. At time equal to one, the PT stress in the PT tendons was 741 MPa. This step corresponds to the physical post-tensioning process of the PT tendons.

- Step 2 (Quasi-static loading): Starting from time equal to one, a cyclical loading protocol was applied to the SC-EBF system. The cyclic loading protocol expressed in terms of the SC-EBF's story drift ratio is adapted from the experiment loading protocol by Ricles et al. (2006). This loading protocol includes first three cycles with an amplitude of 0.005, and the following every three cycles with an amplitude increment of 0.005. The loading protocol applied to the SC-EBF systems is plotted in Figure 7-6. This step represented the cyclic loading process of the SC-EBF system and was terminated once the PT tendons yield.

7.2.3. Analytical Force Displacement Derivation for K-type SC-EBF Systems

7.2.3.1. General Behavior of the K-type SC-EBF Systems

The gap opening process of the SC-EBF structure with two rocking link beams is the same as that of the SC-EBF structure with one rocking link beam, which can be divided into five distinct phases. In phase I, the EBF beams are in full contact with the two rocking link beams and the contact compression stress is uniformly distributed over the contact surface. In phase II, the contact stress at the bottom flange reduces to zero while maximum contact stress occurs at the top flange of each rocking link beams at the left side. In phase III, the compression zone shrinks and the zero contact stress location

moves upward to the mid-depth of each rocking link beams. The PT tendons are on the verge of being further stretched. In phase IV, the zero contact stress location continues to move upwards at the left side of each rocking link beams. PT tendons are elongated due to gap opening. In phase V, zero contact stress location is near the top flanges of the two rocking link beams at the left side.

Usually the fuse device is designed to be much weaker than the primary frame of the SC-EBF structure. Hence the interaction effect between the fuse device and the SC-EBF structure is assumed to be negligible so that the mechanical properties of the SC-EBF system can be decoupled, i.e., the force displacement relationship of the SC-EBF system equipped with fuse devices can be calculated by superimposing those of the SC-EBF's frame and fuse devices. This calculation strategy which greatly simplifies the analytical formulation process is schematically illustrated in Figure 7-7.

7.2.3.2. Force-Displacement Relationship

The force displacement relationship of the SC-EBF frame is governed by three key parameters: the initial stiffness K_1 , the effective linear limit force V_y (which is equal to the base shear force at gap opening), and post-gap-opening stiffness K_2 . The internal force distribution of the rocking link beam in the SC-EBF frame under the applied lateral load is shown in Figure 7-8.

Referring to the relationship proposed by Richards (2010), the elastic deformation of an EBF is comprised of four parts: the axial deformation of the braces, the axial deformation

of the beam, the shear deformation of the beam, and the bending deformation of the beam. Before gap opening, the lateral elastic stiffness of the SC-EBF is identical to that of a conventional EBF. Therefore, the initial stiffness K_1 of the SC-EBF frame is calculated using the equation proposed by Richards (2010), which is expressed in Equation 7-1:

$$K_1 = \frac{1}{\frac{1}{2E} \left(\frac{L_d}{A_d} \right) \left(\frac{L_d}{a} \right)^2 + \frac{1}{2E} \left(\frac{a}{A_b} \right) + \frac{1}{G} \left(\frac{H^2 e}{A_{bv} L^2} \right) + \frac{H^2 e^2}{12EIL}} \quad \text{Equation 7-1}$$

Where: terms L , L_d , e , a , and H are the SC-EBF's full bay width, brace length, rocking link beam length, beam length, and bay height shown in Figure 7-8; terms E and G are the elastic modulus and shear modulus of A992 steel; A_d , A_b , and A_{bv} are the brace's section area, beam's section area, and the beam's web area respectively.

The PT tendons are further stretched after the gap opens between the beam end plates and the rocking link beam ends. The bending moments at the end sections of the rocking link beam are equal to the force couples formed by the PT tendon forces and the compression forces resultant over the contact surfaces. From the research work by Christopoulos (2002), the compression contact stress is assumed to be linearly distributed over the flange thickness of the link beam. Therefore, the effective linear limit force V_y of the bare SC-EBF frame without fuse devices can be calculated as Equation 7-2:

$$V_y = 2P = 2 \cdot \frac{M \cdot L}{H \cdot e} = \frac{2 \cdot 2F_{PT0} \cdot \left(\frac{1}{2}h - \frac{1}{2}t_f \right) \cdot L}{H \cdot e} = \frac{2F_{PT0} \cdot (h - t_f) \cdot L}{H \cdot e} \quad \text{Equation 7-2}$$

Where V_y is the effective linear limit force the SC-EBF frame; h and t_f are the section depth and flange thickness of the rocking link beam; M is the total rocking link beam end moment at gap opening, which is equal to $2 \cdot 2F_{PT_0} \cdot \left(\frac{1}{2}h - \frac{1}{2}t_f\right)$. The first factor 2 in the M calculation is to account for a total of two pairs of PT tendons installed on both sides of one rocking link beam. The second factor 2 in the M calculation is because two rocking link beams are used.

After gap opening, the increment of the PT tendon force is proportional to the gap opening distance at the mid-height of each rocking link beam, which is calculated from Equation 7-3.

$$F_{PT} = \beta \cdot E_{PT} \cdot A_{PT} \cdot \frac{\Delta_{PT}}{L} + F_{PT_0} = F_{PT_0} + \beta \cdot E_{PT} \cdot A_{PT} \cdot \frac{\gamma_{gap} \cdot (h - t_f)}{L}$$

Equation 7-3

$$\Delta_{PT} = \frac{h_w}{2} \cdot \gamma_{gap} \cdot 2 = (h - t_f) \cdot \gamma_{gap}$$

The relationship between the link rotation angle γ , the gap opening angle γ_{gap} , and lateral drift Δ_{push} is expressed in Equation 7-4:

$$\theta \cdot L = \frac{\Delta_{push}}{H} \cdot L = \gamma \cdot e = (\gamma_{gap} + \gamma_0) \cdot e$$

Equation 7-4

Considering the force equilibrium relation for the SC-EBF frame, the relationship between the lateral force P and the PT tendon force F_{PT} is expressed in Equation 7-5:

$$P = \frac{V \cdot \frac{1}{2}L}{H} = \frac{M \cdot L}{H \cdot e} = \frac{F_{PT} \cdot (h - t_f) \cdot L}{H \cdot e} \quad \text{Equation 7-5}$$

Take derivatives of both sides of Equation 7-5, the post-gap-opening stiffness K_2 of the SC-EBF frame is expressed in Equation 7-6.

$$K_2 = \frac{dV_{base}}{d\Delta_{push}} = \frac{2 \cdot dP}{d\Delta_{push}} = \frac{2\beta \cdot E_{PT} \cdot A_{PT} \cdot (h - t_f)^2 \cdot L}{H^2 \cdot e^2} \quad \text{Equation 7-6}$$

Where: E_{PT} is the elastic modulus of the PT tendons; A_{PT} is the section area of the PT tendons; F_{PT0} is the initial PT force in the PT tendons; γ_0 is the critical link rotation angle at gap opening; β is a parameter that is used to account for the stress loss of the PT tendons due to the deformation of the SC-EBF during the loading process as a result of the increased PT tendon force. The meaning of β is the same as that is illustrated in Chapter 6.

7.2.3.3. Contribution from Fuse Device

In the initial configuration of the SC-EBF shown in Figure 7-9, the top corners of the two rocking link beams are coinciding with points C_1 and C_2 on the left-side beam end plate. The ends of a fuse plate's centerline are located at points A and B at the mid-depths of the two rocking link beams. The center lines of the two rocking link beams are pointing to points of O_1 and O_2 on the left-side beam end plate. Unit vectors \vec{e}_1 (i.e., \mathbf{i}) and \vec{e}_2 (i.e., \mathbf{j}) are defined to be parallel and perpendicular to the longitudinal axis of the beam respectively in the initial configuration of the SC-EBF. The extensions of the fuse plate's

center line are coinciding with points E_1 and E_2 at top flange of the upper rocking link beam and bottom flange of the lower rocking link beam respectively. In the displaced configuration of the SC-EBF shown in Figure 7-10, when the SC-EBF is pushed to the right by a lateral load, points A, B, C_1 , C_2 , O_1 , O_2 , E_1 , and E_2 move to the new locations of A' , B' , C_1' , C_2' , O_1' , O_2' , E_1' , and E_2' respectively and the angle between the displaced beam's longitudinal axis and the horizontal direction is assumed to be equal to the story drift ratio θ . As the elastic deformation of the rocking link beam is negligible, the length of each rocking link beam's diagonal line is assumed to be unchanged. The fuse's relative end displacement $\Delta h'$ with respect to θ is schematically illustrated Figure 7-10, which is expressed in Equation 7-7:

$$\Delta h' = \overline{C_2 F} = \gamma_{gap} \cdot \overline{C_1 C_2} = (\gamma - \gamma_0) \overline{C_1 C_2}$$

Equation
7-7

Where: $\overline{C_1 C_2} = 246.4 \text{ mm}$; γ is the link rotation angle corresponding to θ ; and γ_0 is the link rotation of the rocking link beams at gap opening.

The calculation of the critical link rotation angle γ_0 at gap opening is illustrated in Figure 7-11. The maximum contact stress occurs at the top flange of the rocking link beam. The link rotation angle γ_0 is calculated from the compression strain from the center of the top flange at the left side of the rocking link beam, which is expressed in Equation 7-8:

$$F_{PT_0} = F_C = E \cdot \varepsilon_0 \cdot b_f \cdot t_f$$

$$\gamma_0 = \frac{\varepsilon_0 \cdot e}{\frac{1}{2}(h - t_f)} = \frac{2F_{PT_0} \cdot e}{E \cdot t_f \cdot b_f \cdot (h - t_f)} \quad \text{Equation 7-8}$$

Where: terms t_f , b_f , e , and h are the rocking link beam's flange thickness, flange width, length, and depth respectively; ε_0 is the compression strain at the center of the top flange.

The angle θ_0 formed by the beam's longitudinal axis to the horizontal axis at gap opening is calculated from Equation 7-9.

$$\theta_0 = \frac{\Delta}{H} = \frac{F_y}{K_1 H} \quad \text{Equation 7-9}$$

After gap opening, the link rotation angle γ is equal to the sum of the gap opening angle γ_{gap} and the critical link rotation angle γ_0 at gap opening. The tension force of the PT tendons is proportionally increased with gap opening angle γ_{gap} . Based on the force equilibrium of the SC-EBF frame, the relationship between the gap opening angle γ_{gap} and PT tendon force is expressed in Equation 7-10.

$$F_{PT} = F_{PT_0} + 2 \cdot \beta \cdot E_{PT} \cdot A_{PT} \cdot \frac{\Delta_{PT}}{L} = F_{PT_0} + \beta \cdot E_{PT} \cdot A_{PT} \cdot \frac{\gamma_{gap} \cdot (h - t_f)}{L} \quad \text{Equation 7-10}$$

From the force displacement relationship of the SC-EBF frame, the relationship between P and θ is expressed in Equation 7-11:

$$\theta = \theta_0 + \frac{2P - V_{by}}{K_2 \cdot H} \quad \text{Equation 7-11}$$

It is assumed that the link rotation angle γ is linearly related to θ before gap opening as the deformation of the SC-EBF structure is very small. Therefore, the relationship of γ with respect to θ is expressed in Equation 7-12:

$$\gamma = \begin{cases} \gamma_{gap} + \gamma_0 & \text{for } \theta > \theta_0 \\ \frac{\theta}{\theta_0} \gamma_0 & \text{for } \theta \leq \theta_0 \end{cases} \quad \begin{array}{l} \text{Equation} \\ 7-12 \end{array}$$

7.2.3.4. Force Displacement Relationship of the Fuse Devices

FE analysis was conducted on the fuse device (perforated AISI 316L stainless steel plate with slits) that was treated as the substructure. The end displacements of the fuse device recorded from the FE analysis of the SC-EBF structure are input to the substructure of the fuse member. Meshing was further refined in the substructure model of the fuse member. From the FEM simulation results, the cyclic shear force versus end displacement relationship of the fuse device used for the SC-EBF system in this study are plotted in Figure 7-12.

7.2.3.5. Contribution of Fuse Shear to SC-EBF Structure

Based on the equilibrium relations shown in Figure 7-13, a moment increment of ΔM is added to the interface between the beam plate and the rocking link beams, in order to balance the top and bottom end moments (denoted as M') of the fuse device due to its shear force (denoted as V'). Relationship among the fuse shear force V' , end moment M' , and the increment of the pushover force ΔP is shown in Equation 7-13.

$$\begin{cases} M' = V' \cdot \frac{1}{2} h' \\ \Delta P = \frac{M' \cdot L}{H \cdot e} \end{cases} \quad \begin{array}{l} \text{Equation} \\ 7-13 \end{array}$$

Where: h' is the length of the perforated plate; L is the total width of the SC-EBF structure; and H is the height of the SC-EBF structure.

Hence the base shear force increment due to the fuse devices is expressed Equation 7-14:

$$\Delta V_b = 2\Delta P \quad \text{Equation 7-14}$$

7.2.3.6. Validation of the Analytical Force Displacement Derivations for the SC-EBF Structure

The accuracy of the analytical formulation on the force displacement relationship of the SC-EBF structure with two rocking link beams is verified by comparing with the FE analysis results. For the investigated K-type SC-EBF structure with two rocking link beams, the hysteresis lateral force vs. drift curves obtained from FEM simulation and analytical derivation are plotted in Figure 7-14. It can be observed that the analytically derived curve match well with the corresponding FEM simulation curve for the investigated SC-EBF structure with two rocking link beams.

7.2.4. FEM Simulation: Results and Discussions

A total of seven key locations were selected from the K-type prototype SC-EBF structure with two rocking link beams to evaluate the internal force responses in this study.

Internal forces including the axial force, shear force, and bending moment were recorded at the selected sections during FE simulation. The selected key locations are marked in Figure 7-15, including the left side (section A-A), middle (section B-B), and the right side (section C-C) of the left-side beam, the middle (section D-D) and bottom end (section E-E) of the left-side column, the middle section (section F-F) of the left-side brace, and the left side section (section G-G) of the upper rocking link beam.

7.2.4.1. EBF Beam

The axial force history at section A-A is plotted in Figure 7-16. The axial force in the left-side beam of the K-type SC-EBF structure was normalized by the beam's axial yield force N_P , which is equal to the product of nominal yield stress of A992 steel and the beam's gross cross-section area. The maximum N/N_P ratio was observed during the last loading cycle at the drift ratio of approximately 2.8%. As the total PT tendon area in the SC-EBF with two short link beams is much higher than the PT tendon area in the SC-EBF with one short link beam (case 1), the observed axial force is naturally much higher than the SC-EBF structure with one rocking link beam.

The shear force histories at section A-A, section B-B, and section C-C for the K-type SC-EBF structure with two short rocking link beams are plotted in Figure 7-17. The shear forces in the left-side beam of the K-type SC-EBF structure were normalized by the beam's shear strength V_P , which was equal to the product of the material's nominal shear yield stress ($=0.6f_y$) and web area. The V/V_P ratio at the three selected sections of the

beam was identical, since there is no other transverse external force acting along the beam.

The bending moment histories at these three sections of the EBF beam for the SC-EBF system with two short rocking link beams are plotted in Figure 7-18. The bending moments were normalized by the beam's plastic bending moment M_p , which was equal to the nominal yield stress multiplied by the beam's plastic section modulus. It can be observed that the M/M_p ratio was smallest near the beam-to-column joint (section A-A) and largest near the beam-to-link joint (section C-C), which is consistent with the moment distribution pattern in the EBF subjected to lateral load.

7.2.4.2. EBF Column

The shear force histories at the middle-length section (section D-D) and the bottom section (section E-E) of the left-side column for the K-type SC-EBF structure with two short rocking link beams are plotted in Figure 7-19. The shear forces were normalized by the column's shear strength V_p , which was equal to the product of the material's nominal shear yield stress ($=0.6f_y$) and web area for I-section steel shape. It can be observed that the V/V_p ratio was fairly small in the column up to the maximum drift ratio. This phenomenon is in agreement with the theoretical analysis, as column is primarily subjected to axial force. The V/V_p ratios at the two selected sections in each K-type SC-EBF case were generally identical as no lateral force was acting along the column.

The axial force history at section D-D is plotted in Figure 7-20. The axial force in the column was normalized by the column's axial yield force N_p , which is equal to the product of nominal yield stress of A992 steel and the column's gross cross-section area. The maximum N/N_p ratio was observed during the last loading cycle at the drift ratio of approximately 2.8%. It should be noted that the calculated column axial force was induced by the lateral load only, and the gravity load was not combined; hence the axial force in the column was generally low.

7.2.4.3. EBF Bracing

The axial force history of the middle-length section (section F-F) of the left-side brace for the SC-EBF structure with two rocking link beams is plotted in Figure 7-21. Similar to the afore-mentioned beam axial force normalization procedure, the bracing axial force of the SC-EBF structure was normalized by the bracing's axial yield strength N_p , which was equal to the nominal yield stress multiplied by the brace's gross section area. Shown in Figure 7-21, the brace's maximum F/F_p ratio was 0.3 at the peak drift ratio.

7.2.4.4. Rocking Link Beam

The axial force history on the left end section of upper rocking link beam (section G-G) is plotted in Figure 7-22. The axial force in the upper rocking link beam of the SC-EBF structure were normalized by the rocking link beam's axial yield strength N_p , which was equal to the nominal yield stress multiplied by the rocking link beam's gross section area. It can be observed that the N/N_p ratio was fairly low.

The shear force history of the left end section of upper rocking link beam (section G-G) in the SC-EBF structure with two rocking link beams is plotted in Figure 7-23. The shear force in the upper rocking link beam of the SC-EBF structure was normalized by the rocking link beam's plastic shear strength V_p , which was equal to the product of the material's nominal shear yield stress ($=0.6f_y$) and the upper rocking link beam's web area.

The bending moment history of the left end section of upper rocking link beam (section G-G) for the SC-EBF structure with two rocking link beams is plotted in Figure 7-24. The bending moment in the upper rocking link beam of the SC-EBF system was normalized by the rocking link beam's plastic shear strength M_p , which was equal to the nominal yield stress multiplied by the rocking link beam's plastic section modulus.

7.2.4.5. PT Tendon

The tensile stress in the PT tendons versus the drift ratio of the SC-EBF structure with two rocking link beams is plotted in Figure 7-25. The minimum nominal yield stress of G270 PT tendon is 1670 MPa, which is also indicated in Figure 7-25. The occurrence of the PT tendon yielding is set as one of the ultimate limit state for the SC-EBF structures, as the ultimate fracture stress of the PT tendon is very close to its yield stress. Shown in Figure 7-25, the minimum yield stress of the PT tendon was even not reached at the lateral drift ratio of 2.7% for the SC-EBF system with two short rocking link beams. This drift ratio is even larger than the maximum allowable drift ratio of the K-type SC-EBF structures with one long rocking link beam (case 3 and case 4); hence the goal of

increasing the ductility of the SC-EBF structures with short rocking link beams can be achieved by using two short rocking link beams.

7.2.4.6. Fuse Damage Index

Fracture of the fuse devices should be avoided by all means in the SC-EBF design, since the lateral drift ratio of the SC-EBF would be significantly increased once fracture occur so that the frame can take over the additional force carried out by the fuse devices. With reference to the research conducted by Kanvinde and Deierlein (2007) on the cyclic void growth model (CVGM) for predicting the ductile fracture initiation of structural steel, the damage index is defined as the ratio of the cyclic void growth index (CVGI) to the critical cyclic void growth index ($CVGI_{critical}$), which is expressed in Equation 7-15. The damage index should be controlled below one to prevent ductile fracture initiation.

$$Damage = \frac{CVGI}{CVGI_{critical}} \quad \text{Equation 7-15}$$

The definition of CVGI and $CVGI_{critical}$ can be found in Chapter 2.

The Von Mises plastic strain contour of the fuse plate at 2.7% lateral drift ratio of the SC-EBF structure with two rocking link beams is shown in Figure 7-26. It can be concluded from Figure 7-26 that fracture is expected to be initiated at the highest plastic strain locations. The damage index history was calculated from the identified critical locations of the substructure model of the fuse plate, as shown in Figure 7-26. Fracture initiation was predicted during the 11th loading cycle, as indicated in Figure 7-27, which

corresponds to the lateral drift ratio of 2%. However, typically the load carrying capacity was not reduced even after a few loading cycles beyond the predicted fracture occurrence, which is observed from the experiment on the perforated cast steel link beam with slits (Zhang 2015).

7.2.4.7. Cyclic Loading Behavior of K-type SC-EBF Structure with Two Rocking Link Beams

The behaviors of the K-type SC-EBF structure with two rocking link beams were assessed in this chapter. Detailed data of its cyclic loading behaviors are listed in Table 7-2. Compared to the K-type SC-EBF structures with one short rocking link beam (case 1) and with one long rocking link beam (case 3), the initial stiffness K_1 of the SC-EBF structure with two short rocking link beams is between that of case 3 and that of case 1. The post-gap-opening stiffness K_2 of the SC-EBF structure with two short rocking link beams is very close to that of case 3, and is much smaller than that of case 1. The effective linear limit force V_{by} of the SC-EBF with two short rocking link beams is higher than those of case 1 and case 3. The maximum allowable drift ratio of the SC-EBF with two short rocking link beams is slightly higher than that of case 3, and is much higher than that of case 1. Therefore, the SC-EBF structure with two rocking link beams combines the advantages of the SC-EBF structure with one short rocking link beam and the SC-EBF structure with one long rocking link beam.

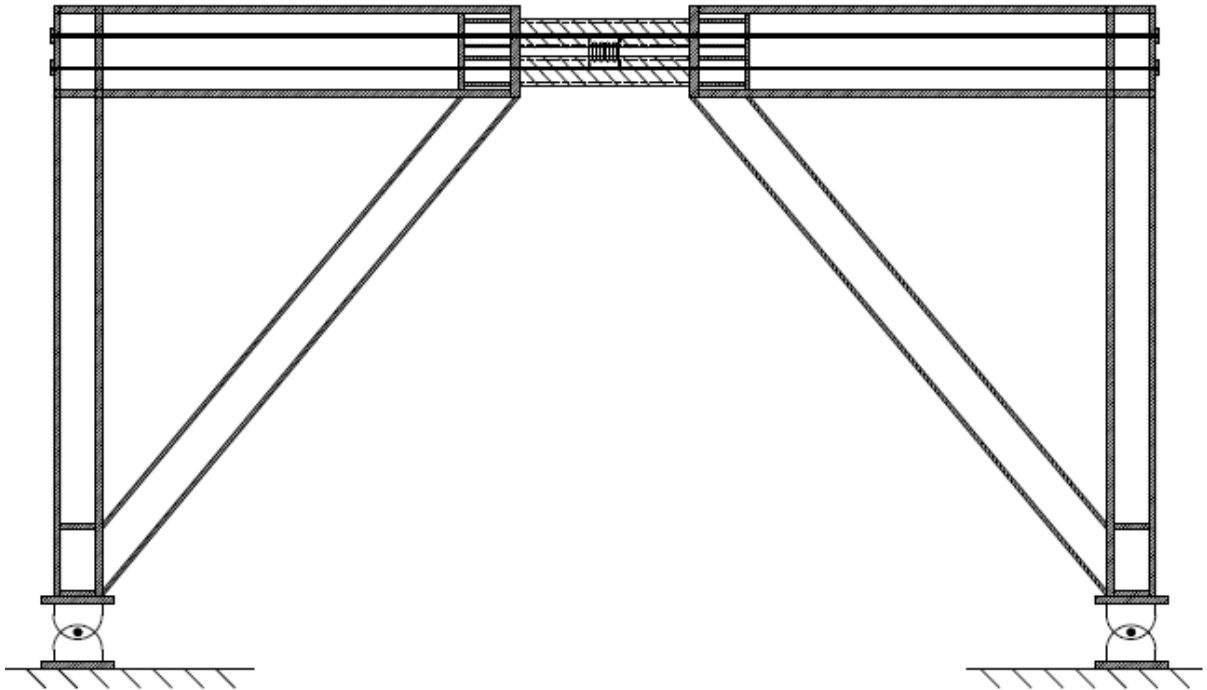


Figure 7-1 General configuration of the K-type SC-EBF structure with two rocking link beams

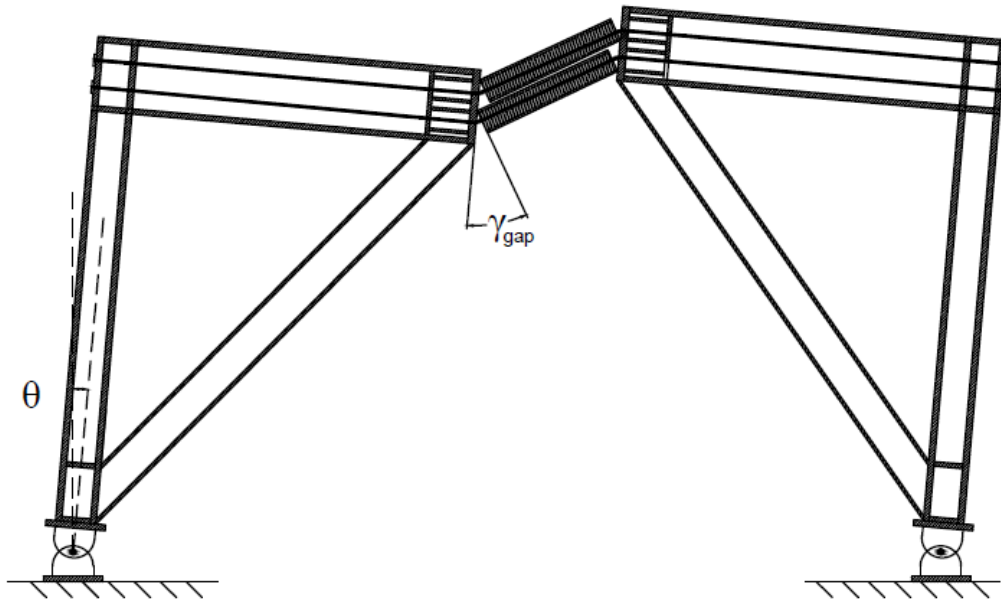


Figure 7-2 Gap opening mechanism

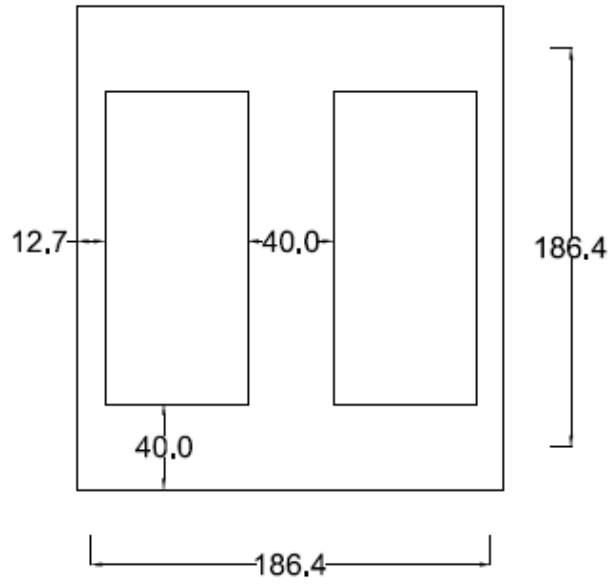


Figure 7-3 Section dimensions of the rockling link beam

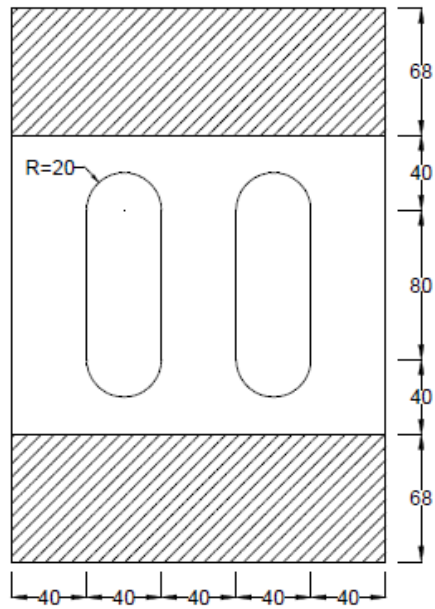


Figure 7-4 Section details of the perforated fuse plate

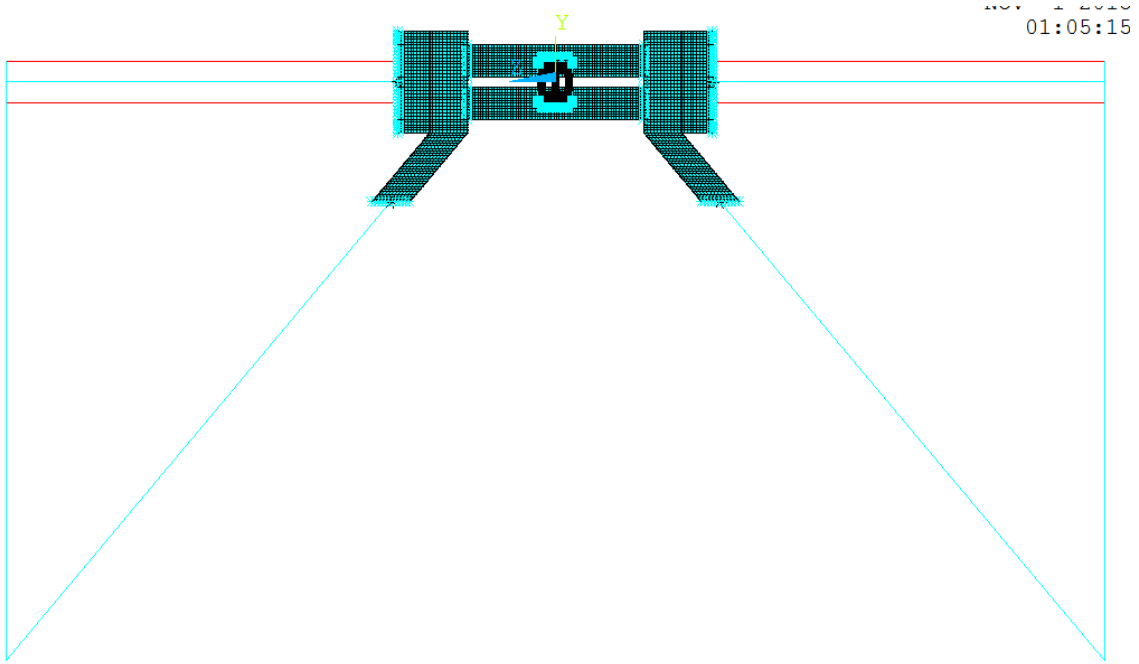


Figure 7-5 Finite element model of the SC-EBF structure with two short rocking link beams

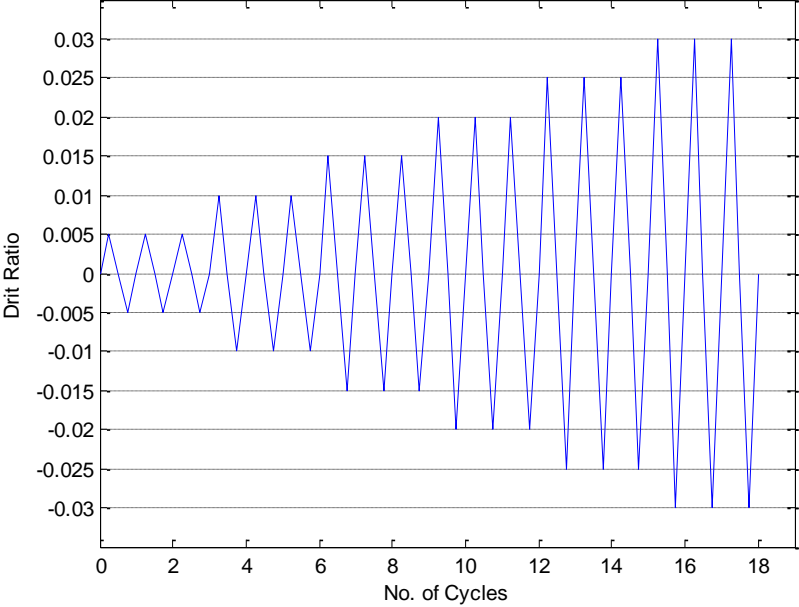


Figure 7-6 Cyclic loading protocol for the SC-EBF structure

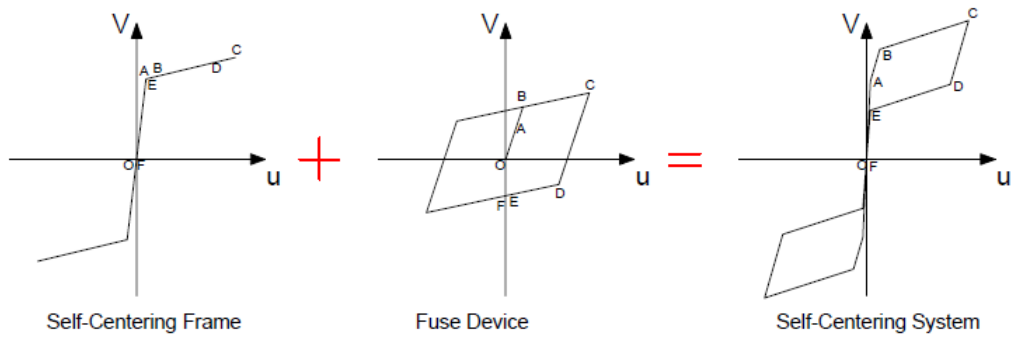


Figure 7-7 Force displacement relationship calculation principle for SC-EBF structure

Points O, A, B, C, D, E, and F correspond to the occurrence of the following affairs:

- O: No external load is applied;
- A: Gap between the rocking link beam and the beam starts to open;
- B: Fuse devices start to yield in the loading direction;
- C: Desired drift is reached;
- D: Fuse devices start to yield in the reversed loading direction;
- E: Gap between the rocking link beam and the beam starts to close;
- F: External load is reduced to zero.

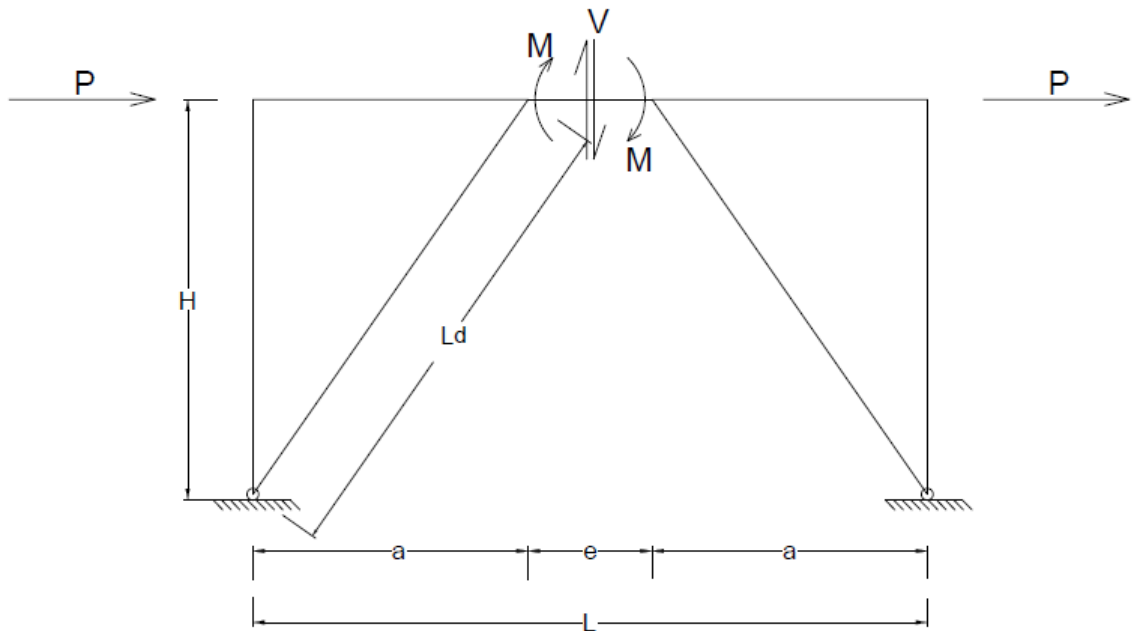


Figure 7-8 Force distributions at the rocking link beams under the lateral load

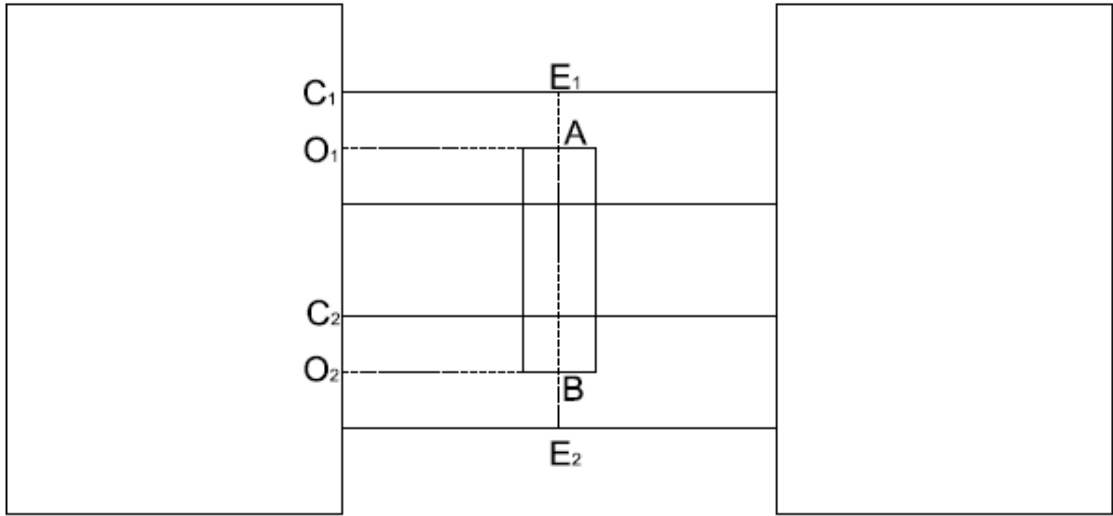


Figure 7-9 Initial configuration of the SC-EBF frame

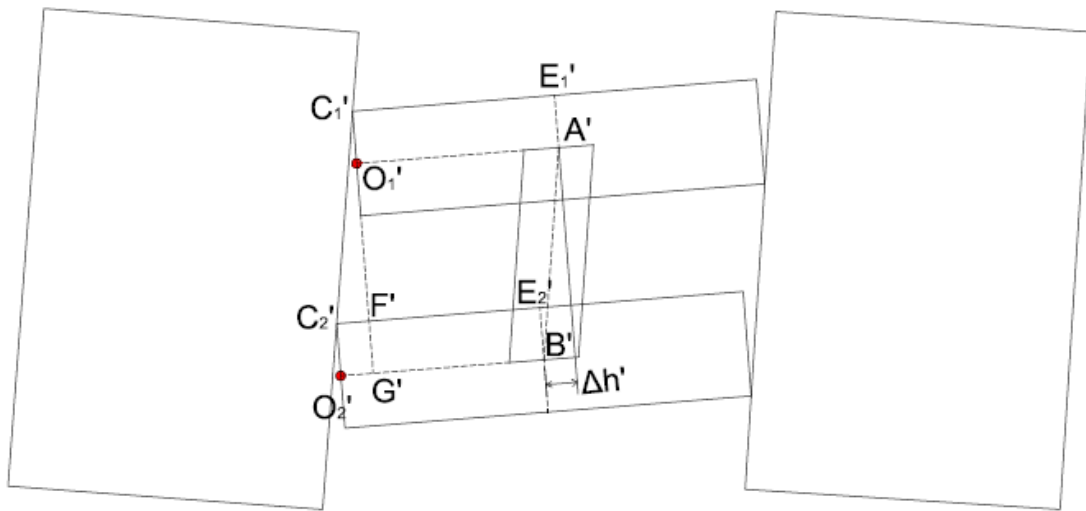


Figure 7-10 Displaced configuration of the SC-EBF frame

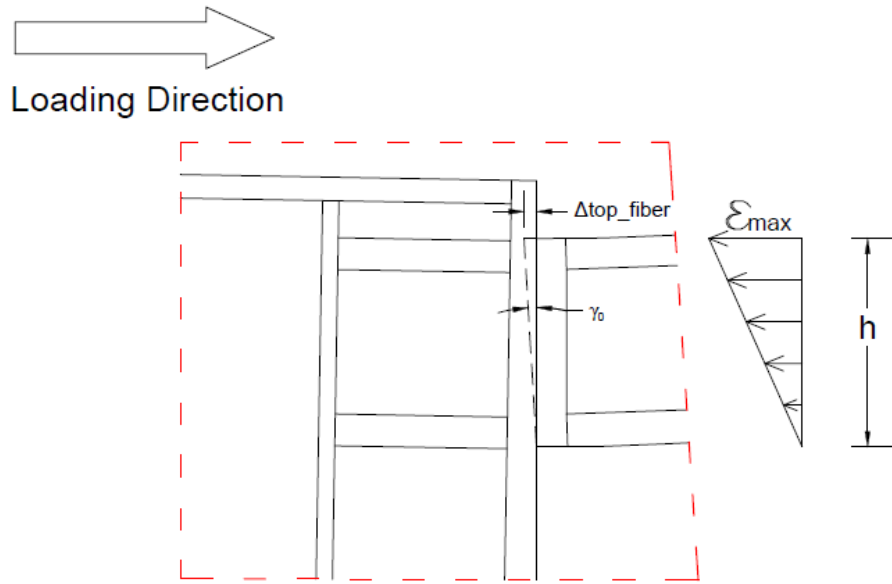


Figure 7-11 Critical link rotation angle determination

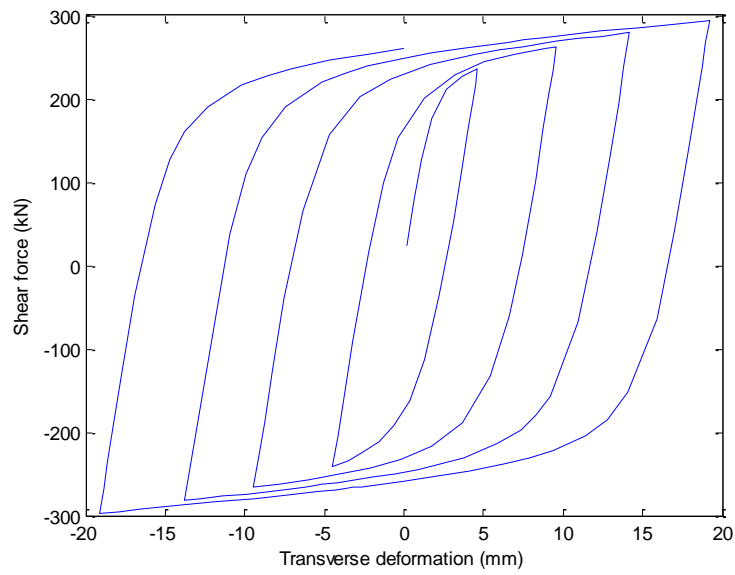


Figure 7-12 Hysteresis force displacement relationship of a single fuse device

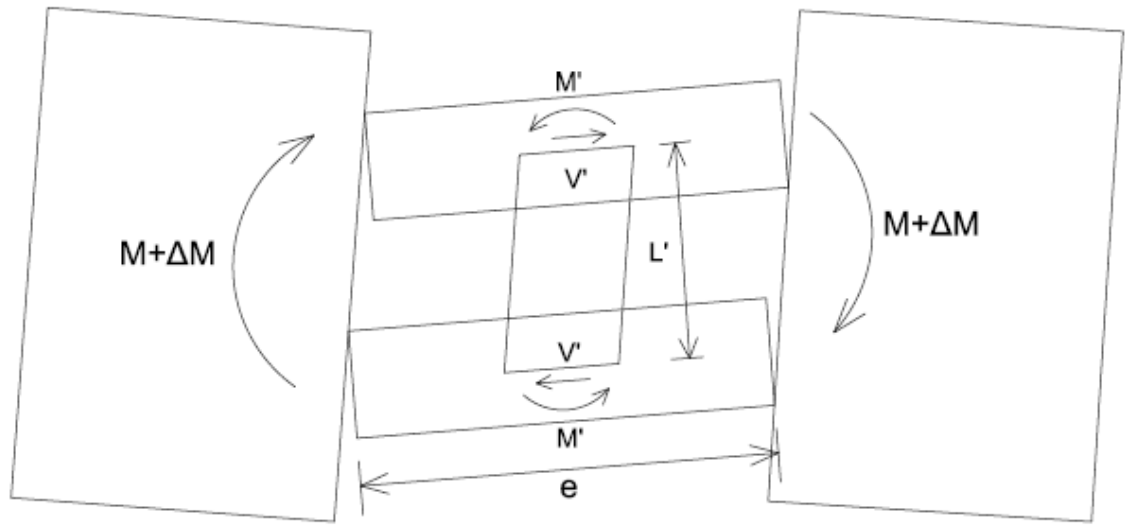


Figure 7-13 Moment equilibrium at the rocking link beams

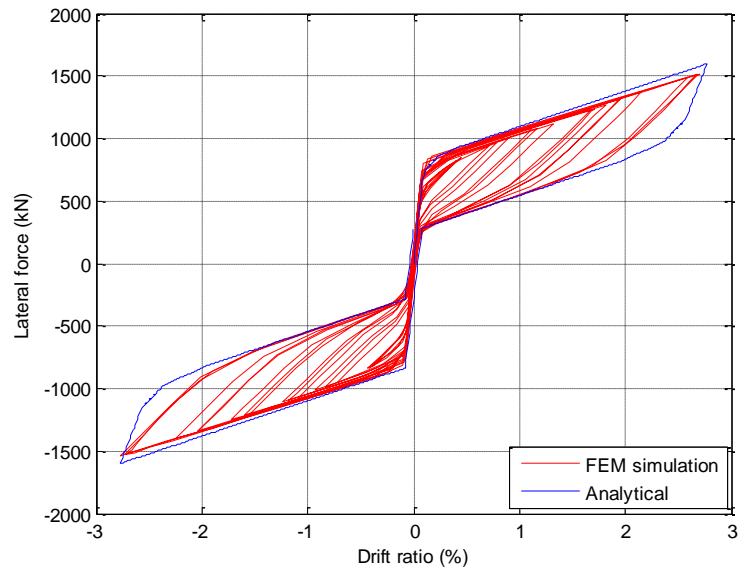


Figure 7-14 Hysteresis force displacement relationship comparison

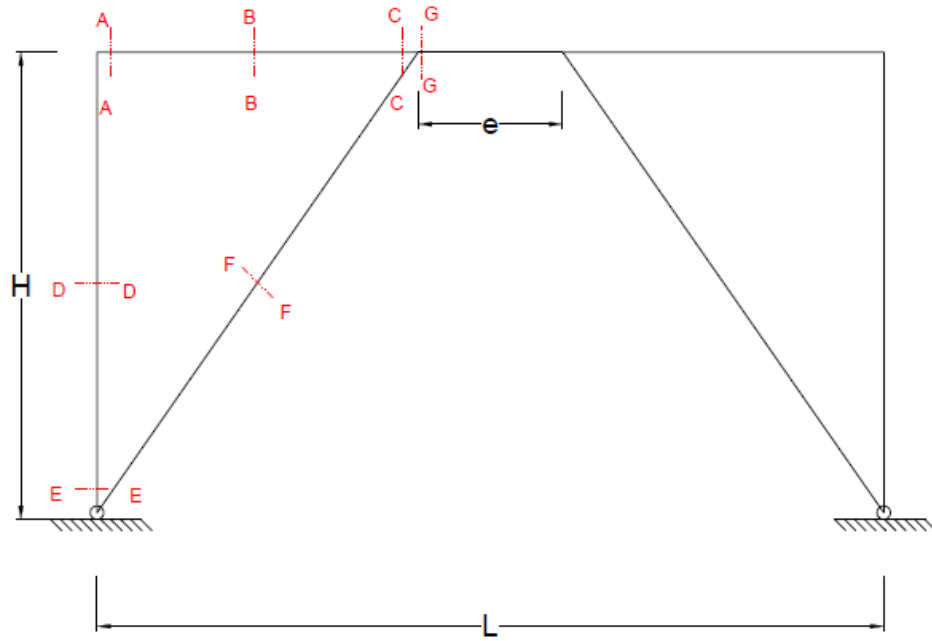


Figure 7-15 Critical locations in the SC-EBF structure

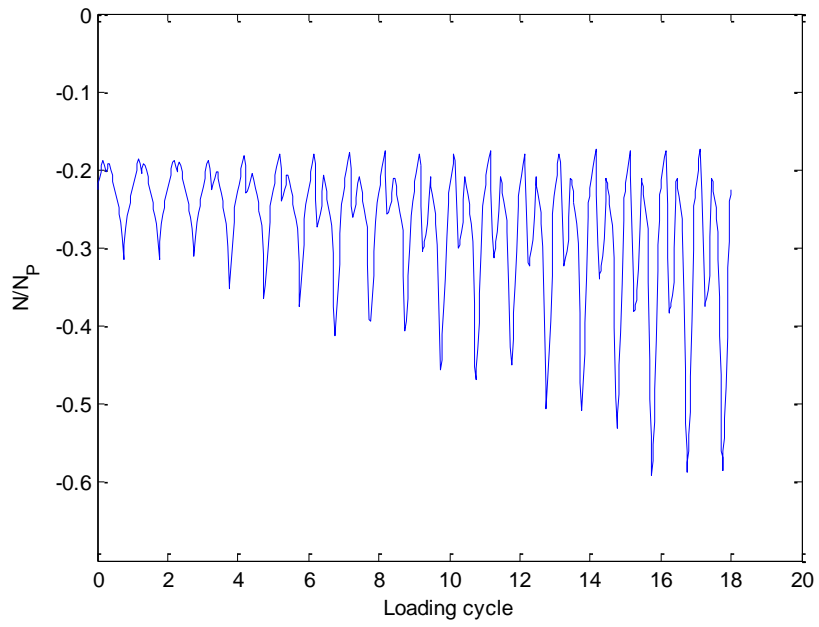


Figure 7-16 Normalized beam axial force at section A-A

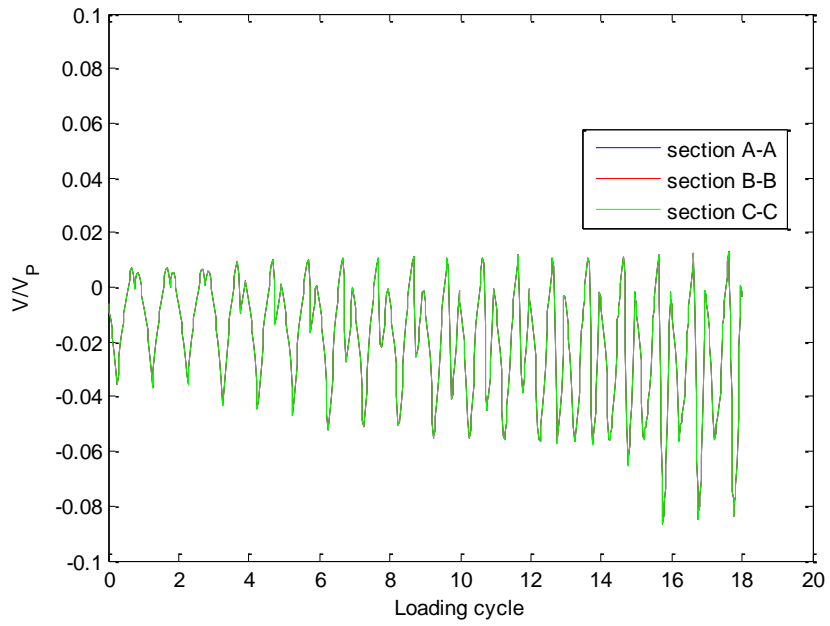


Figure 7-17 Normalized beam shear force at section A-A, B-B, and C-C

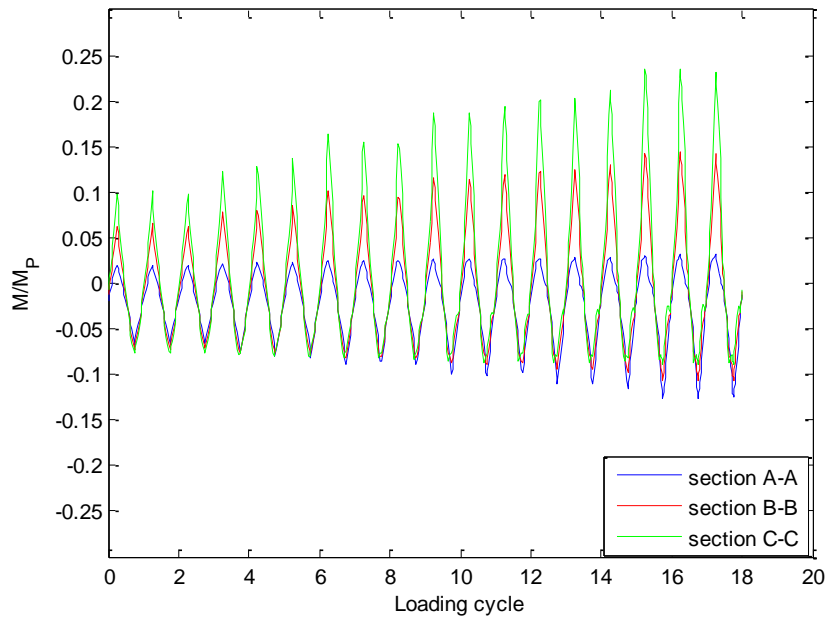


Figure 7-18 Normalized beam bending moment at section A-A, B-B, and C-C

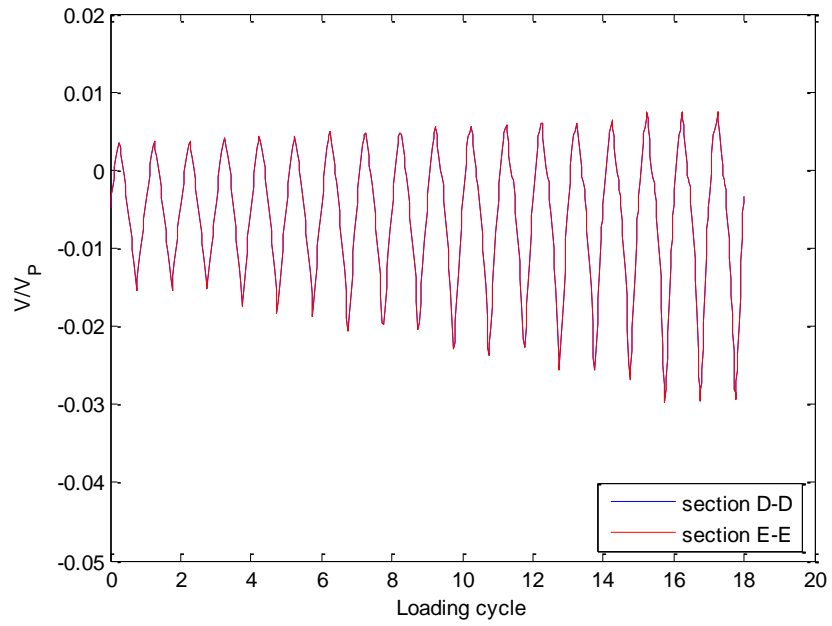


Figure 7-19 Normalized column shear force at section D-D and E-E

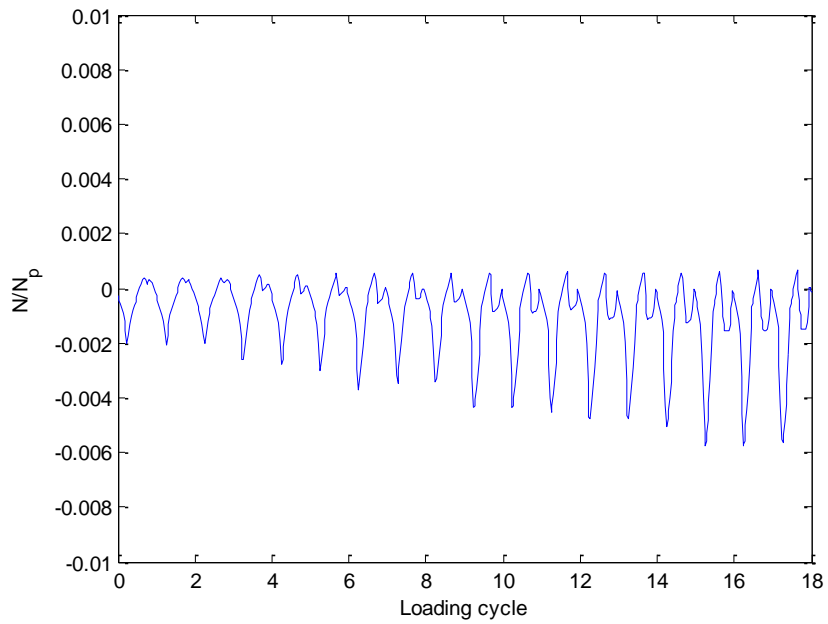


Figure 7-20 Normalized column axial force at section D-D

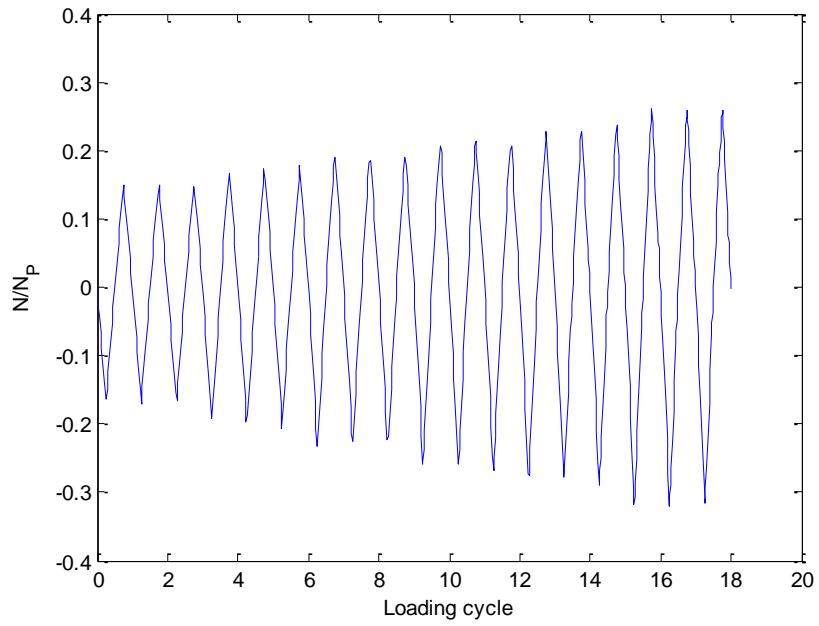


Figure 7-21 Normalized brace axial force at section F-F

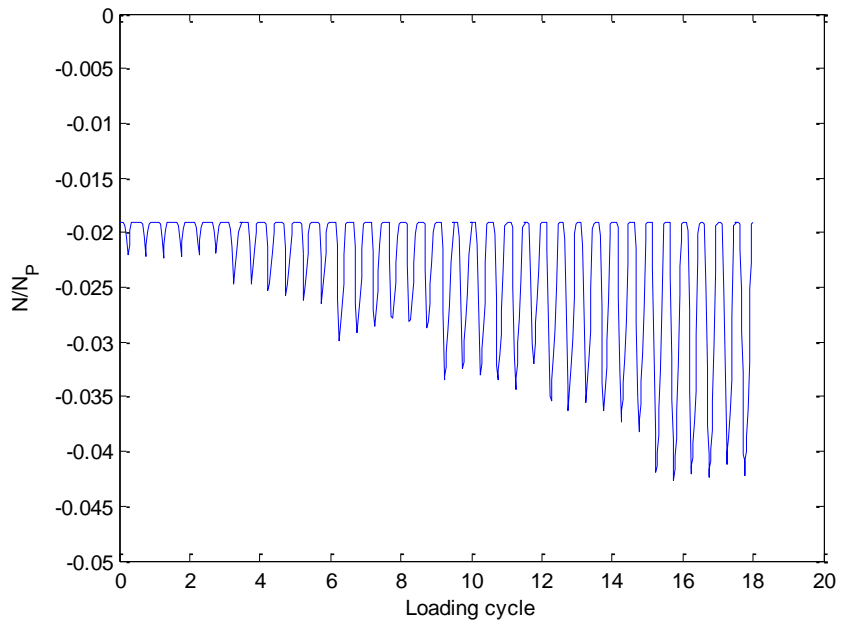


Figure 7-22 Normalized link beam axial force at section G-G

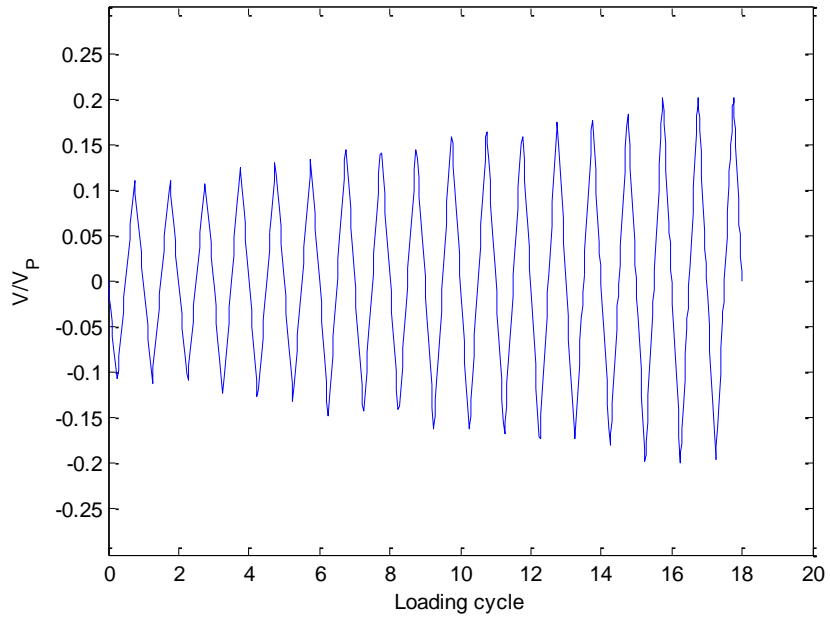


Figure 7-23 Normalized link beam shear force at section G-G

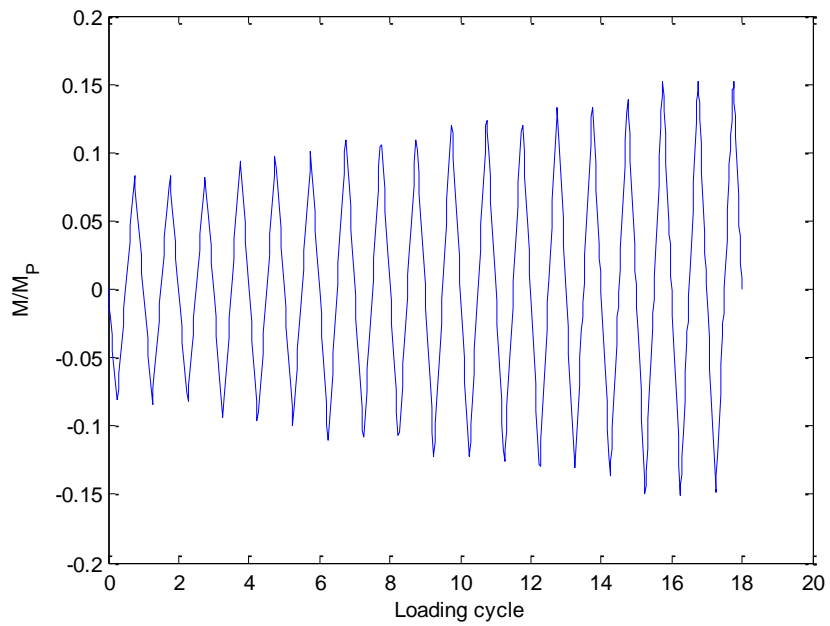


Figure 7-24 Normalized link beam bending moment at section G-G

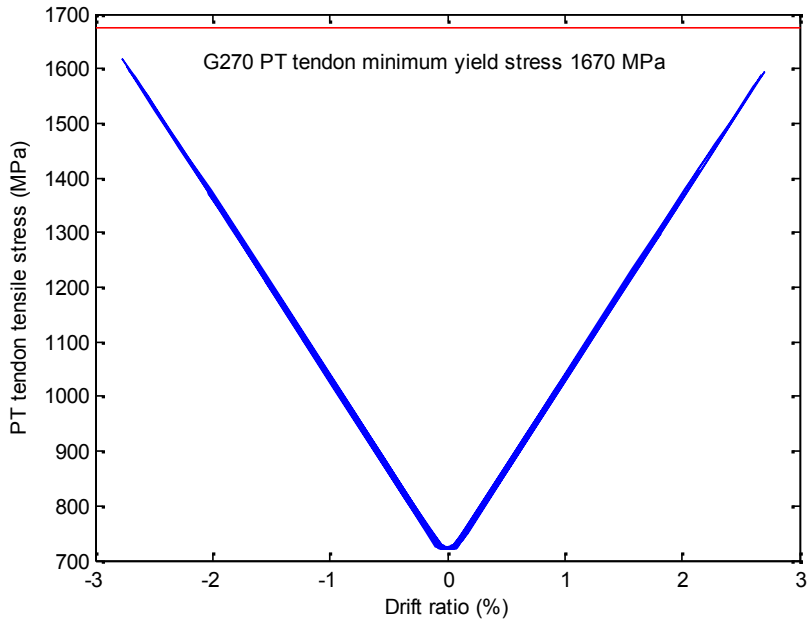


Figure 7-25 Tension stress in PT tendons vs. drift ratio

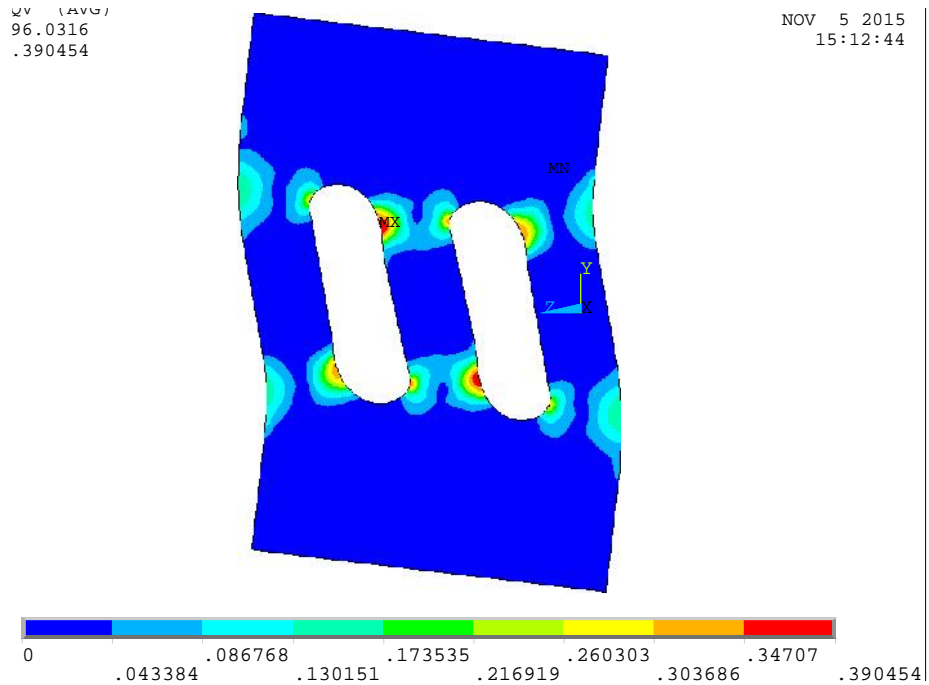


Figure 7-26 Contour plot of von Mises plastic strain of fuse panel at 2.7% lateral drift ratio of the SC-EBF structure

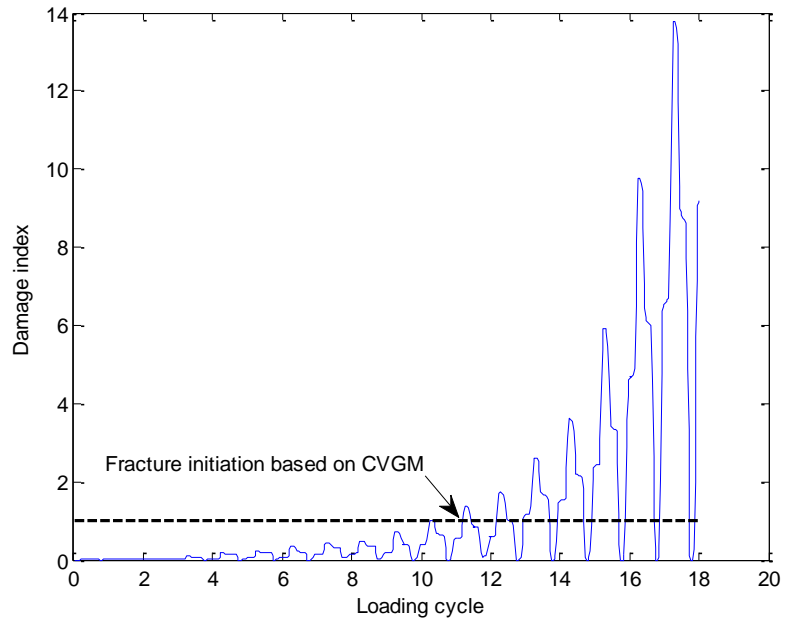


Figure 7-27 Damage index evolution with the load cycles

Table 7-1 Section properties of K-type SC-EBF structure members

Structural Member	Section	L (mm)	t_f (mm)	b_f (mm)	t_w (mm)	h (mm)
Beam	W24x104	2700	19.1	325.1	12.7	612.1
Column	W14x233	3367	43.7	403.9	27.2	406.4
Brace	W10x60	4395	17.3	256.5	10.7	259.1

Table 7-2 Properties of prototype K-type SC-EBF structure with double rocking link beams

K_1 (kN/mm)	209.8
K_2 (kN/mm)	7.22
F_y (kN)	557.3
α	3.44%
β_E	28.42%
F_u (kN)	1520
δ_u	2.8%

Chapter 8 : Summary, Conclusions, and Future Works

8.1. Research Summary

The self-centering eccentrically braced frame (SC-EBF) is a very promising seismic resistant structural system which possesses comparable elastic stiffness and load capacity to conventional eccentrically braced frames (EBF) while has no or very little residual drift after strong earthquakes. Furthermore, some of the challenging problems encountered in the design of self-centering moment resisting frames (SC-MRF), such as complicated floor design, has the potential to be cost-effectively solved. Hence the SC-EBF system provides a promising option in seismically resilient structural systems. A pilot study is conducted here to investigate the cyclic load behaviors of a variety types of SC-EBF structures. A competitive SC-EBF design can exhibit high initial stiffness, high ductility, proper strength and post-gap-opening stiffness. The main objective of this study is to achieve the self-centering behavior of the SC-EBF system in a prototype design and to study the contribution of key structural components to its overall cyclic load behaviors. It is hoped that the fundamental research of this dissertation study will provide building blocks for future design procedures for the SC-EBF systems. A summary of the research work aimed towards this objective is listed as follows:

In Chapter 2 the seismic-resistant structures utilizing different principles of self-centering mechanisms are introduced. The SC-EBF system investigated in this study was initially modified from the prototype SC-EBF system investigated by Cheng et.al. (2012).

Previous study of the behaviors of various types of shear links and shear walls was also

presented in this chapter, as the hysteretic energy dissipation devices used in the SC-EBF systems in this study are designed on the basis of the AISI 316L stainless steel perforated shear links.

In Chapter 3 the mechanical properties of AISI 316L stainless steel under large inelastic strains are experimentally calibrated. The elastic modulus of AISI 316L stainless steel is determined from the uniaxial tension test, and the material constants for the combined hardening model for the AISI 316L stainless steel are calibrated from cyclic loading test of round bars under large inelastic reversal strains. As ductile fracture under low-cycle-fatigue load is typically the governing mode in controlling the ductility of stainless steel perforated shear links, the void growth model (VGM) and the cyclic void growth model (CVGM) proposed by Kanvinde and Deierlein (2006, 2007) are calibrated for AISI 316L stainless steel from the experimental data from cyclic loading test of stainless steel notched bars.

In Chapter 4 the cyclic behaviors are evaluated for conventional shear links made of ASTM A992 steel, AISI 316L stainless steel, and G20Mn5QT cast steel. The material's ultimate strain of AISI 316L stainless steel is much higher than the ultimate strain of A992 structural steel and G20Mn5QT cast steel; hence the ductility of the shear links made of AISI 316L stainless steel is much higher than the ductility of the shear links made of A992 steel and G20Mn5QT cast steel. This behavior is reflected in the CVGM, where ductile fracture initiation is not observed in any of the selected AISI 316L stainless steel shear links during the entire loading process. However, the use of AISI 316L

stainless steel conventional shear links as the fuse devices in this study could cause other problems, for example, flange or web local buckling at large link rotation angle, and the strength of conventional AISI 316L stainless steel shear link is so high which could well exceed the desired strength range of the fuse devices for self-centering EBF structures. Hence web perforations are necessary to tune the strength properties of the AISI 316L shear links into the target range.

In Chapter 5 the cyclic behaviors of two types of AISI 316L stainless steel perforated shear links are evaluated through nonlinear finite element analysis. The accuracy of numerical model of perforated shear links are verified by comparing the experiment results with the numerical simulation results of the perforated cast steel shear links. Generally the ductility of AISI 316L stainless steel shear links with perforated slits are slightly lower than the ductility properties of the AISI 316L stainless steel shear links with perforated circular holes, yet the mechanical properties of the AISI 316L stainless steel shear links can be tuned with more flexibility by adjusting the sizes of the perforated slits; hence slit perforation pattern is selected for the fuse devices used for the SC-EBF systems in this study.

In Chapter 6 two types of SC-EBF systems are studied: K-type SC-EBF structure and D-type SC-EBF structure. For each type of the SC-EBF systems, four design cases with varying PT area and rocking link beam length are considered. The yielding of the PT strand is set as one of the controlling limiting state of the SC-EBF systems, as the yield stress of PT tendon is close to its fracture stress, and the load capacity of the SC-EBF

would be completely lost once the PT strand fractures. The characteristics of the SC-EBF systems are evaluated in terms of initial stiffness, post-gap-opening stiffness, effective linear limit force, maximum allowable drift ratio, and hysteretic energy dissipation capacity. Although the required PT strand usage is lower in the SC-EBF systems with short rocking link beams to achieve the same effective linear limit force, the ductility (represented by the maximum allowable drift ratio) of the SC-EBF systems with short rocking link beams is much lower than the SC-EBF systems with long rocking link beams, which is not desired in the ductile design for seismic-resistant structures. Additionally, the hysteretic fuse devices for both the SC-EBF systems with short rocking link beams and SC-EBF systems with long link beams must be specially designed to accommodate the large axial deformation.

In Chapter 7 a modified design of SC-EBF system with short rocking link beams is studied. In this modified design, two vertically parallel short rocking link beams are utilized in the SC-EBF system, which is different from the SC-EBF system investigated in Chapter 6, where only one rocking link beam is used. Two pairs of PT tendons are post-tensioned between the beam-to-column joints, with each pair being positioned at the mid-height of each rocking link beam. The fuse device used in the SC-EBF system with two rocking link beams is fabricated from AISI 316L stainless steel plate with perforated slits. This type of fuse device is very simple in design, and takes advantage of the shear yielding mechanism, which provides more stable energy dissipation.

8.2. Outcomes and Conclusions

1. AISI 316L stainless steel is proved to be very appealing in the application of fuse devices for seismic energy dissipation. However, due to the material's significant plastic strain hardening properties, web or flange buckling tends to be the dominant failure mode in controlling the strength and ductility performance of the AISI 316L stainless steel shear links made from hot-rolled sections. When hot-rolled sections are used, the strength of stainless steel shear links usually fall outside the desired strength range of the fuse devices in the SC-EBF systems; hence web perforations are generally necessary to ensure the strength of the stainless steel shear links tuned into the target range.
2. The cyclic load behaviors of stainless steel shear links with perforated circular holes and the stainless steel shear links with perforated slits are evaluated. Both types of perforated AISI 316L stainless steel shear links can reach the minimum required link rotation angle of 0.08 radians, yet the ductility of stainless steel shear links with perforated circular holes is generally higher than the ductility of the stainless steel shear links with perforated slits. It is verified in this study that the strength and stiffness of the perforated stainless steel shear links with circular holes are linearly related to the web area perforation ratio ρ if ρ is less than 16%; yet the strength and stiffness properties of the perforated stainless steel shear links with slits can be analytically calculated from the summation of the strength and stiffness values of segregated T-section modules and inner strip modules. Hence although the ductility of the stainless steel shear links with perforated slits is

lower than the ductility of the stainless steel shear links with perforated circular holes, more flexibility in tuning the mechanical properties of stainless steel shear links is possible by perforating slits on the web area of stainless steel shear links.

3. For the investigated K-type SC-EBF cases with one rocking link beam, the SC-EBF cases with short rocking link beams generally exhibit larger initial stiffness, post-gap-opening stiffness, effective linear limit force than the SC-EBF cases with long rocking link beams. To reach the same value of the effective linear limit force, the required usage of PT tendons is lower in the SC-EBF cases with short rocking link beams than the SC-EBF cases with long rocking link beams.

Generally the maximum drift ratio of the SC-EBF cases with short rocking link beams is smaller than the maximum allowable drift ratio of the SC-EBF cases with long rocking link beams if the same length of PT is used. This is because the link rotation angle of the SC-EBF system with short rocking link beam is much larger than the SC-EBF system with long rocking link beam at the same lateral drift ratio; hence the PT tendon force increases much more rapidly with the increasing drift ratio in the SC-EBF cases with short rocking link beams, rendering the SC-EBF system with short rocking link beam less ductile than the SC-EBF system with long rocking link beam when the same PT tendon length is used for both.

4. A modified design of the SC-EBF system with two vertically parallel short rocking link beams is also examined, which combines the advantages of both the SC-EBF with one short rocking link beam and the SC-EBF with one long rocking

link beam. The elastic stiffness and the post-gap-opening stiffness of the SC-EBF with two rocking link beams are closer to the elastic stiffness and the post-gap-opening stiffness of the SC-EBF with one long rocking link beam case, yet the effective linear limit force and the energy dissipation capacity of the SC-EBF with two rocking link beams are higher than the SC-EBF system with one short rocking link beam case; and the maximum allowable drift ratio of the SC-EBF with two rocking link beams is even higher than the maximum allowable drift ratio of the SC-EBF with one long rocking link beam case.

5. For the SC-EBF system with one rocking link beam, the applied fuse device must be specially designed from hot-rolled AISI 316L stainless steel link. Special designs must be applied to the fuse link beam to release the large axial stress due to gap opening. Especially in the SC-EBF cases with long rocking link beams, the stainless steel fuse link beams become very slender. To tune the mechanical properties of the stainless steel fuse links and to prevent local buckling from happening prior to yielding under the shear force during the loading process, slits are perforated over the web area and transverse stiffeners are provided at very close spacing. However, the fuse device used for the SC-EBF with two rocking link beams is directly made from the AISI 316L stainless steel plate with perforated slits, which is very simple in design and could reduce the cost for the fuse device (because no finger joint is needed).
6. Analytical method is proposed to predict the force-displacement relationships of the K-type SC-EBF system under cyclic loading. The analytical force-

displacement expressions for the investigated SC-EBF cases match well with the finite element analysis results. The analytical formulas are believed to be useful building blocks for future design methodology development for SC-EBF systems.

8.3. Recommendations for Future Research

1. Although self-centering behavior is observed for the investigated SC-EBF systems in this study, the member sizes for the prototype SC-EBF structures in this study are not optimized for multistory building design. To ensure the observance of self-centering behaviors in these prototype structures, the section sizes of the beams, columns, braces, and the rocking link beams might be over-designed for large stiffness and strength. Future research is suggested to further optimize the sizes of these structural members for a more economical design.
2. The fuse devices adopted for the SC-EBF with two rocking link beams in Chapter 7 can be further optimized for higher ductility. Currently based on the CVGM criteria, ductile fracture is observed during the loading cycle corresponding to 3% drift ratio, while the PT tendon is still far below its yield stress. The sizes of the perforated slits can be adjusted to postpone the initiation of ductile fracture.
3. Experimental testing of full-scale SC-EBF structure is desirable for further study of its behavior.

REFERENCE

- AISC. (2010). "Seismic provisions for structural steel buildings." ANSI/AISC 341-05. Chicago, IL.
- ANSYS (2015). ANSYS Mechanical APDL, version 15.0, ANSYS Academic Teaching Introductory. ANSYS, Inc., Canonsburg, Pennsylvania, USA.
- Alavi, E. and Nateghi, F. (2013). "Experimental study on diagonally stiffened steel plate shear walls with central perforation." *J. Constr. Steel Res.*, 89, 9-20
- Anderson, T.L. (1995). *Fracture mechanics*, 2nd Ed., CRC, Boca Raton, Fla.
- Ashraf, M., L. Gardner, and D.A. Nethercot. (2006). "Finite element modelling of structural stainless steel cross-sections." *Thin-Walled Structures*, 44: 1048-1062.
- Beremin, F.M. (1981). "Cavity formation from inclusions in ductile fracture of A508 steel." *Matallurgical Transactions*, Vol. 12 a, PP 723-731
- Bhowmick, A.K., Grondin, G.Y., Driver, R.G. (2014). "Nonlinear seismic analysis of perforated steel plate shear walls." *J. Constr. Steel Res.*, 94, 103-113
- Chaboche, J.L. and G. Rousselier. (1983). "On the plastic and viscoplastic constitutive equations—Part II: application of internal variable concepts to the 316 stainless steel," *J. Pressure Vessel Technol.* 105(2), 159-164.

- Chaboche, J.L. (2008). "A review of some plasticity and viscoplasticity constitutive theories," *International Journal of Plasticity*, 24(10): 1642 - 1693.
- Cheng, C.T., Hsu, C.H., Lin, K.C. (2012). "Seismic Behavior of Self-centering Designed Eccentrically Braced Frames." *The 15th World Conference on Earthquake Engineering, Lisbon, Portugal*.
- Chi, W.M. (2000), "Prediction of steel connection failure using computational fracture mechanics." *PhD Dissertation*, Stanford University, Stanford, California
- Christopoulos, C., Filiatrault, A., Uang, C.M. (2002) "Self-centering post-tensioned energy dissipating (PTED) steel frames for seismic regions." *Doctoral Dissertation*, University of California, San Diego, USA.
- Dusicka, P., A.M. Itani, and I.G. Buckle. (2004). "Evaluation of conventional and specialty steels in shear link hysteretic energy dissipators." *13th World Conference on Earthquake Engineering*. Vancouver, B.C., Canada.
- Gardner, L. (2005). "The use of stainless steel in structures." *Prog. Struct. Engng Mater*, 2005: 7:45-55.
- Gardner, L., and D.A. Nethercot. (2004). "Numerical modeling of stainless steel structural components—a consistent approach." *Journal of Structural Engineering*, 130: 1586-1601.

Garlock, M.M., Sause, R., Ricles, J.M. (2007) "Behavior and Design of Posttensioned Steel Frame Systems." *J. Struct. Eng. ASCE*, 133(3)

Hancock, J. W., and Mackenzie, A. C. 1976. "On the mechanics of ductile failure in high-strength steel subjected to multi-axial stress states." *J. Mech. Phys. Solids*, 24(3), 147-169.

Henry, R.S., Aaleti, S., Sritharan, S., Ingham, J.M. (2010). "Concept and Finite-Element Modeling of New Steel Shear Connectors for Self-Centering Wall Systems." *J. ENG. MECH-ASCE*, 136(2).

Hu, X., Zhang, Y., Nasim, S.M., Ingham (2012). "Seismic Performance of Reinforced Concrete Frames Retrofitted with Self-Centering Hybrid Wall." *Advances in Structural Engineering*, 15(12).

Iwasaki, T., Kawashima, K., Hasegawa, K., Koyama, T., and Yoshida, T. (1987). "Effect of Number of Loading Cycles and Loading Velocity on Reinforced Concrete Bridge Piers." 19th Joint Meeting US-Japan Panel on Wind and Seismic Effects, UJNR, Tsukuba.

Jacobsen, A., Hitaka, T., Nakashima, M. (2010). "Online Test of Building Frame with Slit-Wall Dampers Capable of Condition Assessment." *J. Constr. Steel Res.*, 66, 1320-1329

- Kanvinde, A.M. and Deierlein, G.G. (2006). "Void growth model and stress modified critical model to predict ductile fracture in structural steels." *J. Struct. Eng. ASCE*, 132(12)
- Kanvinde, A.M. and Deierlein, G.G. (2007). "Cyclic void growth model to assess ductile fracture initiation in structural steels due to ultra low cycle fatigue." *J. Struct. Eng. ASCE*, 133(6)
- Kasai, K. and Popov, E. (1986). "General behavior of WF steel shear link beams." *J. Struct. Eng.*, 112(2): 362–382.
- Kaufmann, E.J., Metrovich B.R., and Pense A.W. (2001). "Characterization of cyclic inelastic strain behavior on properties of A572 Gr. 50 and A913 Gr. 50 rolled sections." ATLSS report, No. 01–13. Bethlehem, PA: Lehigh University
- Ke, K. and Chen, Y. (2014). "Plastic-Energy-Based Seismic Assessment of Steel Frame-Steel Shear Wall with Slits." *J. Tongji Univ.*, 42(6)
- Kim, H.J. and Christopoulos, C. (2008) "Friction Damped Posttensioned Self-Centering Steel Moment-Resisting Frames." *J. Struct. Eng. ASCE*, 134(11)
- Kim, H.J. and Christopoulos, C. (2009) "Seismic design procedure and seismic response of post-tensioned self-centering steel frames." *Earthquake Engng. Struct. Dyn.*, 38, 355-376

- Koppal, M. and Eatherton, M.R. (2013). "Perforated Steel Plate Shear Walls for Tunable Seismic Resistance." *Structures Congress ASCE*
- Li, R., Zhang, Y., Tong, L. (2015). "Numerical study of the cyclic load behavior of AISI 316L stainless steel shear links for seismic fuse device." *Frontiers of Structural and Civil Engineering*, 8(4), 414-426
- Mago, N.M. (2013). "Finite Element Analysis of Eccentrically Braced Frames with Replaceable Link." HERA Report R4-145, Heavy Engineering Research Association, Manukau
- MacRae, G. and Clifton, C. (2013) "Low Damage Design of Steel Structures." *Steel Innovations 2013 Workshop, Christchurch, New Zealand*
- Malley, J.O., and Popov, E. (1984). "Shear links in eccentrically braced frames." *Journal of Structural Engineering*, 110(1): page number.
- McClintock, F.A. (1968). "A criterion for ductile fracture by the growth of holes." *Proc.*, ASME Meeting APM-14, ASME
- McMeeking, R. M., and Parks, D. M. (1979). "On criteria for J-dominance of crack-tip fields in large scale yielding." *Elastic-plastic fracture, ASTM STP 668*, ASTM, West Conshohoken, Pa., 175–194.
- Norris, D. M., Jr., Reaugh, J. E., Moran, B., Quinones, D. F. (1978). "A plastic-strain, mean-stress criterion for ductile Fracture." *J. Eng. Mater. Technol.*, 100(3), 279–286.

- Okazaki, T. and Engelhardt, M.D. (2007). "Cyclic loading behavior of EBF links constructed of ASTM A992 steel." *J. Constr. Steel Res.*, 63, 751-765
- Panontin, T. L., and Sheppard, S. D. (1995). "The relationship between constraint and ductile fracture initiation as defined by micromechanical analyses." *Fracture mechanics: 26th Volume, ASTM STP 1256*, ASTM, West Conshohoken, Pa., 54–85.
- Park, R. (1989). "Evaluation of Ductility of Structures and Structural Assemblages from Laboratory Testing." *Bulletin of the New Zealand National Society for Earthquake Engineering*, Vol. 22, No. 3.
- Rasmussen, K.J.R. (2003). "Full-range stress–strain curves for stainless steel alloys." *Journal of Constructional Steel Research*, 59(1): 47-61.
- Rice, J. R., and Tracey, D. M. (1969). "On the ductile enlargement of voids in triaxial stress fields." *J. Mech. Phys. Solids*, 17(3), 201-217.
- Richards, P. W., and Uang, C. M. (2003). "Development of testing protocol for short links in eccentrically braced frames." *Rep. No. SSRP–2003/08*, Dept. of Structural Engineering, Univ. of California at San Diego, La Jolla, Calif.
- Richards, P. W., Uang, C. M. (2006)." Testing protocol for short links in eccentrically braced frames." *J. of Structural Engineering*, 132(8).
- Richards, P.W. (2010) "Estimating the Stiffness of Eccentrically Braced Frames." *Practice Periodical on Structural Design and Construction, ASCE*, 15(1)

- Ritchie, R.O., Server, W.L., and Wullarert, R.A. (1979). "Critical fracture stress and fracture strain models for the prediction of lower and upper shelf toughness in nuclear pressure vessel steels." *Metallurgical Transactions*, Vol. 10A, pp 1557-1570
- Ricles, J. M., Sause, R., Peng S.W., Lu, L.W. (2002) "Experimental Evaluation of Earthquake Resistant Posttensioned Steel Connections." *J. Struct. Eng. ASCE*, 128(7)
- Ricles, J. M., Sause, R., Wolski, M., Iyama, J. (2006) "Post-Tensioned Moment Connections with A Bottom Flange Friction Device for Seismic Resistant Self-Centering Steel MRFs." *The 4th International Conference on Earthquake Engineering, Taipei, Taiwan*.
- Rojas, P., Ricles, J.M., Sause, R. (2005) "Seismic Performance of Post-tensioned Steel Moment Resisting Frames with Friction Devices." *J. Struct. Eng. ASCE*, 131(4)
- Prinz, G.S. and Richards, P.W. (2009). "Eccentrically braced frame links with reduced web sections." *J. Constr. Steel Res.*, 65, 1971-1978.
- Rai, D.C. and Wallace, B.J. (1998). "Aluminium shear-links for enhanced seismic resistance." *Earthquake Engng. Struct. Dyn.*, 27, 315-342
- Sause, R., Ricles, J.M., Roke, D.A., Chancellor, N.B., Gonner, N.P. (2010) "Large-Scale Experimental Studies of Damage-Free Self-Centering Concentrically-Braced Frame under Seismic Loading." *Structures Congress, ASCE*, 1498-1509

- Seo, C.Y. and Sause, R. (2005) "Ductility Demands on Self-Centering Systems under Earthquake Loading." *ACI Structural Journal*, 102(2)
- Shi, G., Wang, F., Dai, G., Shi, Y., Wang, Y. (2012). "Experimental study of high strength structural steel Q460D under cyclic loading." *China Civil Engineering Journal*, 45(7)
- Uang, C.M. (1989). "Establishing R (or R_w) and C_d factors for building seismic provisions." *J. Struct. Eng. ASCE*, 117(1)
- Vian, D., Bruneau, M., Purba, R. (2008). "Special perforated steel plate shear walls with reduced beam section anchor beams. II: analysis and design recommendations." *J. Struct. Eng. ASCE*, 135(3)
- Wu, Q., Chen, Y., Zhou, F. (2012) "Cyclic loading tests of Q345B under large inelastic strains." *China Sciencepaper Online*, [2012-06-21].
<http://www.paper.edu.cn/releasepaper/content/201206-325>.
- Zhang, Z. (2015). Experimental Study on Hysteretic Behavior of Replaceable Cast Steel Shear Link Beams, Master thesis, Department of Structural Engineering, Tongji University, Shanghai, China.